Yrast and near yrast structure of nuclei around A $\sim$ 200 involving high-j orbitals

By

Soumik Bhattacharya

Enrolment No: PHYS04201404003

Variable Energy Cyclotron Centre, Kolkata

A thesis submitted to the
Board of Studies in Physical Sciences

In partial fulfillment of requirements

for the Degree of

DOCTOR OF PHILOSOPHY

of

HOMI BHABHA NATIONAL INSTITUTE

Dec, 2019

Homi Bhabha National Institute

Recommendations of the Viva Voce Committee

As members of the Viva Voce Committee, we certify that we have read the dissertation prepared by Soumik Bhattacharya entitled "Yrast and near yrast structure of nuclei around A~200 involving high-j orbitals" and recommend that it may be accepted as fulfilling the thesis requirement for the award of Degree of Doctor of Philosophy.

Chairman –	Dr. Chandana Bhattacharya	C. Bhattacharya 15-5-2020
Guide / Convener –	Dr. Sarmishtha Bhattacharyya	S. Bhattacharyya 15-5-2020
Co-guide - (if any)		
Examiner -	Prof. H.P. Sharma	H. Sharma 15-5-2020
Member 1-	Dr. Parnika Das	Parnika Das 15/5/2020
Member 2-	Prof. Anjali Mukherjee	

Final approval and acceptance of this thesis is contingent upon the candidate's submission of the final copies of the thesis to HBNI.

I/We hereby certify that I/we have read this thesis prepared under my/our direction and recommend that it may be accepted as fulfilling the thesis requirement.

Date: 15-5-2020

Place: KOLKATA

Signature
Co-guide (if any)

S. Bhattacharyya 15/5/2020.
Signature
Dr. Sarmishtha Bhattacharyya
Guide

Homi Bhabha National Institute

Ph.D. Thesis Evaluation Report

1. Name of the Constituent Institution: **VARIABLE ENERGY CYCLOTRON CENTRE**
2. Name of the Student: Soumik Bhattacharya
3. Enrolment No.: PHYS04201404003
4. Title of Thesis: Yrast and near yrast structure of nuclei around A ~ 200 involving high-j orbitals
5. Name of the Board of Studies: **PHYSICAL SCIENCES**

Recommendation

Tick one of the following:

1. The thesis in is present from is commended for the award of the Ph.D. Degree [XXX]
2. The thesis is commended for the award of the Ph. D. degree. However, my Suggestion for improving the thesis may be considered at the time of the viva voce examination and if the viva voce board deems it appropriate, the same may be incorporated in the thesis based on the discussion during the viva voce examination. The revised thesis need not be sent to me. [ ]
3. The thesis should be revised as peer the suggestions enclosed. I would like to see The revised thesis incorporating my suggestions before I give further Recommendation. [ ]
4. The thesis is not acceptable for the award of the Ph. D. degree. [ ]

Date: **14 February 2020** (Signature):

Name of Examiner: **PROF. P.H. REGAN**
And Affiliation **UNIVERSITY OF SURREY, UK**

Homi Bhabha National Institute

Ph.D. Thesis Evaluation Report

1. Name of the Constituent Institution:	**VARIABLE ENERGY CYCLOTRON CENTRE**
2. Name of the Student:	Soumik Bhattacharya
3. Enrolment No.:	PHYS04201404003
4. Title of Thesis:	Yrast and near yrast structure of nuclei around A ~ 200 involving high-j orbitals
5. Name of the Board of Studies:	**PHYSICAL SCIENCES**

Recommendation

Tick one of the following:

1. The thesis in its present form is recommended for the award of the Ph.D. Degree ☐

2. The thesis is recommended for the award of the Ph. D. degree. However, my Suggestion for improving the thesis may be considered at the time of the viva voce examination and if the viva voce board deems it appropriate, the same may be incorporated in the thesis based on the discussion during the viva voce examination. The revise thesis need not be sent to me. X

3. The thesis should be revised as peer the suggestions enclosed. I would like to see The revised thesis incorporating my suggestions before I give further Recommendation. ☐

4. The thesis is not acceptable for the award of the Ph. D. degree. ☐

Date: 27-4-2020

HPSharma

(Dr H P Sharma)
Professor
Department of Physics
Institute of Science
BHU Varanasi 221005

Contents

List of Figures

List of Tables

Chapter 7

Summary and Future scope

7.1 Summary

In the present thesis work, high spin level structures of odd-Z ^{199}Tl, odd-N ^{199}Hg and odd-odd ^{200}Tl nuclei, of A$\sim$200 mass region near $Z = 82$ have been studied and the effect of the available high-j orbitals on the shape of these nuclei have been investigated using the techniques of high resolution in-beam γ ray spectroscopy. The information of the yrast and near yrast levels at high and moderate spins have been considerably extended with definite spin parity were determination for most of the levels. The newly observed band structures, identical partner bands and single particle levels are compared with the systematics of the neighboring nuclei and interpreted in the light of contemporary theoretical calculations. The nuclei of interest (^{199}Tl($Z = 81, N = 118$), ^{199}Hg ($Z = 80, N = 119$) and ^{200}Tl ($Z = 81, N = 119$)) in the present thesis work are situated just one neutron or proton away from each other, yet exhibits variety of structures. The shapes and level structures of these nuclei are found to be highly dependent on the individual effect of the proton and neutron single particle orbitals as well as on the interplay of them with the core.

The excited states of the nuclei studied in the present thesis were populated by using both heavy and light (α beam) ion induced fusion-evaporation reactions. Both ^{199}Tl and ^{199}Hg were populated using the α beam from K-130 Cyclotron, Kolkata whereas the high spin states of ^{200}Tl were populated by ^{7}Li beam from BARC-TIFR Pelletron facility, Mumbai. The advantage of using α beam is to get a uniquely populated channel at a particular energy with a population of many near-yrast exotic structures involving different high-j orbitals which is one of the main aim of the present work. The Compton Suppressed Clover HPGe detectors of Indian National Gamma Array (INGA) at VECC, Kolkata and TIFR, Mumbai were used to detect the de-exciting γ rays and the time stamped data were collected using digital data acquisition system in singles as well as double coincidence trigger conditions to study the properties of ^{199}Hg and ^{200}Tl nuclei respectively. A in-house array (VENUS) with six Compton suppressed Clover HPGe detectors and a VME base data acquisition system with analogue electronics set up was used at VECC for the collection of list mode data for ^{199}Tl and partly for ^{199}Hg experiments. Symmetric and asymmetric $\gamma - \gamma$ matrices have been built from the raw data and analyzed for obtaining the coincidence relationships and determining the DCO ratio, IPDCO ratio values to obtain the spins and parities of the levels. The coincidence relation verification from $\gamma - \gamma$ matrix and $\gamma - \gamma - \gamma$ coincidence cube, intensity balance of the feeding and decaying γ rays from a particular level and angular distribution measurements were also performed for proper placements and proper assignments of multipolarity of the γ rays in the level scheme where and when needed.

The shapes and the properties of the nuclei, obtained experimentally in this thesis work, were interpreted in the framework of cranked shell model calculations using Woods-Saxon potential including Struntisky shell correction and pairing correlation. The total Routhian surfaces (TRS) were calculated as a function of Frequency using this model in the $\beta_2 - \gamma$ deformation mesh points with minimization on hexadecapole deformation β_4. The minima in these plots give the equilibrium deformation of the nuclei.

The spectroscopic information of ^{199}Tl has been enriched considerably through the observation and placement of 53 new transitions in the level scheme and assigning the spins and parities to the different levels. A few near-yrast structures involving the intruder $\pi h_{9/2}$ have been observed in this odd-mass nucleus and extended beyond the band crossing. It has been observed, while comparing the band structures with the other neighbouring odd-A Tl isotopes, that the remarkable similarity of the first few states belonging to the $\pi h_{9/2}$ band in odd-A Tl nuclei continues to persist till the $N = 118$ isotope. However, after the band crossing of the yrast states, the 3-quasi particle (qp) configuration $\pi h_{9/2}^{-1} \otimes \nu i_{13/2}^{2}$, in all lighter odd mass Thallium isotopes, become non-yrast at $N = 118$ for ^{199}Tl. From the alignment plot it has been found that a neutron pair alignment in $\nu f_{5/2}$ or in $\nu p_{3/2}$, with a lesser alignment gain, becomes more favourable than a pair breaking in $\nu i_{13/2}$ and the yrast configuration (for band B2 in Fig. 4.5 in Chapter 4) changes to $\pi h_{9/2}^{-1} \otimes \nu (f_{5/2}/p_{3/2})^2$ in ^{199}Tl which continues to be present in the next odd-mass ^{201}Tl isotope as well. A new positive parity band (band B3 in Fig. 4.5 in Chapter 4.) with almost the same initial alignment as in band B2 has been found in ^{199}Tl, which is interpreted to generate from $\pi h_{9/2}^{-1} \otimes (\nu i_{13/2} \otimes \nu j_{-})^2$ configuration where $j_{-} = f_{5/2}, p_{3/2}$. A new $11/2^{-}$ state, which is already reported in neighbouring Au nuclei with a band structure above it, has been identified for the first time in this nucleus and has been interpreted as due to the involvement of the $\pi h_{11/2}$ orbital. However, no band structure has been found to be built above it. The TRS calculations suggest oblate deformation for the 1-qp negative parity $\pi h_{9/2}$ band, whereas the low-lying 1-qp $\pi s_{1/2}$ positive parity band (B5) appears to be near spherical, which are in good agreement with the experimental observation. A shape evolution from γ-soft shape to a triaxial shape at higher frequency, through an axially deformed oblate shape, is predicted for the 3-qp positive parity band. However, with limited spin obtained through α-induced reaction in ^{199}Tl, this triaxial shape cannot be confirmed experimentally from the present data.

Three new near yrast band structures as well as a few single particle levels in ^{199}Hg have been established with the placement of 31 new transitions in the level scheme. The yrast $\nu i_{13/2}$ band has been extended beyond $25/2^{+}$ for the first time and found to continue with the same configuration ($\nu i_{13/2}^{1}$) up to $31/2^{+}$ spin through non yrast states. It has been noticed that the similarities of the low-lying states in the decoupled $\nu i_{13/2}$ band in odd-A Hg nuclei continues to persist up to the $N = 119$ isotope. The non-observance of the pair breaking in the $\nu i_{13/2}$ orbital, is the striking difference of the 3-qp structures in the neighbouring lighter odd mass Hg isotopes. This has been interpreted as due to Pauli blocking effect of the odd neutron in the last available space in $i_{13/2}$ orbital as the neutron number reaches $N = 119$ in case of ^{199}Hg. A non-yrast $\Delta I = 2$, E2 band is observed to decay to the yrast $\nu i_{13/2}$ band through a set of $\Delta I = 1$

transitions, of predominantly E2 character. A comparison of the calculated Polarization and DCO ratio values for one of the $\Delta I = 1$ connecting transitions (945 keV) (from band B2 to band B1 in Fig. 5.3 in chapter 5) with the experimental values yields a large E2 mixing (78%). All the other connecting transitions are also found to be predominantly E2 from their DCO and IPDCO ratio values. The experimental findings, therefore, indicate towards the possible observation of wobbling band, in this mass region for the first time. The wobbling bands are the signature of triaxiality in nuclei. Since the neighbouring region is established as a rich ground to find triaxial shapes from the earlier studies, the possibility of the appearance of this kind of exotic structure is expected in ^{199}Hg. The increasing value of wobbling energy, E_{wobb} as a function of spin suggests ^{199}Hg nucleus as a longitudinal wobbler which involves a odd neutron in high-j $i_{13/2}$ orbital. Along with the observation of $n_\omega = 0$ (band B1) and $n_\omega = 1$ (band B2) band, another rotational band with same parity (band B3) is also identified in ^{199}Hg which decays to the band B1 as well as to the band B2. This could be interpreted as the $n_\omega = 2$ wobbling partner band. But as this band is not well extended in spin, the nature of it could not be confirmed in the present thesis. Another new partner band with $23/2^+$ (same parity as the yrast band) as the band head, has been established for the first time and interpreted as the signature partner band of the yrast 1-qp $\nu i_{13/2}$ band.

A negative parity semi-decoupled band has also been observed in the present work and the spins and parities of the states, which were tentatively assigned previously, are confirmed in the present thesis with the help of polarization measurements. It has been found that the states, belong to this band, is continued up to $39/2^-$ spin with the same $(\nu i_{13/2})^2 \otimes \nu(j_-)^1$ configuration, where $j_- = f_{5/2}, p_{3/2}, p_{1/2}$.

The combined effect of neutron ($i_{13/2}$) and proton ($h_{9/2}$) high-j orbitals on the shape of the nucleus near A$\sim$200 mass has been explored by studying the level structures of ^{200}Tl ($Z = 81, N = 119$). The high spin states of ^{200}Tl has been extended significantly, up to the spin of $22\hbar$ and excitation energy of $\sim$ 5.2 MeV, through the observation and placement of 60 new transitions in the level scheme. A few band structures involving the intruder $\pi h_{9/2}$ and high-j neutron orbitals have been observed in this odd-odd nucleus. The shape driving effect of the $\pi h_{9/2}$ orbital plays important role to drag the nucleus towards oblate deformation, in spite of being close to ^{208}Pb ($Z = 82, N = 126$) magic nucleus. The systematics of the ^{200}Tl are compared with the band structures in the other odd-odd Tl isotopes. It has been observed that the $\pi h_{9/2} \otimes \nu i_{13/2}$ band in the odd-odd Tl nuclei still exists up to $N = 119$ neutron number and a strongly coupled band structure has been formed. The band crossing for the main yrast band are interpreted to be generated from a pair of neutron alignment in the $\nu i_{13/2}$ orbital which is the case for the lighter even mass Thallium isotopes as well. The shapes corresponding to the different bands, and band crossing phenomena have been discussed in the light of the cranking model calculations. Oblate deformation is obtained for the 2-qp bands in ^{200}Tl while interestingly, the 4-qp band seems to have a triaxial deformation. The band crossing frequencies and the alignment gains in these bands are in good agreement with the cranking calculations. The calculations also predict that the $\pi h_{9/2} \otimes \nu i_{13/2}$ band becomes γ-soft after the band crossing due to the alignment of a pair of neutrons in the $\nu i_{13/2}$ orbital. It would be interesting to extend the 4-qp bands to higher rotational frequencies to compare their shape and alignment gains.

In the present thesis it was found that the high-j proton or neutron orbitals highly influence the shapes of the Tl and Hg nuclei in such a way so as to induce deformation near $Z = 82, N = 126$ spherical shell closure, which resulted into deformed band structures. The even A Hg nuclei (which can be considered as the underlying even-even core of these nuclei studied in this thesis work) are observed to have a decoupled band structure based on slightly oblate shape. With an extra proton occupying the shape driving $\Omega = 9/2$ projection of intruder $\pi h_{9/2}$ orbital, with a little excitation energy, the nuclei are driven towards deformation and a strongly coupled band has been observed in both ^{199}Tl, ^{200}Tl nuclei. On the other hand, the effect of single neutron in the $\Omega = 1/2$ projection of high-j $\nu i_{13/2}$ orbital generates a non-yrast band structure in odd mass ^{199}Hg nucleus (with a band head of $15/2^+$) along with the $\nu i_{13/2}$ decoupled band, which is a possible wobbling partner band, indicating triaxial shape. All the nuclei studied in the present thesis show that the proton pair alignment is less favourable than the neutron pair alignment in the available orbitals. Beyond mass A$\sim$200 the band structure is absent for all the Hg and Tl nuclei. Therefore, it may be inferred that the $N = 120$ is considered as the boundary of deformed structure, after which the Tl and Hg nuclei show near spherical shape and the excited states are mostly of single particle structures. It may be noted that, with $N = 120$ the $\nu i_{13/2}$

orbital is full and the effect of this shape driving orbital is absent beyond $N = 120$ to deform the nucleus.

7.2 Future Scope

The exciting results of the present thesis work draw interest for further studies in both experimental and theoretical directions, such as:

For ^{199}Tl nucleus a new $11/2^+$ level has been found to exist. A band structure on the top of this level has been observed in all the nearby Au nuclei ($Z = 79$) which is interpreted as of $\pi h_{11/2}$ configuration. This level in ^{199}Tl is also interpreted to be generated from the proton $h_{11/2}$ orbital, but no band structure has been observed above it. It will be interesting to investigate the band structure, build on the $\pi h_{11/2}$ for the odd mass Thallium nuclei, as seen in all nearby Au nuclei. This will provide an important information as weather $Z = 79$ (Au nuclei) are the limit for the $\pi h_{11/2}$ orbital to induce deformation i.e. the extent of the $\pi h_{11/2}$ orbital to influence a deformed shape in a nucleus close to proton shell closure $Z = 82$.

In the study of ^{199}Hg, many non yrast band structures have been observed. One of them is showing the signature of possible wobbling motion. To confirm this, the mixing ratios of all the connecting transitions from the proposed wobbling bands to the yrast band have to be determined. Therefore further experiment to populate the non-yrast states of ^{199}Hg with higher statistics is warranted. Also the search for this similar kind of structures in nearest odd isotope ^{197}Hg as well as in lighter odd mass Hg isotopes is obvious and seeks immediate attention. The analogous lower lying states similar to that of the proposed wobbling band have already been reported in $^{191-195}$Hg. But the higher states of the same configuration and the nature of the connecting transitions are yet to be discovered. As the nuclei in mass region A$\sim$190-200 are prone to triaxial shapes, as already reported in ^{194,195,198}Tl as a form of chirality, the wobbling mode of excitation of a triaxial nucleus may be a possible to be present in these nuclei.

Along with all the possible future experimental endeavor for the odd mass Hg nuclei in this region, theoretical calculations are also necessary as a part of the important investigation to establish the wobbling structure in odd mass Hg nuclei for the first time. However, wobbling motion is a manifestation of a triaxial nucleus. The structures of band B1 and B2 in ^{199}Hg are, therefore, indicate the possibility of triaxial shape. This seeks an urgent validation via cranking model calculations with Woods-Saxon potential. Though the observed levels in $^{191-193}$Pt, analogous to that of ^{199}Hg, were well reproduced with Triaxial Rotor Model calculations, the current study does not include any theoretical canvas to interpret the wobbling motion in ^{199}Hg. Therefore, the yrast and non yrast states observed in ^{199}Hg are needed to be reproduced through model based calculations (like Triaxial Rotor Model or Tilted axis Cranking model) for the possibility of presence of γ deformation in this nucleus.

The investigation in the present thesis work, along with the results of the similar works done in recent past, establishes the effect of this intruder orbitals near the heaviest known proton spherical shell closure at $Z = 82$ to induce deformation (both axial and triaxial) in nuclei of A$\sim$190-200 region. It would be interesting and important to extend such studies for the heavier nuclei close to the heaviest known neutron shell closure at $N = 126$ to investigate the effect of the neutron intruder orbitals (with even higher j).

Another important aspect, which has not been addressed in the present thesis work, is the investigation of the presence and decay of the possible isomers at higher excitation energies in these nuclei. As the excitation energy increases, more and more particles will be occupying the high-j ($h_{9/2}, i_{13/2}$) orbitals. This would generate high angular momenta in these nuclei which would form yrast traps.

SUMMARY

In the present thesis, the effect of odd particle (nucleon) occupying high-j orbitals in driving the spherical structure of nuclei near shell closure towards deformation and generating higher angular momentum states, has been explored. For this purpose the structures of three neighbouring odd-even, even-odd and odd-odd nuclei below $Z = 82$ shell closure, viz., ^{199}Tl ($Z = 81, N = 118$), ^{199}Hg ($Z = 80, N = 119$), ^{200}Tl ($Z = 81, N = 119$) have been experimentally investigated using γ-ray spectroscopy methods. For ^{199}Tl, the odd valance proton is responsible for the generation of the lower lying states as single particle excitations and the collective features are observed for the band built on the high-j $\pi h_{9/2}$ orbital. For ^{199}Hg, the protons are paired and the level structures are solely depend on the odd neutron. By studying both the ^{199}Tl and ^{199}Hg nuclei, the individual effect of single neutron and single proton on the spherical core can be explored. The effect of both proton and neutron single particle excitations, as well as the residual interaction between them, can be well understood by investigating the odd-odd ^{200}Tl, with one odd proton and one odd neutron with respect to the closed ^{198}Hg core.

In the present thesis work, the excited states of the ^{199}Tl and ^{199}Hg were populated using the α beam from K-130 Cyclotron, Kolkata and the high spin states of ^{200}Tl were populated using ^{7}Li beam from BARC-TIFR Pelletron-LINAC facility, Mumbai. The yrast and near-yrast structures of these nuclei are studied using the VECC Array for NUclear Spectroscopy (VENUS) and Indian National Gamma Array (INGA) setup, consisting of Compton suppressed Clover HPGe detectors.

The spectroscopic information for each nuclei are extended considerably with the observation of several new transitions and the assignment of spins and parities to the newly found band structures as well as single particle levels.

Both the odd and even mass Thallium ($^{199-200}$Tl) nuclei, are found to have strongly coupled band structure, based on $\pi h_{9/2}$ orbital and extended beyond the band crossing frequency. Appearance of many non yrast bands, involving other available orbitals, indicates a structural change beyond $N = 120$ as the neutron number is approaching $N = 126$ magic shell closure.

The collective structures based on the deformed core are found to persist till the $N = 120$ for the Thallium ($Z = 81$) nuclei, after which the single particle structure dominates. The odd mass ^{199}Hg are situated in the transitional region of triaxial Pt ($Z = 78$) nuclei and spherical Pb ($Z = 82$) nuclei, which make it a suitable candidate to observe the competition between the single particle excitations and collective structures. The observation of few collective bands, as the partners of the decoupled $\nu i_{13/2}$ band, indicates a non-axial shape for this nucleus and the possibility of the appearance of the multi-phonon bands is explored. A new signature partner of the yrast band of ^{199}Hg is proposed in the present work.

The present thesis explored the role of the high-j orbital (mainly $\pi h_{9/2}$ and $\nu i_{13/2}$) in nuclei near A$\sim$200 region and below $Z = 82$ shell closure. It is found that the band structures still persist up to $N = 120$ neutron number, after which the collective features diminish due to the unavailability of the $\nu i_{13/2}$ orbital near the Fermi level in Thallium and Mercury nuclei.

Chapter 1

Introduction

The journey to know the atomic nucleus as a hadronic many-body system and the era of nuclear physics research began when Ernest Rutherford proposed its existence in 1911 [1] by the first nuclear reaction experiment by bombarding α particles on a gold foil. Bohr was the first person who helped us to understand the nucleus with a simple model explaining Rutherford's experiment in 1913 [2]. Initially the nuclei were assumed to be of spherical shape till 1924 when Wolfgang Pauli's suggestion leads us to understand that an excited nucleus could exist in a variety of shapes. In 1936 the proposal of Bohr and Fritz Kalckar suggested that the shape of a nucleus could be probed by measuring the gamma-ray photons decaying from an excited nucleus [3]. Since then, over 80 years, gamma-ray spectroscopy is considered and established as an essential tool to probe the structure of atomic nuclei exploring its various nature. First in 1939, the Liquid Drop Model (LDM) was proposed by Niels Bohr which could explain the most of the bulk properties (like binding energy) of nuclei known till then [4]. But it needed a quantum background to explain a few phenomena like the magnetic moments, two neutron or two proton separation energies etc. at nucleon numbers 2, 8, 20, 28, 50, 82 and 126, the so-called "magic numbers". The nuclei possessing protons or neutrons equal to these magic numbers, show extra stability with respect to the binding energy which gave rise to the concept of the most successful model "shell model" [5] involving quantum property in it. Nucleus mainly exhibits two kinds of behaviour: single particle and collective excitations. Our knowledge of

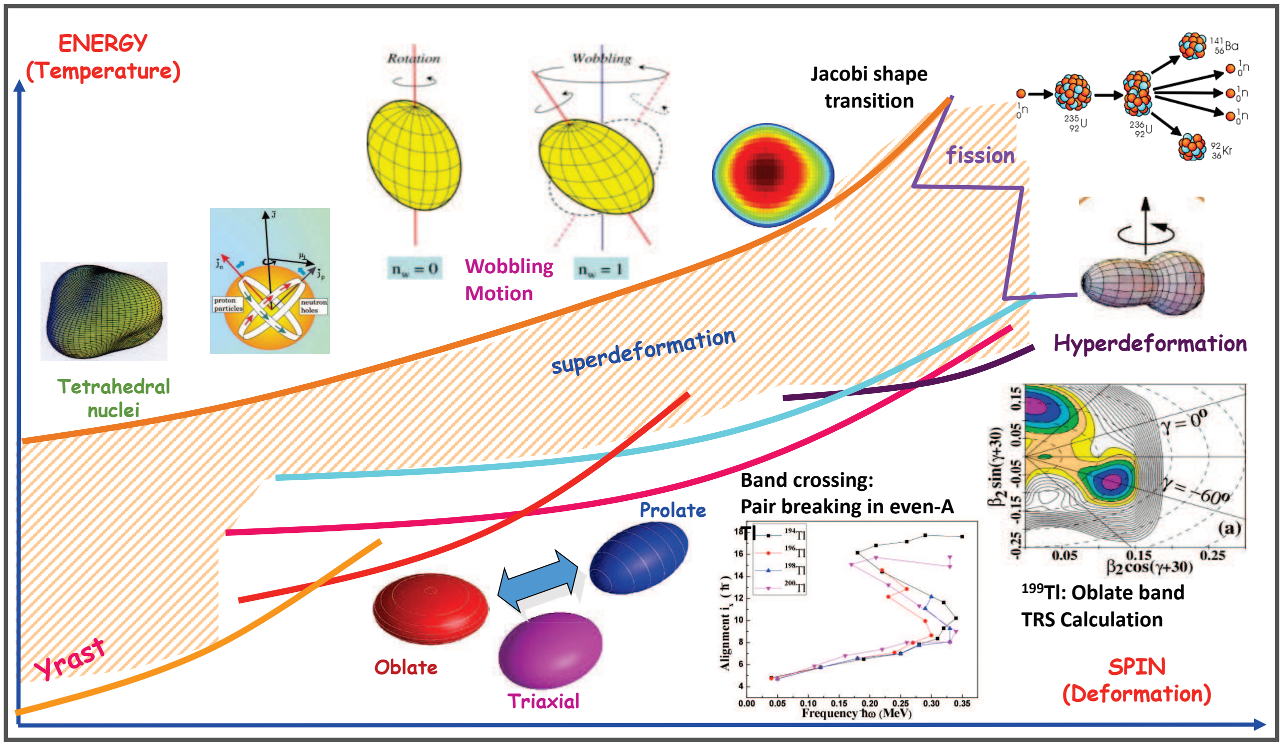

Figure 1.1: A schematic showing a sample of various nuclear structure phenomena, discovered from the 1980s to recent years.

behaviour of a nucleus is mainly owe to Aage Bohr, Ben Mottelson and James Rainwater who developed a theory based on the relationship between collective and single particle motion in the nucleus [6, 7, 8] which earned them a Nobel Prize in physics in 1975. Over the last and present centuries, many nuclear models have been developed and based on that, the theoretical interpretations of the experimental findings have been proposed to know the nature of the behaviour of the nucleus under various conditions. But the exact nature of the nuclear force is yet to be known, even after 100 years of its discovery. In this regards the NUCLEUS is still very much young and still surprises us with its exotic behaviour appearing as a function of excitation energy and angular momentum. A few of the phenomena has been depicted in the Fig. 1.1.

The strongly interacting fermions inside a nucleus display a remarkable diversity of phenomena and symmetries, which probably would not have been possible to observe without the combination of modern heavy and light-ion accelerators and multi-detector γ ray arrays. Availability of the state-of-the art γ ray detector arrays and variety of energetic beams from modern accelerators, led to reveal a series of new, exotic and often unexpected nuclear structure phenomena. The key issue, which concerns most of the experimental endeavors probing the properties of nuclei at high spin and energy, is the generation of angular momentum in nuclei by various modes of excitation. There are mainly two basic modes: Single particle excitation and collective excitation. The first: single particle (nucleon) excitations are experimentally observed as the complex, irregular excitation pattern of spherical or weakly deformed nuclei, having their nucleon number (neutron or proton number or both) in the proximity of the so called magic numbers. These single particle excitations reveals the intrinsic structure of the nucleus, involving the available single particle orbitals near Fermi surface. The second: the collective mode of motion reflects a regular sequence of energy levels as a function of angular momentum. Mainly the nuclei having nucleon number away from the shell closures exhibit such kind of excitations with deformed structure. The collective states are mainly the manifestation of different types of deformation and the underlying symmetries. The prolate or oblate shapes of nuclei are experimentally observed as the regular rotational energy level sequences. The phenomena, representing the triaxial shape of nuclei are very rare to observe experimentally. Recently, with the availability of modern high efficiency gamma-arrays, these rarely observed experimental phenomena were become possible to be explored. The triaxial shapes, which are related with the exotic phenomena like Chiral symmetry breaking or Wobbling motion of nuclei has gained its added attention of the researchers. The interplay of the single particle & collective excitation has remain a subject of intense discussion over the past couple of decades. An even more interesting aspect of the present day nuclear structure study is concerned with the shape polarization effect of the single particle orbitals in heavy nuclei with proton and neutron Fermi levels near the spherical shell closures.

A nucleus can be populated to its excited states and at high angular momenta by a few processes, such as, fusion evaporation reaction, Coulomb excitation, transfer reaction, β-decay, nuclear fission etc. Among them, the transfer reaction and the β-decay populate the nuclei with limited angular momentum. In order to reach high spins, fusion-evaporation reaction provides the most efficient way to populate the nucleus at high excitation energy and spin with reasonable cross section. The population of nucleus in the energy-angular momentum space depends on the reaction mechanism. The state, which is energetically lowest for a particular angular momentum, is usually called the yrast state. The other higher energetic states corresponding to the same angular momentum are called non-yrast states. The virtual line, connecting the set of observed yrast states is called the yrast line and no states exist below this yrast line. In heavy-ion induced fusion evaporation reaction, the nulcei are produced with sufficient energy as well as angular momentum. After few particle evaporation and emission of few γ rays, the nuclei come near the yrast line and then mostly decay through the yrast line upto the ground state. Whereas, in light-ion induced fusion evaporation reaction, the "entry" states [4] of the nuclei after particle evaporation are situated far from the yrast line and in this case, the nucleus passes through many non-yrast or near yrast states via γ decay. It is important to study both these two types of population of excited states and corresponding decay pathways, as they probe complimentary structures in an excited nucleus. In particular, the non-yrast excited states exhibit single particle as well as some of the low lying symmetry breaking exotic structures.

The nuclei near the magic shell closures are vast laboratories to test the interplay between the single particle excitations and collective behaviour. The excitations in the nuclei with proton number near $Z = 82$ magic number are expected to show single particle structures due to the proximity of spherical shell closure. Indeed, for ^{207}Tl ($Z = 81, N = 126$), the spins and parities of a few low lying states were interpreted as originated primarily due to the proton-hole excitation in the available orbitals near the Fermi level [11, 12]. As per the spherical shell model picture, the $\pi s_{1/2}$, $\pi d_{3/2}$, $\pi h_{11/2}$, $\pi d_{5/2}$ orbitals are available for the odd proton-hole with respect to the doubly magic ^{208}Pb ($Z = 82, N = 126$) core, which generates the lowest four states in ^{207}Tl, namely $1/2^+, 3/2^+, 11/2^-, 5/2^+$. Similarly, the low lying states in ^{209}Bi ($Z = 83, N = 126$), which has only a single valance proton particle outside the $Z = 82$ and $N = 126$ shell closures, could be interpreted as the pure proton single particle states. The spins and parities of few low-lying states in ^{209}Bi are $9/2^-, 7/2^-, 13/2^+, 5/2^-$ [13], which are interpreted as generated from the $h_{9/2}, f_{7/2}, i_{13/2}, f_{5/2}$ orbitals, respectively, which lie above the

$Z = 82$ proton shell closure. On the other hand, the $9/2^-[505]$ and $1/2^-[541]$ components of the high-j $\pi h_{9/2}$ orbital, situated above the $Z = 82$ shell closure, comes down in energy and intrude below the $Z = 82$ shell for oblate and prolate deformations, respectively. These orbitals can then be accessible by the valance proton in Tl nuclei at a reasonably low (∼1 MeV) excitation energy. Moreover, the high-j $\nu i_{13/2}$ orbital, situated just below the $N = 126$ shell closure, also has the similar shape driving property. These orbitals are, therefore, instrumental in breaking the spherical symmetry of a nucleus and induce deformation. The presence of unique parity high-j orbitals leads to the observation of long live isomers in the isotopes situated below $Z = 82$ shell closure. The effect of these proton and neutron orbitals on the structure of a nucleus can be better studied in Tl (odd-Z) and odd-N Hg ($Z = 80$) nuclei in $A = 200$ region having neutron number below $N = 126$. Due to the induced deformation for those high-j orbitals, these nuclei, are often observed to form, strongly coupled as well as decoupled band structures, built on the isomeric states involving high-j orbitals. The odd mass Thallium nuclei mainly show rotational oblate band structures based on $\pi h_{9/2}$ orbitals in $^{191-201}$Tl [20, 21, 16, 17, 18], whereas for odd mass Hg nuclei ($^{191-199}$Hg), the $\nu i_{13/2}$ orbital is responsible for the appearance of decoupled band structures with small deformation [17, 18, 15, 22, 28] at very low excitation energy. In odd-odd nuclei below $Z = 82$, $N = 126$ shell closure, both odd proton and odd neutron can occupy high-j orbitals. The strongly coupled oblate band structures is observed in even mass (odd-odd) Thallium isotopes($^{190-200}$Tl) [7, 8, 26, 10, 11, 12] with $\pi h^{-1}_{9/2} \otimes i_{13/2}$ configuration. Beyond $N = 120$ these band structures are not observed both in Thallium and Mercury nuclei. Instead, their level structures are mainly dominated by single particle excitations as reported in ^{202,203,206}Tl [4, 23, 5] and ^{202,203,204,205}Hg [33, 34, 35]. This transition of the excitation pattern in nuclei around A∼200 region with increasing neutron number needs more experimental attention to understand the physics underneath.

The availability of high-j orbitals for both protons and neutrons gives rise to the possibility of observation of variety of new structural effects in these nuclei. For odd-odd isotopes in A∼200 region, angular momenta of the valance proton, neutron and the core, generate different deformed band structures, depending on the relative orientations of the angular momentum vectors. If the three angular momenta are in a planer geometry, then a sequence of M1 transitions (a dipole band) is expected. This is interpreted as to be generated from the scissor like structure of the angular momentum vectors of the two valance particles and are known as magnetic rotation(MR) band. This type of structure has been reported in a few nuclei in this region, e.g. ^{194}Tl [26] and ^{198}Bi [36] which satisfy the above orientations. Unlike the magnetic rotational band, the three-dimensional orientation of the angular momenta of the odd quasi-particles and the collective rotation of the core can be in a aplaner geometry, for a triaxial shape. This three angular momenta can be represented by a left-handed or right–handed orientation defining the chiral geometry of the system. In order to realize the MR and chiral bands in nuclei, the angular momentum of the involved particle and hole need to be large. In case of MR band, the larger the particle and hole angular momentum, the band can be extended up to higher spins, and is experimentally easier to identify. On the other hand, the chiral doublet bands can be realized only for a triaxial nucleus with the odd particles occupying high- and low-Ω orbitals (Ω is the projection of the single particle angular momentum j on to the symmetry axis). Availability of high-j protons and neutron orbitals($h_{9/2}, i_{13/2}$) and the occupation of the $\Omega = 9/2$ of the high-j $h_{9/2}$ orbital by the proton particle and the lowest projection ($\Omega = 1/2, 3/2$) of high-j $i_{13/2}$ orbital by the neutron hole, makes the Thallium nuclei of mass 200 region good candidates to exhibit the MR and chiral symmetry breaking phenomena, which is one of the experimental signature of triaxiality. Degenerate rotational bands, interpreted as the chiral partner bands have already been reported recently in $^{194,195,198}Tl$ [37, 16, 38]. The evidence of triaxial shapes are also reported in 190-200 mass region for Platinum nuclei ($Z = 78$) ^{191}Pt, ^{193}Pt [5, 6]. Therefore Mercury ($Z = 80$) nuclei, below $Z = 82$, are also expected to show signatures of triaxiality. On the neutron deficient side, the nuclei below $N = 120$ also show super-deformed bands in $^{191,193,195}Tl$ [41, 42, 43] and ^{193}Hg [44] isotopes. Whereas for the nuclei above $N = 120$, complex single particle structure arises due to the octupole excitation in $^{204,205}Tl$ [6, 24]. Therefore, the transition region near $N = 120$ for Thallium (Z=81) and Mercury ($Z = 80$) nuclei are of great interest to discover such exotic phenomena and explore the competition between single particle and collective behaviour, governed by the deformation and the relative orientations of the angular momentum vectors.

As the nuclei, beyond $Z = 82$ are difficult to produce experimentally using fusion evaporation reaction, information about the orbitals beyond $Z = 82$ shell closure are limited. The study of the evolution of these high-j orbitals (i.e. $\pi h_{9/2}, \pi i_{13/2}$), which are intruding from upper shell, provides valuable information about the single particle excitations as a function of excitation energy beyond the $Z = 82$ magic shell closure. The theoretical calculations are also very much dependent on the experimentally observed single particle levels to predict the existence of the next new spherical or deformed magic number in this region.

The presence of different kinds of single particle as well as collective nature of excitations demands the complete study of yrast as well as near yrast states of the nuclei near 200 mass region. The low lying states at moderate spin are often found to decay through many non-stretched transitions. The investigation of multi-polarity and the nature of the stretched and non-stretched transitions are necessary to uniquely identify the spins and parities of the states associated with it. Using α or other light ion beams, the the non-yrast structures of the desired nuclei can be probed with sizable cross section. A Compton-suppressed Clover HPGe detector array is, therefore, not only necessary but also an inseparable part of the experiments. Other than the sufficient number of detectors to increase the $\gamma - \gamma$ coincidence efficiency, the arrangement (angular orientation) of the detectors is equally important to achieve the information of the multi-polarity through DCO ratio, angular distribution (or angular correlation) measurements and also the information about polarization of the transitions to determine the parity of the decaying states.

In the present thesis, the effect of the odd nucleons, occupying high-j orbitals, in driving the structure of nuclei towards deformation and their influence in generating higher angular momentum states in these nuclei, has been explored. For this purpose the structure of three neighbouring odd-even, even-odd and odd-odd nuclei below $Z = 82$ shell closure, viz., ^{199}Tl ($Z = 81, N = 118$), ^{199}Hg ($Z = 80, N = 119$) and ^{200}Tl ($Z = 81, N = 119$) has been experimentally investigated using γ ray spectroscopy method. For ^{199}Tl, the odd valance proton is responsible for the generation of the low lying states whereas, for ^{199}Hg the protons are paired and the level structure are solely depends on the single particle levels occupied by the odd neutron. By studying both the ^{199}Tl and ^{199}Hg nuclei, the individual effect of the single neutron and the single proton on the spherical core can be explored. The combined effect of both proton and neutron single particle levels, as well as the residual interaction between them can be well understood by studying the odd-odd ^{200}Tl ($Z = 81, N = 119$) which has an extra odd proton and neutron with respect to the ^{198}Hg core.

Different near yrast structure of ^{199}Tl that has been studied experimentally by fusion-evaporation reaction are presented. The shape driving effect of the $\pi h_{9/2}$ orbital, induce oblate deformation and thus bring collectiveness into the system and strongly coupled band structure built with $9/2^-$ as band head. Due to the large spin difference between the high-j π $h_{9/2}$ orbital and the other low lying states corresponding to $\pi s_{1/2}$, π $d_{3/2}$ orbitals the $9/2^-$ state becomes isomer. The neutron number for ^{199}Tl is 118, which is close to $N = 126$ shell closure and thus with a little excitation energy the neutron pairing is also probable to break. Though the oblate structure still persist upto ^{201}Tl [18] ($N = 120$), with further increasing neutron number odd mass Thallium nuclei have not exhibited collective structures, rather reported to have core excited states [24]. In the present thesis the ^{199}Tl nucleus was produced by 30 MeV α beam at VECC, Kolkata K-130 cyclotron. The level scheme has been extended significantly beyond band crossing. DCO (Directional Correlation from Oriented states), IPDCO (Integrated Polarization Directional Correlation from Oriented states) ratio (defined in chapter 3.) and Angular distribution were used to determine the spin and parity of the newly observed states. The band crossing in the yrast band based on π $h_{9/2}$ and in the partner bands has been discussed considering the pair breaking in the available orbitals near proton and neutron Fermi levels. Many non-yrast states have been observed due to the population of the excited states via light ion induced (α) reaction. Few states are also observed which bypass the $9/2^-$ isomer. Total Routhian Surface (TRS) calculation has been performed which indicates the deformation for the different states observed in ^{199}Tl. The band structures and the possible occurrence of collectivity are discussed in comparison with the neighbouring nuclei.

The effect of a single neutron particle on the spherical core has been studied in ^{199}Hg. With proton number paired ($Z = 80$) and being very closed to $Z = 82$ shell closure, the protons are more or less behaving inert so far as to generate the excited states in Mercury nuclei. The presence of high-j neutron orbital near the neutron Fermi level and accessed by the odd neutron produce low-lying spin gap isomer and a decoupled band structure on that. Such decoupled bands have been reported in all the nearby odd mass Hg nuclei [15, 18, 22, 28] and has been described as the coupling of a decoupled $\nu i_{13/2}$ neutron with the states of corresponding even Hg core [35]. The use of α-beam from the $K - 130$ cyclotron, Kolkata to study ^{199}Hg resulted the population of its moderate spin states. The yrast and near yrast states of the nuclei has been populated and studied using VENUS (VECC Array for NUclear Spectroscopy) set up, consisting of 6 Compton Suppressed Clover HPGe detectors. The yrast states are identified as the decoupled rotational band based on $\nu i_{13/2}$ orbital with $13/2^+$ band head. A recent study by Negi *et. al.* [29] also populated the high spin states of ^{199}Hg by multinucleon transfer reaction and extended the semi-decoupled band structure on $21/2^-$ spin. They have also found a new band based on the tentatively assigned $33/2^+$ state. But they could not extend the yrast $\nu i_{13/2}$ band beyond $25/2^+$ spin. Whereas, the yrast band of same configuration in lower mass odd-A Hg isotopes are extended upto $41/2^+$ spin. One of the motivation to study ^{199}Hg in the present thesis was to investigate the reason of the non observance of this band beyond $25/2^+$ spin. In the present study the levels beyond $25/2^+$ spin have been identified, which belong to semi-decoupled band. In all other lower mass odd Hg isotopes the $\nu i_{13/2}$ bands experience a back-bending with a $i_{13/2}$ neutron pair alignment, which is absent for the ^{199}Hg nucleus. Most importantly, the present study could identify the signature partner of the $\nu i_{13/2}$ band for the first time. The appearance of various non-yrast bands with the underlying symmetry breaking phenomena, as well as the possibility of exotic shapes in this region, are discussed in the present work.

The combined effect of both neutron and proton orbitals on the core can be well investigated in the platform with odd-odd nucleus. ^{200}Tl ($Z = 81, N = 119$) nucleus is a good candidate to test the effect of both neutron and proton on the spherical ^{198}Hg core as well as to extend the knowledge of the interactions between available neutron and proton orbitals. As the neutron number increases towards $N = 126$ shell closure, it is an open question whether the shape driving effects of the proton as well as neutrons are strong enough to stabilize the triaxial shape, so that band structure similar to the chiral doublet bands reported in lighter Thallium isotopes still persists for the heavier odd-odd Tl isotopes. The high spin states of ^{200}Tl have been populated using ^{7}Li beam from the BARC-TIFR Pelletron LINAC facility and INGA (Indian National Gamma Array) set up was used to detect the γ rays. The present work considerably extend the level scheme of ^{200}Tl upto higher excitation energy and angular momentum and search for the shapes of the nuclei in lower as well as higher spin. The involvement of the high-j orbitals in forming the band structures is also explored.

The present thesis is an experimental endeavor to study the effect of the high-j orbital on the shape of the nuclei near A$\sim$200 region with the comparative study of the band structures of three neighbouring nuclei: ^{199}Tl, ^{199}Hg and ^{200}Tl. The Nuclear models, relevant to the current thesis, experimental procedures and interesting results, obtained from the level structures of the above nuclei are also discussed. The interesting outcomes of the present thesis and the future scopes of the present studies are highlighted.

Bibliography

[1] E. Rutherford. Philosophical Magazine, Sixth Series, 21:669, 1911.

[2] N. Bohr. Philosophical Magazine, 26:1, 1913.

[3] N. Bohr and F. Kalckar. Mat.-Fys. Medd., 14:10, 1937

[4] A. Bohr and B. R. Mottelson, "Nuclear structure, vol. II", Benjamin Reading, Massachusetts 1975. Ch 4.

[5] M. G. Mayer, Phys. Rev. 75, 1969 (1949).

[6] L. J. Rainwater. Phys. Rev., 79:432, 1950.

[7] A. Bohr and B. R. Mottelson. Dan. Mat.-Fys. Medd., 27:16, 1953.

[8] A. Bohr and B. R. Mottelson. Collective Nuclear Motion and the Unified Model in Beta and Gamma Ray Spectroscopy. North Holland, Amsterdam, first edition, 1955.

[9] Gammasphere:The Beginning...1993-1997.http://nucalf.physics.fsu.edu/ riley/gamma/. 1.1, 1

[10] B. Herskind, Proc. Int. Conf. Nucl. Phys., Italy, 1 17 (1983).

[11] P. Grabmayr *et. al.* , Jour. of Phys. G **18**, 11 (1992).

[12] M. Rejmund *et. al.*, Eur. Phys. J A **8**, 161 (2000).

[13] M. Lipoglavsek *et. al.*, Phys. Lett. **B 593**, 61 (2004).

[14] W. Reviol *et al.*, Phy. Scr. T **56**, 167 (1995).

[15] J. O. Newton, F. S. Stephens, and R. M. Diamond, Nucl. Phys. A **236**, 225 (1974).

[16] T. Roy *et. al.*, Phys. Lett. B **782**, 768 (2018).

[17] R. M. Lieder *et al.*, Nucl. Phys. A **299**, 255 (1978).

[18] S. Das Gupta *et. al.*, Phys. Rev C **88**, 044328(2013).

[19] R. M. Lieder *et al.*, Nucl. Phys. A **248**, 317 (1975).

[20] H. Hübel, A. P. Byrne, S. Ogaza, A. E. Stuchbery, and G. D. Dracoulis, Nucl. Phys. A **453**, 316 (1986).

[21] D. Proetel, D. Benson, Jr., A. Gizon, J. Gizon, M. R. Maier, R. M. Diamond and F. S. Stephens, Nucl. Phys. A **226** 237 (1974).

[22] N. Nenoff *et al.*, Nucl. Phys. A **629**, 621 (1975).

[23] D. Mertin, R. Tischler, A. Kleinrahm, R. Kroth, H. Hübel, and C. Günther, Nucl. Phys. A **301**, 365 (1978).

[24] C.Y. Xie *et al.*, Phy. Rev. C **72**, 044302 (2005).

[25] A.J. Kreiner *et al.*, Phy. Rev. C **21**, 933 (1980).

[26] H. Pai *et. al.*, Phys. Rev C **85**, 064313 (2012).

[27] A.J. Kreiner, M. Fenzl and W. Kutschera, Nucl. Phys. A **308**, 147 (1978).

[28] A.J. Kreiner, M. Fenzl, S. Lunardi and M.A.J. Mariscotti, Nucl. Phys. A **282** 243 (1977).

[29] A.J. Kreiner *et al.*, Phys. Rev C **23**, 748 (1981).

[30] N. Fotiades *et al.*, Phys. Rev C **76**, 014302 (2007)

[31] M. G. Slocombe *et al.*, Nucl. Phys. A **275**, 166 (1977).

[32] O. Hausser *et al.*, Phys. Lett. B **64**, 273 (1976).

[33] P. Zeyen *et al.*, Z. Phys. A **325**, 451 (1986).

[34] P. Schuler *et al.*, Z. Phys. A **325**, 451 (1986).

[35] A. R. Poletti *et al.*, Nucl. Phys. A **580**, 64 (1994).

[36] H. Pai *et. al.*, Phys. Rev C **90**, 064314 (2014).

[37] P.L. Masiteng *et. al.*, Phys. Lett. B **719**, 83 (1988).

[38] E. A. Lawrie *et. al.*, Phys. Rev. C **78**, 021305(R) (2008).

[39] T. L. Khoo, F. M. Bernthal, C. L. Dors, M. Piiparinen, S. Saha, P. J. Daly, and J. Meyer-Ter-Vehn, Phys. Let. **60**, 341 (1976).

[40] S. K. Saha, M. Piiparinen, J. C. Cunnane, and P. J. Daly, Phys. Rev. C **15**, 94 (1977).

[41] S. Pilotte *et. al.*, Phys. Rev C **49**, 718 (1994).

[42] P.B. Fernandez *et. al.*, Nucl. Phys. A **517**, 386 (1990).

[43] F. Azaiez *et. al.*, Z. Phys. A **338**, 471 (1991).

[44] M. J. Joyce *et. al.*, Phys. Lett. B **340**, 150 (1994)

[45] R. Broda *et al.*, Phys. Rev. C **84**, 014330 (2011).

[46] J. Wrzesi′nski *et. al.*, Eur. Phys. J. A **20**, 57 (2004).

[47] C. Gunther *et. al.* Phys. Rev. C **15**, 1298, (1977).

[48] D. Negi *et al.*, Phys. Rev. C **100**, 014329 (2019).

Chapter 2

Nuclear Models

A quantum many body system like atomic nucleus is a laboratory to test the strongly interacting neutrons and protons. The nucleons are bound with the short-range strong nuclear force but unfortunately, that is not well understood and the exact form of strong interaction, experienced by the nucleons, is not known. There is no single nuclear model that can explain all the properties of a nucleus. Instead, a particular model is considered which can best describe the phenomenon under investigation. The success of a model depends on how good it be able to produce the known results, and as well as be able to predict phenomena not yet discovered. Thus, different nuclear models have been proposed based on different phenomena, experimentally observed in atomic nuclei. In this chapter, a few of the relevant models with respect to present thesis work will be briefly described.

2.1 The Liquid Drop Model

The liquid drop model was first proposed by George Gamow [1] as an attempt to explain the experimental observable of a nucleus. This model treats the nucleus as a macroscopic drop of a charged incompressible fluid composed of nucleons. The binding energy per nucleon as a function of mass number A for a nucleus is found to be almost constant ($\sim$ -8.5 MeV), which indicates the saturation properties of the nuclear force. In an attempt to explain this behavior, Bethe-Weizsäcker proposed the semi-empirical mass formula [2, 3]:

$$B(N, Z) = a_V\, A + a_S\, A^{\frac{2}{3}} + a_C\, \frac{Z^2}{A^{\frac{1}{3}}} + a_I\, \frac{(N\, -\, Z)^2}{A} + \delta(A) \tag{2.1}$$

The experimental data can be fitted by the formula [4] and the values of the constant terms have been found to be a_V = -15.68 MeV; a_S = 18.56 MeV; a_C = 0.717 MeV; a_I = 28.1 MeV. The last term of equation 1.1, $\delta(A)$ is the pairing energy which is given by,

$$\begin{aligned}
\delta(A) &= 34.\, A^{-\frac{3}{4}} MeV \quad for\ even - even\ nuclei \\
&= 0 \qquad MeV \quad for\ even - odd\ nuclei \\
&= -\, 34.\, A^{-\frac{3}{4}} MeV \quad for\ odd - odd\ nuclei
\end{aligned}$$

Each of the terms of the above equation has a theoretical basis. The first term of equation 1.1 is usually known as the volume term and is based on the strong nuclear force. This force has a very limited range and nucleons only interact with their nearest neighbors. The number of particles that interact is roughly proportional to A($\propto$ r^3; r is nuclear radius) i.e. the volume of the nucleus. Hence it is called the volume term. The second term is generally assumed to be generated from the surface tension of the nuclei which reduce the binding energy of the system and thus the second term is proportional to A$^{2/3}$($\propto$ r^2) i.e. the surface area of the liquid (nucleus) drop. The third term is known as the coulomb term which takes into account coulomb energy associated with the coulomb repulsion of the charged nucleons (i.e. proton) inside the nucleus. Hence the term is proportional to the number of the protons($\propto$ Z^2) inside the nucleus and inversely proportional to the radius of the nuclei. The next term is known as the "symmetry term" which takes care of the relative number of protons to neutrons, so that the nucleus becomes more symmetric. This term becomes more significant in higher mass region where the neutron number (N) tends to increase than the proton number (Z) to overcome the Coulomb repulsion in order to bind the nucleons together. The equation contains the δ(A) term, that accounts for the pairing force between like nucleons (between proton-proton or neutron-neutron). It expresses the experimental facts, that even-even nuclei are more tightly bound (stable) than even-odd nuclei, which are in turn more tightly bound than odd-odd nuclei. The Liquid Drop Model (LDM) is the first phenomenological sensible model that could explain few bulk nuclear properties like i) Binding energy per nucleon and nuclear mass, ii) Fissioning of a nucleus and iii) Saturation of nuclear force. But this simplistic model can not explain few other nuclear properties like the actual excited states of the nuclei, the magnetic moments, two neutron or two proton separation energies etc. Moreover it could not explain the so called magic number- 2, 8, 20, 28, 50, 82 and 126, possessing which as proton or neutron number, a nucleus becomes more stable than the neighbouring nuclei. This gave rise to the concept of closed shell nuclei and most successful nuclear model, the "shell model," proposed by Mayer in 1949 [5].

2.2 Shell Model

It was observed that the nuclei, which have certain number of neutrons and protons, are more stable against excitations than the neighbouring nuclei. These numbers, nomenclature as so called "magic numbers", are 2, 8, 20, 28, 50, 82 and 126. Experimentally it has been observed that the nucleon separation energies across the nuclear chart showed large and sudden drop at the magic numbers. These observations pointed towards a shell structure of the nucleus, similar to the electronic shell structure in the atoms and led to the proposition of the shell model [6]. The shell model presumes the nucleons in the nucleus as independent particles. They are assumed to be moving in almost unperturbed single particle orbits, in a uniform, spherically symmetric, mean field produced by all the nucleons in the nucleus. Unlike the atomic case, where the central mean field is provided by the Coulomb field of the heavy nucleus at the center of mass, in the nuclear case the mean field is produced by the nucleons themselves. The nuclear "shell model", independently proposed by Mayer [5] and Haxel, Jensen and Suess [7],in 1949 which was not only capable of explaining the magic numbers but also the magnetic moments, spins and energies of the levels etc [8, 10]. The Hamiltonian of the Shell model picture consists of two terms, kinetic energy of the constituent nucleons and the potential due to the interaction between two nucleons *i.e.* a two body potential energy term and is represented by:

$$\mathcal{H} = T + V = \sum_{i=1}^{A} -\frac{\hbar^2}{2m_i}\nabla_i^2 + \frac{1}{2}\sum_{i,j=1}^{A} V_{i,j} \tag{2.2}$$

The first term is from the kinetic energy of each nucleon and $V_{i,j}$ is the two-body potential corresponding to the nucleon-nucleon interaction. We therefore introduce an average one body potential $U(r_i)$ that is 'felt' by all the (A) nucleons and the equation converges to a one body problem, leaving a small two body term. Hence the Hamiltonian can be rewritten by adding and subtracting $U(r_i)$ as,

$$\mathcal{H} = \sum_{i=1}^{A} [T_i + U(r_i)] + \left(\frac{1}{2}\sum_{i,j=1}^{A} V_{i,j} - \sum_{i=1}^{A} U(r_i)\right) = \mathcal{H}_0 + \mathcal{H}_{res} = \sum_{i=1}^{A} h_0(i) + \mathcal{H}_{res} \tag{2.3}$$

where $\mathcal{H}_0$ is the Hamiltonian which represent the one body part, describing the motion of A nucleons in the mean field $U(r_i)$. The rest two body term is represented by the Hamiltonian $\mathcal{H}_{res}$ and known as the "residual interaction". The one body part $U(r_i)$ appearing in $\mathcal{H}_0$ is chosen wisely so that the residual interaction part $\mathcal{H}_{res}$ becomes small enough to be treated as a non-relativistic perturbation. In microscopic theory [11] starting from nucleon nucleon interaction or self-consistent hertree-fock calculation mean field potential can be found [12, 4]. But depending on the different observables in the nucleus, the potential $U(r_i)$ can be chosen phenomenologically. An analytic 'Woods-Saxon' potential has been proven to be the most appropriate potential till now, which is given by

$$V_{WS}(r) = -\frac{V_0}{1 + exp[(r - R)/a]} \tag{2.4}$$

where V_0 is the depth of the potential ($\sim$ 50 MeV), radius $R \approx 1.2A^{1/3}$ fm and the surface thickness a $\approx$ 0.5 fm. In the above equation $V(r)$ has been shown to depend on r only. Such a potential is spherically symmetric and hence the model is called the "spherical shell model". The exact analytical solution of the equation 1.3 using Woods-Saxon potential is not possible. For a analytically solvable solution we go for a simple potential. For a spherical nucleus, the potential should be spherically symmetric, and should depend only on the distance from the center of the nucleus. Although different potentials can be used, the three-dimensional symmetric harmonic oscillator potential is arguably the simplest yet relevant:

$$V_{HO}(r) = -\frac{1}{2}m\omega_0^2(r^2 - R_0^2) \tag{2.5}$$

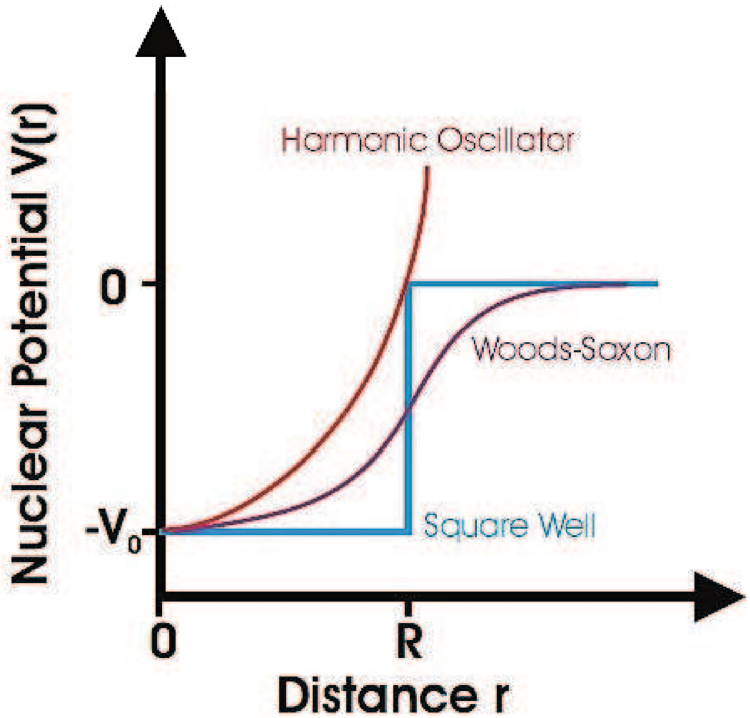

Figure 2.1: Three phenomenological potential well used to model the nuclear potential as a function of nucleus radius r. V_0 is the well depth, r the distance from the origin and R the nuclear radius.

which was used as a mean field where R_0 is the mean radius of nucleus, m is the mass of a nucleon, and ω_0 is the oscillator frequency of the simple harmonic motion (SHM) of the nucleon. The different model, adopted for the nuclear potential have been shown in Fig. 2.1 as a function of distance(r) from the center of the nucleus. For a spherically symmetric potential the wave function $\Phi(r, \theta, \phi)$ can be divided into two independent component; a)radial part $R_{nl}(r)$ and b) spherical harmonics $Y_{lm}(\theta, \phi)$ and the Schrodinger equation of the three-dimensional harmonic oscillator then becomes:

$$\mathcal{H}\Phi_{nlm}(r, \theta, \phi) = \left[\frac{-\hbar^2}{2m}\nabla^2 + V_{HO}(r)\right]\Phi_{nlm}(r, \theta, \phi) = E_N\Phi_{nlm}(r, \theta, \phi) \tag{2.6}$$

Where E_N are the energy eigenvalues corresponding to the major oscillator quantum number N. The shell energies (energy eigen-values) are given by

$$E_N = \left(N + \frac{3}{2}\right)\hbar\omega_0 \tag{2.7}$$

such that

$$N = 2(n-1) + l, \quad n = 1, 2, 3, ... \quad and \quad l = 0, 1, 2, .. \tag{2.8}$$

where, N is the *principal* quantum number and n,l,m are the *radial* ,*orbital* and *magnetic* quantum number respectively. Each N shell can contain a maximum number of $(N+1)(N+2)$ nucleons, where the parity π of the levels in the shell is given by $\pi = (-1)^l = (-1)^N$. Thus an oscillator shell contains only states with same parity.

Table 2.1: The degenerate levels of nucleus, that have been generated from Simple Harmonic Oscillator Potential and corresponding nucleon number per shell.

N[1]	n	$Parity$	$allowedl$	$Levels\ label$	$E_n(\hbar\omega)$	$NucleonNo$	$Total$
0	0	$+Ve$	0	$1s$	3/2	2	2
1	1	$-Ve$	1	$1p$	5/2	6	8
2	1	$+Ve$	2	$1d$	7/2	10	
2	2	$+Ve$	0	$2s$	7/2	2	20
3	1	$-Ve$	3	$1f$	9/2	14	
3	2	$-Ve$	1	$2p$	9/2	6	40
4	1	$+Ve$	4	$1g$	11/2	18	
4	2	$+Ve$	2	$2d$	11/2	10	
4	3	$+Ve$	0	$3s$	11/2	2	70
5	1	$-Ve$	5	$1h$	13/2	22	
5	2	$-Ve$	3	$2f$	13/2	14	
5	3	$-Ve$	1	$3p$	13/2	6	112

[1]Each horizontal line separate the major shells. Each shell has few degenearate levels corresponding to same energy.

However, from table 2.1 above shell energies still do not reproduce the experimentally observed magic numbers above 20. So some modification need to be done to the potential to explain the magic numbers. An extra attractive term proportional to l^2 had been added to the harmonic oscillator potential which basically flatter the potential. The effect of this term increases with orbital angular momentum. Hence, high angular momentum particles would feel a stronger attractive interaction that lowers their energy. In brief terms, the addition of an l^2 term is equivalent to a more attractive potential at larger radii. The relation of the single-particle levels produced by a harmonic oscillator potential, along with the addition of an l^2 term is illustrated in the middle panel of Fig. 2.2. Like the case of atomic physics, the degeneracy of each level is $2(2l+1)$, which is the number of nucleons that can be put in each level. Though, this modification makes the nuclear potential more realistic, still it could not reproduce the magic numbers observed experimentally [6].

Latter Haxel, Jensen, Suess [7] and Maria Geopart Mayer [5] independently introduced a spin-orbit coupling f(r).$\overrightarrow{l}.\overrightarrow{s}$ term into the nuclear Hamiltonian. They showed that the inclusion of a spin-orbit potential(which is actually a idea brought from atomic physics) could give the proper separation of the sub-shells. In nuclear physics the term $\overrightarrow{l}.\overrightarrow{s}$ is much more significant than that of in atomic physics. $f(r)$ is the strength of the spin orbit coupling and s is the intrinsic-spin angular momentum quantum number. Both the angular momentum now coupled to the total angular momentum $\overrightarrow{j}$

$$\overrightarrow{j} = \overrightarrow{l} + \overrightarrow{s} \tag{2.9}$$

The coupling removes the degeneracy $2(2l+1)$ of the states and split the levels into two component corresponding to $j = l \pm \frac{1}{2}$ (intrinsic spin of a single nucleon is $\pm\,\frac{1}{2}$). This splitting is proportional to l and leads to the $j = l + \frac{1}{2}$ states lower in energy than the $j = l - \frac{1}{2}$ states. The effect of this attractive spin orbit term becomes significant in higher j orbital and the $j + \frac{1}{2}$ level intrude in the lower major shells and thus sub-shells now properly reproduce the magic numbers. The right panel in Fig. 2.2 shows the distribution of the orbitals due to the

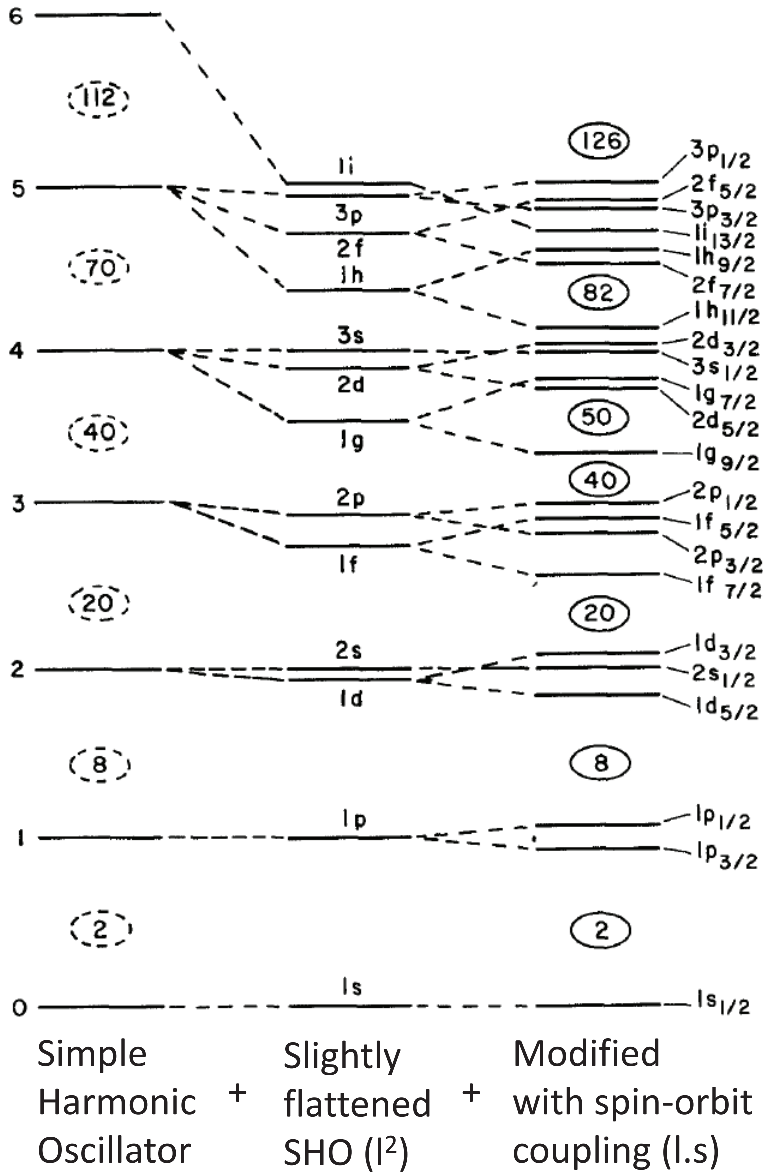

Figure 2.2: Single-particle energies for S.H.O. potential, a modified harmonic oscillator with l^2 term, and a realistic shell model potential with both l^2 and spin orbit (l.s) terms. From Ref. [6].

addition of the l.s term to the nuclear potential. A particle with total angular momentum j has magnetic substates $m, j = |j, |j + 1, ... + j$ or $(2j + 1)$ values, degenerate in energies. Thus, following the Pauli exclusion principle the number of nucleons (of each type protons, neutrons), in each single particle orbit (labeled by j) can hold $(2j + 1)$ nucleons. The states are therefore labelled uniquely by n, l and j quantum number, for example $1i_{13/2}$ states represents n=1, l=6 and j= 6+$\frac{1}{2}$=13/2 quantum numbers associated. In the single particle shell model, the nuclear properties are determined by the outermost valance nucleon only. Ground state properties of many nuclei which are close to magic numbers, can be explained successfully by this model. However, for most of the nuclei which are away from shell closure, it is necessary to take into account the effect of all the nucleons outside the closed core.

2.3 Nuclear shapes

When one moves away from magic shell closure, some systematic and simple behaviour has been observed in the nuclei, such as: large ground state quadrupole moment, enhanced $E2$ transition probability, rotor like energy spectra etc. These experimentally observed phenomena indicates the coherent participation of the nucleons to generate a motion such as rotation or vibration. These collective behaviours of the nucleon is named as Collective model and described by A. Bohr and B. Motelsson in Ref. [13]. In this model the nucleus is considered to be a incompressible fluid and the deformed nuclear radius $R(\theta, \phi)$ can be expressed as a small additional term δr with the spherical radius R_0 as

$R(\theta, \phi) = R_0 + \delta\mathrm{r}(\theta, \phi) = R_0 \left(1 + \frac{\delta r}{R_0}\right)$

and the second (smaller) term in the parentheses can be expanded in terms of spherical harmonics as:

$$R(\theta, \phi) = R_0 \left[1 + \sum_{\lambda=0}^{\infty} \sum_{\mu=-\lambda}^{\lambda} \alpha^*_{\lambda\mu} Y_{\lambda\mu}(\theta, \phi)\right] \tag{2.10}$$

Where the $\alpha^*_{\lambda\mu}$ represents the shape parameter and λ is the order of the multipole. We assume the volume of the nucleus remain unchanged, the θ, ϕ are measured with respect to the three axes coordinate system. The λ=0 term can be ignored, since such deformation results in a volume change and is not expected upto a very high excitation energy. The dipole term

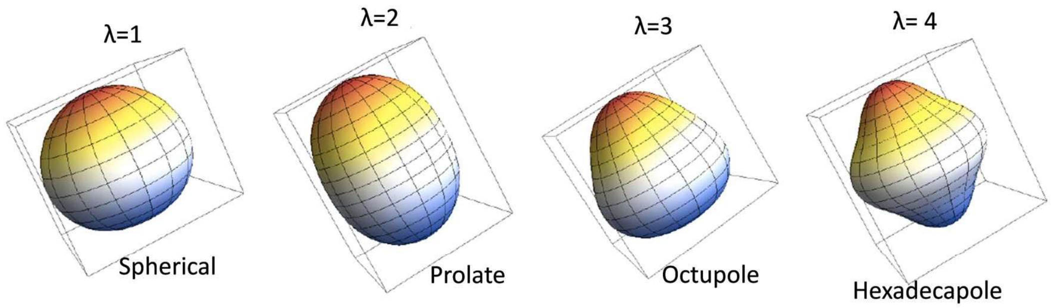

Figure 2.3: Shapes of the multipoles as perturbations of a sphere. From left to right: dipole (λ=1), quadrupole ($\lambda = 2$), octupole (λ= 3) and hexadecapole (λ=4). The monopole corresponds the volume change and is not shown. Fig taken from Ref. [14].

(λ=1) corresponds the displacement of the center-of- mass; by fixing the coordinate origin at the center of mass, we can fix $\alpha_{1\mu} = 0$. The higher order terms, $\lambda = 2, 3, 4$ correspond to quadrupole, octupole and hexadecapole deformations (see Fig. 2.3) respectively. Terms having $\lambda = 2$ describe shapes which are either oblate (which has two semi major axes equal) or prolate spheroids (which has two semi minor axes equal). Considering the nucleus to have only the quadrupole deformation ($\lambda = 2$), which is the lowest significant order of interest, Eq. 2.10 can be written as:

$$R(\theta, \phi) = R_0 \left[1 + \sum_{\mu=-2}^{2} \alpha^*_{2\mu} Y_{2\mu}(\theta, \phi) \right] \tag{2.11}$$

This Eq. 2.11 gives five $\alpha_{2\mu}$ coefficients. Three of these parameters determine the orientation of the nucleus in space and correspond to the three Euler angles. The $\alpha_{2\mu}$ are chosen such that $\alpha_{21} = \alpha_{2-1} = 0$ and $\alpha_{22} = \alpha_{2-2}$. The remaining α_{20} and α_{22} are independent variables and are typically converted to polar coordinates, through two new shape parameters, β_2 and γ (the "Lund convention"Ref. [15]).

$$\alpha_{20} = \beta_2 \; cos\gamma \tag{2.12}$$

$$\alpha_{22} = \frac{1}{\sqrt{2}} \beta_2 \; sin\gamma \tag{2.13}$$

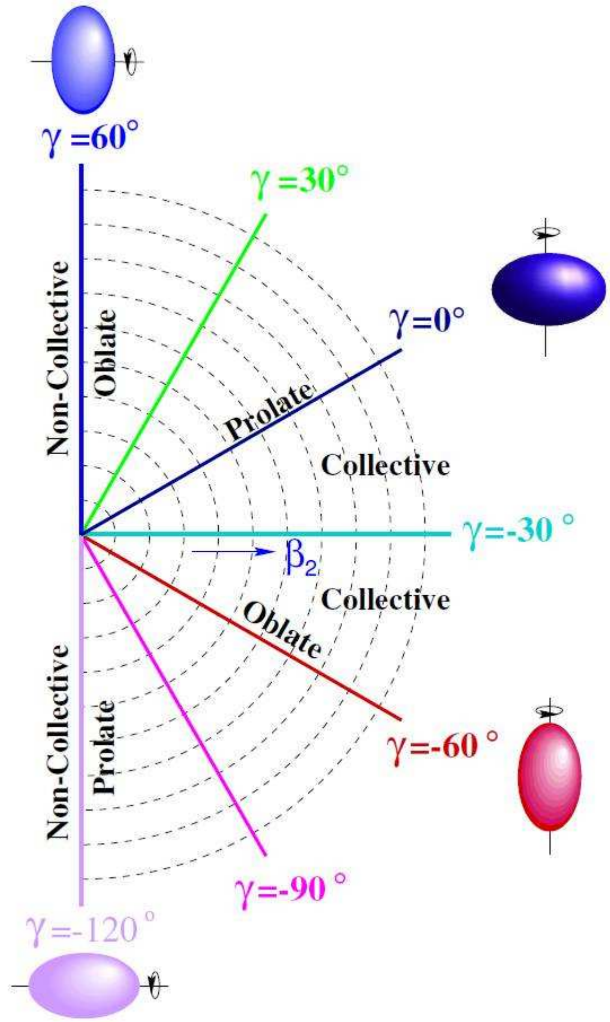

Figure 2.4: The Lund convention for describing quadrupole shapes of nucleus in the (β_2,γ) plane.The deformation parameter β_2 plays the role of the radial variable, while γ, the triaxiality parameter, serves as the polar angle. The collective region lies between γ = 0^o-60^o, while rotations along the γ=60^o and γ =-120^o axes are purely non-collective in nature. Fig taken from Ref. [16].

So out of five $\alpha_{2\mu}$ coefficients, with proper parameterization, Equation 2.11 can be represented by only two independent parameter β_2 and γ, which are used to describe the nuclear shape upto quadrupole deformation.

$$R(\theta, \phi) = R_0 \left[1 + \beta_2 \sqrt{\frac{5}{16\pi}} \left(cos\gamma(3cos^2\theta - 1) + \sqrt{3} sin\gamma \; sin^2\theta \; cos2\phi \right) \right] \tag{2.14}$$

β_2 represents the total deformation of the nucleus and referred to "quadrupole deformation parameter", whereas γ is the "triaxiality parameter" which represents the deviation of the shape of nucleus from axial symmetry. The different nuclear shapes, depending on different value of β_2 and γ, are shown in Fig. 2.4. According to the Lund convention, γ=0^o corresponds to a prolate shape (Rugby ball shape) undergoing a collective rotation about an axis which is perpendicular to its symmetry axis and γ=-60^o represents an oblate shape (shape of a orange) nuclei exhibiting collective rotation around a axis, perpendicular to the symmetry axis. The value $-60^o \leq \gamma \leq 0^o$ represents triaxiality (where the three major axes are not equal to each other) in nuclei. γ=60^o and γ=-120^o value also represents oblate and prolate shapes respectively but for those case the rotation is about their symmetry axes and no experimental observation of rotational bands are expected.

2.4 Deformed Nuclear shapes: Nilsson Model

To describe a large number of experimental observable energy levels of deformed nuclei one needs to introduce a new potential with deformation in it. One such potential is proposed by Sven G. Nilsson [18] as the modified harmonic oscillator potential (or Nilsson potential) in 1955 and further studied in 1969 [19, 20, 21]. In this context the Deformed Shell Model (DSM) has been introduced which considers nucleus to be of axially symmetric deformed shape where x and y axes are equal to each other but lesser(for oblate shape) or greater (for prolate) than the z (symmetry) axis. It is assumed that a single nucleon is moving about a deformed nucleus. As in Spherical Shell Model (SSM), terms proportional to l^2 and $\overrightarrow{l}.\overrightarrow{s}$ has been introduced in the deformed potential Hamiltonian also. For l^2 term the potential becomes flatter specially for heavier elements and $l.s$ term reproduces the experimentally observed magic numbers and thus it reproduces the proper order and energies of the levels in the spherical limits(β_2=0).

For axially deformed nucleus (x=y$\neq$z) the Hamiltonian can be written as

$$\mathcal{H}_{Nilsson} = -\frac{\hbar^2}{2m}\nabla^2 + \frac{1}{2}m\left[\omega_x^2(x^2+y^2) + \omega_z^2 z^2\right] + C\overrightarrow{l}.\overrightarrow{s} + Dl^2 \tag{2.15}$$

The coefficients C, D are constants and usually written in terms of κ and μ as follows

$$\kappa = \frac{C}{2\hbar\omega_0} \tag{2.16}$$

and

$$\mu = \frac{2D}{C} \tag{2.17}$$

The values of these two variables are adjusted to reproduce the observed levels of spherical nuclei with β_2=0 and the experimentally observed levels for deformed nuclei with $\beta_2 \neq 0$. The typical values for κ are found to be around 0.06 whereas the value of μ varies from 0 to ≈ 0.7 depending on different shells. The ω_x, ω_y and ω_z are the one-dimensional oscillator frequencies in the x, y and z directions, respectively. These ω_x and ω_y are of same value and all the frequencies can be parameterized and expressed in terms of the spherical oscillator frequency ω_0 involving the axial deformation (ϵ_2) of the nucleus as:

$$\omega_x^2 = \omega_y^2 = \omega_0^2 \left(1 + \frac{2}{3}\epsilon_2\right) \tag{2.18}$$

and

$$\omega_z^2 = \omega_0^2 \left(1 - \frac{4}{3}\epsilon_2\right) \tag{2.19}$$

ϵ_2 is the nuclear deformation parameter and is related with the parameter β_2, defined in Fig. 2.4 and in Equation 2.12 as $\epsilon_2 \approx 0.95\ \beta_2$. With the coordinate transformation, the new parameterization has been introduced in Nilsson model for quadrupole deformation as $\epsilon_{20}= \epsilon_2$ cosγ and $\epsilon_{22}=\frac{2}{\sqrt{3}}\epsilon_2$ sinγ. The spherical oscillator frequency generally depends on the size of the nucleus and expressed as $\hbar\omega_0 \approx 41A^{-1/3}$. The spherical oscillator frequency (ω_0^3=$\omega_x\ \omega_y\ \omega_z$) is assumed to be constant and can be rewritten in terms of

$$\omega_0 = \left(1 - \frac{4}{3}\epsilon_2^2 - \frac{16}{27}\epsilon_2^3\right)^{-1/6} = constant \tag{2.20}$$

Under the above conditions and replacing the values of ω_x, ω_y and ω_z in Equation 2.15, we may write the Nilsson Hamiltonian as:

$$\mathcal{H}_{Nilsson} = -\frac{\hbar^2}{2m}\nabla^2 + \frac{1}{2}m\omega_0^2 r^2 - m\omega_0^2 r^2 \epsilon_2 \frac{4}{3}\sqrt{\frac{\pi}{5}}Y_{20}(\theta,\phi) + C\overrightarrow{l}.\overrightarrow{s} + Dl^2 \tag{2.21}$$

where r^2=x^2+y^2+z^2 is the nuclear radius and Y_{20} is the spherical harmonics. The Nilsson Hamiltonian satisfy the schrödinger equation $\mathcal{H}_{Nilsson}\phi_i$=$E_i\phi_i$ where ϕ_i and E_i is the wave function and the Eigen energy of the i^{th} particle. respectively. In the limit of large deformation (i.e. $\epsilon_2 \rightarrow 0$) the l^2 and $\overrightarrow{l}.\overrightarrow{s}$ term is negligibly small and can be ignored. The Nilsson Hamiltonian in Equation 2.21 then reduced to anisotropic Harmonic oscillator which can have two independent oscillation about x-y plane and along z axis. Therefore along these two directions, the good quantum numbers are $(n_x + n_y)$ and n_z separately. Like the case in one dimensional harmonic oscillator energy, represented by quanta n_i as E_i=$\hbar\omega_i(n_i$+$1/2)$, the eigen values of the Equation 2.21 goes asymptotically to:

$$E(n_x, n_y, n_z) = \hbar\omega_x (N - n_z + 1) + \hbar\omega_z \left(n_z + \frac{1}{2}\right), N = n_x + n_y + n_z \qquad (2.22)$$

Since $\mathcal{H}_{Nilsson}$ is independent of the angle ϕ around the z-axis, the Hamiltonian is independent of rotation about the z axis. The projection of both orbital ($\overrightarrow{l}$) and Spin ($\overrightarrow{s}$) angular momentum ($\overrightarrow{L}_z$ and $\overrightarrow{S}_z$ respectively) on the symmetry axis z are commonly denoted by Λ and Σ respectively and their sum, the projection of the total angular momentum on the symmetry axis (z), is indicated by Ω. So the energy in Equation 2.22 and the states now can be very conveniently written in terms of the so called asymptotic quantum number as $\Omega^\pi[Nn_z\Lambda]$. In DSM orbital angular momentum l and total angular momentum j are no longer a good quantum number, rather the only conserved quantum numbers are N, π and Ω. When the deformation $\epsilon_2 \rightarrow \propto$, we can neglect l^2 and $\overrightarrow{l}.\overrightarrow{s}$ term, n_z and Λ also become approximately good quantum numbers (asymptotically"). $\Omega^\pi[Nn_z\Lambda]$ now can identify the states uniquely where N is the principal quantum number denoting the major shell, n_z is oscillation quanta along the symmetry z-axis(the number of wave function in z direction) and parity π of the states. The Nilsson energy levels (in unit of $\hbar\omega_0$) calculated from the Equation 2.21 as a function of deformation parameter ϵ_2 are shown separately for neutron in range (82≤N≤126) and for proton in range (50≤N≤82) in figure 2.5 and figure 2.6 respectively. From the definition, for $\epsilon_2 > 0$ the nucleus is said to be of prolate shape and for $\epsilon_2 < 0$ it is of oblate shape.

From the above discussion we have Ω=Λ+Σ=$\Lambda \pm \frac{1}{2}$, where Ω is the projection of one valance particle on the symmetry-z axis. For multiple valance particle, the total projection of each

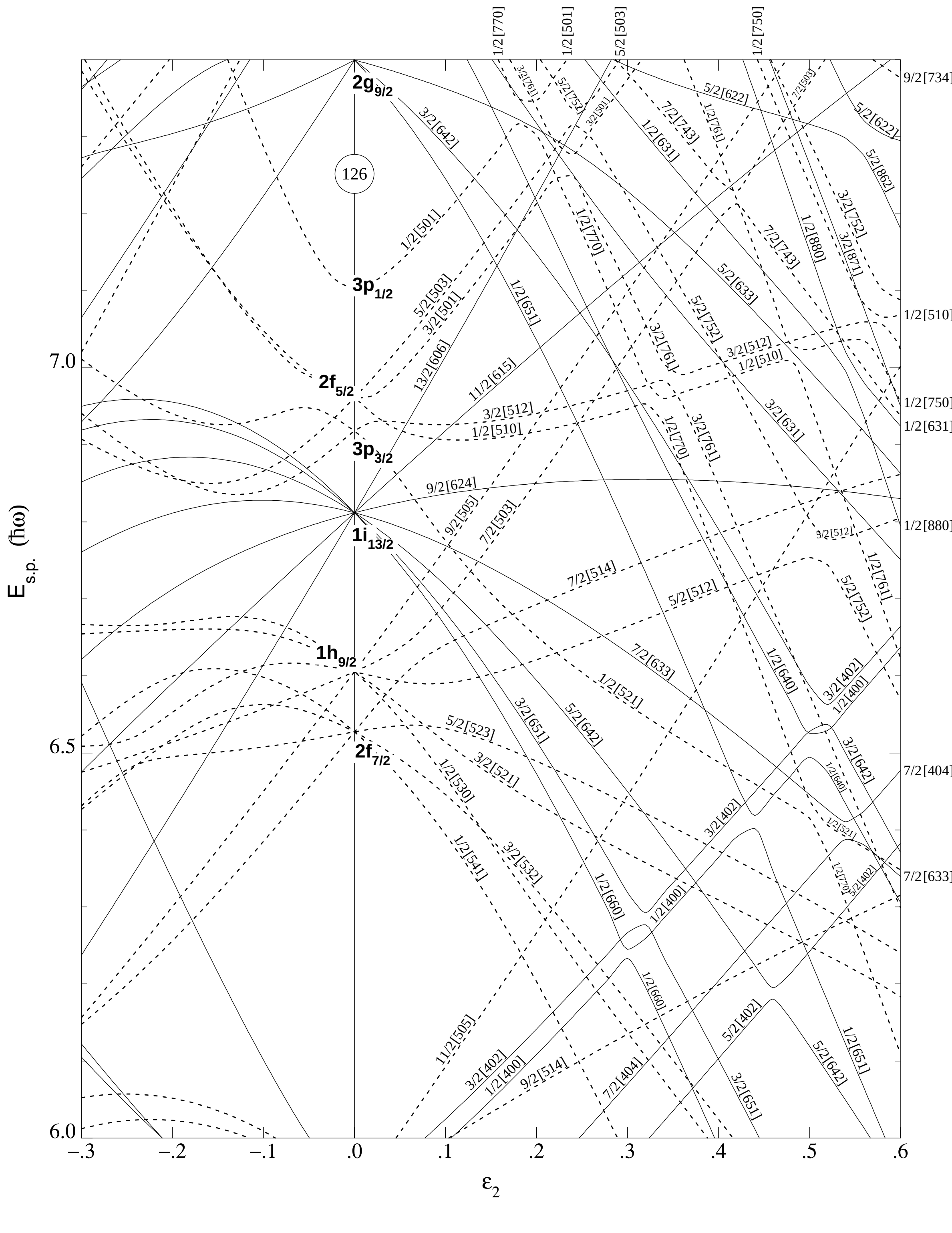

Figure 2.5: Nilsson diagram of single particle levels, calculated from equation 2.21 for neutrons (82$\leq$ N$\leq$ 126) as a function of deformation. The solid lines correspond to positive parity orbitals and the dashed. lines correspond to negative parity orbitals. Figure taken from ref. [22].

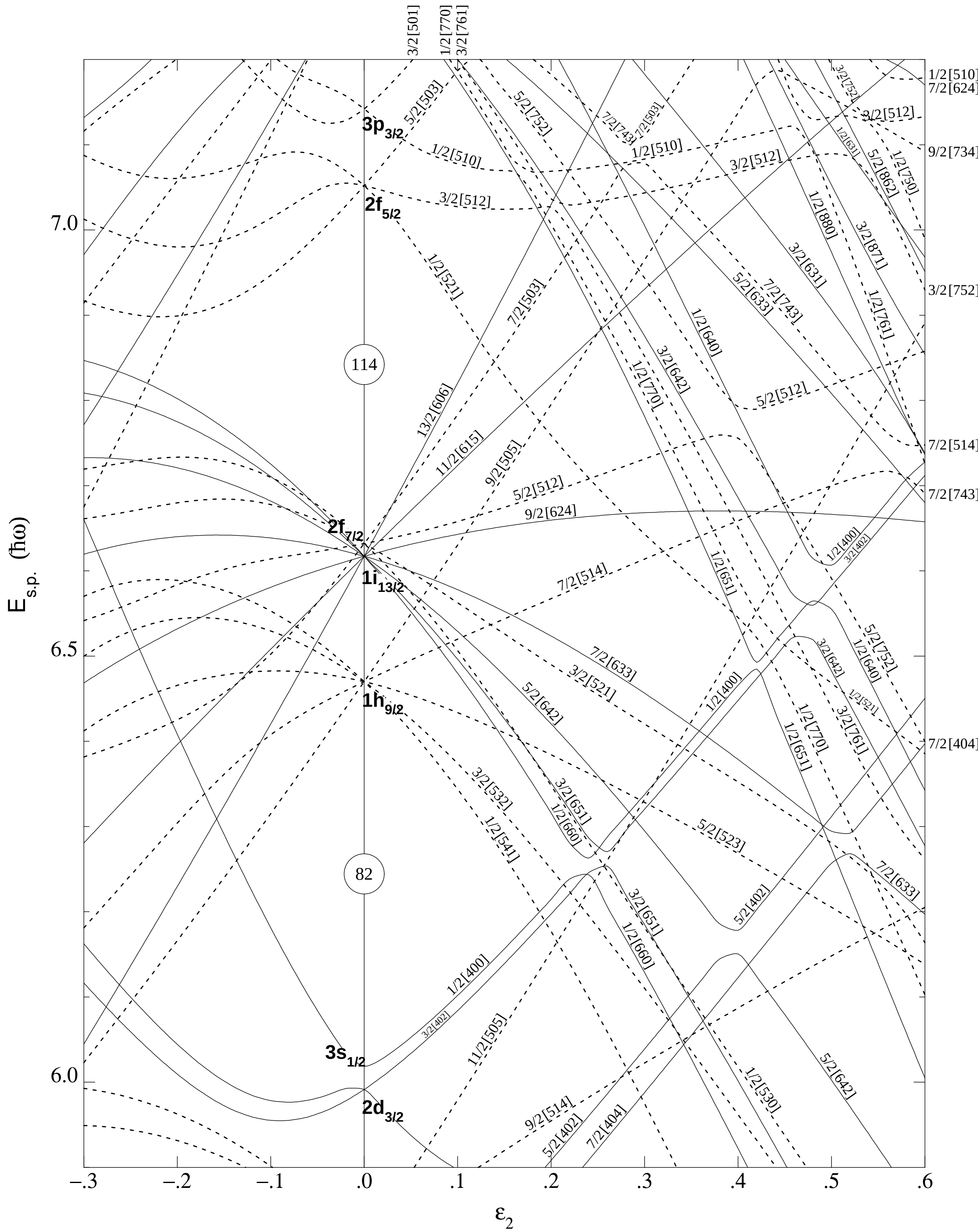

Figure 2.6: Nilsson diagram of single particle levels, calculated from equation 2.21 for protons (50≤ Z≤ 82) as a function of deformation. The solid lines correspond to positive parity orbitals and the dashed. lines correspond to negative parity orbitals. Figure taken from ref. [22].

nucleon is denoted as

$$K = \sum_{i=1}^{val.nucl.} \Omega_i \tag{2.23}$$

For a single valance nucleon (i=1) equation 2.23 reduced to $K = \Omega$. The details schematic diagram of the projections of angular orbital momentum $\overrightarrow{l}$, spin angular momentum $\overrightarrow{s}$ and total angular momentum $\overrightarrow{j}$ on symmetry axis are shown in Figure 2.7

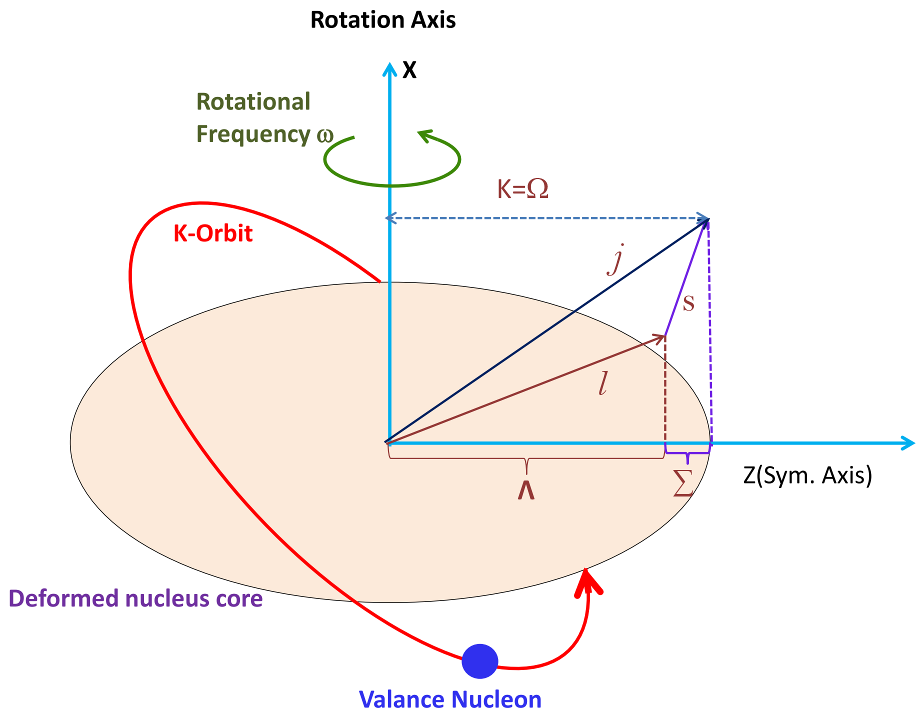

Figure 2.7: The nucleon has orbital angular momentum l and spin angular momentum s. The total angular momentum is j so that $j = l + s$. The projection of the orbital angular momentum(l) and spin angular momentum (s) on the symmetry axis is represented by Λ and Σ respectively. Projection of a single valance particle total angular momenta j on the symmetry axis of a deformed nucleus is represented by. $\Omega = \Lambda + \Sigma$.

The possible values of the quantum numbers n_z and Λ are given by

$$n_z = 0, 1, 2, ..., N \tag{2.24}$$

and

$$\Lambda = (N - n_z), (N - n_z - 2), (N - n_z - 4), ..., 0 \; or \; 1 \tag{2.25}$$

It is the loss of sphericity which makes a preferred direction in space for the nucleon to rotate, and thus the $2j+1$-fold degeneracy of a given j-state is lifted, for $\epsilon_2 < 0$ or < 0. Only a degeneracy of two is remaining (i.e. the state with $\pm\Omega$ have same energy) which is actually a reflection of a time-reversal symmetry. For a particular j the Ω can have the values, ranging from $-j \geq \Omega \geq j$. Nilsson Model was proven to be of very useful in predicting the shapes of nuclei. The levels with lower Ω are shifted downward for positive deformation $\epsilon_2 > 0$ (prolate shape) and upward for negative deformation $\epsilon_2 < 0$ (oblate shape) as can be seen from figure 2.5 and figure 2.6 . This effect becomes more pronounced for high j, low Ω orbitals and plays an important role in modifying the shapes of nuclei. Due to the increasing difference between the energy levels corresponding to different Ω values with deformation for different Ω values are greater for higher j orbital, some of the (Ω) energy levels can intrude in adjacent major shells from lower or upper major shells. These orbitals are called intruder orbital. $\pi h_{9/2}$ and $\nu i_{13/2}$ are two such intruder orbitals in the range of $50 < Z < 82$ and $82 < N < 126$ which intrude in the different parity major shells resulting to some spin gap isomer in those nuclei. The Nilsson model (DSM)has been successfully used to describe a large amount of data for nuclei with moderate to large ground state deformation. However, to describe the rotational behaviour of a deformed nucleus, the Nilsson model (DSM) Hamiltonian has to be accordingly modified to a deformed rotating potential which is achieved in the Cranking model as described in the next section.

2.5 Cranking Model

For rapidly rotating nuclei, the single particle model are mainly described in the framework of the cranking model. The model deals with the microscopic effect of a rotating nucleus on the motion of a single particle. The Cranking model first mathematically formulated by Inglis [23, 24] and has been further developed by Bengtsson and Frauendorf [25]. By introducing a body fixed frame with the nucleus, which rotates with constant angular velocity ω with respect to the laboratory fixed frame in space, the motion of the rotating nucleons in the rotating frame becomes simpler to describe. The rotation is treated classically and the nucleons are considered as independent particles moving in an average rotating potential. The transformation of the coordinate axes are shown in figure 2.8. The intrinsic (body fixed) frame and axis (1, 2,

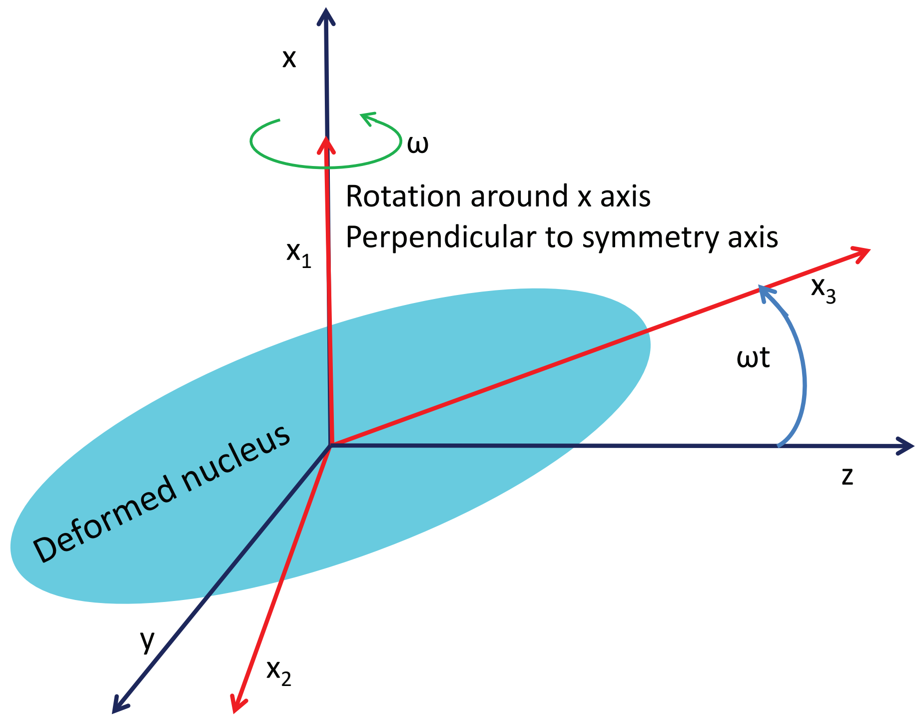

Figure 2.8: x, y, z is the principle axis in the laboratory frame. The body-fixed coordinates (x_1, x_2, x_3) rotates around the laboratory axis with frequency ω.

3) ,which has a fixed orientation with respect to the nuclear potential is used to describe the motion of the nucleons and is shown in figure 2.8. If intrinsic coordinates (in body fixed frame) rotate around an axis perpendicular to the symmetry axis and the symmetry axis coincides with the intrinsic axis, x3, and the intrinsic axis, x1, coincides with the laboratory axis x (which is the rotation axis as well), than the total cranking Hamiltonian for N particle system is given by:

$$H_\omega = H^0 - \omega J_x = \sum_{\nu=1}^{N} h_\nu^0 - \omega j_{x\nu} \tag{2.26}$$

where, H_ω is the total Hamiltonian in the rotating frame(body fixed frame), H_0 is total Hamiltonian in the laboratory system and J_x is the projection of total angular momentum onto the rotation axis. On the other hand, $h_\nu^\omega = h_\nu^0 - \omega j_{x\nu}$ is the single particle Hamiltonian in the rotating frame, h^0_ν is the single particle Hamiltonian in the laboratory system and $j_{x\nu}$ is the projection of total angular momentum of single particle onto the rotation axis. The $-\omega j_{x\nu}$ term contains the Coriolis and centrifugal forces in the rotating frame. The Coriolis force is responsible to align the angular momentum of the nucleons along the rotation axis [26]. The eigenvalues of this Hamiltonian (H_ω), are known as Routhians. Solving this Hamiltonian in equation 2.26 in terms of eigen function $\mid \nu^\omega\rangle$, the total energy in the laboratory frame is given by,

$$E = \sum_{\nu=1}^{N} e^\omega_\nu + \omega \sum_{\nu=1}^{N} \langle \nu^\omega \mid j_x \mid \nu^\omega \rangle \tag{2.27}$$

where e^ω_μ represents the eigenvalues (i.e. single particle Routhian) in the rotating frame. This cranking model can calculate various parameters like projection of total angular momentum (I_x) and aligned angular momentum (i_x) onto the rotation axis in the following manner,

$$I_x = \sum_{\nu=1}^{N} \langle \nu^\omega \mid j_x \mid \nu^\omega \rangle \tag{2.28}$$

The slope of the Routhian energy is related to the alignment (i_x) which can be defined as

$$i_x = -\frac{de^\omega_\nu}{d\omega} \tag{2.29}$$

The Coriolis term -ω j_x in the cranking Hamiltonian breaks the time reversal symmetry in the nucleus.As a result Nilsson quantum number Ω is no more consider to be a good quantum number. Only parity (π), which describes the symmetry under reflection along with signature quantum number α remain as good quantum number. Signature quantum number describes the symmetry under a rotation of 180° the nucleus about the rotation axis. This two quantum number can be utilized to define the nuclear states. The rotation operator is defined by

$$\mathcal{R}_x = exp(-i\pi j_x) \tag{2.30}$$

with the eigenvalues

$$r = exp(-i\pi\alpha) \tag{2.31}$$

Signature quantum number α [27] is related to the total angular momentum by

$$I = \alpha \ mod \ 2 \tag{2.32}$$

Systems with an even number of nucleons have $\alpha = 0$ or 1, while for odd number of nucleons the system posses the value of $\alpha = \pm\frac{1}{2}$. The signature quantum numbers corresponding to the favoured and unfavoured states are defined as

$$\alpha_f = \frac{1}{2}(-1)^{j-1/2} \qquad \alpha_{uf} = \frac{1}{2}(-1)^{j+1/2} \tag{2.33}$$

j is the angular momentum of the odd valance particle of the system. If the nuclei has multi particle configuration, the favored signature is calculated from the equation

$$\alpha_f = \frac{1}{2}\sum_i(-1)^{j_i-1/2} \tag{2.34}$$

This model can predict the rotation effect on single particle energy levels in deformed nucleus but for the total nuclear energy Total Routhian Surface(TRS) calculation is appropriate.

2.6 Total Routhian Surface (TRS) calculations

In this thesis, the total Routhian surface (TRS) calculations have been performed to predict the structure of nuclei, as described by Nazarewicz *et.al.* [28, 29]. The total Routhian $E^\omega(Z, N; \beta, \gamma)$ of a nucleus (Z,N) as a function of deformation(β, γ) can be obtained from the sum of the liquid-drop energy, shell correction energy and the pairing correction energy within the cranked Woods-Saxon, Bogolyubov, Strutinsky approach as:

$$E^\omega(Z, N; \beta, \gamma) = E^\omega_{LD}(Z, N; \beta, \gamma) + E^\omega_{shell}(Z, N; \beta, \gamma) + E^\omega_{pair}(Z, N; \beta, \gamma) \tag{2.35}$$

The liquid drop model energy E^ω_{LD} is calculated with nuclear surface energy E^ω_{surf}, nuclear Coulomb energy E^ω_{Coul} and the nuclear rotational energy E^ω_{rot} as

$$E^\omega_{LD}(Z, N; \beta, \gamma) = E^\omega_{surf}(Z, N; \beta, \gamma) + E^\omega_{Coul}(Z, N; \beta, \gamma) + E^\omega_{rot}(Z, N; \beta, \gamma) \tag{2.36}$$

The nuclear rotational energy is calculated with equation

$$E^{\omega}_{rot}(Z, N; \beta, \gamma) = \frac{\hbar^2 I(I+1)}{2J_{rig}} \tag{2.37}$$

where J_{rig} is the rigid body moment of inertia at a given deformation with density distribution of at $r_0 = 1.2fm$. The shell correction energy is calculated using the Strutinsky shell corrections method with a deformed Woods-Saxon potential.The Hartree-Fock-Bogoliubov code of Nazarewicz *et al.* [28, 29] has been utilized for the TRS calculations to interpret the ground state deformations as well as configurations in this thesis work. The TRS have been calculated in $(\beta_2, \gamma, \beta_4)$ deformation mesh points with minimization on β_4. The details calculation procedure is described in the reference [30, 43]. The code can also generate the single particle Routhians which can predict the involvement of the possible single particle orbitals near the Fermi level.

2.7 Deduced quantities for rotational bands of a deformed nucleus

The common feature of a deformed system is that it can rotate about an axis(x) perpendicular to the symmetry axis(z) leading to the observation of the rotational band. The rotational Hamiltonian is given by the equation [28]:

$$H = \frac{\hbar^2}{2\mathcal{J}} R^2, R = \mathcal{J}\omega, \mathcal{J} = \frac{R}{\omega} \tag{2.38}$$

Where $\mathcal{J}$ is the moment of inertia and R is the rotational angular momentum and ω is rotational frequency of the deformed rotor. To characterize a rotational band one needs to deduce the quantities, like, moments of inertia, rotational frequency, aligned angular momentum and Routhian energies etc. from the level scheme. The rotational energy of a level of a ground state rotational band with spin I can be expressed in the form of the energy of a deformed rotor:

$$E_{rot}(I) = \frac{R^2}{2\mathcal{J}} = \frac{\hbar^2}{2\mathcal{J}} I(I+1) \tag{2.39}$$

$$E_{rot}(I) \approx \frac{\hbar^2}{2\mathcal{J}} I^2 \tag{2.40}$$

$$\frac{dE_{rot}(I)}{d(I^2)} = \frac{\hbar^2}{2\mathcal{J}} \tag{2.41}$$

I is the rotational angular quantum number (angular momentum). The moment of inertia in Eq. 2.41 are defined as Kinematic Moment of Inertia (KMI) of the rotational band. Combining Eq. 2.38 and Eq. 2.41 the KMI is defined as $\mathcal{J}^{(1)}$, defined as,

$$\mathcal{J}^{(1)} = \frac{\hbar I_x(I)}{\omega(I)} = [\frac{2}{\hbar^2}\frac{dE_{rot}(I)}{d(I^2)}]^{-1} \tag{2.42}$$

Comparing the last two term of the above Eq. 2.42 the frequency of the rotor (rotational band) is found to be:

$$\omega(I) = \frac{1}{\hbar}\frac{dE_{rot}(I)}{d(I)} \tag{2.43}$$

The Dynamic Moment of Inertia(DMI) represented by $\mathcal{J}^{(2)}$ is defined as the change of the Moment of Inertia(KMI) with respect to the spin(I). The DMI is a significant quantity as the rotational band may not have fixed Moment of Inertia when it rotates with a high angular momentum and due to the centrifugal force, the MoI may changes. The DMI is related to the curvature (second derivative) of the E versus I curve:

$$\mathcal{J}^{(1)} = [\frac{1}{\hbar^2}\frac{d^2E_{rot}(I)}{d(I^2)}]^{-1} = \hbar\frac{dI}{d\omega(I)} \tag{2.44}$$

The Dynamic moment of inertia can be represented considering the expression of KMI ($\mathcal{J}^{(1)}$) from Eq. 2.42 as:

$$\mathcal{J}^{(2)} = \hbar\frac{dI}{d\omega(I)} = \hbar\frac{d[\omega\mathcal{J}^{(1)}]}{d\omega(I)} = \hbar[\mathcal{J}^{(1)} + \omega\frac{d\mathcal{J}^{(1)}}{d\omega(I)}] \tag{2.45}$$

It is evident from the above that in the limit of rigid rotation $\mathcal{J}^{(2)} \approx \mathcal{J}^{(1)}$.

Usually a rotational band is defined as a sequence of a E2 transitions connecting 0^+, 2^+, 4^+ and so on spin levels. So if the gamma energy decaying from E_I level to E_{I-2} is defined by E_γ then according to Eq. 2.39,

$$E_\gamma(I) = E_{I+2} - E_I = \frac{\hbar^2(4I-1)}{2\mathcal{J}} \tag{2.46}$$

As per the real scenario, the rotational band is not form on the ground state and has a band head of spin K. Then the rotational energy is changed according to the equation

$$E_{rot}(I) = \frac{R^2}{2\mathcal{J}} = \frac{\hbar^2}{2\mathcal{J}} I_x(I_x + 1) \tag{2.47}$$

Where I_x is the projection of the total angular momentum(I) on the rotation axis and is given by:

$$I_x(I) = \sqrt{I(I+1) - K^2} \approx \sqrt{\left(I + \frac{1}{2}\right)^2 - K^2}. \tag{2.48}$$

K is the projection of the total angular momentum onto the symmetry axis. As pointed out,the value of K is, normally, equal to the band-head spin for strongly coupled band, and the spin I in all the above equations should be replaced with I_x From the experimental point of view, all the above expression of the different rotational quantity are changed and the modified expression are used to deduced them experimentally from the level scheme.

The **rotational frequency**, for an axially symmetric deformed nucleus which rotates about an axis (x) perpendicular to the symmetry axis, can be written as [25], following simple steps from the Eq. 2.43

$$\hbar\omega(I) = \frac{dE_{rot}(I)}{dI_x} \approx \frac{E_{rot}(I+1) - E_{rot}(I-1)}{I_x(I+1) - I_x(I-1)}, \tag{2.49}$$

$$\approx \frac{E_\gamma}{2}(I \gg K), \tag{2.50}$$

in analogy with a classical rotor.

Expression for the two moments of inertia (kinematic moment of inertia and dynamic moment of inertia) for deformed nucleus are expressed as: . The **Kinematic moment of inertia** is defined as

$$J^{(1)} = \frac{\hbar I_x(I)}{\omega(I)}. \tag{2.51}$$

and the **Dynamic moment of inertia** is defined as,

$$J^{(2)} = \frac{\hbar dI_x(I)}{d\omega(I)}, \tag{2.52}$$

$$\approx \frac{4}{\Delta E_\gamma} \hbar^2 MeV^{-1}, \tag{2.53}$$

For even-even nuclei the dynamic moment of inertia (DMI), $J^{(2)}$, is independent of spin, I. This property is very useful in cases where spin and parity of a given rotational band are not known (e.g for super-deformed bands).

The **experimental aligned angular momentum**, represented by i_x, is the single particle contribution to the nuclear angular momentum and defined as,

$$i_x = I_x(I) - I_x^{ref}(I). \tag{2.54}$$

where,

$$I_x^{ref}(I) = \Im_0\omega + \omega^3\Im_1 \tag{2.55}$$

is the reference angular momentum of the core and is calculated as prescribed by Ref. [26] in terms of the Harris parameters. $\Im_0$ and $\Im_1$ are the Harris parameters. These Harris parameters, used in the above equation, can be determined by fitting the experimental points in the I_x versus ω plot.

The **experimental Routhian** (single-particle) of a nuclear level is defined by,

$$e^{\omega}_{expt}(I) = E^{\omega}_{expt}(I) - E^{\omega}_{ref}(I) \tag{2.56}$$

where,

$$E^{\omega}_{expt}(I) = \frac{1}{2}\left[E(I+1) + E(I-1)\right] - \omega(I)I_x(I) \tag{2.57}$$

and the reference is calculated by

$$E^{\omega}_{ref}(I) = -\frac{1}{2}\omega^2\Im_0 - \frac{1}{4}\omega^4\Im_1 + \frac{1}{8\Im_0}. \tag{2.58}$$

The obtained values from the above alignments and Routhians and can be directly compared with the experimental values to understand the different properties of the nucleus.

Bibliography

[1] G. Gamow Proceedings of the Royal Society of London, **126**:632, (1930).

[2] C.F.Von Weizsäcker, Z. Phys. **96**, 431 (1936).

[3] H.A. Bethe, Rev. Mod. Phys. **8**, 82 (1936).

[4] P. Ring and P. Schuck, The Nuclear Many-Body Problem, Springer-Verlag Berlin Heidelberg (1980).

[5] M. G. Mayer, Phys. Rev. **75**, 1969 (1949).

[6] R.F. Casten, Nuclear Structure from Simple Perspectives, Second Edition, Oxford Science Publication.

[7] O. Haxel, J.H.D. Jensen and H.E. Suess, Phys. Rev. **75**, 1766 (1949).

[8] M.G. Mayer and J.H.D. Jensen, Elementary Theory of Nuclear Shell Structure (John Wiley, 1955).

[9] A. Bohr, Mat. Fys. Medd. Dan. Vid. Selsk. **26** No. 14 (1952).

[10] E. Feenberg, Shell Theory of the Nucleus (Princeton University Press, 1955).

[11] B. D. Day, Rev. Mod. Phys., **39**, 719 (1967).

[12] N. E. Reid, M. K. Banerjee, G. J. Stephense Jr., Phys. Rev. **C5**, 41 (1972).

[13] A. Bohr, Mat. Fys. Medd. Dan. Vid. Selsk. **26** No. 14 (1952).

[14] Alvise Raccanelli et. al.,arXiv:1306.6646v2 [astro-ph.CO] 14 Aug 2013.

[15] G. Andersson et al., Nucl. Phys. **A 268**, 205 (1976).

[16] P. A. Pipidis's Thesis (Structural behavior of ^{157,158,159}Dy in the I=30-50l spin regime and the high-spin domain of ^{158}Er up to and above band termination).

[17] Ali Al-Khatib's Thesis (High-Spin γ ray Spectroscopy of ^{124}Ba, ^{124}Xe and ^{125}Xe).

[18] S. G. Nilsson. Binding States of Individual Nucleons in Strongly Deformed Nuclei. K. Dan Vidensk. Selsk. Mat. Fys. Medd.**29(16)**, (1955). 3.5, 3.7, 3.8

[19] S. G Nilsson C. F. Tsang A. Sobiczewski Z. Szymánski S. Wycech C. Gustafson I. L. Lamm P. Möller and B. Nilsson. On the Nuclear Structure and Stability of Heavy and Superheavy Elements. Nucl. Phys. **A, 131**, 1 (1969). 3.5, 4.5.

[20] B. Nilsson, Inclusion of a P4 Term in the Deformed Shell Model Potential. Nucl. Phys. **A, 129**, 445(1969) 3.5.

[21] B. R. Mottelson and S. G. Nilsson. Clasification of the Nucleonic States in Deformed Nuclei. Phys. Rev. **99**, 1615 (1955). 3.5, 3.7, 3.8.

[22] R. B. Firestone, et al., Table of Isotopes (John Wiley and Sons, Inc., New York (1999)).

[23] D.R.Inglis, Phys. Rev. **96**, 1059 (1954).

[24] D.R.Inglis, Phys. Rev. **97**, 701 (1955).

[25] R. Bengtsson and S. Fraunendorf, Nucl. Phys. **A 327**, 139 (1979).

[26] F. Stephens, Rev. Mod. Phys. **47**, 43 (1975).

[27] A. Bohr and B. R. Mottelson: Nuclear Structure, vol. II (W. A. Benjamin, Inc., New York, 1975)

[28] W. Nazarewicz et al., Nucl. Phys. **A 512**, 61 (1990).

[29] W. Nazarewicz et al., Nucl. Phys. **A 435**, 397 (1985).

[30] G. Mukherjee et al., Phys. Rev. **C 64** (2001) 034316.

[31] G. Mukherjee et al., Nucl. Phys. **A 829**, 137 (2009).

[32] R. F. Casten, Nuclear Structure from Simple Perspectives, Second Edition, Oxford.

[33] R. Bengtsson and S. Fraunendorf, Nucl. Phys. **A 327**, 139 (1979).

[34] S.M. Harris, Phys. Rev. **138** B509 (1965).

[35] H. Pai Thesis (Study of nuclear structure near the Z = 82 and N = 82 shell closures).

[36] T. Roy Thesis (Study of high spin states in nuclei near Z=82).

[37] D. L. Hill and J. A. Wheeler, Phys. Rev. **89**, 1102 (1953).

[38] T. Bengtsson and I. Ragnarsson, Nucl. Phys. **A 436**, 14 (1985).

[39] H. Hübel, Contribution to Weatherill Symposium, Philadelphia, 1991 (unpublished).

[40] G. Baldsiefen et al., Nucl. Phys. **A 574**, 521 (1994).

[41] R.M. Clark and A.O. Macchiavelli, Ann. Rev. Nucl. Part. Sci. **50** , 1 (2000).

[42] A.O. Macchiavelli et al., Phys. Rev. **C 58** R621 (1998).

[43] A.O. Macchiavelli *et al.*, Phys. Rev. C **57**, R1073 (1998).

[44] H. Hübel, Prog. Part. Nucl. Phys. **54**, 1 (2005).

Chapter 3

Experimental Techniques and Data Analysis

Nuclear structure information can be studied in details by observing the energy of the decaying γ-rays from the excited nuclear state, and by measuring the intensity, Polarization the angular dependence of them with respect to beam axis. All the information are gathered to build the level scheme, which is basically the unique microscopic energy levels of the nucleus. Due to the intensity drop of the γ rays with increasing spin and energy as well as to probe the non-yrast weakly populated states we need a detector array with high resolution and high efficiency to detect these γ rays. The present thesis involve the population of neutron deficient nuclei in high excitation energy and spin which can be achieved mainly with fusion evaporation reaction. In this chapter, the details experimental procedure to extract the information of the high spin excited states of atomic nuclei in A$\sim$200 region and the setup used for various experiments will be discussed.

3.1 Population of High Angular Momentum States in Nuclei

There have been several methods of production of nuclei at high angular momentum like a) Fusion evaporation reaction, b) Fusion-Fission reaction, c) Transfer reaction d) Coulomb excitation etc. Among them, the heavy ion induced fusion-evaporation reaction is the most efficient method to populate the nuclei under consideration at high excitation energy and spin as well as with high cross section. The formation and the de-excitation mechanisms of the Compound Nucleus(CN) following fusion-evaporation reaction have been shown in Fig. 3.1(a). The projectile, with an energy higher than the coulomb barrier, collides with the target nucleus, and formed compound nucleus by fusing together. The compound nucleus formation time scale is within 10^{-22} to 10^{-20} sec. The energy are shared by the constituent nucleon, if the compound nuclei sustain more than 10^{-20} sec [1] and fully equilibriated with respect to thermodynamic equilibrium. The "hot" and fast rotating nucleus then cools down by particle evaporation[2] within $\sim 10^{-16}$ sec. Evaporating particles are mostly light mass particle, like neutrons, protons, or alphas. Probability of evaporation of protons, or alphas (being a charged particles) are less than that of neutrons due to their coulomb barrier. Compound nucleus loses excitation energy on an average of about 8 MeV (one neutron separation energy) and only a few units(about $1\hbar$) of angular momentum per neutron evaporation, and the residual nuclei after particle evaporation remains with sufficient amount of angular momentum and complete alignment of the compound nucleus is still preserved. At higher excitation energy, γ-decay (γ rays from Giant Dipole Resonance) which is a Electro-Magnetic interaction, is also possible. But the particle decay, being a strong interaction process, is a much more probable. Particle evaporation is no longer possible when the excitation energy comes below the particle emission threshold and the residual nucleus enters the 'entry-line' [4] which is roughly 8 MeV (i.e. one neutron binding energy) above the 'Yrast line'. The yrast line is virtual line corresponds to the nuclear states with minimum excitation energy for a given spin. From the entry-line residual nucleus tries to minimize its energy via subsequent emission of statistical γ rays which are mainly of E1 character. They take away only a few units of angular momentum, but much of energy. Since

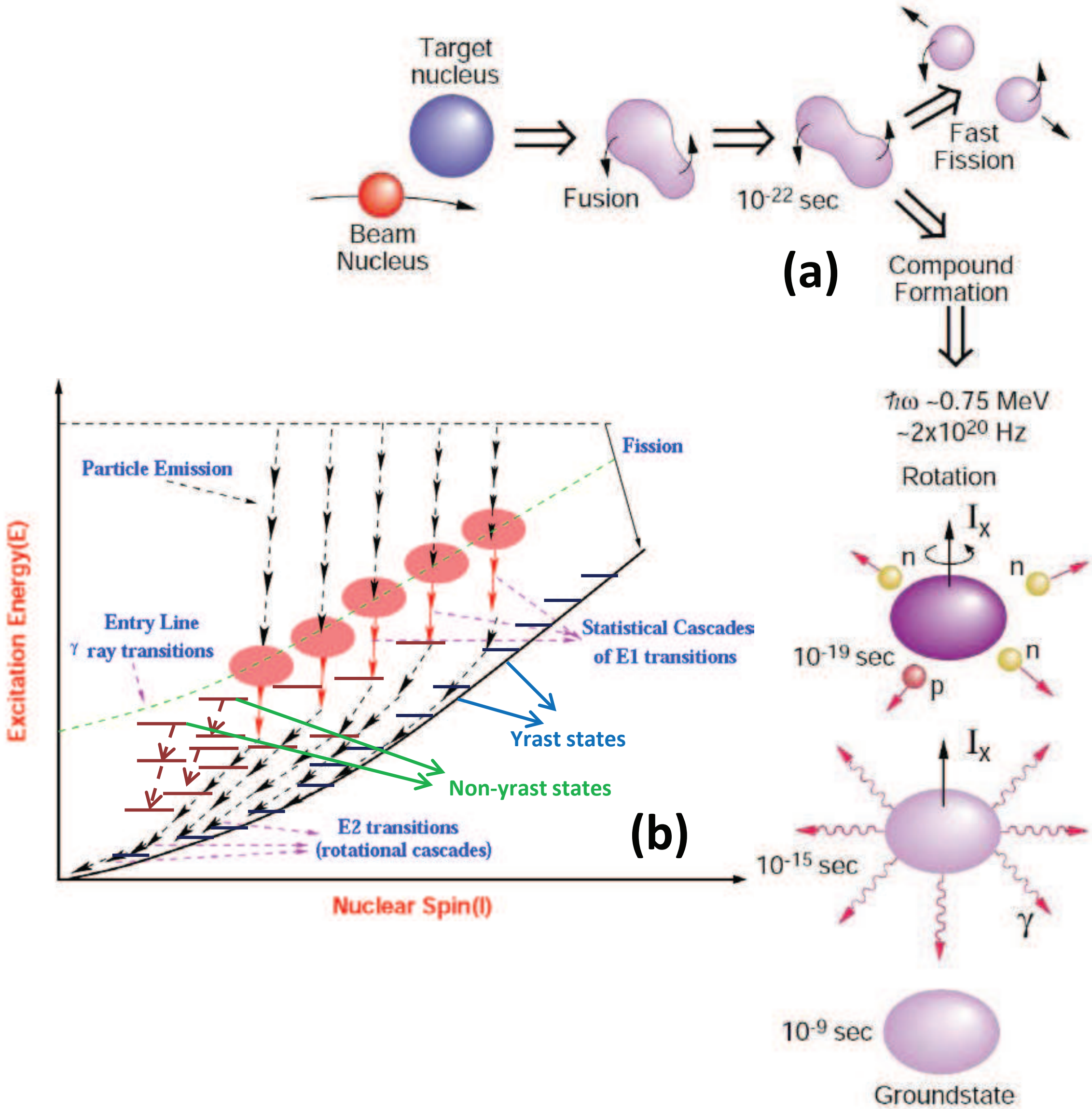

Figure 3.1: Formation and decay of the compound nucleus via various processes in a fusion-evaporation reaction.(a) Schematically showing the formation of CN with the time scale of different processes. Figure is taken from ref. [3]. (b) The entry line for discrete γ-transitions and decay of γ rays via yrast and non-yrast state.

the nuclear level density is very high around the entry-line, statistical γ ray transitions are called quasi-continuum transitions and the nuclei comes closure to the 'yrast line'. After that, the residual nucleus radiates it energy and comes to the ground state by emitting a cascade of discrete γ transitions along the yrast line and the states on, or very near to yrast line are populated as shown in Fig. 3.1(b). These are generally collective E2 rotational cascades in case of deformed nuclei. Some times when the nucleus is produced at lower angular momentum and high energy, after the particle evaporation the excited nucleus comes to a states below the entry line (particle threshold value) but far away from the yrast line. Thus the nucleus passed through many non-yrast states via γ-decays. In γ ray spectroscopy, these discrete γ rays are detected to understand the nuclear structure information. Within about 10^{-9} seconds the total decay process is completed.

Understanding of the nuclear bahaviour at low and medium spin regime demands information on yrast as well as near yrast excited states. This can provide valuable information regarding low lying single particle excitation as well as exotic near yrast-structures. These states can be populated suitably using light ion beams and investigated using γ-spectroscopy techniques. With the availability of light ion projectile like α, proton etc. from K-130 Cyclotron, VECC, Kolkata, extensive study of these kind of structure is possible, which is one of the motivation of present thesis.

3.2 γ-radiation detection with High-Purity Germanium (HPGe) detectors

The basic information about Energies, spins, parities of the levels can be obtained by measuring the Energies, angular correlations, linear polarization of the decaying γ rays from excited states. For the detection of the γ rays in a detector the γ rays must interact and lose its energy in the detector medium. The γ rays interact with matter mainly through three process; Photoelectric effect, Compton Scattering and Pair Production and transfer partial or complete γ ray energy to the electrons within the detector material. Among the three processes photoelectric effect is the important one for γ ray spectroscopy experiment because γ ray deposits its full energy in this process. In γ ray spectroscopy, the absolute necessary condition for choosing the detector is to obtain good energy resolution. Specially, for good photopeak efficiency (achieved by using high Z material) and low noise, semiconductor detector made of High Purity Ge(HPGe) crystals is the best option for detection of γ rays photons in γ spectroscopy experiment.

High-purity Germanium semiconductor detectors is the main tool for high resolution γ ray spectroscopy. The effective volume of the detector to detect the γ rays actually is the compensated depletion region, formed by the simple reverse bias p-n junction characteristics. For a semiconductor detector, the depletion depth is given by [6]

$$d = \left(\frac{2\epsilon V}{eN}\right)^{1/2} \tag{3.1}$$

where, V is the reverse bias voltage, N represents the net impurity concentration in the initial semiconductor material, ϵ is the dielectric constant and e is the electronic charge. To increase the active volume of the detector determined by the thickness d of the depletion region, the detectors should be more pure (i.e. the impurity concentration N should be as low as possible) and the reverse bias voltage(V) should be increased. At 10^{10} atoms/cm^3 impurity concentration(which is the impurity for a HPGe detector), a reverse bias voltage of 1 kV can produce a depletion depth of 1 cm. HPGe detector has an excellent energy resolution (typically$\sim$2 keV at 1 MeV) compared to gas detectors or scintillators. HPGe detector must be operated at liquid nitrogen(LN2) temperature (77 K) to reduce the thermal fluctuation which leads to the leakage current due to its smaller band gap ($\sim$ 0.7 eV). Unlike Ge(Li) or Si(Li) detectors, these detectors need not always be kept at liquid nitrogen temperature, when not in use. However, time resolution of HPGe detector ($\sim$ 10 ns) is poor in comparison with scintillator detectors. The details testing and characterization of a special type of HPGe detector, i.e. Clover HPGe detector, that has been used to detect the γ rays in the experiments related to the present thesis, are discussed in the next section.

3.3 Characterization of a Clover detectors

Clover HPGe detectors form an essential part of any high efficiency experimental facility for exploring the structure of nuclei. Clover detector is a composite detector consists of four n-type coaxial HPGe tapered crystals placed in a four-leaf clover arrangement using a single cryostat [7] as shown in Fig. 3.2. The main advantage of Clover, over single crystal HPGe detector is its

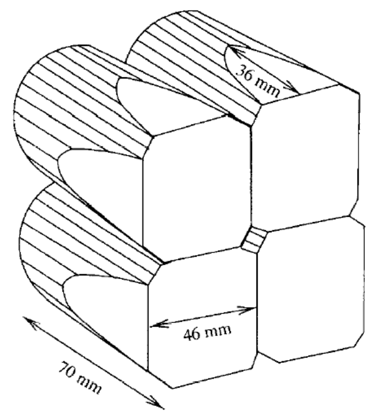

Figure 3.2: A schematic geometry of Clover detector [7].

granular configuration which allows us (a) to get back the Compton scattered events back to the photopeak to increase the photopeak efficiency (b) determination of polarization asymmetry by using the ratio of parallel and perpendicular component of Compton scattering events from the adjacent crystals of a clover detector c) better Doppler correction by measuring the angle of the incident photons more accurately.

To determine the properties of the detector, the γ rays, decaying from ^{152}Eu, ^{133}Ba and ^{60}Co radioactive sources are measured by the clover detector. The pre-amplifier signal from each crystal has been processed with Ortec model 672 Spectroscopic Amplifier with a shaping time 6μs for 1 kcps and with 3μs for 5 kcps and the data were collected in in event by event mode mode using a CAMAC based data acquisition system with master gate generated from the OR of all four crystals of the Clover detector. The energy resolution of the crystals from the different Clover detectors lies in the range of 1.85-2.02 keV at 1332 keV(from ^{60}Co) with 6μs shaping time. Detail testing has been reported in Ref. [8].

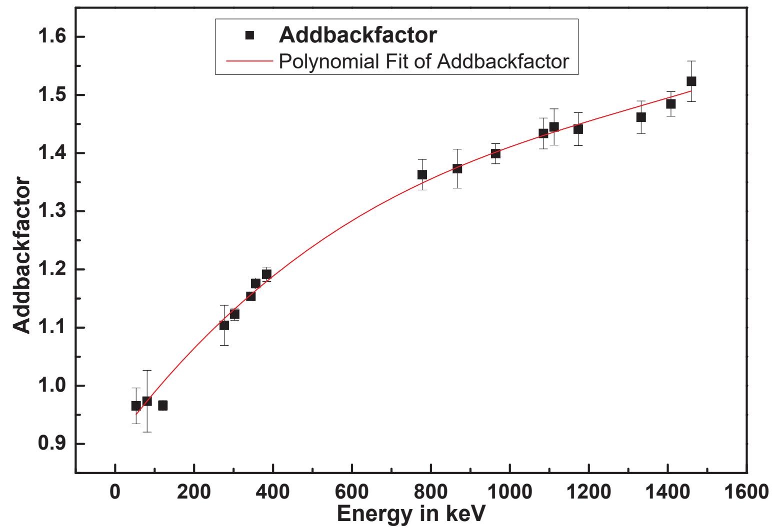

Figure 3.3: Variation of add-back factor with γ ray energy at a distance of 20 cm.

• Clover detector in Addback mode:

Due to the difficulties in growing high purity Ge crystals, big size of HPGe crystals are rare. The configuration of Clover detectors, having a close pack geometry of 4 crystals, can be utilized to achieve a full photopeak efficiency of a single HPGe crystal of same size, as the total volume of the four crystals together, with the addback mode. Due to photoelectric effect γ ray deposits its full energy in any one of the four individual crystal of a clover HPGe detector. Due to Compton scattering, a partial energy of the γ ray is absorbed by any one crystal, and the scattered γ ray can be absorbed by other neighboring crystal. For a particular event, if we add the deposited energy of each crystals of a clover detector we can get back the full energy of the primary γ ray and it will contribute to the full energy photopeak in the spectrum. Thus we can recover the Compton scattered event within the crystals and increase the efficiency of the Clover detector as a whole. This process is called a addback of a Clover detector and it defined as

$$addbackfactor = \frac{Total\ counts\ of\ a\ photopeak\ adding\ the\ energy\ in\ four\ crystal\ in\ one\ event}{The\ sum\ of\ the\ counts\ of\ phtopeak\ of\ all\ the\ crystals}. \tag{3.2}$$

This is done offline where the information about the firing of each crystal is stored on event by event basis(Listmode data). The add-back factors for various γ ray energies have been obtained from the ^{152}Eu, ^{133}Ba and ^{60}Co radioactive sources and has been shown in Fig. 3.3.

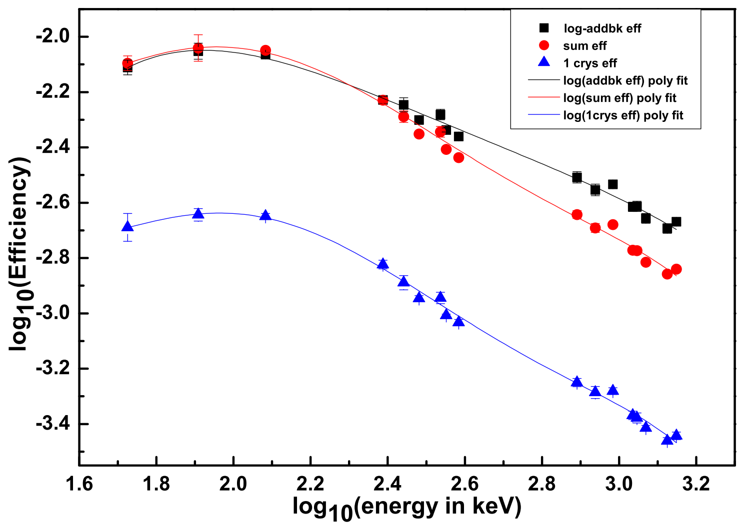

Figure 3.4: Addback efficiency along with the sum efficiency and efficiency of a crystal of the Clover detector as a function of energy. The Logarithmic value of the absolute efficiency has been fitted with a polynomial function.

It can be observed that the ratio is close to one at lower energies due to the lower Compton scattering cross section at these energies. The factor then starts increasing with increasing γ ray energies, as the probability of Compton scattering becomes comparable with the photo electric effect and the add-back mode starts contributing. Beyond 1 MeV γ ray energies, the factor almost gets saturated. At 1332 keV the addback factor was found to be about 1.48±0.03 which slightly lower than the reported value 1.52 at 1332 keV in previous measurements [9]. It is also observed that, due to summing effect specially at lower distance, the addback factor becomes less than 1.0 at lower energies. The absolute addback efficiency was obtained using the above set up keeping the standard radioactive sources(with known activity) at various distances. The absolute addback efficiency of the Clover detector along with the efficiency of a single crystal and efficiency in simple adding at a distance of 20cm is shown in Fig. 3.4. It is clear that the efficiency in addback mode effectively increases after 200 keV energy due to the recovering of Compton scattered events.

- **Timing characteristics of a Clover detector.**

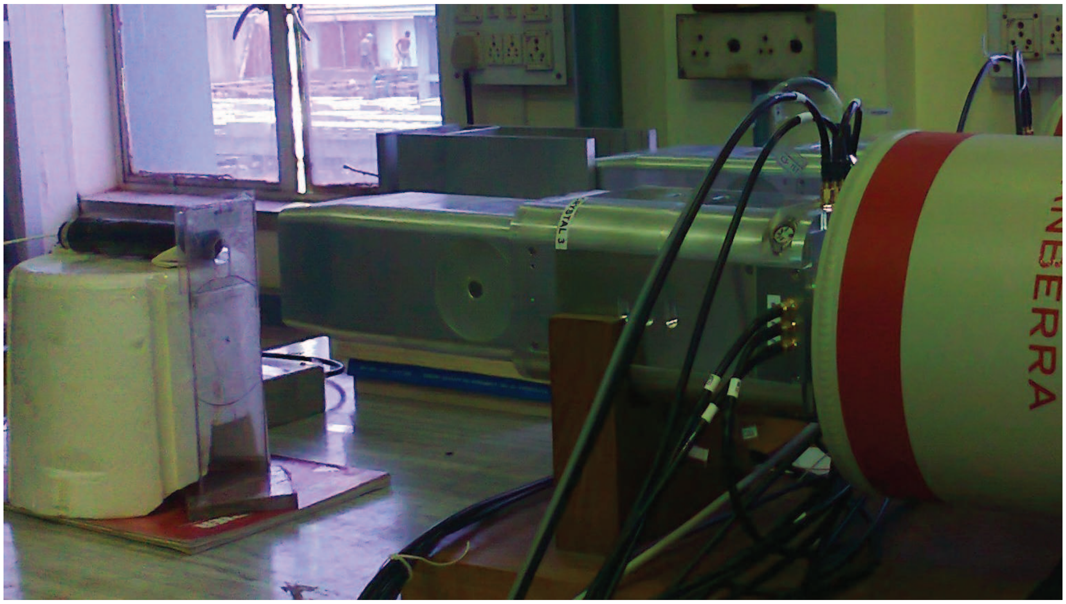

Figure 3.5: Experimental set up for the coincidence timing measurements of Clover detectors with respect to a fast timing BaF2 detector.

Timing resolution of the Clover detector was obtained with respect to a 1" × 1" BaF_2 scintillator detector of timing response 300ps. Coincidence List mode data was taken with ^{60}Co source with a trigger condition of (BaF2). AND. (OR of all crystal). The experimental setup is shown in Fig. 3.5. The timing of the Clover detector were measured with a Time to Amplitude Converter(TAC) using the OR of the signals from all crystals of Clover detector as a start and signal from BaF_2 detector as a stop, after a suitable delay. The TAC spectra of each crystal as well as the OR of all crystals are displayed in Fig. 3.6.

In Fig. 3.6(A) it is seen clearly that there is a time mismatch (of about 5ns) between the individual crystals. Fig. 3.6(B) shows the same TAC projections after selection of 1332 keV in BaF_2 and 1173 keV in individual crystals. The typical time resolution of the Clover detector with respect to fast BaF2 detector, is obtained about 8ns, without energy selection and without time matching of individual crystals. The individual crystals show the time resolution of about 5ns as shown in Fig. 3.6(A), which is improved to about 4ns after particular energy selection in BaF2 and one crystal of clover detector.

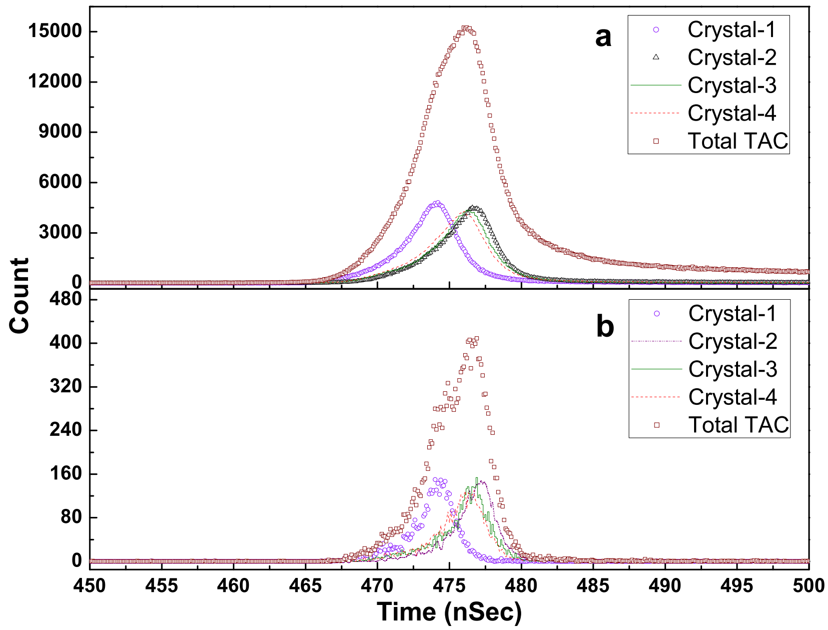

Figure 3.6: Total TAC and projection of TAC of individual crystal (A) without and (B) with energy selection of 1173 and 1332 keV γ rays from ^{60}Co with the above set up.

3.4 Experimental set up

In the present thesis work, the experiments were carried out in K-130 cyclotron using the VECC Array for NUclear Spectroscopy (VENUS) setup which consisted of six Clover detectors at the time of present thesis. For the other experiments, Indian National Gamma Array (INGA), at BARC-TIFR Pelletron facility, Mumbai as well as at K-130 Cyclotron,VECC, Kolkata were used which also consisted of clover detectors. Along with the study of the high spin states of different nuclei around A 200, an offline coincidence setup of one Clover detector and one single crystal LEPS detector has also been used to study the low lying states of the ^{199}Hg. In the following sections, details of these experimental setup are discussed.

3.4.1 VECC Array for NUclear Spectroscopy(VENUS)

The study of near yrast structures of nuclei in moderate spin regime involves the population of nuclei in high excited state by light ion induced fusion evaporation reaction. In view of this, a moderate in-house array of Compton suppressed Clover HPGe detectors has been used for the experiments of the present thesis at VECC, Kolkata using the α beam from K-130 Cyclotron. VECC array for NUclear Spectroscopy (VENUS), which at the time of the present thesis consists

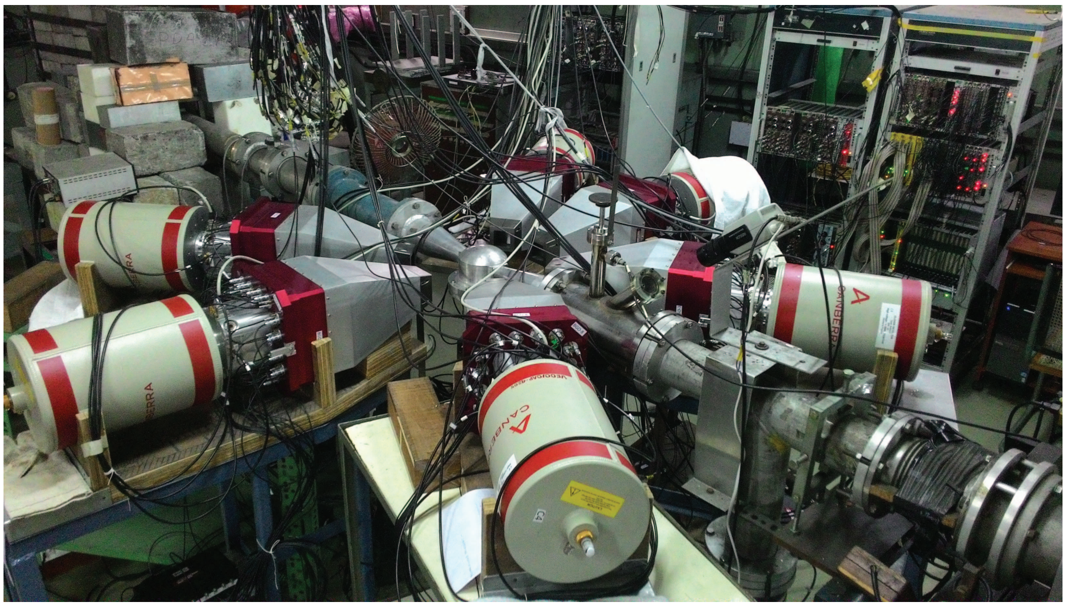

Figure 3.7: Setup of Compton Suppressed Clover HPGe detectors of the VENUS array at VECC K-130 Cyclotron beam line.

of six Clover HPGe detectors along with the BGO shields, are expected to expand with more Clover as well as ancillary detectors of fast timing scintillators. The modular support structure of VENUS array is designed to accommodate different numbers of detectors at different angles with variable target to detector distance, depending on the requirements and perspective of the experiments.

For the experiments of present thesis, six Clover detectors with BGO shields have been placed in median plane around the beam line with two detectors at backward 30°, two at forward 45° and 55° and two at 90° angles with respect to the beam direction according to the experimental

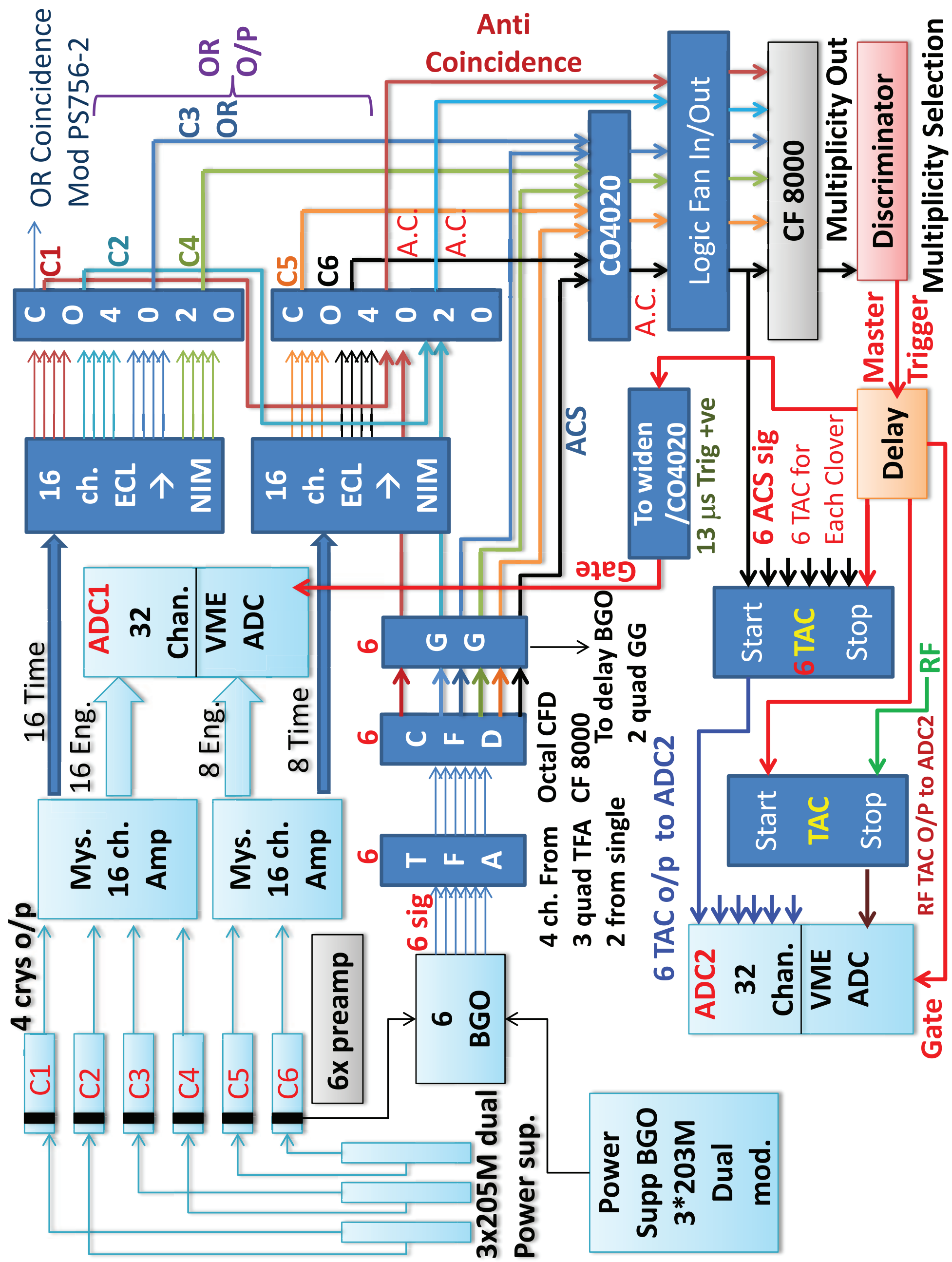

Figure 3.8: Block diagram of the electronics set up of VENUS array that has been set for the experiment in K-130 Cyclotron.

requirements. The detectors set up along with beam line are shown in Fig. 3.7. The aluminum end cap of Clover detectors are placed at a distance of 26 cm from the target position.

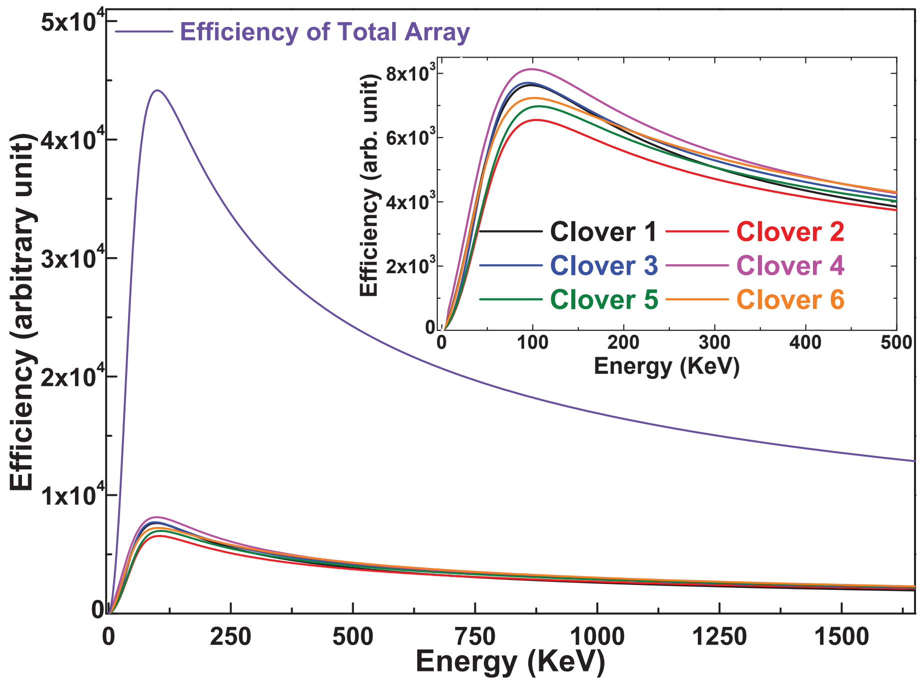

Figure 3.9: The efficiency of all the six Clover detectors of VENUS individually as well as of the array, that has been set for the experiments in K-130 Cyclotron.

For the processing of the 24 pre-amplifier signals from the 24 crystals of six Clover detectors, standard NIM electronics has been used. The preamplifier energy pulse were processed by 16-channel high resolution Mesytec Amplifiers with 4 μs shaping time, which give analog energy signals as well as ECL standard logic signals. The Gaussian shaped energy signals were processed through high resolution 14-bit Mesytec VME ADCs. The logic ECL outputs of 16-channel amplifiers were converted to NIM standard and used to make OR (with ORTEC CO4020 module)of 4 crystal signals of each Clover detector. The BGO signals, were processed with NIM standard TFA (ORTEC model 863 Quad-TFA) and CFDs(ORTEC model 584) and the anti-coincidence 'VETO' condition for the corresponding Clover detectors were applied using the quad logic unit ORTEC-CO4020. Other relevant logic electronics was set up, to collect the data with singles ($M_\gamma \geq 1$) as well as with doubles ($M_\gamma \geq 2$) [30]Master trigger condition. The time difference of the 'Master trigger' with each of the Clover detectors as well as with respect to the radio frequency (RF) of the beam bursts were recorded using individual Time to Amplitude Converter (TAC) modules. A VME based data acquisition system with 32 channel

Mesytec ADC was used. LAMPS [11] DAQ software were used to collect the LIST mode data as well as offline analysis. Master rate of 7-8K events/sec for trigger $M_{\gamma} \geq 1$ could be collected with VME system without any dead time.

The Efficiency of the array along with the efficiency of the individual detectors are calculated and shown in the Fig. 3.9. The Addback efficiency of all the Clover detectors follow the same trend.

3.4.2 Indian National Gamma Array at VECC (INGA-VECC)

In the present thesis we use the INGA set up with light ion beams from K-130 cyclotron at VECC for one of our experiments [12]. In this INGA campaign, seven Compton suppressed Clover HPGe detectors were used. Fig. 3.10 shows the setup of this array. The structure could

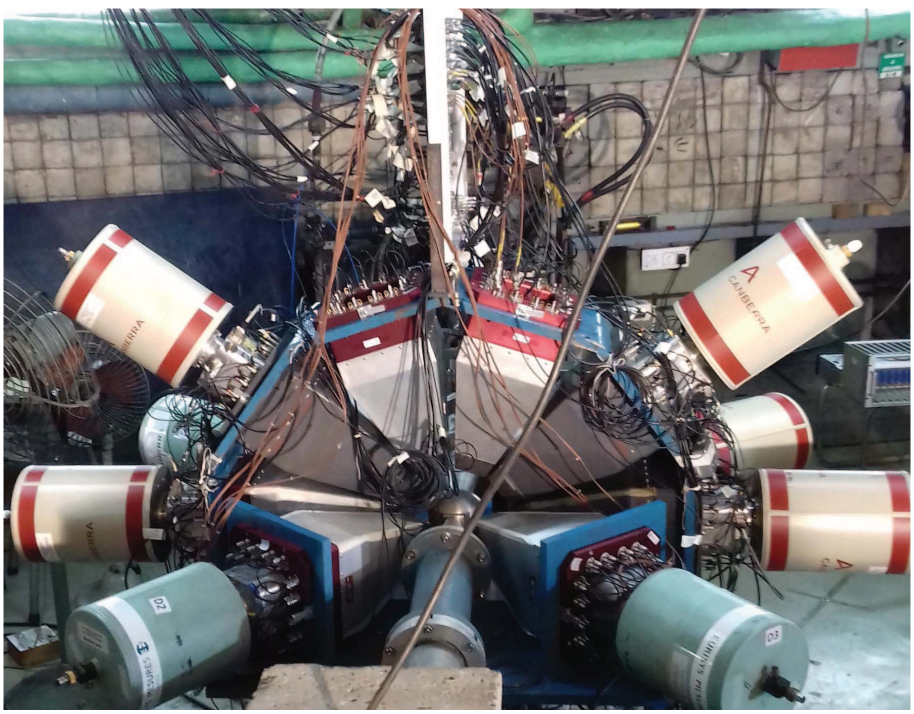

Figure 3.10: The INGA Phase-I setup at K-130 Cyclotron VECC.

hold up to ten detectors. In phase-I setup 7 Clover detectors were put in the array along with their BGO shields. The Clover detectors were put at different angles: 4 at 90° (2 in-plane and

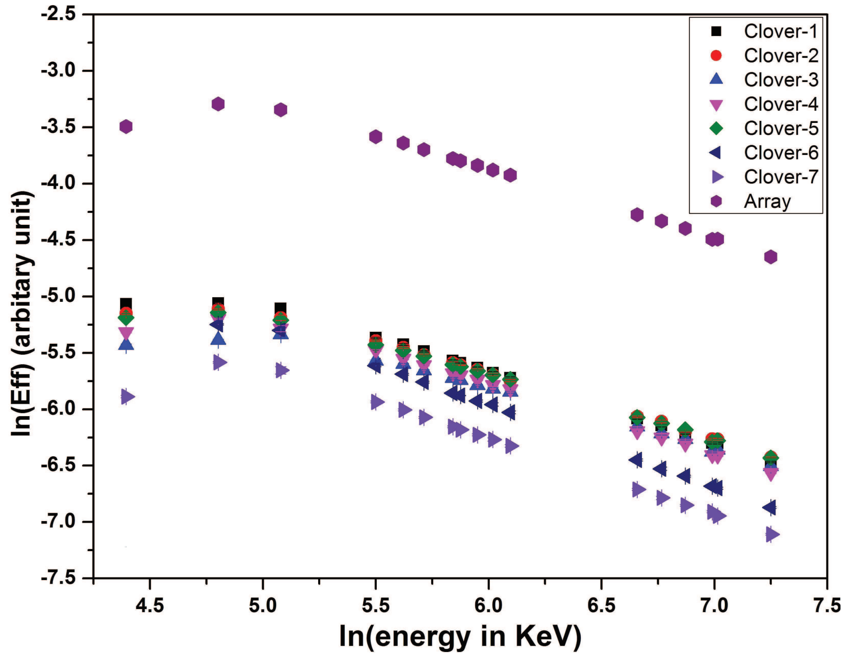

Figure 3.11: The Efficiency of INGA setup used for the present thesis, at VECC along with all the individual detector's efficiency.

2 out-of-plane), 2 at 125° and 1 at 40° with respect to the beam direction. The detectors face (aluminum cap) were placed at a distance of 25 cm from the target position. The Efficiency of all the detectors that had been used in the campaign as well as the efficiency of the whole array is shown in the Fig. 3.11 The raw Pre-amplifier pulses from the Clover detectors were processed using 250-MHz 16-channel 12-bit PIXIE digitizers [13], belongs to UGC-DAE CSR, Kolkata Centre. The Digital Signal Processing (DSP) system only recorded the events with the Compton suppression in both coincidence ($\gamma - \gamma$) as well as singles mode. An alternative VME based data acquisition system with 16-channel Mesytec analog amplifiers and other NIM electronics was also setup and tested. The Electronics set up for the signal processing were almost same with the set up for the VENUS as shown in Fig. 3.8. The data sorting and analysis procedure is discussed in the preceding chapter.

3.4.3 Indian National Gamma Array at TIFR

The INGA campaign TIFR, Mumbai were used to detect the de-exciting γ rays from the excited states of ^{200}Tl. For the experiement in the present thesis 15 Compton suppressed Clover HPGe detectors were used in the INGA setup at a distance of 22 cm from the target. A picture

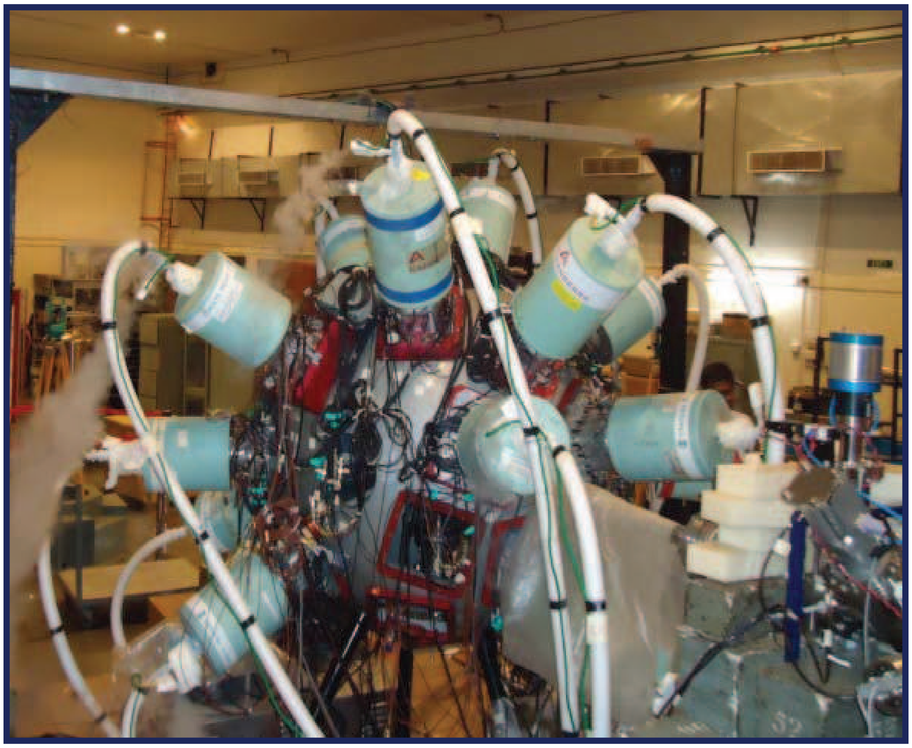

Figure 3.12: The INGA set up at BARC-TIFR Pelletron facility, TIFR, Mumbai.

of this setup of this array has been shown in Fig. 3.12. The detectors were arranged in six different angles with two detectors each at 40°, 65°, 115°, 140°, while four detectors were at 90° and three were at 157°. The time stamped data were collected using a PCI-PXI based digital data acquisition system developed by XIA LLC with a sampling rate of 100MHz. Six Pixie-16 modules were used to process preamplifier pulses from Clover HPGe detectors and each channel was processed after satisfying the veto condition of respective BGO Anti Compton Shield. Time stamped data were collected when at least two clovers were fired within a coincidence time window of 150 ns and the coincidence trigger was kept open for 1.5 μs for the double trigger condition. The detailed description of the DDAQ has been given in the Refs. [14, 16, 17]. The data sorting and analysis routine “Multi pARameter timestamped based COincidence Search program (MARCOS)”, developed at TIFR, sorts the time stamped data to generate $\gamma - \gamma$ matrix and $\gamma - \gamma - \gamma$ cube in a Radware compatible format for further analysis.

3.5 Data Analysis

The List mode data from different experiments were collected in different data acquisition systems. Depending on the acquisition system, different data sorting routine have been utilized. For the sorting of time stamped DSP data, from INGA-TIFR and INGA-VECC experiments, populating ^{200}Tl and ^{199}Hg nuclei respectively, two different routines (MARCOS [14] and IUCPIX [13]) were used. For the sorting of data from the experiments, performed at K-130 Cyclotron, VECC to study the properties of ^{199}Tl and ^{199}Hg, LAMPS sorting routine has been utilized [11]. For analyzing the sorted data from different experiments throughout the thesis work, INGASORT [18], LAMPS [11] and RADWARE [19] have been used. The energy of the different gamma rays are determined by carrying out the energy calibration using standard radioactive sources (^{152}Eu and ^{133}Ba). To develop the level schemes, which is a fingerprint of nuclear structure, the LIST mode data have been sorted into two-dimensional symmetric $\gamma - \gamma$ (4K $\times$ 4K) matrices with a typical gain of 0.5 keV/channel and $\gamma - \gamma - \gamma$ cubes with 2keV/channel, after energy and efficiency calibration of all the detectors. The experimental observables in γ ray spectroscopy study are energy, intensity and relative time of γ rays, whereas spin, parity of the nuclear levels are deduced quantities from the experimental data. The coincidence relations between different transitions and their relative intensities are used to build the level scheme. The spin and parity of the nuclear levels are determined by the information of the multipolarity and nature of γ transitions, decaying from the corresponding levels.

3.5.1 Spin-Parity assignment to the nuclear levels

Determination of spin-parity of the nuclear excited states is an important aspect of the gamma spectroscopic measurements. The electromagnetic radiation is produced by localized oscillating (varying with time) charge and current densities and it can be described in terms of a multiple moment expansion. For the electromagnetic field, a multipole expansion is a series expansion of the potential produced by the above localized source, in terms of spherical harmonics or related angular functions. Legendre's polynomial can represent the model functions in a spherical harmonics (in a spherical coordinate system) and the different terms are known as the multipole moments like dipole moments, quadruple moments etc. In this case, the leading terms in a multipole expansion are generally the most significant, and the higher order terms at large distances can be approximated by the first few terms of the expansion. A classical electromagnetic field (here γ rays) that is produced by oscillating charges and currents transmits angular momentum as well as energy. In quantum domain, it follows that a multipole transition of order 2^l transfers an angular momentum of $l\hbar$ per photon, where l belongs to the multipole order. If we consider a gamma transition , decaying from an initial state of spin and parity with I_i and π_i to a final state of I_f, π_f, the conservation of angular momentum requires, $I_i = l + I_f$ where l is the angular momentum quantum number. The conservation of angular momentum, during an electromagnetic transition between the above two states, follows the selection rule on the possible angular momentum carried off:

$$|I_i - I_f| \geq l \geq |I_i + I_f|, l \neq 0 \tag{3.3}$$

It can be seen from Eq. 3.3, that the γ ray which link the two states, can take a minimum value of angular momentum equal to l. These transitions and the states are referred to as "stretched", while others with higher multipole (higher l) are labeled as unstretched. The value of l are defined as multipolarity of the transition. The conservation of the parity of the two linking states determine Electric(E) or Magnetic(M) nature of the emitted radiation following the equation:

$$\pi(Ml) = (-1)^{l+1} \tag{3.4}$$

$$\pi(El) = (-1)^{l} \tag{3.5}$$

Thus, the states with same parity are linked through the M1, E2 or higher multipole transitions; whereas the states with different parity are connected through E1, M2 transitions mainly. E0 transitions are not allowed since the photon(γ ray) , which has an intrinsic spin of $1\hbar$, has to carry at least one unit of angular momentum. Similarly, M0 transitions are also not found experimentally because the magnetic monopoles do not exist. The radiation field will be a sum of the multipole contributions; however, usually these lower order multipoles mainly dominates. Furthermore, since magnetic transitions of a particular multipole order are less probable than electric transitions of the same order, the probability of emission of a M1 transition always competes with the probability of the emission of an E2 transition.

• **Angular Distribution:** In a fusion evaporation reaction, the angular momentum of the compound nucleus is aligned in a plane perpendicular to the beam direction (z-axis). The emission of neutrons from the excited nuclei, in 4π directions, causes some smearing of the direction of polarization. However, the alignment of the residual nuclei still preserved for a long time (nanoseconds). If the γ rays are emitted from a nucleus in such a state, their relative intensities depend on the angles with respect to the beam direction. The angular distribution of the relative intensities of the γ rays (with respect to the beam axis) depends on the multipolarity of the transitions which in turn related to the spin parity of the initial and final states. The theoretical Angular Distribution of a γ-transition, decaying from a state I_i to a state I_f with l and l' mixed multipolarities can be represented by the equation [21]:

$$W(\theta) = \sum_{\mu} A_{\mu} P_{\mu}(cos\theta) \tag{3.6}$$

where the angular distribution co-efficients A_{μ} depend on the multipolarity of the γ photon, mixing ratio δ and the m-population width. $P(\theta)$ are Legendre polynomials. The angular distribution of different multipolarities transitions, for both stretched and non-stretched one and having the contribution of mixing ratio δ of higher multipolarity transition can be calculated from the above equation using the prescription in Ref. [21]. Angular distribution depends on different spin sequences of initial and final levels and thus the multipolarity of a particular transition can be determined comparing the experimental values of the angular coefficients with the theoretical values. To compare with the experimental angular intensity distribution of a particular gamma ray, the higher multipole orders of Eq. 3.6 are ignored and the equation is reduced up to three terms well known Legendre polynomial function as

$$W(\theta) = A_0(1 + a_2P_2(cos\theta) + a_4P_4(cos\theta)) \tag{3.7}$$

where θ is the detector angle with respect to the beam axis and A_0 is the normalization parameter. a_2 and a_4 coefficients are defined as a_2=$\alpha_2A^2_{max}$, a_4=$\alpha_2A^4_{max}$, details of which can be found in Ref. [22]. The experimental data are then fitted with the Eq. 3.7 and the values of a_2 and a_4 are compared with theoretical ones to find out the multipolarity and mixing ratio, as well as, to infer the stretched and non stretched nature of the transitions.

• **DCO ratio analysis:** In an experiment with a large array structure, the information of the multipolarities of the γ rays are usually obtained from the analysis of the ratio of Directional Correlation from Oriented states (DCO) [22]. For this purpose, an asymmetric γ-γ matrix, with X-axis containing the data from the detectors near 0° (θ_1) and Y-axis containing the data from the 90° (θ_2) detectors is generated. The DCO ratio of a transition (γ_1) is then obtained from the ratio of its intensities at two angles θ_1 and θ_2 gated by another transition (γ_2) of known multipolarity, as per the following expression.

$$R_{DCO} = \frac{I_{\gamma_1}\text{at } \theta_1\text{, gated by } \gamma_2 \text{ at } \theta_2}{I_{\gamma_1}\text{at } \theta_2\text{, gated by } \gamma_2 \text{ at } \theta_1} \tag{3.8}$$

For a pure stretched quadruple or dipole transition, the R$_{DCO}$ should be close to unity when gated by a pure transition of same multipolarity. For the gating transition of different multipolarity, the R$_{DCO}$ value depends on the nature of the gating transition. Typically if θ_1 is chosen to be very closed to 0° (e.g. -23°) with respect to the beam axis, the values of R$_{DCO}$ come out to be $\sim$ 1.0 (2.0) for pure stretched dipole (quadruple) transitions when gated with a stretched pure dipole transition. On the other hand for a stretched quadruple gate, the values are found to be $\sim$ 0.5 (1.0) for pure stretched dipole (quadruple) transitions. By definition, the value R$_{DCO}$ can only predicts the multipolarity of stretched and pure (zero mixing) transition. For non stretched or highly mixed transitions, one has to carry out the angular distribution measurements to infer the proper multipolarity of the transitions.

• **Polarization calculation:** The close-pack configuration of four Ge crystals in a Clover detector allows to assign the Parity of the most excited states from the polarization measurement.

The information regarding the type (electric or magnetic) of the transitions are obtained from the Integrated Polarization Directional Correlation (IPDCO) asymmetry parameter(Δ_{IPDCO}) following the prescription of Ref. [23, 24]. The Compton suppressed Clover detectors placed at 90° with respect to beam direction are usually used for polarization measurement for maximum polarization sensitivity. The IPDCO asymmetry parameter is defined as,

$$\Delta_{IPDCO} = \frac{a(E_\gamma)N_\perp - N_\parallel}{a(E_\gamma)N_\perp + N_\parallel} \tag{3.9}$$

where $N_\parallel$ and $N_\perp$ are the number of counts corresponding to the counts of the Compton scattered components of a γ ray in the planes parallel and perpendicular to the reaction plane, respectively. Here, $a(E_\gamma)$ is the correction factor due to geometrical asymmetry of the detector array w.r.t. the target position or asymmetry w.r.t the four crystals of a Clover Ge detector. This factor [$a(E_\gamma)$=$N_\parallel/N_\perp$] can be obtained using scattered components of γ rays from an unpolarized source. The $a(E_\gamma)$=$N_\parallel/N_\perp$ factor is obtained from different γ ray energy from standard unpolarized ^{133}Ba and ^{152}Eu radioactive sources. In order to extract the parallel and perpendicular scattered component of a γ transition, two asymmetric E_γ-E_γ matrices, corresponding to parallel and perpendicular scattered events of the Clover detectors at 90° along one axis and the coincident γ rays from the other detectors along another axis, were constructed. From the projected spectra of the above matrices, the number of counts in the perpendicular ($N_\perp$) and parallel ($N_\parallel$) scattering for a given γ ray was obtained. The positive and negative values of Δ_{IPDCO} indicate the electric and magnetic nature of the transitions respectively. If the transitions are non stretched or mixed, the nature of transitions cannot be inferred only from the Δ_{IPDCO} value. The Polarization(P) value then needs to be found out from the experimental Sensitivity(Q). The asymmetry parameter Δ_{IPDCO} is related to the Polarization value with the relation

$$P = \Delta/Sensitivity(Q). \tag{3.10}$$

. The polarization sensitivity is a experimental factor which arise due to the extended source of the emitted radiation and the geometrical asymmetry caused by the orientation of the detectors at 90°. To find out the experimental value of Q for a particular set up, few E2 transitions (with different energies) with known Δ_{IPDCO}, produced in the same experiment are chosen. From the experimental angular distribution coefficients of those E2 transitions, Polarization (P_{cal}) value is calculated following the equation:

$$\mathrm{P}(90^{\circ}) = \pm\frac{a_2 H_2 - 7.5 a_4 H_4}{2 - a_2 + 0.75 a_4}. \tag{3.11}$$

where the $\pm$ sign is for without (with) parity change respectively. . The value of a_2 and a_4 are calculated from the relation a_2=$\alpha_2 A_2$, a_4=$\alpha_2 A_4$ as already defined in previous subsection and A_2, A_4 etc are calculated as

$$\mathrm{A}_{\mu}(\gamma) = A_{\mu}(I_i l l^{'} I_f) = \frac{F_{\mu}(I_f l l I_i) + 2\delta(\gamma) F_{\mu}(I_f l l^{'} I_i + \delta^2(\gamma) F_{\mu}(I_f l^{'} l^{'} I_i)}{1 + \delta^2(\gamma)} \tag{3.12}$$

Where δ is the mixing of multipole l with higher multipole $l'(= l + 1)$, the F_{μ} coefficients are listed in Ref. [27]. μ is the order of multipole. Details of this calculation can be found in Ref. [22]. The value of Q has been calculated for different energy range using the above formulation, plotted as a function of energy of γ rays. Using the value of this Q, the Polarization values(P_{cal}) of unknown, mixed or non-stretched transitions are calculated and compares with the theoretical value of Polarization (P) and from that one can predict the exact multi-polarity with the information of the mixing δ as well.

The DCO ratio and Polarization asymmetry measurements have been done for J^{π} assignments of the most of the levels of the nuclei, studied in the present thesis. For crucial cases of non-stretched or mixed transitions, careful analysis, involving the comparison with theoretical values have been performed.

Bibliography

[1] T. D. Thomas, Ann. Rev. Nucl. Sci. 18, 343 (1986).

[2] J. R. Grover and J. Gilat, Phys. Rev. 157, 802 (1967).

[3] Gamma Sphere Online Booklet (nucalf.physics.fsu.edu/ ∼riley/gamma/).

[4] B. Herskind, Proc. Int. Conf. Nucl. Phys., Italy, 1 17 (1983)

[5] Ali Al-Khatib's Thesis (High-Spin γ ray Spectroscopy of ^{124}Ba, ^{124}Xe and ^{125}Xe).

[6] G.F. Knoll, Radiation Detection and Measurement.

[7] S.L. Shepherd *et. al.*, Nucl. Instrum. Methods Phys. Res. **A 434**, 373 (1999).

[8] Soumik Bhattacharya *et. al.* Int. Symp. on Nucl. Phys. **58** 904 (2013).

[9] G. Duchene *et. al.*, Nucl. Instrum. Methods Phys. Res.**A 432**, 90 (1999).

[10] Soumik Bhattacharya *et. al.* DAE Symp. of Nucl. Phys. **61** , 98 ,(2016).

[11] A. Chatterjee, Priv. comm. (2001); http://www.tifr.res.in/ ∼pell/lamps.html.

[12] Soumik Bhattacharya *et. al.* DAE. Int. Symp. on Nucl. Phys. **63** 904 (2018).

[13] S. Das *et al.*, Nucl. Instrum. Methods. **A 893**, 138 (2018).

[14] R. Palit *et al.*, Nucl. Instrum. Methods Phys. Res. **A 680**, 90 (2012).

[15] S. Venkataramanan *et al.*, Proc. DAE-BRNS Symp. Nucl. Phys. **52**, 149 (2007).

[16] R. Palit, Proc. DAE Symposium on Nuclear Physics, BITS Pillany, Rajasthan, India, Vol. **55**, I11 (2010).

[17] R. Palit, AIP Conf. Proc. **1336**, 573 (2011).

[18] R.K. Bhowmik *et. al.*, Proc. DAE Symp. Nucl. Phys. **44B**, 422 (2001).

[19] D. C. Radford Nucl. Instrum. Methods Phys. Res. **A 361**, 297 (1995).

[20] A. Krämer-Flecken *et al.*, Nucl. Instrum. Methods Phys. Res. A **275**, 333 (1989).

[21] H. Morinaga and T. Yamazaki, In-beam gamma-ray spectroscopy (North-Holland Pub. Co., Amsterdam, 1976).

[22] Soumik Bhattacharya *et. al.* DAE. Symp. on Nucl. Phys. **59** 120 (2014).

[23] K. Starosta *et al.*, Nucl. Instrum. Methods Phys. Res. A **423**, 16 (1999).

[24] Ch. Droste *et al.*, Nucl. Instrum. Methods Phys. Res. A **378**, 518 (1996).

[25] R. Bengtsson and S. Fraunendorf, Nucl. Phys. **A 327**, 139 (1979).

[26] S.M. Harris, Phys. Rev. **138** B509 (1965).

[27] T. Yamazaki, Nucl. Data **A3, 1** (1967).

[28] R. F. Casten, Nuclear Structure from Simple Perspectives, Second Edition, Oxford.

Chapter 4

Yrast and non yrast spectroscopy of ^{199}Tl using α-induced reaction

4.1 Introduction

The Fermi surface for the proton in Thallium nuclei situated just below $Z = 82$ shell closure. Therefore the $1/2^{+}$ spin-parity of the ground state of the odd mass Tl isotopes can be interpreted as generated by the occupation of one proton hole in $3s_{1/2}$ orbital [1, 2, 3]. It is evident from the Nilsson diagram that high-j ($\pi h_{9/2}, \pi i_{13/2}$, $\nu i_{13/2}$ near A$\sim$200) orbitals comes down in energy for both prolate and oblate deformation and intrude into the neighbouring major shells. Thallium isotopes(Z=81), with only one proton below the $Z = 82$ shell closure, are the most appropriate candidates to extend our knowledge on the polarizing effect of the high-j proton intruder orbitals (e.g $\pi h_{9/2}, \pi i_{13/2}$) or high-j neutron orbitals (e.g. $\nu i_{13/2}$) on the shape of a nucleus, which are otherwise near-spherical at their ground state. Consequently, rotational bands based on the $\pi h_{9/2}$ and the $\nu i_{13/2}$ orbitals have been observed from neutron number $N = 102$ [4] up to the neutron number as close as $N = 120$ [25] to the $N = 126$ spherical shell closure. Several interesting and exotic phenomena, like Magnetic rotational bands [9] and Chiral bands [14, 13, 15] have been reported in the Thallium isotopes around A$\sim$200 mass region. The properties of these various exotic modes of excitation need proper nuclear models for explanation and spur interest in understanding the configurations involved. It is, therefore, interesting to investigate the interplay of the single particle structures (involving high-j orbitals) and the collectiveness of the underlying core that generates the above exotic phenomena, below the $Z = 82$ shell closure region [7, 1, 2]. It is known that the high-j orbitals, specially, $\pi h_{9/2}$ and $\nu i_{13/2}$, induce oblate shape in the nuclei near A 200 [3] region. In the case of the odd-A Tl nuclei, a wide diversity of shapes and structures have been observed from prolate shapes in neutron deficient ^{183,185,187}Tl [4, 14], super-deformed structures in ^{189,191,193,195}Tl [15, 16, 17, 18, 19] to weakly deformed oblate band structures in ^{191,193,195,197,201}Tl [20, 21, 17, 25], depending on the neutron Fermi level and the excitation energy. In the heavier isotope ^{203}Tl, which is close to the doubly magic ^{208}Pb nucleus, rotational structure has not been observed on $\pi h_{9/2}$ orbital [23]. With more neutrons, being close to the N=126 shell closure, excited states corresponding to the octupole core excitation were also observed [24] in ^{205}Tl. Although deformed shapes based on the $\pi i_{13/2}$ intruder orbital have been observed for the lighter Tl isotopes, no such band structure has been reported in heavier odd-mass Thallium isotopes[23, 24]. A survey of the excitation energies of these states in the heavier isotopes indicates that it becomes more and more non-yrast with the increase in neutron number [25]. In the neighboring isotope ^{197}Tl, an excited state corresponding to the $\pi i_{13/2}$ orbital has been reported but no band structure was observed on top of this state [26]. A recent work extend the band structure on the 1-quasi-particle(qp) and 3-qp structure in ^{197}Tl beyond band crossing with observation of two new Magnetic Rotational (MR) bands based on 3-qp and 5-qp structure [10].

It is interesting to note that the shape polarizing effect of the $\pi h_{9/2}$ orbital still continues to generate deformed band structures for the isotopes ^{200,201}Tl, as reported in our previous work [12, 25]. However, the 3-qp configuration, observed after the band crossing of the $\pi h_{9/2}$ oblate band, in the $N = 120$ isotope ^{201}Tl was interpreted to be different with smaller gain in aligned angular momentum compared to the other lighter isotopes. This is possibly because of the fact that the neutron Fermi level moves up and away from the $\nu i_{13/2}$ orbital with the increase in neutron number reducing the probability of breaking a neutron pair in $\nu i_{13/2}$. For spherical shape, the neutron Fermi level is expected to be situated around the $3p_{3/2}$ orbital above the

$i_{13/2}$ orbital for $N \geq 114$. However, for oblate deformation, as it is the case for the Tl isotopes, it would move up to lie close to the $2f_{5/2}$ orbital for $N \geq 118$. Therefore, it is important to study the band crossing behaviour of ^{199}Tl to understand the relative position of the $\nu i_{13/2}$ orbital.

The available information on the excited states in ^{199}Tl was very scarce and limited to a few low-lying states which precludes one to get any idea about the $\nu i_{13/2}$ alignment. One of the first experiments to observe the excited states of ^{199}Tl was performed way back in 1970 by J.O. Newton et al. [29], with a few Ge(Li) detectors. Although only a few levels could be identified in that work, but importantly, the existence of deformed $\pi h_{9/2}$ state was predicted by them. Information on the low-spin states in ^{199}Tl was also reported from the Elctron Capture decay (EC-decay) study of ^{199}Pb [16]. The band based on the $\pi h_{9/2}$ in ^{199}Tl have been extended by N. Marginean *et. al.*[31] with a set of $LaBr_3$(Ce) detectors, along with 6 HPGe detectors [31]. A few new excited states could be identified in that work, but the main focus of that experiment was to measure the lifetime of the excited states using the fast scintillator detectors in combination with the HPGe detectors. It may be noted that the chiral bands in ^{195}Tl [14] and MR band in ^{197}Tl [10] are found to occur at higher excitation energy beyond the band crossing. Untill recently [32], the states beyond the band crossing were not known and experimental studies need attention to probe the effect of the available high-j orbital in band structures as a function of increasing neutron number around A$\sim$200.

In the present thesis, we have used the α induced fusion evaporation reaction to populate ^{199}Tl to investigate the yrast and non-yrast states in ^{199}Tl as well as the band crossing behaviour of the $\pi h_{9/2}$ band [30]. With the availability of high efficiency, high resolution new generation HPGe Clover detectors, it has become possible to obtain more complete information about the detailed band structures of ^{199}Tl. Many new transitions and states has been established with proper spin-parity assignments. The band structure has been interpreted in comparison with the neighbouring isotopes. Total Routhian Surface calculation has been done and compared with the experimental results.

4.2 Experiment and Data Analysis

The excited yrast and near yrast states of ^{199}Tl were populated using ^{197}Au(α,2n) fusion evaporation reaction with a 30 MeV α beam from the K-130 Cyclotron at VECC, Kolkata. The beam energy was chosen to maximize the population of the 2n evaporation channel. A unique reaction channel can be populated via alpha induced reaction with large cross section. The decaying γ rays from the excited states were detected using **VE**CC **A**rray for **NU**clear **S**pectroscopy (VENUS) [30] at VECC, at a distance of $\sim$ 26 cm from the target position. The signals from the 6 Clover detectors were processed using 16 channel Mesytec amplifiers and the energy signal were collected with 13 bit high resolution 32 channel VME ADCs and VME based data acquisition system using LAMPS [31]. Standard NIM analogue electronics were used to process the signal from BGO shields and for other trigger logic to collect the data with two master trigger conditions, singles mode (atleast one Clover "fires") for the angular distribution measurement and doubles mode (atleast any two Clovers "fire") for the γ - γ coincidence measurements. Six Time-to-Amplitude-Converters (TACs) were used to measure the time between the individual OR of all the crystals of a Clover detector and the Master trigger. Another TAC was used for timing measurements of the events with respect to the RF signal from Cyclotron. The efficiency and energy calibrations of each detector were carried out using ^{133}Ba and ^{152}Eu standard radioactive sources, placed at the target position. The details of the experimental set up of VENUS is described in Chapter 3.

Data were sorted using LAMPS [31], INGASORT [20] and Radware [19] software packages. A symmetric γ-γ matrix was generated to obtain the coincidence relations of the γ rays and an asymmetric DCO matrix was also formed using the data from the two detectors each in the backward (30°) angle and at 90° angle to find out the Directional Correlation from Oriented states (DCO ratio)as per the prescription in Ref. [22] for various transitions. The 90° detectors are also used for the measurements of Integrated Polarization from Directional Correlation of Oriented states (IPDCO) [23, 24] for assigning the parity of the states. The raw data from all the 24 crystals were calibrated and gain matched to 0.3 keV/ch to form six addback spectra. These are used for generating the E_γ-E_γ 2-D matrix by selecting the prompt part of the TAC

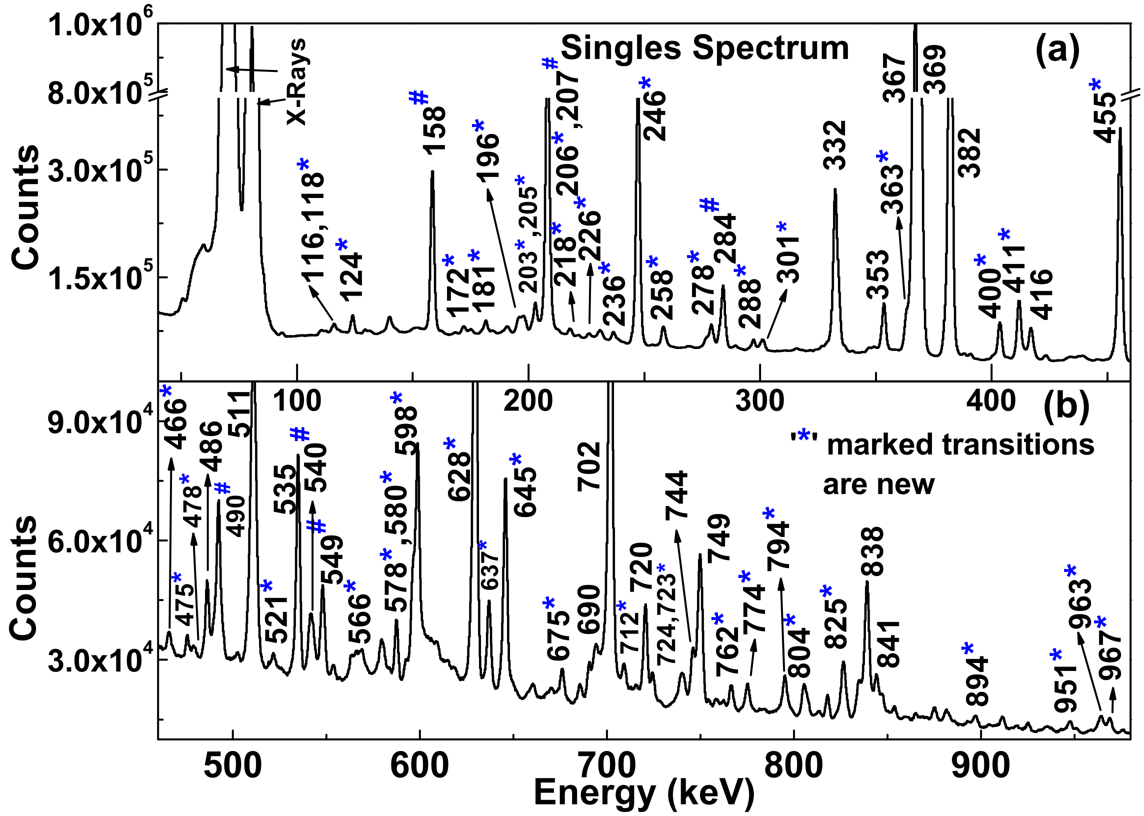

Figure 4.1: Total spectrum of γ rays detected in singles trigger condition in the reaction ^{197}Au(α,2n). (a) The lower energy part (upto 460 keV) and (b) the higher energy part (461-980 keV) of the spectrum. The new transitions observed in the present work are marked with '*'. The other transitions, marked with '#' are from decay of ^{199}Tl or from neighboring nuclei

spectrum of each clover as well as the prompt part of the RF-γ TAC to select the prompt γ-γ coincidence events.

A spectrum obtained from the current data in singles trigger mode is shown in Fig. 4.1. Almost all the γ rays observed in this singles spectrum in Fig. 4.1 belong to ^{199}Tl. Other than the known transitions, the new transitions from the present measurement are marked with '*'. All the other transitions marked with '#', are either from the beta decay of ^{199}Tl to ^{199}Hg or from neighboring nuclei which were also populated in the above reaction but with very less cross-section. This indicates the advantage of using α beam to produce ^{199}Tl nucleus almost uniquely with very small contamination from the other channels.

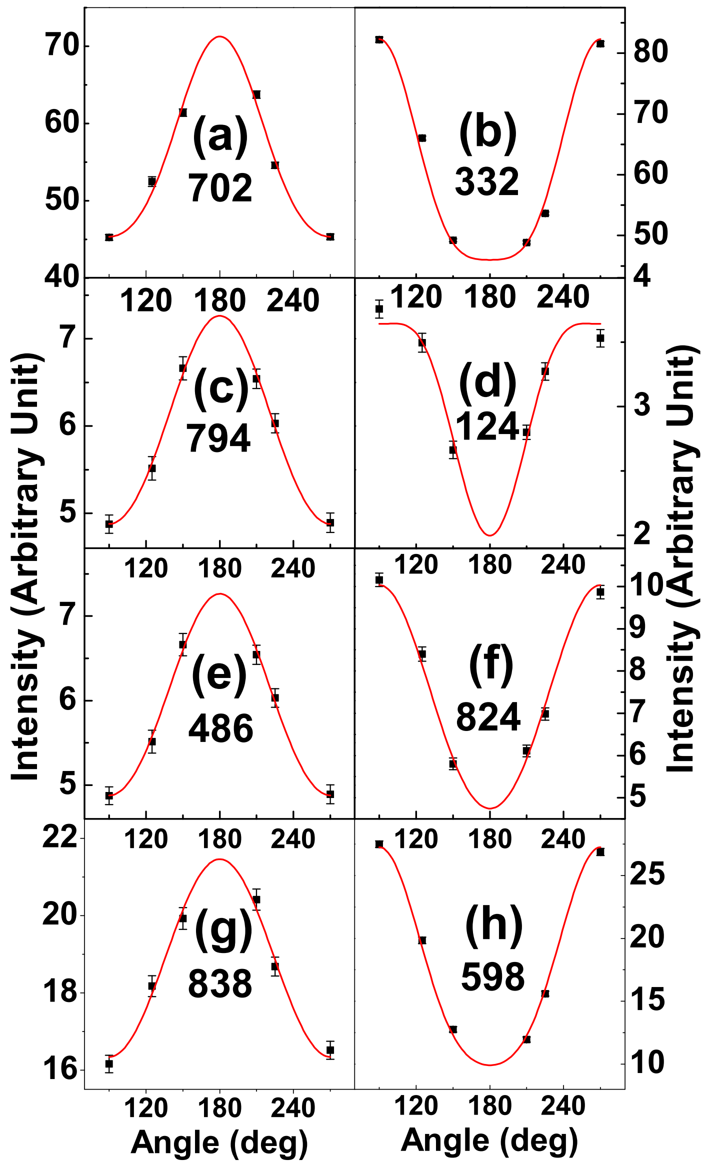

Figure 4.2: Angular distribution of various transitions in ^{199}Tl obtained in the present work. (a),(c),(e),(g) are for quadrupole transitions. (b),(d),(f),(h) are for dipole transitions. The transition energies are also shown in each plot.

The angular distribution of the γ rays, the DCO ratios and the IPDCO values were used to determine the multipolarities and the natures (E/M) of the transitions in order to assign the spins and parities (J^{π}) of the states. The angular intensity distribution of the transitions of

^{199}Tl from the singles data, after correcting for the efficiency of the respective detectors, is used for fitting the well known Legendre polynomial function,

$$W(\theta) = a_0(1 + a_2P_2(cos\theta) + a_4P_4(cos\theta)) \tag{4.1}$$

where, θ is the detector angle with respect to the beam axis and a_0 is the normalization parameter as described in Chapter 3. The value of these angular distribution coefficients (a_0, a_2, a_4) could be utilized to confirm the multipolarity as well as the stretched and non-stretched nature of the transitions. Fig. 4.2 represents the angular distribution of some of the stretched dipole and stretched quadrupole transitions from the current data. The 702 keV and 332 keV transitions are reported as pure quadrupole and dipole, respectively from the previous work [31] and can be clearly verified from the nature of their fit. Multipolarity of the two newly assigned transitions of energy 794 keV (Quadrupole) and 124 keV (dipole) can also be inferred from their angular distribution nature. The 486 keV transition was previously assigned as M1 by N. Marginean *et. al.*[31] which established to be of higher multipolarity (Quadrupole) from the current angular distribution analysis. The dipole nature of the 598 keV transition could only be confirmed from its angular distribution, shown in the Fig. 4.2(h), as the DCO ratio for this transition, in a gate of stretched transition, was not possible to obtain from the current data.

The multipolarity of most of the transitions, however, was obtained from the DCO ratios(R_{DCO}), as defined in Chapter 3. The x and y-axis of this asymmetric γ-γ DCO matrix are the addback spectra of the two 90° detectors and of two backward 30° detectors, respectively. In the present experimental setup typical value of R_{DCO} for a dipole or quadrupole transition (for γ_1) comes out to be 1.0 when gated by a transition of same multipolarity (γ_2). But when gated by known quadrupole (dipole) γ_2 then the DCO ratio value of $\gamma_1$comes out to be close to 0.5(2.0) for dipole (quadrupole) transition. This definition is only true when both γ_1 and γ_2 are stretched transition and mixing ratio (δ) of the higher order multipole is small. The parities of the most of the excited states, populated in the present work could be assigned from the polarization measurements i.e. (IPDCO) asymmetry parameter following the prescription of Ref. [23, 24] as stated in Chapter 3. The 90° detectors are used for this purpose to maximize the sensitivity of the polarization measurements. The IPDCO asymmetry parameter (Δ_{IPDCO}) as described in Chapter 3, is used to determine the nature of the observed γ rays. The correction factor, a(E_γ) [$= \frac{N_\parallel}{N_\perp}$] which addresses the geometrical asymmetry of the detector array or asymmetry in the response of the four crystals of a Clover Ge detector, is obtained from the known γ rays from unpolarized source. In the present work, it is obtained from the γ rays of ^{199}Hg produced from the β-decay of the ground state of ^{199}Tl having a half life of 7.42 hours [41]. The decay γ rays from the excited ^{199}Hg were recorded in the singles trigger mode in the same experiment at the end of the in-beam measurement. The variation of a(E_γ) factor as a function of γ ray energies is shown in Fig. 4.3. The solid line in this plot is the fitting of the data points with a linear equation $a(E_\gamma)=a_0+a_1E_\gamma$. These fitted values of a_0 and a_1 have been used to determine the Δ_{IPDCO} as prescribed in Chapter 3. For various transitions in ^{199}Tl, the Δ_{IPDCO} values are given in Table 4.1. The DCO ratio and the Δ_{IPDCO} values of various known and new transitions are also shown in Fig. 4.4.

4.3 Results

The level scheme of ^{199}Tl, as obtained in the present work is shown in Fig. 4.5. The level scheme is significantly extended compared to the previous work [31] with the placement of 53 new transitions establishing few new bands with different configurations. These bands and sequences of transitions are named as B1, B2, B3, B4, B5, B6, B7 in Fig. 4.5 for the convenience of describing them. The level scheme has been formed, based on the coincidence relationships, relative intensities of the transitions and the spin-parity assignments of the associated energy levels from angular distributions, R_{DCO}, and Δ_{IPDCO} values. The energy of the γ ray transitions observed in this work, the corresponding initial level energies and intensities, the spins and parities of the initial and final levels along with the other relevant quantities in ^{199}Tl from the present work are tabulated in Table: 4.1.

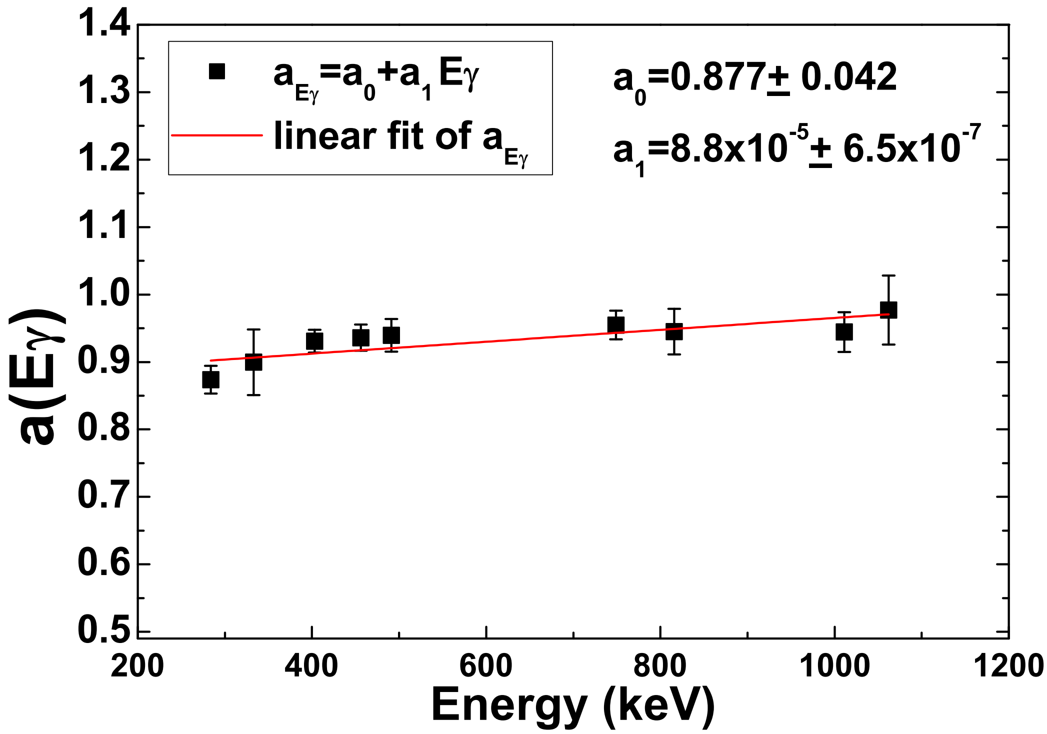

Figure 4.3: (color online) Asymmetry factor from various decay transitions in ^{199}Hg produced in the present work and Linear fit of that with respect to energy.

The level scheme has been extended in mainly two parts, one corresponds to the bands B5, B6, and B7 which bypass the known 28.4 ms $9/2^-$ isomer [29]; and the second, above this isomer represented by bands B1, B2, B3 and B4. The 748.9 keV $9/2^-$ isomer (28.4 ms) was known from the previous decay study of ^{199}Pb [16], and from Ref. [1] by pulse beam method. Band B1 in Fig. 4.5 is built on this isomer. The coincidence gate of the 332 keV transition in Fig. 4.6(a) shows all the transitions (except the 702 and 749 keV transitions which are parallel with respect to it) which belong to band B1.

All the new transitions from the other sequences above the $9/2^-$ isomer i.e. 328, 466, 388, 406, 181, 172, 124, 578, 218, 804 keV etc. are also seen in the coincidence spectrum of 332 keV in Fig. 4.6(a). A coincidence spectrum corresponding to the newly identified 794 keV transition is shown in Fig. 4.6(b) belonging to band B1. Transitions, which belong to band B1 but are not in coincidence with 794-keV transitions are: 328, 466, 638, 388, 406, 578, 744, 804 keV and

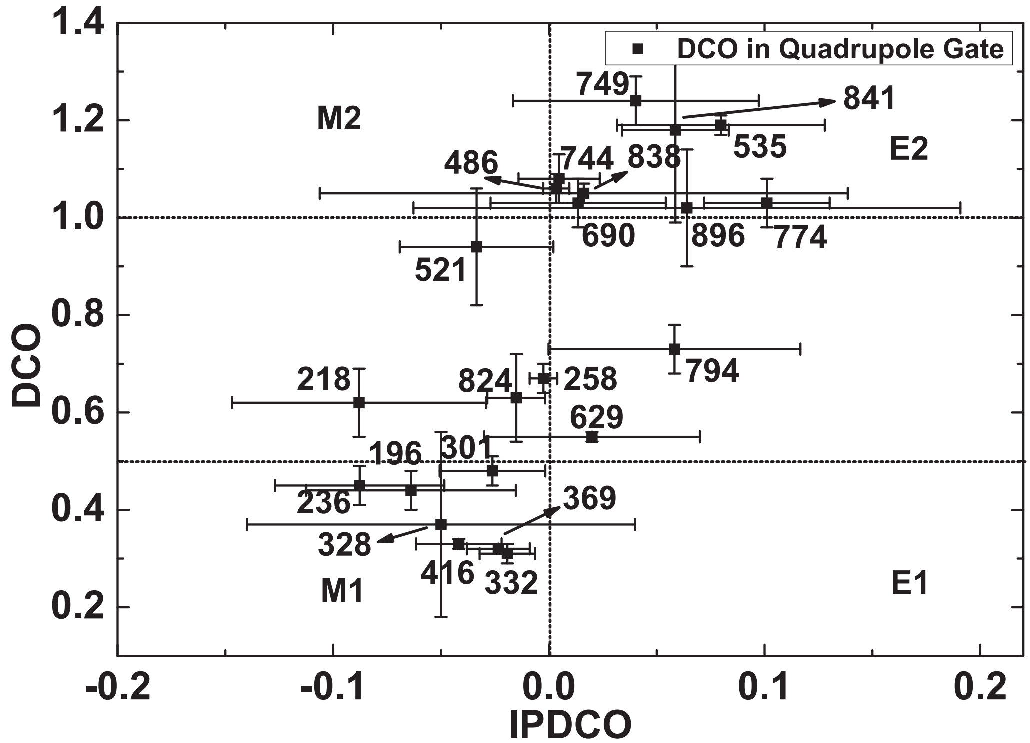

Figure 4.4: DCO ratio vs polarization asymmetry (Δ_{IPDCO}) of various transitions in ^{199}Tl obtained from different quadrupole gates as indicated. The dotted lines parallel to X-axis correspond to the values for dipole and quadrupole transitions in a pure quadrupole gate, respectively and are shown to guide the eye. The dotted line parallel to Y-axis is to guide the eye for $+ve$ and $-ve$ values of Δ_{IPDCO} for electric and magnetic transitions, respectively.

can be verified comparing Fig. 4.6(a) and Fig. 4.6(b). They are placed parallel to the 794 keV transition in the level scheme. Similarly, in the coincidence gate of 749 keV(belongs to band B1) 328, 466, 388, 406, 578 keV transition can be seen along with other transitions in band B1. Only 804 and 744 keV transitions are absent from the coincidence spectrum of 749 keV, thus these two transitions are parallel to both 794 and 749 keV transition. While comparing the coincidence gates of the 749 and 794 keV transitions from Fig. 4.6(b) and (c) it is clear that they are in coincidence with each other, while the cascade 416 & 332 keV (466 & 328 keV) corresponding to the crossover transition of 749 keV (794 keV) is only present in 794 keV (749 keV) gate confirming their relative placements in the level scheme. The DCO ratios of the

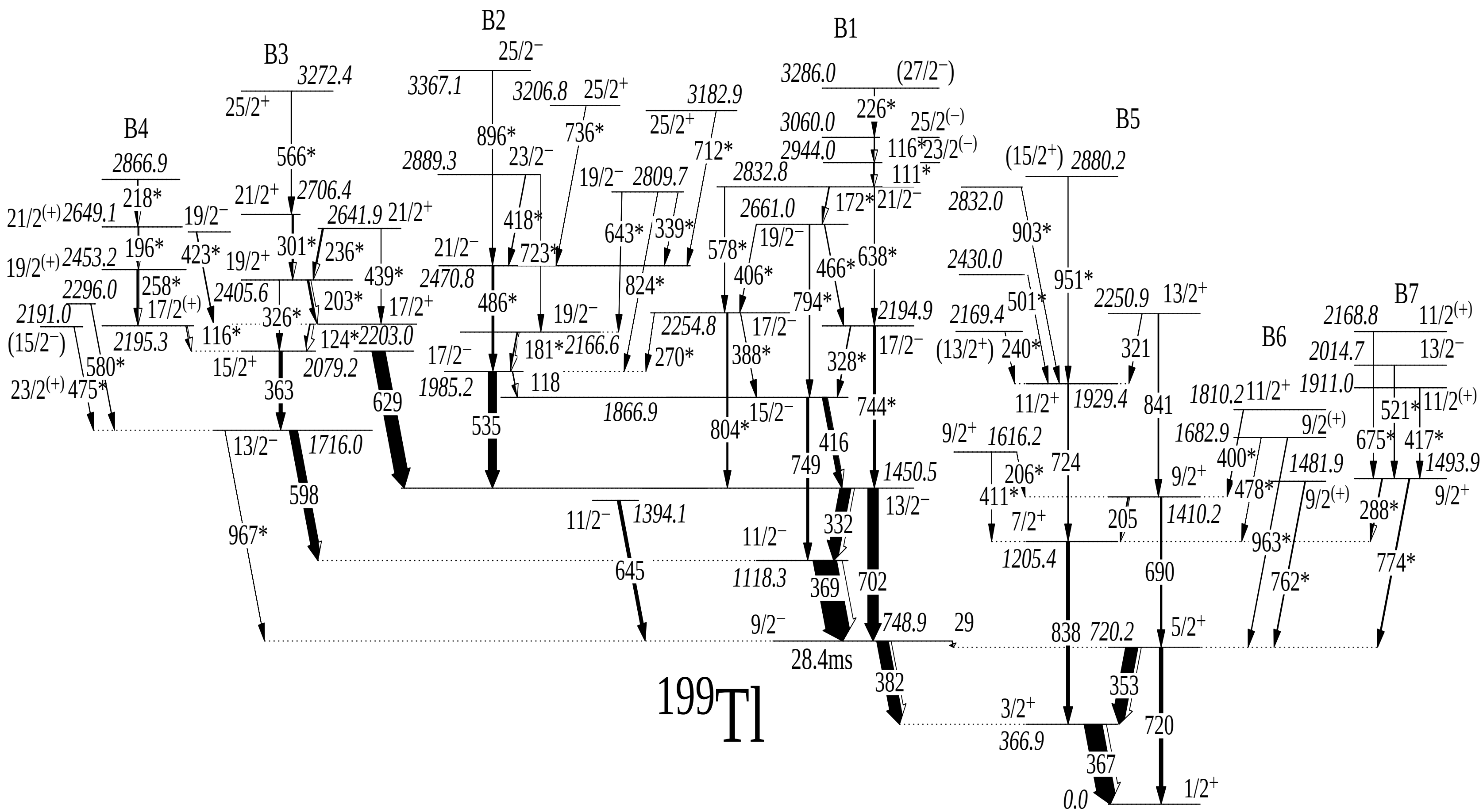

Figure 4.5: Level scheme of ^{199}Tl, as obtained from the present work. New transitions are marked as '*'.

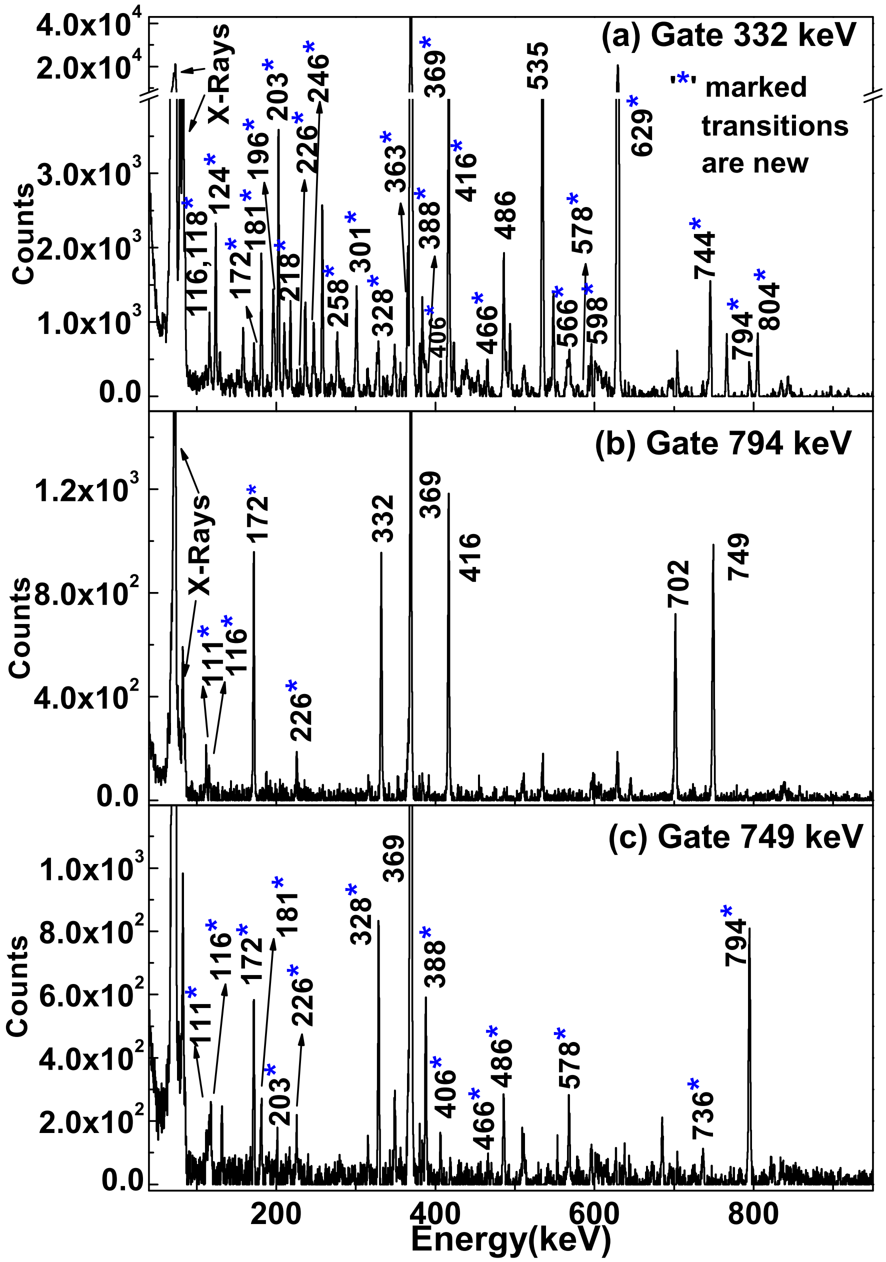

Figure 4.6: Coincidence spectra corresponding to gates of (a) 332 keV, (b) 794 keV, (c) 749 keV transitions pertaining to the band B1 and partly from the band B2, B3, B4 in ^{199}Tl. '*' marked transitions are newly placed in the level scheme.

416, 388, 328, 406, 466, 172 keV transitions are found to be around 0.5 in Quadrupole gates, thus are marked as dipoles in Table 4.1. Comparing the coincidence gates of 749 keV and

744 keV, two different cascades (466 & 328 keV and 406 & 388 keV) of M1 transitions appear between $19/2^-$ and $15/2^-$ spin levels. The 638, 466 and 172 keV γ rays are clearly present in the gate on 744 keV (not shown) whereas the absence of 328 keV and 794 keV γ rays confirms the 744 and 794 keV as parallel transitions. The cross-over transitions corresponding to the uppermost levels of band B1 could not be identified from the present data. It is clearly seen from the Fig. 4.6(b)and (c) that the 332 keV transition is present in the 794 keV gate whereas in the gate of 749 keV gate only the 328 keV transition is present which ensures a new 328 keV transition in coincidence with the 749 keV transition but parallel with 794 keV transition. The spin and parity of the 2254.8 keV level has been fixed as $17/2^-$ based on the $E2$ character of the 804 keV transition. The 578 keV transition also determined to be of E2 nature and thus the J^π of 2832.8 keV level is fixed as $21/2^-$. The 172, 111, 116 and 226 keV transitions are present in all the gates shown in Fig. 4.6(a),(b),(c) but the 172-keV transition is not in coincidence with 578 or 638 keV transitions. This leads to the placement of the 172 keV γ ray in parallel with the 638 and 578 keV transitions, whereas the 111, 116 and 226 keV γ rays are placed on top of 2832.8 keV level of the band B1. Though the Δ_{IPDCO} value of 172 keV transition could not be determined, the J^π of the 2832.8 keV and 2661.0 keV levels, established it as a $M1$ transition. The J^π of the three top most levels in band B1 are determined only from the R_{DCO} values of the 111, 116 keV transitions, as their Δ_{IPDCO} could not be found and the parity of those levels are put in parentheses. Thus the band B1 is extended upto J^π of $(27/2^-)$ with the placements of these transitions.

A new band structure marked as band B2 in Fig.4.5 has been established based on the level at 1985.2 keV which decays to the main band (B1) through the 535 keV and 118 keV transitions. The spin and parity of the band head of B2 at 1985.2 keV is fixed as $17/2^-$ on the basis of the $E2$ nature of the 535 keV transition, determined from its measured R_{DCO} value of 1.09(2) (in quadrupole gate) and Δ_{IPDCO} as 0.08(5). The presence of the transitions 181, 270, 418, 486, 643, 712, 723, 824 and 896 keV belonging to band B2, are evident from the coincidence spectrum gated by the 535 keV transition as shown in Fig. 4.7(a). But the 181, 270, 643, 824 keV transitions are not observed in 486 keV gated spectrum of Fig. 4.7(b). Inference can be drawn from the above fact that 181, 723, 824 and 643 keV γ rays are in parallel with

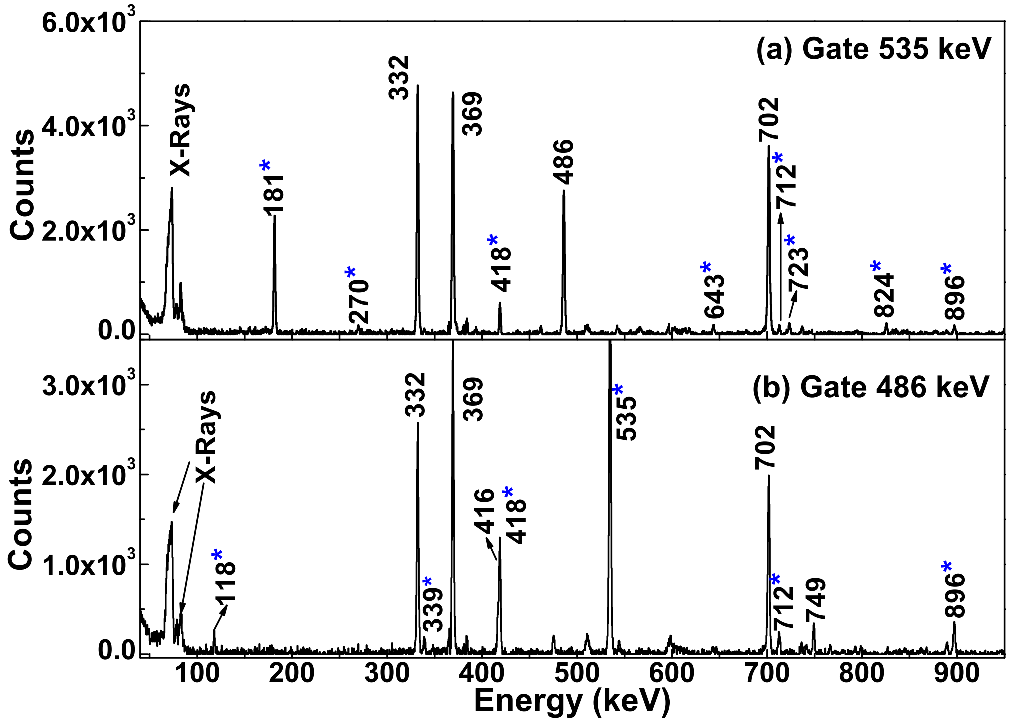

Figure 4.7: Coincidence spectra gated by (a) 535 keV and (b) 486 keV corresponding to the transitions of band B2 in ^{199}Tl. '*'marked transitions are newly placed in the level scheme.

486 keV γ rays. The band B2 has been formed depending on various coincidence conditions. The 486 keV transition was reported as a $M1$ transition in the previous work [31]. However, in the present work, the multipolarity and nature of the 486 keV transitions (E2) has been fixed from the DCO ratio of 1.05(2) (in quadrupole 535 keV gate), angular distribution value and Δ_{IPDCO} value of 0.15(8) which fixed the J$^\pi$ of the 2470.8 keV level as $21/2^-$. The Δ_{IPDCO} value of the 723 keV transition could not be measured due to the contamination of 724 keV transition from band B5. But M1 character of the 418-keV transition, deduced from its DCO and Δ_{IPDCO} values, fixed the spin of the 2889.3 keV level as $23/2^-$. Appearance of the 118 keV γ ray and absence of the 181 keV γ ray in the 486 keV gate also confirms that the 118 & 181 keV cascade (both M1) transitions and 535 & 486 keV cascade transitions are in parallel to each other. With the placement of these transitions and their cross-overs in this band, the band B2 has been extended upto $25/2^-$. The presence of the connecting transitions between the bands B1 and B2 are also seen in Figs. 4.7. The sequence B2 is not established as a well

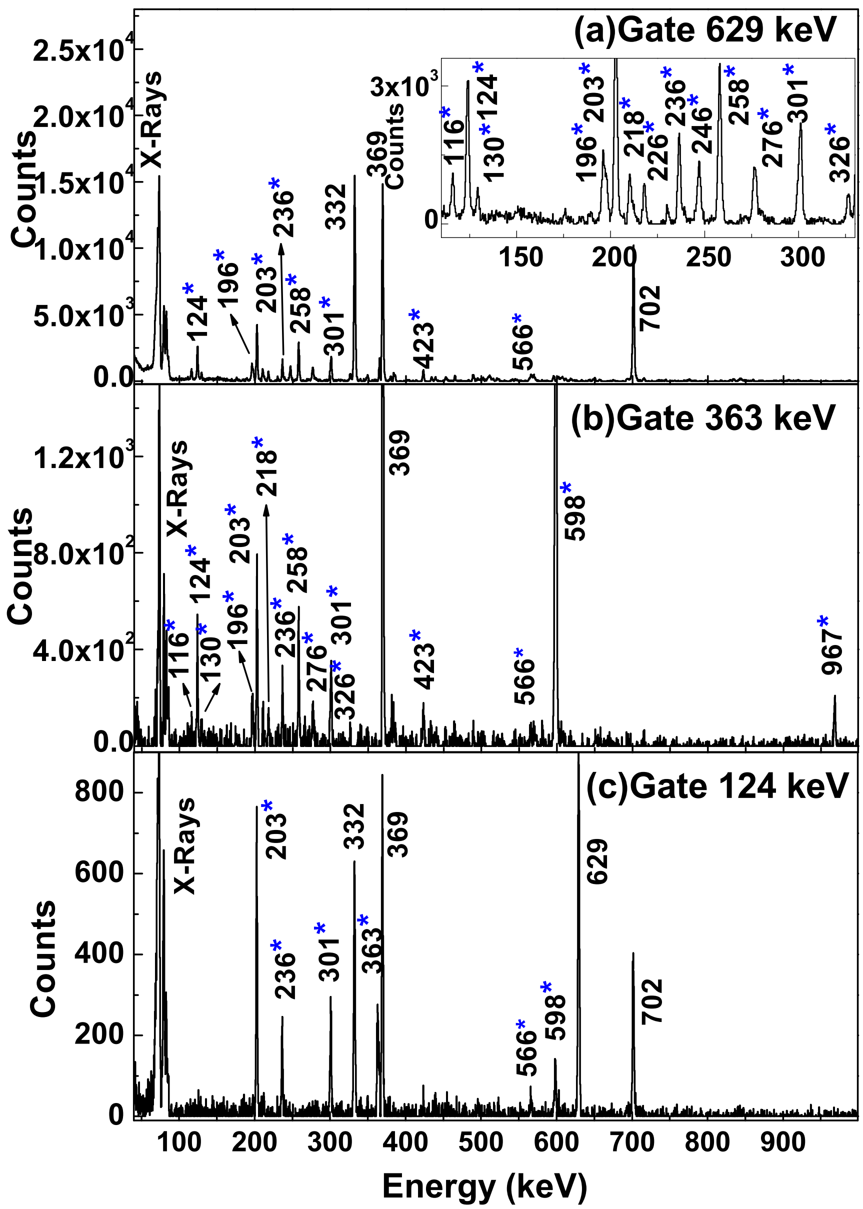

Figure 4.8: Coincidence spectra corresponding to gates of (a) 629 keV, (b) 363 keV, (c) 124 keV transitions corresponding to the band B3 and B4 in ^{199}Tl. '*'marked transitions are newly placed in the level scheme.

developed band, few of the intra band M1 transitions are not observed. The levels of this band are connected with few discrete excited states through 643, 736, 712 keV transitions.

Table 4.1: The energies of the γ ray transitions (E_γ), the energies of the initial levels (E_i), the spins and parities of the initial (J_i^π) and final (J_f^π) levels along with the relative intensities (I_γ) , DCO ratios (R_{DCO}) and IPDCO values (Δ_{IPDCO}) for all the transitions in ^{199}Tl from the present work are shown. The proposed multipolarities of the γ rays are also mentioned.

E_γ (in keV)	E_i (in keV)	$J_i^\pi \rightarrow J_f^\pi$	I_γ(Err) [1]	R_{DCO}(Err)	Δ_{IPDCO}(Err)	Deduced Multipol.
(28.7) [2]	748.9	$9/2^- \rightarrow 5/2^+$	-	-	-	M2
111.2(2)	2944.0	$23/2^{(-)} \rightarrow 21/2^-$	0.92(16)	0.35(9) [3]	-	(M1+E2)
116.0(1)	3060.0	$25/2^{(-)} \rightarrow 23/2^{(-)}$	0.42(12)	0.66(7) [4]	-	(M1+E2)
116.1(1)	2195.3	$17/2^{(+)} \rightarrow 15/2^+$	0.34(13)	1.02(9) [5]	-	(M1+E2)
118.3(1)	1985.2	$17/2^- \rightarrow 15/2^-$	0.31(13)	-	-	(M1+E2)
123.8(1)	2203.0	$17/2^+ \rightarrow 15/2^+$	3.34(31)	1.05(3) [5]	-	(M1)
171.8(1)	2832.8	$21/2^- \rightarrow 19/2^-$	1.10(18)	0.41(7) [4]	-	(M1+E2)
181.4(1)	2166.6	$19/2^- \rightarrow 17/2^-$	3.73(31)	0.61(2) [6]	-0.17(12)	M1+E2
195.9(1)	2649.1	$21/2^{(+)} \rightarrow 19/2^{(+)}$	2.13(58)	0.44(4) [4]	-0.06(5)	M1+E2
202.6(1)	2405.6	$19/2^+ \rightarrow 17/2^+$	7.09(43)	0.52(2) [4]	-0.06(8)	M1
204.8(2)	1410.2	$9/2^+ \rightarrow 7/2^+$	3.95(13)	-	-	(M1+E2)
206.0(1)	1616.2	$9/2^+ \rightarrow 9/2^+$	0.40(3)	0.99(11) [7]	-	M1+E2
217.8(1)	2866.9	$23/2^{(+)} \rightarrow 21/2^+$	1.71(22)	0.62(7) [4]	-0.08(6)	M1+E2
226.0(1)	3286.0	$(27/2^-) \rightarrow 25/2^{(-)}$	0.45(11)	-	-	(M1)
236.3(2)	2641.9	$21/2^+ \rightarrow 19/2^+$	3.37(31)	0.45(4) [4]	-0.09(4)	M1
240.0(2)	2169.4	$(13/2^+) \rightarrow 11/2^+$	0.56(12)	-	-	-
257.9(2)	2453.2	$19/2^{(+)} \rightarrow 17/2^{(+)}$	5.93(38)	1.17(3) [5]	-0.002(6)	(M1)
269.6(1)	2254.8	$17/2^- \rightarrow 17/2^-$	0.40(13)	-	-	-
288.5(1)	1493.9	$9/2^+ \rightarrow 7/2^+$	3.08(21)	-	-	M1

Table 4.1: Continued...

E_γ (in keV)	E_i (in keV)	$J_i^\pi \rightarrow J_f^\pi$	I_γ(Err) [1]	R_{DCO} (Err)	Δ_{IPDCO} (Err)	Deduced Multipol.
300.8(1)	2706.4	$21/2^+ \rightarrow 19/2^+$	4.51(49)	0.48(3) [4]	-0.03(2)	M1
321.5(1)	2250.9	$13/2^+ \rightarrow 11/2^+$	1.14(15)	0.65(6) [8]	-	(M1+E2)
326.4(1)	2405.6	$19/2^+ \rightarrow 15/2^+$	1.78(29)	1.04(16) [4]	0.17(14)	E2
328.0(1)	2194.9	$17/2^- \rightarrow 15/2^-$	2.31(29)	0.53(6) [4]	-0.05(9)	M1
332.2(1)	1450.5	$13/2^- \rightarrow 11/2^-$	47.21(7)	0.46(1) [4]	-0.02(1)	M1
338.9(1)	2809.7	$19/2^- \rightarrow 21/2^-$	0.27(4)	-	-	(M1)
353.3(1)	720.2	$5/2^+ \rightarrow 3/2^+$	52.6(9)	0.80(1) [9]	-0.04(2)	M1+E2
363.2(1)	2079.2	$15/2^+ \rightarrow 13/2^-$	14.18(5)	-	-	(E1) [11]
366.9(1)	366.9	$3/2^+ \rightarrow 1/2^+$	76.22(17)	0.68(14) [10]	-0.03(10)	(M1+E2)
369.4(1)	1118.3	$11/2^- \rightarrow 9/2^-$	100.0(2)	0.32(1) [6]	-0.02(1)	M1+E2
382.0(1)	748.9	$9/2^- \rightarrow 3/2^+$	49.58(6)	-	-	E3 [11]
387.9(4)	2254.8	$17/2^- \rightarrow 15/2^-$	1.08(65)	0.47(9) [4]	-0.07(3)	M1
400.0(1)	1810.2	$11/2^+ \rightarrow 9/2^+$	1.75(9)	1.06(7) [7]	-0.16(4)	M1
406.2(2)	2661.0	$19/2^- \rightarrow 17/2^-$	1.19(20)	0.26(11) [4]	-0.05(4)	M1+E2
410.8(1)	1616.2	$9/2^+ \rightarrow 7/2^+$	0.33(5)	0.85(8) [9]	-0.02(2)	M1+E2
416.4(1)	1866.9	$15/2^- \rightarrow 13/2^-$	18.97(67)	0.33(1) [3]	-0.04(2)	M1+E2
417.1(1)	1911.0	$11/2^{(+)} \rightarrow 9/2^+$	1.83(12)	0.45(6) [10]	-	(M1+E2)
418.5(1)	2889.3	$23/2^- \rightarrow 21/2^-$	2.16(16)	0.47(3) [6]	-0.02(69)	M1
423.2(1)	2626.2	$19/2^- \rightarrow 17/2^+$	3.14(29)	0.59(5) [4]	0.03(18)	(E1)
438.9(3)	2641.9	$21/2^+ \rightarrow 17/2^+$	1.19(10)	1.81(24) [5]	-	(E2)
466.1(1)	2661.0	$19/2^- \rightarrow 17/2^-$	2.09(29)	0.54(7) [3]	-0.02(2)	M1
475.0(1)	2191.0	$(15/2^-) \rightarrow 13/2^{(-)}$	1.31(1)	-	-	(M1)
477.5(1)	1682.9	$9/2^+ \rightarrow 7/2^+$	0.54(1)	0.55(3) [12]	-	(M1+E2)
485.6(1)	2470.8	$21/2^- \rightarrow 17/2^-$	8.96(67)	1.05(2) [6]	0.15(8)	E2
500.6(1)	2430.0	$(-) \rightarrow 11/2^+$	0.68(7)	-	-	-
520.8(1)	2014.7	$13/2^- \rightarrow 9/2^+$	1.90(9)	0.94(12) [10]	-0.03(3)	M2

Table 4.1: Continued...

E_γ (in keV)	E_i (in keV)	$J_i^\pi \rightarrow J_f^\pi$	I_γ(Err) [1]	R_{DCO} (Err)	Δ_{IPDCO} (Err)	Deduced Multipol.
534.7(1)	1985.2	$17/2^- \rightarrow 13/2^-$	34.91(92)	1.09(2) [4]	0.08(5)	E2
566.0(1)	3272.4	$25/2^+ \rightarrow 21/2^+$	2.49(23)	2.01(69) [5]	0.05(3)	E2
578.0(1)	2832.8	$21/2^- \rightarrow 17/2^-$	1.08(31)	1.00(28) [4]	0.05(18)	E2
580.0(1)	2191.0	$(-) \rightarrow 13/2^-$	1.72(3)	-	-	-
597.7(1)	1716.0	$13/2^- \rightarrow 11/2^-$	33.40(49)	-	-	(M1)
628.7(1)	2079.2	$15/2^+ \rightarrow 13/2^-$	56.10(6)	0.55(1) [4]	0.02(5)	E1
637.9(1)	2832.8	$21/2^- \rightarrow 17/2^-$	0.83(27)	-	-	(E2)
643.1(1)	2809.7	$19/2^- \rightarrow 19/2^-$	1.30(27)	0.51(7) [6]	-	(M1)
645.2(1)	1394.1	$11/2^- \rightarrow 9/2^-$	12.40(5)	-	-0.01(1)	M1 [11,13]
674.9(1)	2168.8	$9/2^{(+)} \rightarrow 7/2^+$	1.51(7)	0.52(11) [10]	-	(M1+E2)
690.0(1)	1410.2	$9/2^+ \rightarrow 5/2^+$	6.72(28)	1.03(5) [10]	0.01(4)	E2
701.6(1)	1450.5	$13/2^- \rightarrow 9/2^-$	45.44(6)	0.89(1) [6]	0.07(5)	E2
712.1(1)	3182.9	$25/2^+ \rightarrow 21/2^-$	0.56(7)	1.02(42) [6]	-0.21(7)	M2
720.2(1)	720.2	$5/2^+ \rightarrow 1/2^+$	15.24(9)	-	0.02(15)	E2 [13]
722.7(1)	2889.3	$23/2^- \rightarrow 19/2^-$	0.79(9)	0.98(9) [6]	-	(E2)
724.0(1)	1929.4	$11/2^+ \rightarrow 7/2^+$	3.29(11)	1.06(3) [12]	0.15(10)	E2
736.0(1)	3206.8	$25/2^- \rightarrow 21/2^+$	3.29(11)	0.90(11) [6]	-0.02(2)	M2
744.4(1)	2194.9	$17/2^- \rightarrow 13/2^-$	10.15(52)	1.08(5) [4]	0.005(18)	E2
748.6(1)	1866.9	$15/2^- \rightarrow 11/2^-$	9.52(3)	1.14(4) [3]	0.04(6)	E2
761.7(1)	1481.9	$9/2^{(+)} \rightarrow 5/2^+$	3.52(21)	0.90(11) [10]	-	(E2)
773.7(1)	1493.9	$9/2^+ \rightarrow 5/2^+$	4.95(23)	1.03(5) [10]	0.10(3)	E2
794.1(1)	2661.0	$19/2^- \rightarrow 15/2^-$	3.68(34)	0.88(6) [4]	0.06(6)	E2
804.3(1)	2254.8	$17/2^- \rightarrow 13/2^-$	5.70(38)	0.96(5) [4]	0.09(6)	E2
824.5(1)	2809.7	$19/2^- \rightarrow 17/2^-$	0.83(20)	0.63(9) [4]	-0.02(1)	M1+E2
838.5(1)	1205.4	$7/2^+ \rightarrow 3/2^+$	13.55(5)	1.06(3) [8]	0.03(3)	E2
840.7(1)	2250.9	$13/2^+ \rightarrow 9/2^+$	3.79(5)	1.18(19) [10]	0.10(9)	E2

Table 4.1: Continued...

E_γ (in keV)	E_i (in keV)	$J_i^\pi \rightarrow J_f^\pi$	I_γ(Err) [1]	R_{DCO} (Err)	Δ_{IPDCO} (Err)	Deduced Multipol.
896.3(1)	3367.1	$25/2^- \rightarrow 21/2^-$	1.10(20)	1.02(12) [6]	0.06(13)	E2
902.6(1)	2832.0	$(-) \rightarrow 11/2^+$	-	-	-	(-)
950.8(1)	2880.2	$(15/2^+) \rightarrow 11/2^+$	-	-	-	(E2)
962.7(1)	1682.9	$9/2^+ \rightarrow 5/2^+$	2.20(2)	1.04(7) [10]	0.02(9)	E2
967.1(1)	1716.0	$13/2^- \rightarrow 9/2^-$	0.97(2)	-	0.07(10)	E2

The J$^\pi$ = $15/2^+$ level at 2079.2 keV was known as the highest observed level in Ref.[29]. A cascade of transitions(124, 326, 203, 301 keV) have been observed in the present work, which are placed on top of this level as band B3. A separate branch, B4, has also been established above the 2079.2 keV level through the 116 keV γ ray. These two γ-lines are clearly observed in the 629-keV gated spectrum shown in Fig.4.8 (inset). The newly observed transitions in bands B3 and B4 are shown in the coincidence spectra of the 629-keV, 363-keV and 124-keV transitions, showed in Fig. 4.8(a), (b) and (c) respectively. It can be seen that the 116-keV γ ray is not observed in the spectrum gated by the 124-keV transition, which confirms the

[1]Relative γ ray intensities are estimated from prompt spectra and normalized to 100 for the total intensity of 369.4-keV γ ray.

[2]Unobserved transition, Adopted from Ref [31]

[3]From 794.1 keV (E2) DCO gate;

[4]From 701.6 keV (E2) DCO gate;

[5]From 628.7 keV (E1) DCO gate;

[6]From 534.7 keV (E2) DCO gate;

[7]From 353.3 keV (M1+E2) DCO gate;

[8]From 724.0 keV (E2) DCO gate;

[9]From 366.9 keV (M1+E2) DCO gate;

[10]From 720.2 keV (E2) DCO gate;

[11]Adopted from Ref [29] or [31]

[12]From 838.5 keV (E2) DCO gate;

[13]Multipolarity has been found from angular distribution;

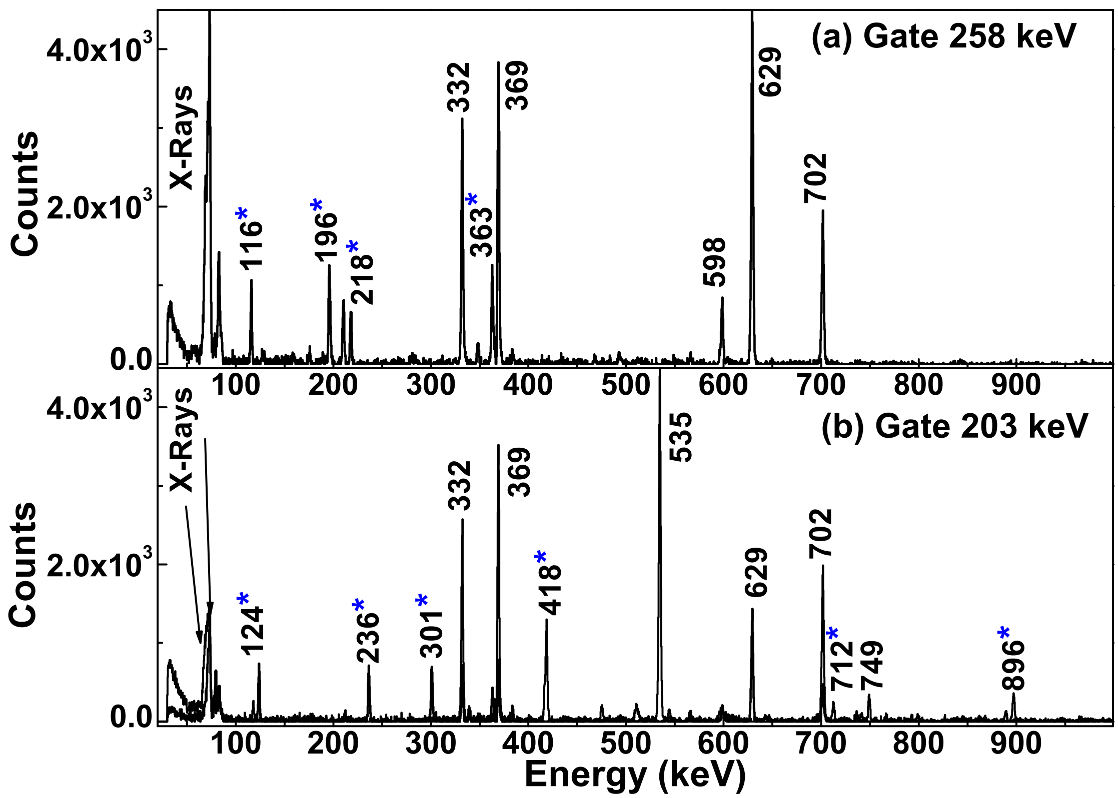

Figure 4.9: Coincidence spectra gated by (a) 258 keV and (b) 203 keV corresponding to the transitions of band B4 and B3 respectively in ^{199}Tl. '*'marked transitions are newly placed in the level scheme.

parallelism of 124 keV and 116 keV transitions and two different branches B3 and B4 on the top of these transitions respectively.

The 416 or 749 keV transitions are absent in the coincidence spectrum of 629 keV while the 702 keV line is in coincidence with it. So the 629 keV γ ray connects with the main band (B1) through 1450.5 keV level. Both the 598 keV and 967 keV lines are present in the gate on 363 keV [Figure 4.8(b)] whereas 629 keV and 702 keV are not present. These coincidence relations place the 363 keV in parallel with 629 keV transition but in a cascade with the 967 keV or 598 keV transition. From DCO ratios, the multipolarities of the 124 keV and 116 keV transitions are assigned as M1. Therefore, positive parity is assigned to the bands B3 and B4. It is clearly seen from Fig. 4.8 that 326 keV does not appear in the spectrum gated by the 124 keV transition

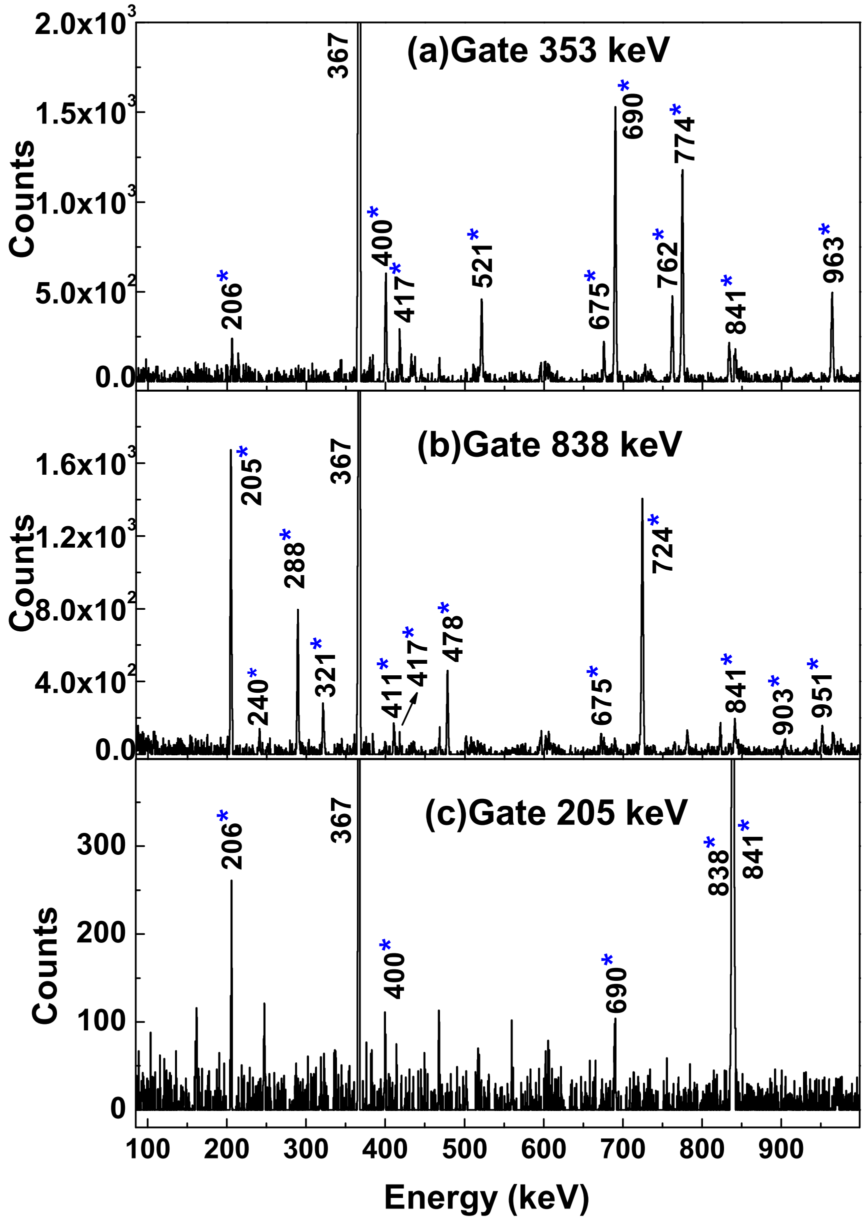

Figure 4.10: Coincidence spectra corresponding to the gates of (a) 353 keV, (b) 838 keV, (c) 205 keV transitions corresponding to the band B5 in ^{199}Tl. '*'marked transitions are newly placed in the level scheme.

while it is present in both 629 keV (fig 4.8(a)inset) and 363 keV gates. Presence of a strong 203 keV line in coincidence with 363 keV transition establishes the 326 keV γ ray as a crossover E2 of the 124 and 203 keV cascade. The bands B3 and B4 are extended up to the excitation energy of 3272.4 keV and 2866.9 keV, respectively. Two different band B3 and B4 can clearly be seen from the spectra Fig. 4.9. Fig. 4.9(a) clearly show the cascades of 116, 196 and 218 keV M1 transition, which are newly established fom the present work. No transitions belonging to band B3 are observed in the spectrum, which leads to the conclusion that both the sequences are independent of each other. The gate on the M1 transition 203 keV reveals some more facts about band B3. Fig. 4.9(b) shows the transitions which are in coincidence with 203 keV. The absence of 439 and 326 keV transitions in the Fig. 4.9(b) further confirms the 439 keV transition as the crossover E2 transition of 203 & 236 keV. The presence of 535, 712, 418 749 and 896 keV in the coincidence gate of 203 keV indicate that the band B3 and B2 has some low energy interconnecting transition between them but from the current data such transition could not be identified.

An independent level has been identified at 1394.1 keV excitation which is connected to the 748.9 keV level by a 645 keV transition. This level has been reported earlier in Ref. [29] but the spin parity was not known properly. The R_{DCO} value of 645 keV transition could not be found due to the lack of suitable gating transition but the Δ_{IPDCO} value suggests it as magnetic transition. The angular distribution suggests this transition as a dipole one. Thus the J^{π} of the level is now assigned as $11/2^{-}$.

The positive parity levels below the long-lived $9/2^{-}$ isomer were mostly known from the previous work of Ref. [29, 31]. The ground state of ^{199}Tl was assigned as $1/2^{+}$ from the earlier study [29] originated from $\pi s_{1/2}$ orbital. A band like structure with sequences of M1 and crossover E2 transitions was reported in the earlier work [31]. This sequence of levels are shown as band B5 in level scheme (Fig. 4.5) obtained in the present work [30]. Two cascades of E2 transitions are seen but some of the interconnecting M1 transitions are not observed. The 367 and 353 keV transitions are confirmed to be (M1/E2) transitions as stated from the earlier work. A 382 keV transition decays from the 748.9 keV 28.4ms isomeric level to the 366.9 keV level. Δ_{IPDCO} value -0.03(10) of the 367 keV transition has fixed the spin of the 366.9 keV level as $3/2^{+}$ and thus the nature of 382 keV γ ray comes out to be as E3 [29]. Fig. 4.10(a),(b) and (c) show the γ rays in coincidence with the 353 keV, 838 keV and 205 keV transitions respectively and belongs to the sequences marked with B5 , B6 and B7 in Fig. 4.5. From Fig. 4.10(a) it can be seen that almost all the transitions which belong to B5, B6 and B7 are present but not the 720, 838, 724, 411, 951, 903 keV γ rays, which are placed either parallel or to a different branch in the level scheme. The DCO ratio and Δ_{IPDCO} of the 838 keV γ ray are 1.06(3)(in the quadrupole gate) and 0.03(3) respectively which fixes the spin of the 1205.4 keV level as $7/2^+$ and the 838 keV γ ray as E2. The presence of the 724 keV and 951 keV in coincidence with the 838 keV γ ray and the absence of the 690, 720 and 353 keV transitions in the spectrum gated on the 838 keV [Fig: 4.10(b)] establish the presence of two parallel cascades of E2 transitions. The presence of 841 keV transition in coincidence with 838 keV gated spectrum indicates the existence of a 205 keV transition which is connecting the two sequences of E2 to each other. The existence of 205 keV and 321 keV in the gate of 838 keV [Fig: 4.10(b)] also supports this fact. The positive Δ_{IPDCO} value 0.15(10) indicates the 724 keV as an electric transition and the R_{DCO}=1.06(3) value in the 838 keV (E2) gate confirms it as an E2 transition. Hence, the 724 keV (E2) gate was used to obtain the DCO ratio of some of the unknown transitions.

The nature of all the other transitions (240, 501, 903, 951 keV) beyond the 1929.4 keV level could not be determined because of low statistics and thus spin-parities of all the levels above 1929.4 keV are tentatively assigned. In the 720 keV gate only the 690, 841 and 206 keV are present from the sequence B5. DCO ratio values of 690 keV and 841 keV are 1.03(5) and 1.18(19) respectively in the quadrupole (E2) gate of 720 keV which also leads to assign them as E2 character and the J^π of the 2250.9 keV level is thus fixed at $13/2^+$. The presence(absence) of the 206 keV(411 keV) transition in the coincidence gate on 205 keV (Fig. 4.10(c)) assigns the 205-206 keV cascade across the 411 keV transition. According to the level scheme, the 690 keV transition should not come in coincidence with the 205 keV transition. On the other hand the 205 keV γ ray should be in coincidence with the 838 and 841 keV transitions. But along with the 838, 841 keV transitions, the 690 keV line also appeared in the coincidence gate on 205 keV in Fig. 4.10(c) due to the contamination of the gate on 205 keV with the 206 keV transition. The DCO ratio value of the 206 keV transition has been found out to be 0.99(11) with respect to the 353 keV (M1+E2) gate and thus its multipolarity is concluded as dipole. The Δ_{IPDCO} and R_{DCO} values of the 411 keV transition also suggest it as M1+E2 nature and thus the J^π of the 1616.2 keV level is assigned as $9/2^+$, thereby fixing the nature of the 206 keV transition as a non stretched M1 transition. The presence of the 321 keV line in both the 838 and 724 keV gates and the presence of the 205 keV line in both the 838 and 841 keV gates, establishes a series of decaying M1 transitions from $13/2^+$ to $11/2^+$ (321 keV), $9/2^+$ to $7/2^+$ (205 keV) and $5/2^+$ to $3/2^+$ (353 keV) levels between the two branches of E2 sequences in B5.

A set of new levels are observed above the 720.2 keV level and the the two sequences of gamma rays are named as B6 and B7 in the level scheme Fig. 4.5(c). All of these γ rays, decay from the sequences B6 and B7 and the connecting transitions to B5 are seen in Fig. 4.10(a),(b) and (c). The 1493.9 keV level (of sequence B7) decays to B5 by the 288 (M1) and 774 (E2) transitions. The nature of the 288 and 774 keV transitions are inferred from the R_{DCO} and Δ_{IPDCO} values shown in Table 4.1 thus the J^π of the 1493.9 keV level is established as $9/2^+$. Multipolarities of almost all the transitions belonging to B6 and B7 are found out from the quadrupole gate on 720 keV or the dipole gate on 353 keV, wherever possible. Few transitions are observed to be in coincidence with 774 and 288 keV and placed above the 1493.9-keV level. Multipolarity of 675 keV transition is concluded as dipole by its R_{DCO} value of 0.52(11) in 720 keV quadrupole gate. Similarly, with the DCO ratio and polarization asymmetry values, the 521 keV transition is found to be of M2 character and 417 keV is tentatively assigned as M1. The spin of 1682.9 keV level is fixed as 9/2 from the multipolarity of the 963 keV transition obtained from its DCO ratio of 1.04(7) from the E2 gate on 720 keV. Automatically the multipolarity of the 478 keV transition, decaying from the 1682.9 keV to 1205.4 keV level is fixed as a dipole. The J^π of the level at 1810.2 keV is assigned as $11/2^+$ from the M1+E2 nature of the 400 keV transition determined from its Δ_{IPDCO} value of -0.16(4) and the R_{DCO} value of 1.06(7) in the 353 keV (M1+E2) gate. Another transition of 762 keV which can be seen in the 353 keV gate (Fig. 4.10(a)) is placed in B6 as an independent single transition decaying from the 1481.9 keV level.

4.4 Discussion

The level scheme of ^{199}Tl from the present work has been divided into a few band structures. The analog of Band B1, based on the intruder $\pi h_{9/2}$ configuration on top of the $9/2^-$ isomer has been observed in all the odd-A Tl isotopes. In this work, this band has been extended beyond band crossing. At higher spins above $13/2^-$, this band has been observed to bifurcate into two structures. The states in band B2 with possibly 3-qp(quasi particle) nature are yrast while the band B1 continues through the non-yrast states. The initial few low lying states in the band-like structure B5 were already known, and the analogs are also known in the neighboring Tl isotopes, ^{195,197}Tl. These states correspond to the single particle orbitals $\pi s_{1/2}$ and $\pi d_{3/2}$, available near proton Fermi level below the $Z = 82$ shell closure. In the present work, these states have been extended through the observation of a sequence of positive parity non-yrast states connected through E2 transitions in the band B5 up to an excitation energy of 2.88 MeV. However, the spacing between the states in this band-like sequences does not seem to correspond to a rotational band of a well deformed nucleus. A few more discrete states have also been observed in the present work and are classified as B6 and B7 sequences in Fig.4.5 which decay to the sequence B5.

The E (level energy) vs. I (level spin) of the different bands(B1, B2, B3 and B5) of ^{199}Tl are plotted in Fig.4.11. The E vs. I plots for different bands in ^{199}Tl are fitted using the rotor equation

$$E(I) = (\hbar^2/2\Theta) * I * (I + 1) + E0,$$

where Θ is the moment of inertia and E0 is a parameter corresponding to the initial energy of the band. One of the simple ways to determine whether a band is of deformed rotational character is from the E vs. I plot, which corresponds to a parabola in the case of a rotational band. The different slopes of the parabola would correspond to different moments of inertia and hence to different origins of the different structure. It may be noted that the variable moment of inertia (VMI) model as proposed by Mariscotti et al. in case of even-even nuclei [43], was not incorporated in these fittings. Though the above equation does not give a satisfactory good fit to a rotor, but it only provides a qualitative description of the band structures and suggest

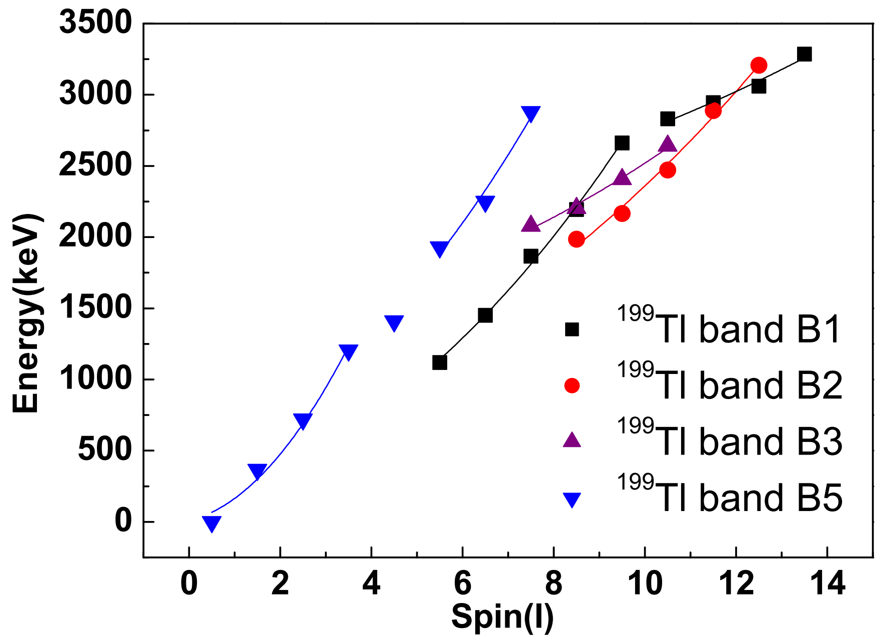

Figure 4.11: Energy vs Spin plot for $\pi h_{9/2}$ configuration for ^{199}Tl as well as for other positive and negative parity bands. The solid lines are the fits using the rotational model formula (see text for details).

that the cranking formalism may be applied to describe the band structures in ^{199}Tl. It is also worth while to point out that the ratio of the energies of the 4^+ and the 2^+ states, E_{4^+}/E_{2^+}, of the neighboring even-even Hg core are well within the rotational limit prescribed in Ref.[43]. Therefore, in the following we have applied the cranking model to describe the bands B1,B2 and B3 in ^{199}Tl.

The aligned angular momentum (i_x) as a function of rotational frequency ($\hbar\omega$) plot for the πh$_{9/2}$ bands of different odd-A Tl nuclei is shown in Fig.4.12. The aligned angular momenta (i_x) of other observed band structures in ^{199}Tl are compared in Fig.4.13 with the similar bands of the neighboring odd-A Tl isotope ^{201}Tl and of the even-even ^{198}Hg core. The band B1, with a $9/2^-$ band head, has a $h_{9/2}$ configuration as has been described in an earlier work [29] which continues up to about 9.5 $\hbar$ of spin. The band B1, along with the corresponding bands in all the odd mass Thallium nuclei show a back-bending around 0.34$\hbar$ frequency. The i_x plot for this band shows a gain in alignment of more than 9 $\hbar$ which can only be achieved by breaking

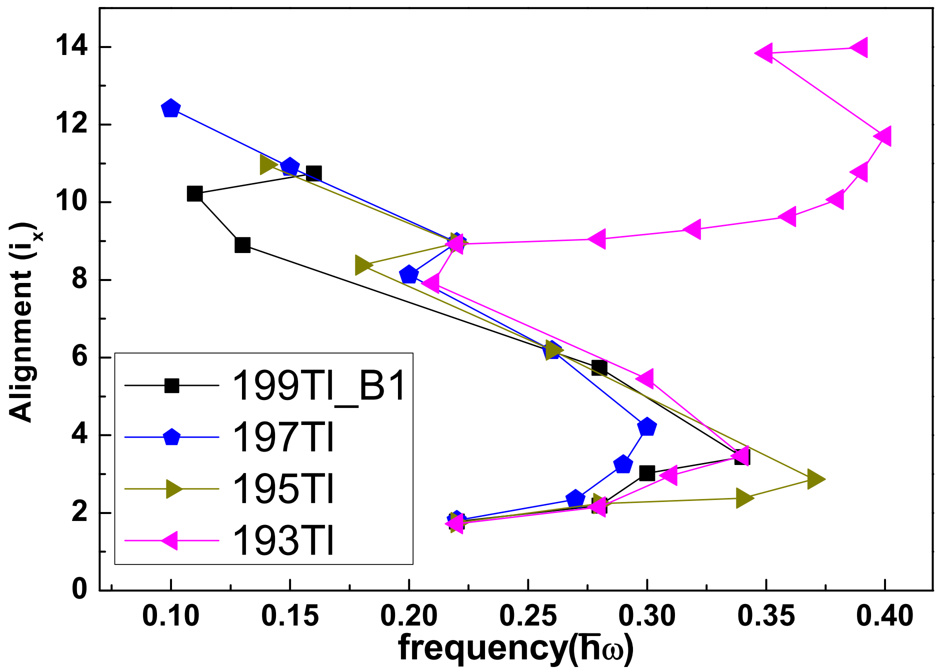

Figure 4.12: Alignment plot for the $\pi h_{9/2}$ bands in odd-mass Tl isotopes. The level energies of the same bands of $^{193-197}$Tl are taken from ref. [20, 21, 17] respectively. The Harris reference parameters are taken as $J_0 = 8\hbar^2 MeV^{-1} and\ J_1 = 40\hbar^4 MeV^{-3}$.

a nucleon pair in high-j orbital. Thus the the band crossing is predicted as the alignment of a pair of neutrons in the $\nu i_{13/2}$ orbital. Hence the upper part of this band corresponds to a configuration with 3-qp, $\pi h_{9/2} \otimes \nu i^2_{13/2}$. The upper part of this band B1 in Fig.4.11 fits to a different parabola with larger moment of inertia, which also indicates towards a change in configuration after 8.5 $\hbar$.

The band B2 is yrast beyond 7.5 $\hbar$, and has a larger moment of inertia than the lower, i.e 1-qp, part of band B1. The alignment (i_x) of band B2 is represented in Fig. 4.13 which shows the gain in alignment for this band ($\sim 4\hbar$) is smaller than the 3-qp part of band B1 (see Fig.4.12). Therefore, the neutron alignments take place in the ($f_{5/2}, p_{3/2}$) orbital with small j which leads to the smaller gain in alignment after pair breaking. Hence the configuration of band B2 is $\pi h_{9/2} \otimes \nu(j_-)^2$ where $j_- = f_{5/2}, p_{3/2}$.

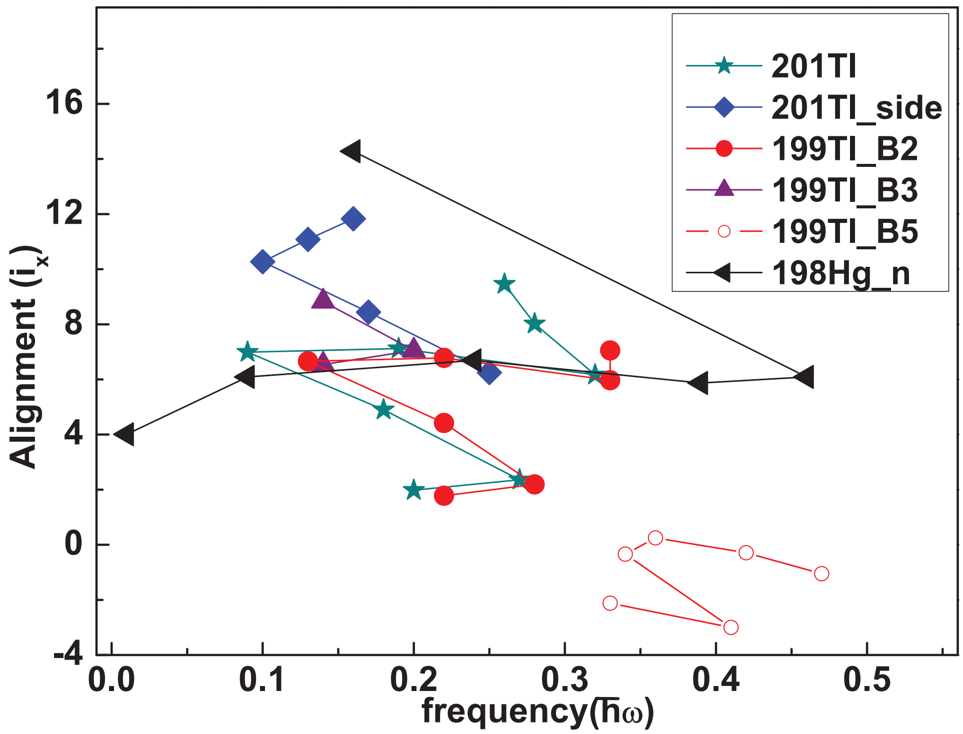

Figure 4.13: Alignment plot for the positive and negative parity bands of ^{199,201}Tl isotopes and comparison with the alignment of negative parity band of ^{198}Hg core. The level energies of the bands of ^{201}Tl and ^{198}Hg are taken from Ref. [25, 35]. The Harris reference parameters are taken as $J_0 = 8\hbar^2 MeV^{-1} and\ J_1 = 40\hbar^4 MeV^{-3}$.

The alignment plots for the other neighboring odd-A Tl isotopes are also shown in Fig. 4.12 and Fig. 4.13. The initial alignment pattern for band B1 in ^{199}Tl matches well with the other lighter Tl isotopes but the alignment for band B2 in ^{199}Tl is similar to that in ^{201}Tl. The gain in alignments for band B2 in ^{199}Tl are also very similar to that of the yrast band of ^{201}Tl . The 3-qp bands with configuration of $\pi h_{9/2} \otimes \nu(j_{-})^2$ are yrast in case of ^{199,201}Tl whereas the 3-qp bands with configuration of $\pi h_{9/2} \otimes \nu i_{13/2}^2$ is yrast in case of lighter Tl isotopes. This change is, apparently, due to the change of neutron Fermi level and indicates that the neutron Fermi level lies close to the negative parity orbitals $(f_{5/2}, p_{3/2})$ for $N \geq 118$.

The positive parity band in ^{199}Tl (marked as band B3 in the level scheme) also shows a rotational structure as is evident from the fits in Fig. 4.11. However, the excitation energy, larger moment of inertia obtained for the fitting of the E vs. I plot and the initial aligned angular momentum of about 6 $\hbar$ (Fig. 4.13) indicates the 3-qp nature of this band. The alignment plot for the 5^- band in the neighboring even-even core of ^{198}Hg is shown in Fig. 4.13 to comapre with the bands in ^{199}Tl, which has only one proton extra than that of ^{198}Hg. The underlying configuration of the 5^- band in ^{198}Hg is interpreted as $\nu(i_{13/2} \otimes j_-)$ [35]. The similarity of the initial alignments of these two suggests a similar neutron configuration for the band B3 in ^{199}Tl as for the 5^- band in ^{198}Hg. Hence a 3-qp configuration of $\pi h_{9/2} \otimes \nu(i_{13/2} \otimes j_-)$ is assigned for this band. This j_- stands for the available neutron orbital $f_{5/2}, p_{3/2}$ near Fermi level. A strong transition (629 keV) from the band head of this band(B3) to the $h_{9/2}$ band(B1) supports this configuration. It may be noted, however, that the contribution of the $h_{9/2}$ proton to the observed aligned angular momentum i_x is very small indicating the involvement of high-Ω component of the $h_{9/2}$ proton orbital, which is expected for an oblate deformation in ^{199}Tl. This band, however, could not be extended much for further discussion.

The single level at the energy of 1394.1 keV can be identified as the state which is coming from the odd proton in ^{199}Tl occupying the $h_{11/2}$ orbital. All the odd-Tl isotopes from ^{195}Tl to ^{205}Tl have a similar level, reported in Ref. [44, 45, 23, 46, 47]. In the case of odd-A Au isotopes ($Z = 79$) from ^{191}Au to ^{197}Au [48, 49, 50, 51] the $11/2^-$ state corresponding to this $\pi h_{11/2}$ configuration is appeared as a spin-gap isomer because this state can decay to the available $1/2^+$, $3/2^+$ and $5/2^+$ (corresponding to the $s_{1/2}$, $d_{3/2}$ and $d_{5/2}$ configurations) states below this level only by the transitions with large multipolarities. However, as the proton Fermi level in Tl isotopes is higher in energy than in Au isotopes, the $11/2^-$ state lies at a relatively higher energy and the intruder $\pi h_{9/2}$ state with oblate deformation comes down in energy and lies below the $11/2^-$ state in Tl isotopes. Thus the availability of $\pi h_{9/2}$ state below the $\pi h_{11/2}$ creating a prompt decay path of the $11/2^-$ state to the $9/2^-$ state via low multipolarity transition as in the case of ^{199}Tl. Therefore, the presence of the intruder $\pi h_{9/2}$ orbital, prevents the $11/2^-$ state in Tl isotopes from being an isomer.

The excitation energy vs spin plot for the two E2 sequences marked as B5 in the level scheme of Fig.4.5 is also shown in Fig.4.11. It can be seen that the data points can be fitted with two parabolic curves, one at lower excitation and another at higher excitation. However, the moment of inertia obtained from this fit ($\sim 6.4\hbar^2 MeV^{-1}$) indicates a low deformation for this configuration. To further understand the characteristics of the band-like structure, marked as B5 in the level scheme of Fig. 4.5, the aligned angular momentum (i_x) of Band B5 is also plotted in Fig. 4.13 with the same Harris reference parameters ($J_0 = 8\hbar^2 MeV^{-1},\ J_1 = 40\hbar^4 MeV^{-3}$) as the ones considered for the rotational bands B1, B2 and B3 of ^{199}Tl. It is clear from this plot that the same sets of Harris parameters does not hold for the structure B5 (i_x becomes -Ve) and a reduced J_0 and J_1 ($J_0 \sim 2.8\hbar^2 MeV^{-1}, J_1 \sim 27\hbar^4 MeV^{-3}$) would be required to fit the initial alignment of this sequence. This also indicates that B5 has much less deformation compared to other bands in ^{199}Tl and the rotational model description may not hold well for the band-like structure B5. Moreover, as mentioned earlier, the lower lying states which are also observed in lighter odd-mass Thallium isotopes were interpreted as the single particle states in previous works of Ref. [29, 26] involving $\pi s_{1/2}$ and $\pi d_{3/2}$ orbitals.

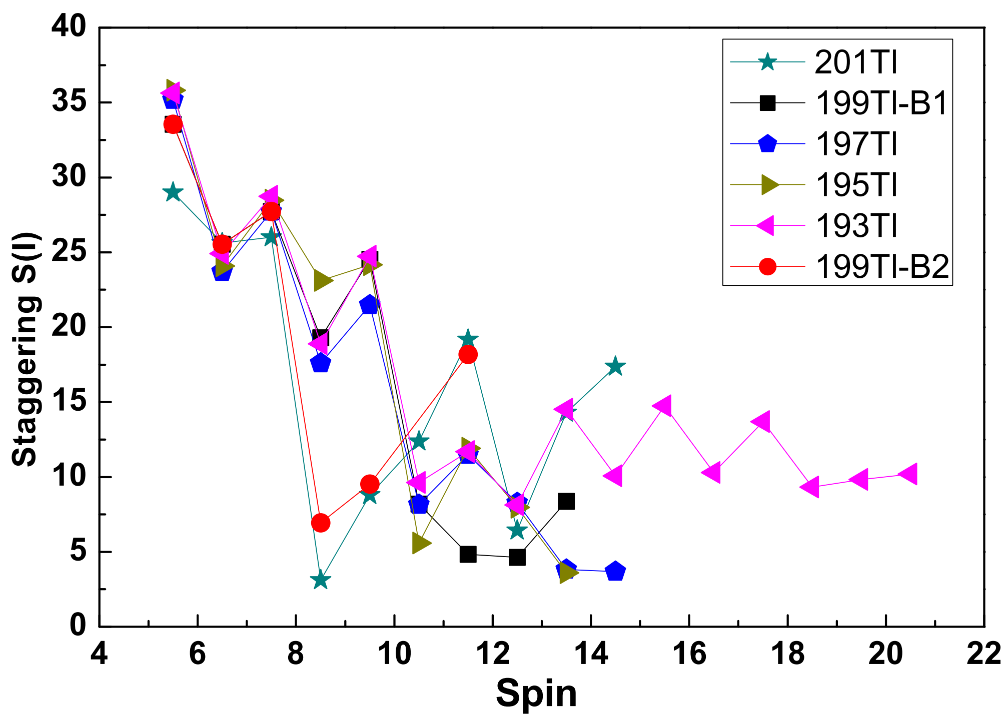

Figure 4.14: Staggering (S(I) = [E(I) - E(I-1)]/2I) plot for the $\pi h_{9/2}$ bands in odd-A Tl isotopes. Data for $^{193-201}$Tl are taken from Ref [20, 29, 21, 17, 25] respectively.

The energy staggering, defined by, $S(I) = [E(I) - E(I-1)]/2I$, where, E(I) is the energy of the state with spin I, is plotted as a function of spin (I) for the band B1 in Fig. 4.14, along with the same bands in neighbouring odd-odd $^{193-201}$Tl. It can be seen from this figure that the staggering (S(I)) plots of all odd-mass Tl isotopes show remarkable similarities, except for ^{201}Tl at higher spin. The staggering in ^{201}Tl, however, matches quite well with that of the band B2 in ^{199}Tl, suggesting similar structure for these two bands. This supports our suggestion of the transitional nature of $N = 118$ in Tl isotopes in deciding the 3-qp yrast configuration.

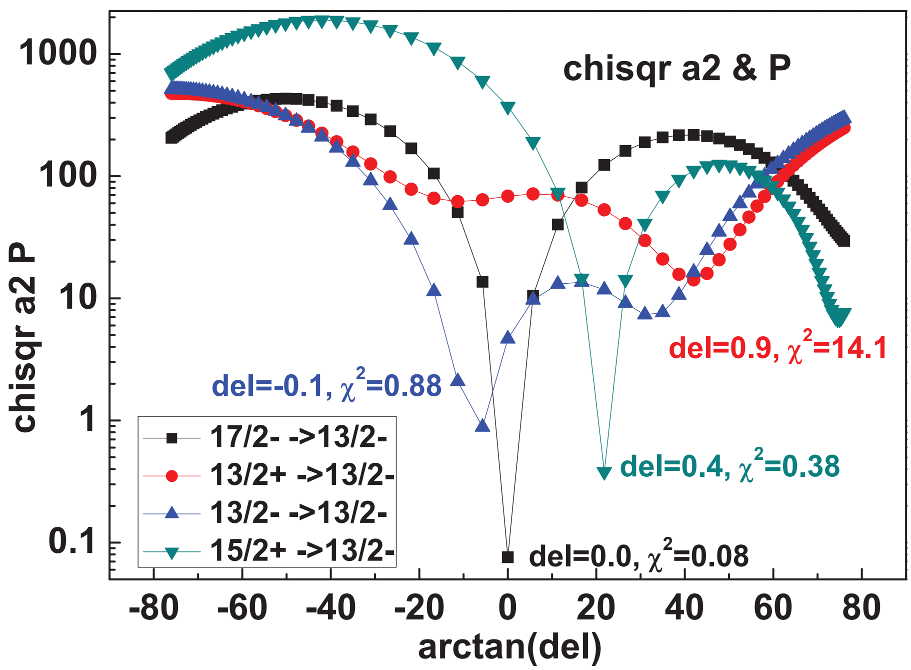

Figure 4.15: $\chi^2(\delta)$ analysis of angular distribution coefficient (a_2) and polarization (P) of 535 keV transition.

From a recent study, Ref [32], Li *et. al.* also observed a level at 1985.2 keV and the spin-parity of the level was tentatively assigned as $13/2^+$. They have also observed a sets of gamma transitions on the top of these level as also reported in the present work [30], which marked in the Fig. 4.5 as band B2. But from the present work, the spin-parity of the band head of band B3 is assigned as $17/2^-$. This needs an extra attention because the configuration of the band is very much dependent on the assignment of the spin-parity to 1985.2 keV level. The band head of B2 can be assigned by determining the multipolarity and nature of the 535 keV transition, which is decaying from that level and connected to the band B1 at 1450.5 keV level with $13/2^-$ spin. The DCO ratio value 1.19(2) in the quadrupole gate of 702 keV and Δ_{IPDCO} value of 0.08(5) also indicates 535 keV as a quadrupole Electric transition. For further confirmation, angular distribution of the connecting transition (535 keV) has been carried out and the distribution pattern also shows it as a quadrupole. To conclude, the Polarization value and the angular coefficient value for different possible spin sequences for the 535 keV transitions with higher multipole mixing (δ) has been calculated and compared with the experimental value. A chi-square minimization calculation considering the angular coefficient a2 and the polarization value P for all the possible cases of 535 keV has been carried out and shown in Fig. 4.15 as function of arctan(δ) (mixing). The plot clearly show that the chi square is minimum for the spin sequence $17/2^-$ state to the $13/2^-$ state with δ=0 mixing. whereas the assignment for the 535 keV transition to decay from $13/2^+$ state to the $13/2^-$ in the Ref [32] by Li *et. al.* does not show any minima with reasonable δ mixing. Therefore the assignment of 535 keV as E2 transition, leading to the spin-parity of the band head of band B2 as $17/2^-$ seems convincingly right.

4.5 TRS calculations

In order to have structural information on the different bands in ^{199}Tl, the Total Routhian Surface (TRS) calculations were performed by the Strutinsky shell correction method using deformed Woods-Saxon potential [37, 38]. The universal parameter set was used for these calculations [41]. The total Routhian energies were calculated in $(\beta_2, \gamma, \beta_4)$ deformation mesh points with minimization on β_4. The procedure for such calculations has been outlined in Ref. [43]. The Routhian surfaces are plotted in the conventional $\beta_2 - \gamma$ plane. The calculations are performed for the 1-qp negative parity configuration corresponding to the $\pi h_{9/2}$ band (B1), for the 1-qp positive parity configuration corresponding to the $\pi s_{1/2}$ band, and for the 3-qp positive parity configuration corresponding to the $\pi h_{9/2} \otimes \nu i_{13/2}(f_{5/2}p_{3/2})$ band.

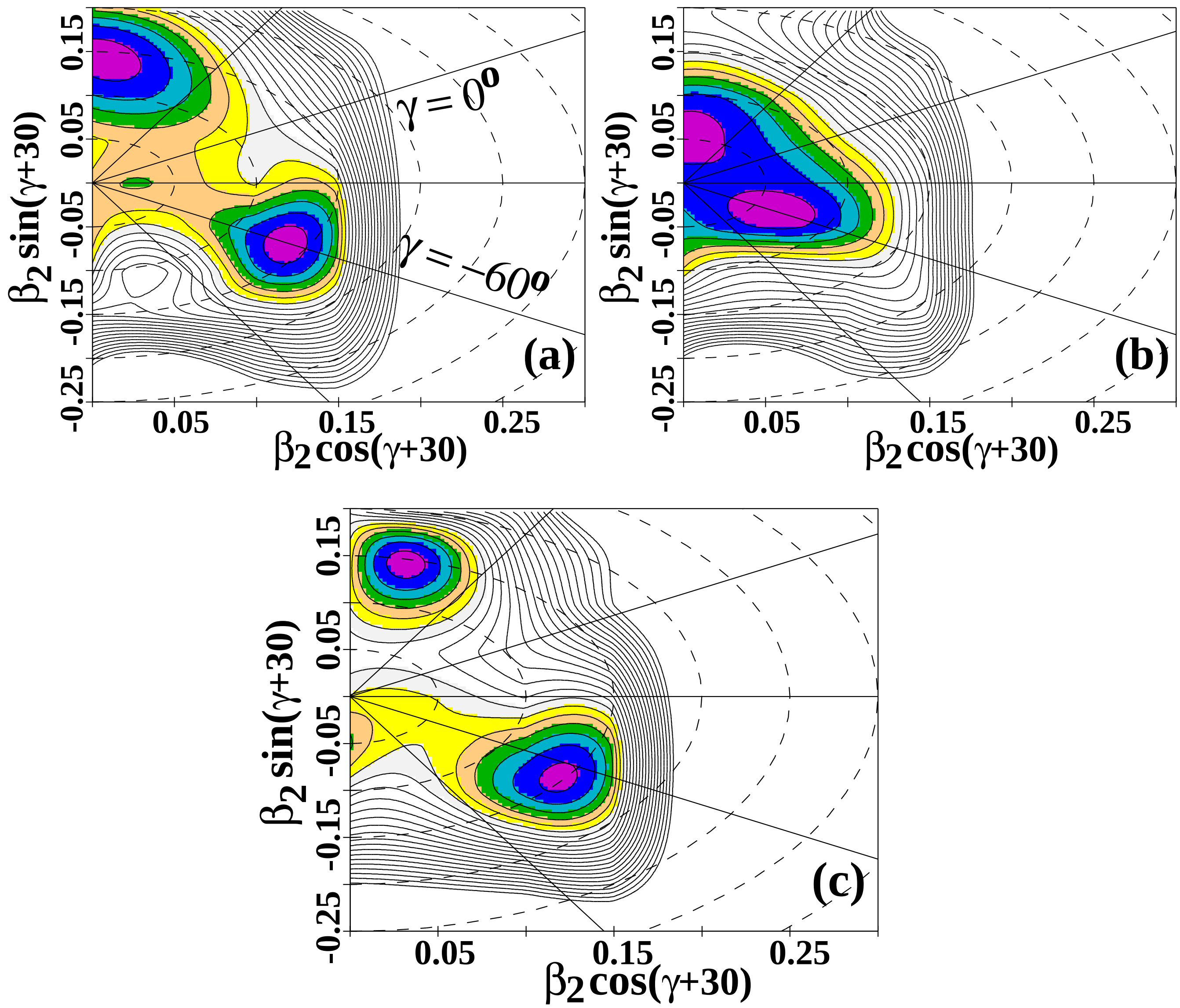

Figure 4.16: (Color online) Calculated total Routhian surface (TRS) plots for the (a) 1-qp negative parity,(b) 1-qp positive parity and (c) 3-qp positive parity bands in ^{199}Tl. These are calculated at rotational frequency $\hbar\omega = 0.11$ MeV and the contours are 350 keV apart.

The TRS plots for these three probable configurations close to the band heads are shown in Fig.4.16. These plots are shown at the rotational frequency of $\hbar\omega = 0.11$ MeV. In these calculations, the nuclear spin (I) is projected out and at near band-head frequencies, which corresponds to the single particle contribution. The surfaces corresponding to the 1-qp negative parity configuration clearly show a minimum at an oblate deformation with $\beta_2 \sim 0.13$ and

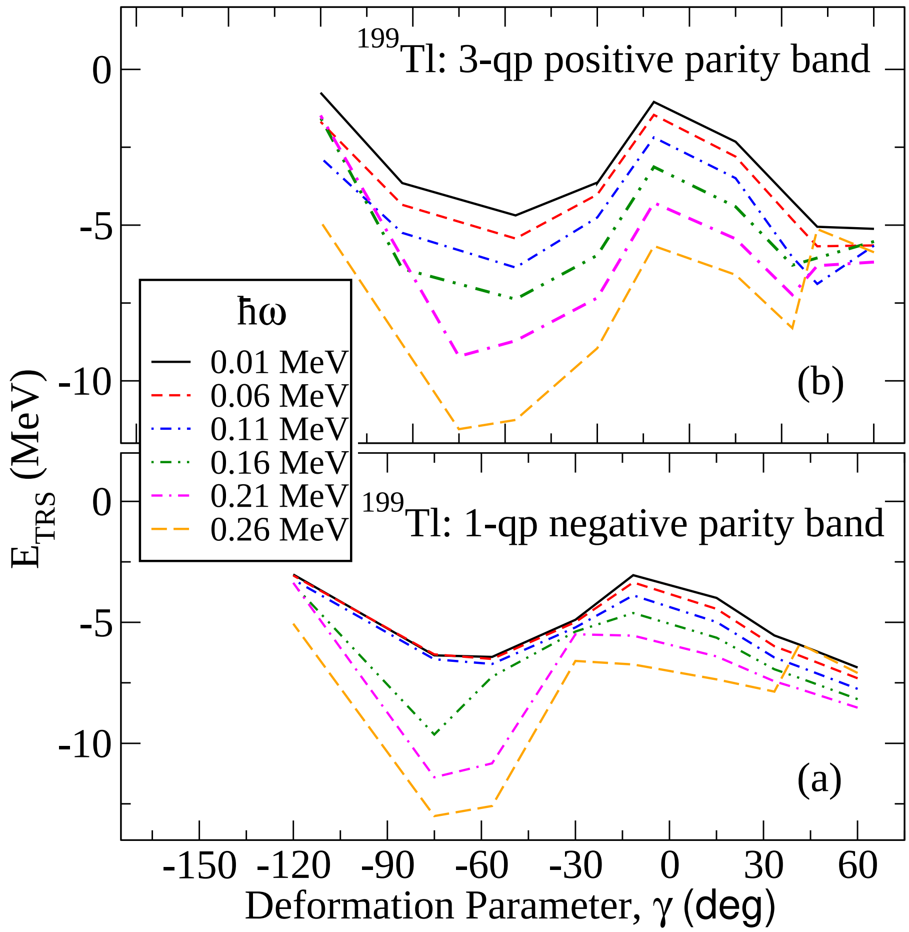

Figure 4.17: (Color online) The calculated TRS energy (E_{TRS}) as a function of the triaxial parameter γ for the (a) 1-qp particle negative parity band and (b) 3-qp positive parity band in ^{199}Tl for different rotational frequencies $\hbar\omega$.

$\gamma \sim -60°$ in Fig. 4.16(a). The calculated projected spin for this configuration comes out to be I = 4.5 $\hbar$, indicating an almost pure $\pi h_{9/2}$ configuration. A second minimum at a non-collective oblate deformation ($\gamma \sim +60°$) also observed from the plot for this configuration. For the case of the 1-qp positive parity band for which I = 0.5 is calculated, the minimum appears close to the spherical shape (Fig.4.16(b)), which is expected for the $\pi s_{1/2}$ configuration for the ground state and in close conformity with the experimental moments of inertia that suggest a near-spherical shape from the observed E vs. I plot. This agrees with the observed band structure of band B5, which does not seem to be a well deformed one. Two minima, one at a collective oblate deformation with $\beta_2, \gamma \sim 0.14, -60°$ and $\sim 0.15, +40°$ are obtained for the 3-qp configuration (Fig.4.16(c)). The difference between the two minima is less than 250 keV. At slightly higher frequencies the triaxial minimum becomes lower in energy. For this configuration, I = 6.5 is obtained for the band head which is close to the observed band head of B3 (in Fig. 4.5).

The variations of the calculated TRS energies, E_{TRS}, for different rotational frequencies, as a function of the triaxial deformation parameter γ are shown in Fig.4.17 for the 1-qp negative parity and the 3-qp positive parity configurations involving the $\pi h_{9/2}$ orbital. In these plots, the value of deformation parameter β_2 was kept around the values corresponding to the minimum in the two-dimensional TRS plots. It can be seen that the shape (corresponding to the minimum in the E_{TRS}) for the 1-qp configuration (Fig.4.17(a)) changes from axially deformed oblate ($\gamma \sim -60°$) at lower rotational frequencies to slightly triaxial with $\gamma \sim -75°$ at higher frequencies. On the other hand, for the 3-qp positive parity band (Fig.4.17(b)) two close lying minima are clearly seen at lower frequencies with some softness against γ near $\gamma \sim -60°$. At $\hbar\omega \sim 0.1 MeV$, E_{TRS} is minimum for a near-triaxial shape with $\gamma \sim +40°$. At a slightly higher frequency of $\hbar\omega \sim 0.16$ MeV, the minimum shifts to an axial oblate shape $\gamma \sim -57°$. At an even higher frequency, the minimum again shifts to around $\gamma \sim -75°$. The band structure, B3 corresponding to this configuration has been observed only up to a few states and these states seem to be due to the oblate deformation. It would be interesting to extend this band and measure the B(E2) values up to higher frequencies to study the above prediction of shape change in this band.

4.6 Summary

Yrast near yrast structure in ^{199}Tl have been populated by using the fusion evaporation reaction ^{197}Au(α,2n) at the beam energy of 30 MeV at K-130 Cyclotron, Kolkata and studied by γ ray spectroscopic techniques using the VENUS setup of 6 Compton suppressed Clover HPGe detectors. The level scheme of ^{199}Tl has been extended considerably through the observation and placement of 53 new transitions up to the excitation energy of ~ 3.4 MeV and spin of $12.5\hbar$.

The spin and parity assignments to different observed bands as well as single levels were done by DCO, IPDCO and angular distribution measurements. A new negative parity state with spin-parity $11/2^-$ has been identified and predicted to come from the involvement of the $\pi h_{11/2}$ orbital. It will be interesting to investigate the band structure, build on this state as seen in all nearby Au nuclei. A few band structures involving the intruder $\pi h_{9/2}$ have been observed in this odd-mass nucleus. The band structures are compared with those of the other neighbouring odd-A Tl isotopes. It has been observed that the remarkable similarity of the low-lying states in the $\pi h_{9/2}$ band in odd-A Tl nuclei continues to persist in the $N = 118$ isotope. However, the 3-qp configuration for the yrast states after band crossing, changes at $N = 118$ for ^{199}Tl which continues to the next odd-mass ^{201}Tl isotope.

The shape of ^{199}Tl for different configurations and its variation with rotational frequency are discussed in the light of the cranking model calculations with Woods-Saxon potential. Oblate deformation is obtained for the 1-qp negative parity $\pi h_{9/2}$ band, whereas the low-lying 1-qp positive parity band, corresponding to the $\pi s_{1/2}$ configuration appears to be near spherical, in good agreement with the experimental observation. An interesting shape evolution from a coexisting and γ-soft shape to a triaxial shape at higher frequency, through an axially deformed oblate shape, is predicted in our calculations for the 3-qp positive parity band. However, this cannot be confirmed from the present data for the population of ^{199}Tl with limited spin obtained through α-induced reaction. Experiment with heavier beams and measurements of lifetimes to obtain B(E2) values and deformation are warranted in future to understand the higher spin states and thereby the contribution of different high-j proton and neutron orbitals.

Bibliography

[1] R.M. Diamond and F.S. Stephens, Nucl. Phys. A **45**, 632 (1963).

[2] V. T. Gritsyna *et. al.* Nucl. Phys. A **61**, 129 (1965).

[3] J. O. Newton *et. al.*, Nucl. Phys. A **148**, 593 (1970).

[4] W. Reviol *et al.*, Phys. Rev C **61**, 044310(2000).

[5] S. Das Gupta *et al.*, Phys. Rev C **88**, 044328(2013).

[6] H. Pai *et al.*, Phys. Rev C **85**, 064313 (2012).

[7] T. Roy *et al.*, Phys. Lett. B **782**, 768 (2018).

[8] P.L. Masiteng *et al.*, Phys. Lett. B **719**, 83 (1988).

[9] E.A. Lawrie *et al.*, Phys. Rev. C **78**, 021305(R) (2008).

[10] A. Covello and G. Sartoris, Nucl. Phys. A **93**, 481 (1967).

[11] I. Hamamoto, Phys. Rep. **10**, No.2, 63 (1974).

[12] K. Heyde *et al.*, Phys. Rep. **102**, No. 5&6, 291 (1983).

[13] M. Huyse *et al.*, Phys. Lett. B **201**, 293 (1988).

[14] G. J. Lane *et al.*, Phys. Lett. B **324**, 14 (1994).

[15] W. Reviol *et al.*, Phys. Rev C **58**, 2644(R) (1998).

[16] S. Pilotte *et al.*, Phys. Rev C **49**, 718 (1994).

[17] P.B. Fernandez et al., Nucl. Phys. A **517**, 386 (1990).

[18] F. Azaiez *et al.*, Z. Phys. A **338**, 471 (1991).

[19] J. Duprat *et al.*, Phys. Lett. B **341**, 6 (1994).

[20] W. Reviol *et al.*, Phy. Scr. T **56**, 167 (1995).

[21] J. O. Newton, F. S. Stephens, and R. M. Diamond, Nucl. Phys. A **236**, 225 (1974).

[22] R. M. Lieder *et al.*, Nucl. Phys. A **299**, 255 (1978).

[23] M. G. Slocombe *et al.*, Nucl. Phys. A **275**, 166 (1977).

[24] J. Wrzesiński et al., Eur. Phys. J. A **20**, 57 (2004).

[25] R. B. Firestone *et al.*, Table of Isotopes (John Wiley and Sons, New York, 1999).

[26] H. Pai *et al.*, Phys. Rev C **88**, 064302 (2013).

[27] S. Nandi *et al.*, Phys. Rev C **99**, 054312 (2019).

[28] Soumik Bhattacharya *et al.*, Phys. Rev. C **95**, 014301 (2017).

[29] J. O. Newton *et al.*, Nucl. Phys. A **148**, 593 (1970).

[30] R.E. Doebler, Wm. C. McHarris, Phys. Rev C **2**, 2422 (1970).

[31] N. Marginean *et al.*, Eur. Phys. J. A **46**, 329 (2010).

[32] C. B. Li *et al.*, Phys. Rev. C **97**, 034331 (2018).

[33] Soumik Bhattacharya *et al.*, Phys. Rev. C **98**, 044311 (2018).

[34] Soumik Bhattacharya *et al.* DAE Symp. of Nucl. Phys. **61** , 98 ,(2016).

[35] http://www.tifr.res.in/ pell/lamps.html

[36] R.K. Bhowmik, S. Muralithar, R.P. Singh, Proc. DAE Symp. on Nucl. Phys., **44B**, 422 (2001).

[37] D. C. Radford, Nucl. Instrum. Methods Phys. Res. A **361**, 297 (1995).

[38] A. Kramer-Flecken *et al.*, Nucl. Instrum. Methods Phys. Res. A **275**, 333 (1989).

[39] K. Starosta *et al.*, Nucl. Instrum. Methods Phys. Res. A **423**, 16 (1999).

[40] Ch. Droste *et al.*, Nucl. Instrum. Methods Phys. Res. A **378**, 518 (1996).

[41] Balraj Singh, Nuclear Data Sheets **108**, 79 (2007).

[42] C. Günther *et al.*, Phys. Rev. C **15**, 1298 (1977).

[43] M. A. J. Mariscotti, Gertrude Scharff-Goldhaber and Brian Buck, Phys. Rev. **178**, 1864 (1969).

[44] K. H. Hicks *et al.*, Phys. Rev. C **25**, 2710 (1982).

[45] L. L. Collins *et al.*, Diss. Abst. Int. **39B**, 3834 (1979).

[46] D. Royer *et al.*, Nucl. Phys. A **158**, 516 (1970).

[47] J. A. Becker *et al.*, Phys. Rev. C **29**, 1268 (1984).

[48] H. Beuscher,P. Jahn, R. M. Lieder,C. Mayer-Boricke,Z. Phys. **247**, 383 (1971).

[49] Z. Plajner,J. Frana, I. Rezanka, A. Spalek, M. Fiser, Z. Phys. **233**, 122 (1971).

[50] K. Farzine,H. v. Buttlar, Z. Phys. **270**, 155 (1974).

[51] A. J. Haverfield, H. T. Easterday,J. M. Hollander, Nucl. Phys. A **64**, 379 (1965).

[52] W. Nazarewicz *et al.*, Nucl. Phys. A **435**, 397 (1985).

[53] W. Nazarewicz *et al.*, Nucl. Phys. A **512**, 61 (1990).

[54] J. Dudek, Z. Szymanski, and T. Werner, Phys. Rev. C **23**, 920 (1981)

[55] G. Mukherjee *et al.*, Nucl. Phys. A **829**, 137 (2009).

Chapter 5

New information on the excited structure of odd-N ^{199}Hg

5.1 Introduction

Nuclei close to ^{208}Pb in mass 200 region show variety of band structures generating from the coupling of odd valance particles with the core. The near spherical shapes of the nuclei near doubly magic shell closure is influenced by the presence of high-j orbital near the Fermi levels. The ground and the low lying excited states of nuclei (Hg; $Z = 80$ and Tl; $Z = 81$) near $Z = 82$ shell closure are dominated by the pure single particle excitation near the Fermi level, whereas the available high-j intruder orbitals both for proton and neutron bring collectivity into the system and various exotic structural phenomena, like, magnetic rotational band in ^{194}Tl [9] and chiral band in ^{194,195,198}Tl [13, 14, 15] have been reported. Thallium isotopes near A$\sim$200, which have just one proton less with respect to $Z = 82$ magic shell closure, also exhibit strongly coupled band structure, based on high-j proton as well as high-j neutron orbital [10, 30, 12, 25] with oblate deformation. Neighbouring Pt ($Z = 78$) isotopes have been found to have triaxial shapes at low spin [5, 6]. It is interesting to investigate the interplay of the collective core with the available single particle orbitals, in particular, the involvement of high-j orbitals that generates the above exotic phenomena below the $Z = 82$ shell closure region [7, 1, 2].

Being adjacent to the triaxial Pt nuclei and oblate Thallium nuclei, the Hg isotopes near 190-200 mass are also expected to have deformed structure built on high-j orbitals and oblate deformed rotational bands have been reported in all the Hg isotopes in this mass region [14, 15, 16]. The ground state band structures in the even mass Hg nuclei $^{190-200}$Hg are identified as a rotation-aligned decoupled band [16, 17, 18, 19, 35, 21]. The level crunching beyond I>6 spin states in even mass Hg nuclei are described to be generated from the interaction of the ground state band with the rotation aligned $\pi h_{11/2}^{-2}$ states in $^{190-196}Hg$ isotopes [16, 17] and $\nu i_{13/2}^{-2}$ states in $^{198-200}Hg$ nuclei [35, 21].

For odd mass Hg nuclei, a single neutron outside the oblate core mainly responsible for the observed structures. The low lying states are purely from the occupation of the odd neutron to the $p_{3/2}$, $f_{5/2}$, and $i_{13/2}$ orbital. With a little excitation energy, all of the Hg nuclei are observed to have decoupled band structure based on $\nu i_{13/2}$ orbital. The band structures in the odd Hg nuclei strongly support the applicability of the Coriolis-decoupling scheme to these nuclei, in which an odd particle in a high-j orbital with a small projection Ω on the symmetry axis of the nucleus is decoupled from the nuclear symmetry axis and aligned along the nuclear rotation axis due to the Coriolis force acting on it. For odd mass Hg in this mass region, with oblate deformation, the odd neutron has access to the $\Omega = 1/2$ projection of $i_{13/2}$ orbital, which, as a result of Coriolis force, decoupled from the oblate even-even Hg core and positive parity decoupled band structure based on $13/2^+$ state has been observed in all the odd mass $^{191-199}Hg$ isotopes [17, 15, 18, 22]. In this coupling scheme only the spin states with $I = j, j+2, j+4$, ... are observed and for the states with spin $I = j+1, j+3, j+5, \ldots$, the odd particle is not fully aligned, and one expects these states at comparatively higher excitation energies.

Along with the observation of decoupled band near ground state, at higher spin, negative parity structure based on 5^- and $21/2^-$ band head is also observed in even and odd mass Hg nuclei, respectively and have been described as semi-decoupled band [23]. It was first suggested by Yates *et al.* [24] that this two-quasi-particle (qp) decoupled bands in even-Hg nuclei have an intrinsic structure, of a completely decoupled high-j $i_{13/2}$ neutron and a low-j neutron of opposite parity in the adjacent $p_{1/2}$, $p_{3/2}$, $f_{5/2}$ orbitals. The states based on $21/2^{-}$ band head for odd Hg isotopes are similar to that of the even Hg isotopes and can be explained as generated due to a decoupled $i_{13/2}$ neutron coupled to the 5^{-}, 7^{-}, 9^{-}, .. states of adjacent even-even Hg nuclei. With enough excitation energy and angular momentum the appearance of super deformed band in ^{193}Hg has also been reported [25].

The data beyond $N = 120$ for Hg nuclei are scarce. In contrast to the neutron deficient Hg nuclei in 190-200 mass region, Hg nuclei beyond mass A>200 with the neutron number approaching the $N = 126$ shell closure, are expected to exhibit mainly single particle behaviour [26] corresponding to a spherical nucleus. Therefore, the Hg nuclei around mass 200 region are of great interest as it is situated just in the transition region of deformed to the spherical shape. The low spin states of ^{199}Hg is known from the decay study of ^{199}Tl [27] which were explained with a quasiparticle-phonon coupling model. The high spin states of ^{199}Hg have been studied by Mertin *et. al.* [28] in which the yrast $i_{13/2}$ band was known only up to $25/2^{+}$ spin whereas, in all the other adjacent odd and even mass Hg isotopes, below $N = 119$, these bands are known at least up to $41/2^{+}$ spin. In all odd-A Hg isotopes from $N = 107$ (^{187}Hg) till $N = 117$ (^{197}Hg), a band crossing has been observed at a spin$\sim$13.5$\hbar$. The study by Mertin *et. al.* on $^{197-199}Hg$[28], did not observe any states beyond $31/2^{-}$ and $29/2^{-}$ spin for ^{197}Hg and ^{199}Hg, respectively so the band crossing information is not complete. Experimental studies, therefore, need attention to probe the yrast and near yrast states to understand the effect of the high-j orbitals in the band structures as a function of increasing neutron number around A$\sim$200. The recent work on the high spin states of $^{197-199}Hg$, populated with multi-nucleon transfer reaction [29] has extended the negative parity semi decoupled band for ^{199}Hg, but they also could not identify any transitions beyond 2106 keV level to extend the yrast positive parity band.

The α induced fusion evaporation reaction has been used in the present work to populate yrast as well as near yrast states in ^{199}Hg in search of low spin exotic structures. Such kind of a structure has already been reported in nearby Thallium nuclei and also expected to appear as a non-yrast states in Hg nuclei. With the help of the new generation HPGe Clover detectors, it has become possible to obtain more complete information about the detailed band structures as well as unambiguous assignment of spin and parity to the states of ^{199}Hg. Many new transitions and states belongs to ^{199}Hg have been observed in the present thesis work. Determination of the parities of the states, which were tentatively assigned from the last work by Negi *et. al.*, has become possible from the present work. Interesting results appeared as a near yrast band structure in ^{199}Hg is reported in this chapter.

5.2 Experiment and Data Analysis

The study of the yrast and the near yrast states of ^{199}Hg has been performed using fusion evaporation reaction ^{198}Pt(α,3n)^{199}Hg, with a beam energy of 36 MeV from the K-130 cyclotron at VECC, Kolkata using two different set up, **VE**CC array for **NU**clear **S**pectroscopy (VENUS) and **I**ndian **N**ational **G**amma **A**rray (INGA). The ^{199}Hg nucleus has been produced with almost negligible contamination of the neighbouring isotopes with a self supporting 7.2 mg/cm^2 enriched ^{198}Pt target.

The six Compton Suppressed Clover HPGe detectors are used to find the coincidence relations. The angular orientation of the detectors of VENUS were used for the DCO ratio, angular distribution as well as polarization measurements, and the details of which can be found in the Ref. [30]. Standard NIM electronics and VME based data acquisition system were used to acquire data in both singles and coincidence trigger condition using LAMPS [31]. The time between the individual OR of all the crystals of a Clover detector and the Master trigger were measured using Six Time-to-Amplitude-Converters (TACs). Another TAC was used for measuring the time information of the events with respect to the Cyclotron RF signal.

For the parity information of the weekly populated non-yrast levels of ^{199}Hg, INGA set up at VECC [32] has been used with more(4) numbers of Clover detectors at 90° angle which were used to deduce the polarization asymmetry ratio. Total 7 Clover HPGe detectors were present at the time of experiment in the INGA-VECC set up. The raw pre-amplifier pulses were processed with digital data acquisition system [33]. The Compton suppressed time stamped list mode data from the Clover detectors were recorded under the trigger condition based on multiplicity (M_γ), set either in singles ($M_\gamma \geq 1$) or in double coincidence ($M_\gamma \geq 2$) mode.

The Standard radioactive sources ^{133}Ba and ^{152}Eu, placed at the target position, were used for the efficiency and energy calibrations of each detector in both the experiments. All the experimental details of these two set up are discussed in chapter 3.

The data of the experiment using VENUS has been sorted with LAMPS [31] sorting and data analysis software. For the digital data from the INGA-VECC campaign, the data were sorted with the IUCPIX sorting package developed by UGC DAE-CSR (Kolkata) [33]. For both the data a symmetric $E_\gamma - E_\gamma$ matrix was generated to verify the coincidence relations of the transitions and analysed with Radware [19] software packages. For the VENUS experiment the $E_\gamma - E_\gamma$ matrix has been gain matched to 0.3 keV/ch after selecting the prompt part of the TAC spectrum of each clover as well as the prompt part of the RF-γ TAC to select the prompt γ-γ coincidence events. The data from the INGA-VECC set up using Digital Signal Processing (DSP) system is gain matched to 0.5 keV/ch for generating the $E_\gamma - E_\gamma$ matrix. An asymmetric DCO matrix was also formed using the data from the two detectors in the backward (30° for VENUS and 55° for INGA-VECC) angle and the detectors at 90° angle to find out the Directional Correlation from Oriented states-DCO ratio (defined in Chapter 3.) as per the prescription in Ref. [22] for various transitions. As per the definition set in the Chapter 3., the typical value of the R_{DCO} for a quadrupole or dipole transition comes out to be 1.0 when gated by a transition of same multipolarity. But when a gate is put on a known quadrupole (dipole) transition, then the DCO ratio value comes out to be close to 0.5(2.0) for dipole (quadrupole) transition. This value of the R_{DCO} is only true when both the γ transitions are stretched and mixing ratio (δ) of the higher multipole order is small. The multipolarity of most of the transitions are found by obtaining their DCO ratio value from the VENUS data and tabulated in Table: 5.1.

The 90° detectors are used for the measurements of Integrated Polarization from Directional Correlation of Oriented states (IPDCO) [23, 24] for assigning the parities of the states. The measurement procedure of the IPDCO ratio (Δ_{IPDCO}) along with the determination of the

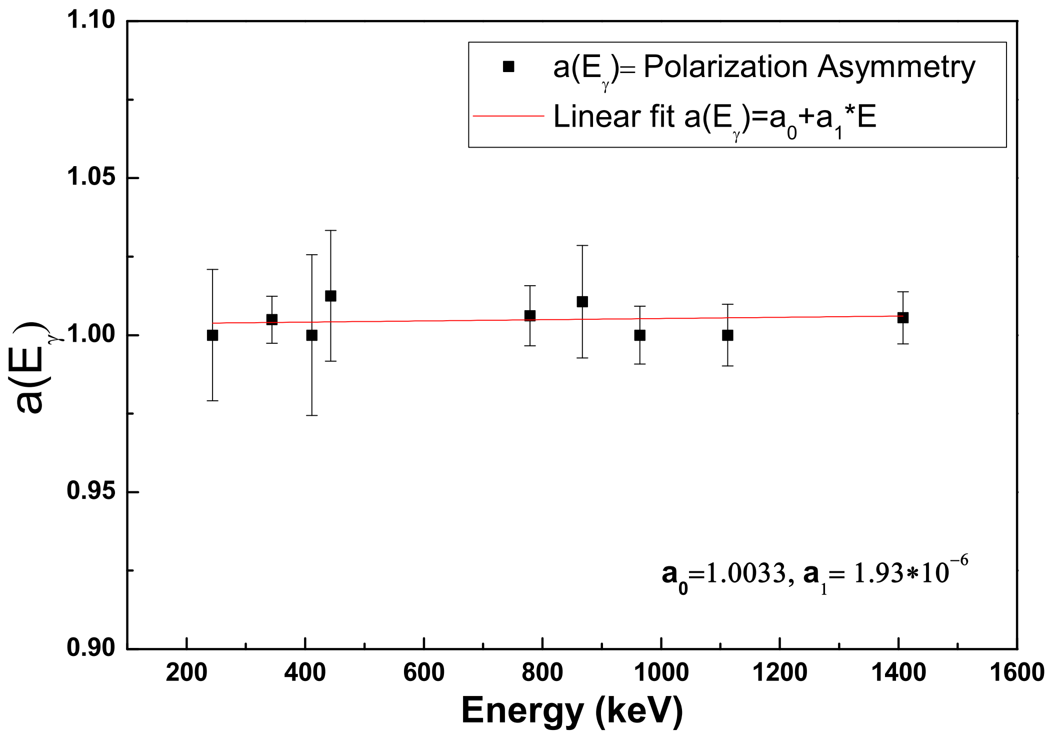

Figure 5.1: (color online) Asymmetry factor from various transitions of standard in ^{152}Eu kept at the target position and Linear fit of that with respect to energy.

Polarization asymmetry parameter a(E_γ) are described in chapter 3. The asymmetry parameter a(E_γ) for the VENUS set up is calculated and described in the chapter 4 in details. As the experimental conditions for the VENUS set up was identical for both the experiments which populates the excited states of ^{199}Tl and ^{199}Hg nuclei, the same asymmetry factor has been used to calculate the IPDCO ratio from the VENUS data.

For the limited numbers of detectors at 90° angle, the Polarization information from the VENUS data were not sufficient to know the nature of the transitions which connects the non-yrast side bands to the yrast main band. For that purpose another experiment with INGA-VECC setup had been performed with more number of detectors at 90° angle. To calculate the Δ_{IPDCO} ratio we have estimated the correction factor, a(E_γ) [$= \frac{N_\parallel}{N_\perp}$] for the INGA-VECC set up. The values of a(E_γ) factor has been calculated for the different energies from a standard ^{152}Eu source and fitted as a function of γ ray energies which is shown in Fig. 5.1. The asymmetry factor is fitted

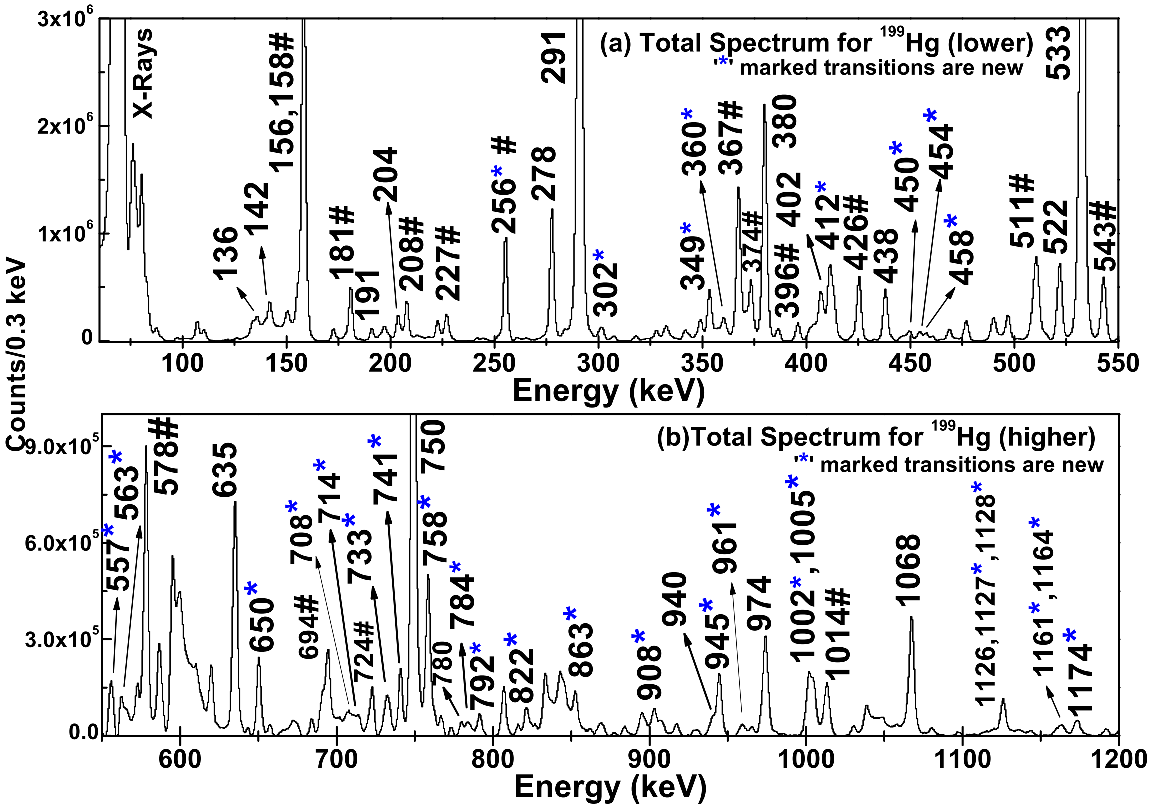

Figure 5.2: Total spectrum of γ transtions detected in singles trigger condition in the reaction ^{198}Pt(α,3n). (a) The lower energy part (upto 550 keV) and (b) the higher energy part (550-1200 keV) of the spectrum. The new transitions observed in the present work are marked with '*'. The other transitions, marked with '#' are the contamination from the excited states of other nuclei

with a linear equation [$a(E_\gamma)=a_0+a_1E_\gamma$] and the fitted values of a_0 and a_1 has been used to determine the Δ_{IPDCO} as prescribed in Chapter 3. For the transitions in ^{199}Hg, Δ_{IPDCO} values are given in Table 5.1.

The DCO ratios and the Δ_{IPDCO} values for different transitions were used to determine the natures (E/M) and multipolarities of the transitions in order to assign the spins and parities (J^π) of the states.

The total projection of the data, obtained with the VENUS set up for the present experiment is shown in Fig. 5.2. The figure is divided into two panels: the upper panel in Fig. 5.2(a) showing the transitions below 550 keV and the lower panel in Fig. 5.2(b) is for the transitions beyond 550 keV up to 1200 keV. The star '*' marked transitions are the new transitions as identified in the present work. It may be noted that most of the transitions are from the ^{199}Hg nucleus whereas few of them (marked with '#') are from the neighbouring (^{198,200}Hg) nuclei which were also produced in the same reaction and from the background radiation contamination.

The coincidence relationships within various transitions in ^{199}Hg are obtained from VENUS as well as INGA-VECC data. Whereas the Spins and the Parities of the states are confirmed from their DCO ratio and Δ_{IPDCO} values from VENUS and INGA-VECC data respectively. The spins and the energies of the initial states along with the corresponding R$_{DCO}$ and Δ_{IPDCO} values of all the transitions belonging to ^{199}Hg are tabulated in Table 5.1.

5.3 Results

The information on the excited states of ^{199}Hg was limited by the data obtained with (α, n) reaction [15, 28] until the recent work done with heavy ion transfer reaction by Negi. *et. al* [29], which populates the excited states of ^{199}Hg up to 8.5 MeV. The latest work have reported the positive parity band based on the $\nu i_{13/2}$ orbital only up to $25/2^+$ spin, whereas the negative parity semi-decoupled band has been extended up to tentative $39/2^-$ spin. The spectroscopic information of ^{199}Hg has been extended significantly in the present work by placing 31 new transitions in the level scheme. The bands, observed in the present work, are marked with B1, B2, B3, B4, B5, B6, B7 and B8 in the level scheme Fig. 5.3 for the convenience of describing them. All the newly observed transitions from the present work are marked with a star '*' mark in Fig. 5.3. The level scheme is formed based on the coincidence relationships among various transitions, their relative intensities, the multipolarities and natures (E/M). Most of the DCO ratio values of the known as well as unknown transitions are found out in the gate of previously known quadrupole (E2) transitions or in the sum gate of them. The newly established quadrupole gate (such as 961 keV, E2 gate) are used to determine the R_{DCO} values of few of the transitions which could not be determined in known quadrupole gate.

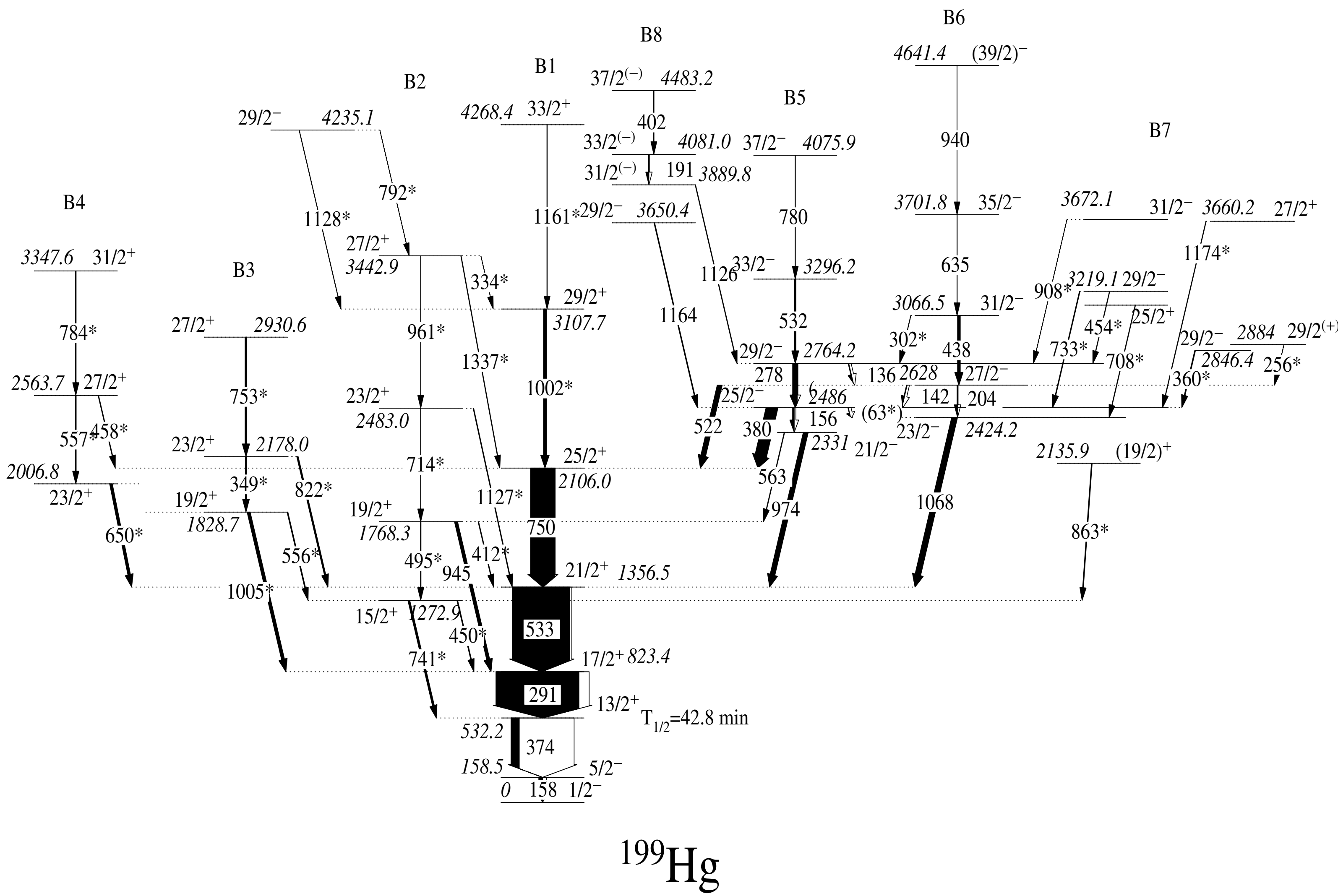

Figure 5.3: Level scheme of ^{199}Hg, as obtained from the present work except the states below 42.8 min isomer (taken from Ref [27]). New transitions are marked as '*'.

The $\nu i_{13/2}$ band in ^{199}Hg is based on a 42.8 min isomer [15] with a $13/2^{+}$ band head. This band is extended up to $33/2^{+}$ spin with the placement of two new transitions 1002 and 1161 keV. The presence of these two transitions can be verified from the total projection in Fig. 5.2 and also from the coincidence gate of the 533 keV transition in Fig. 5.4(a). The coincidence spectrum of newly observed 1002 keV transition in Fig 5.4(b) shows all the transitions which belong to the band B1. The DCO ratio and Δ_{IPDCO} values of these two transitions (1002 and 1161 keV) are listed in Table 5.1 which confirm them as of E2 nature. It has been observed that the intensities of both the transitions after $25/2^{+}$ spin reduced drastically. No other transitions, belonging to the $\nu i_{13/2}$ band (B1) are observed beyond $31/2^{+}$ spin.

A semi-decoupled positive parity band, as also observed in the neighbouring even and odd mass Hg isotopes, are connected to the main band B1 with a set of intense transitions (380, 522, 974 and 1068 keV) and marked in the level scheme as B5 and B6. These bands become yrast beyond $25/2^{+}$ spin. A representative spectrum of the coincidence gate of 278 keV E2 transition, belongs to B5 band has been shown in Figure 5.4(c). Almost all the transitions, belonging to these two bands B5 and B6, can be seen in this figure except 136, 142, 204 and 438 keV transitions, which are placed parallel with 278 keV in the level scheme. The presence of 302 keV transition in the coincidence of 278 keV transitions agrees with the placement of the 302 keV decaying from 3067 keV level to 2764 keV level. The R_{DCO} and Δ_{IPDCO} values of 302 keV confirm it as M1 transition. The band B5 and B6 have been seen to extend up to spin $37/2^{-}$ and $39/2^{(-)}$ respectively. The parities of 3296, 4076 and 3702 keV levels have been confirmed as negative which was tentatively assigned previously [29].

A band like structure, named as B8 in the level scheme 5.3 has been observed to form which is connected to the band B5 and B6 via 1126 and 1164 keV respectively. The R_{DCO} value 0.61 of 1164 keV in a quadrupole (291 keV) gate and the positive value of Δ_{IPDCO} determined the nature of 1164 keV transition as E2 and therefore assigned $29/2^{-}$ spin to the 3650 keV level. The Δ_{IPDCO} value for the 1126 keV transition could not be confirmed from the current data and therefore assumed to be of M1+E2 nature based on its DCO ratio value. Accordingly the spin of the 3890 keV level is assigned as 31/2 and the parity of this level is tentatively assigned as negative, as shown in Fig. 5.3. The 191 keV and 402 keV transitions are found to be of

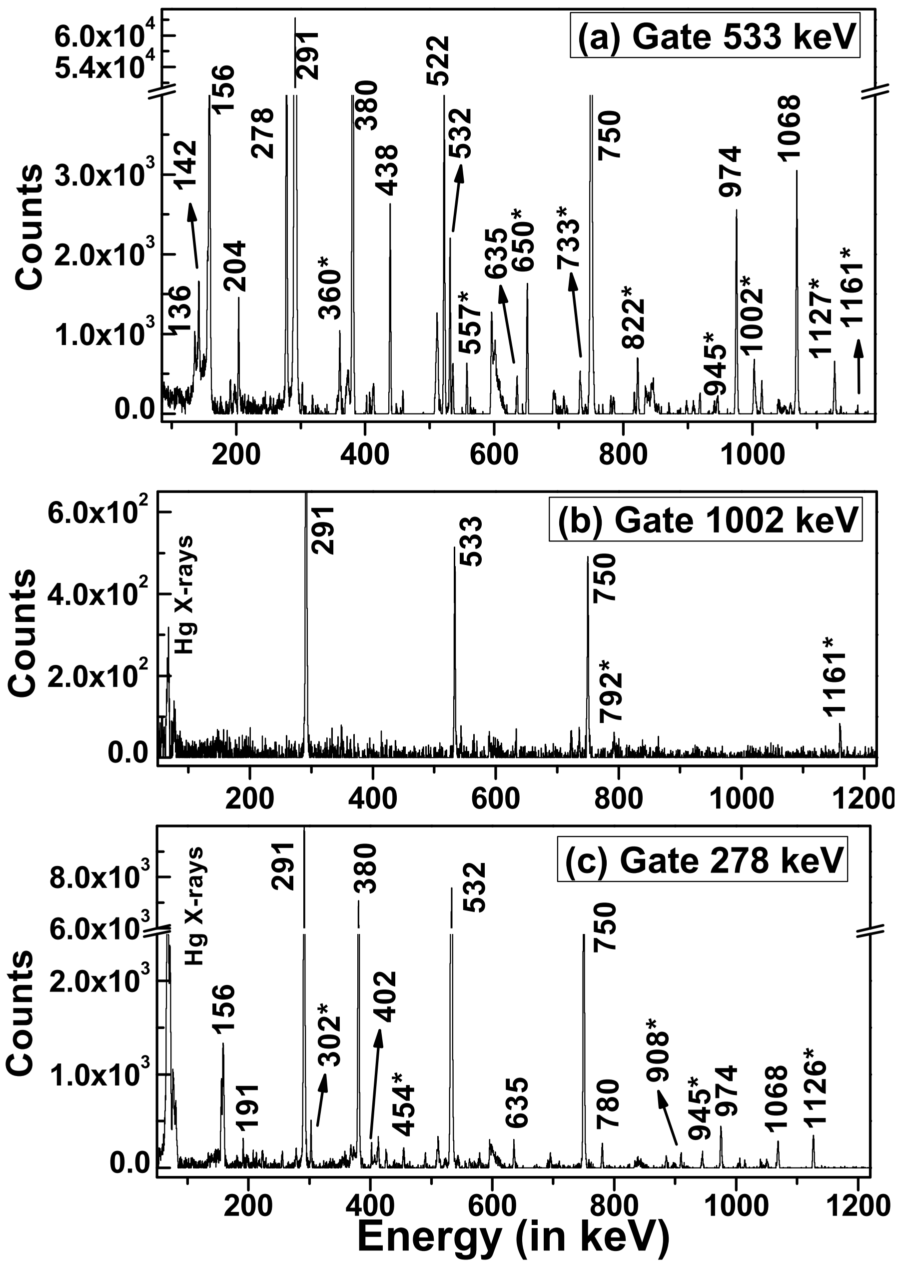

Figure 5.4: Coincidence spectra corresponding to gates of (a) 533 keV, (b) 1002 keV, (c) 278 keV transitions. The first two gated transitions belong to the band B1 and the last one is from the band B5 in ^{199}Hg. '*' marked transitions are newly placed in the level scheme.

M1+E2 and E2 nature, respectively. This band is observed up to 4483 keV excitation energy and 37/2 spin.

A set of newly found discrete levels has been observed in various coincidence gates and marked as B7 in Fig. 5.3. The spins and parities of almost all the levels have been found in suitable gates through DCO ratio and Δ_{IPDCO} values of the decaying transitions from them. Among the new transitions, few of them: 454 keV, 908 keV γ rays can be observed in the coincidence gate of 278 keV in Fig. 5.4(c). These levels mainly decay to the negative parity semi-decoupled structure. All the transitions, belong to this sequence can be observed in the total projection in Fig. 5.2.

Along with the yrast $i_{13/2}$ band, few new non-yrast band structures have also been observed in the present work, marked as band B2, B3 and B4 in Fig. 5.3.

The band marked as B2 is a sequence of three transitions 495, 714 and 961 keV. The presence of these transitions can be verified from Fig. 5.2. The multipolarity of the 961 keV transition has been determined as quadruole as the value of R_{DCO} is obtained as 0.86 from the combined quadrupole gate of 291, 533 and 750 keV. The Δ_{IPDCO} values confirms 961 keV γ ray as of Electric nature. Similarly the 714 keV transition is also found to be of E2 nature from the DCO ratio value in quadrupole gate of 291 keV and the Δ_{IPDCO} value. The DCO ratio values of few transitions of this band have been found in the gate of 961 keV (E2) transitions. The sequence of 495, 714, 961 keV E2 transitions are formed as a band structure (B2) and this band has connecting transitions to the main yrast band (B1) from every level. The 741 keV transition is not in coincidence with any of the transitions in the yrast band (B1) and thus placed just above the isomeric level connecting 1273 keV level to 532 keV level. The lowest spin of band B2 is found to be $15/2^{+}$ from the DCO ratio value 0.58(22) of 741 keV transition in the 961 keV quadrupole gate and positive Δ_{IPDCO} value. The band B2 is found to decay to band B1 through 741, 450, 945, 1127 keV etc. transitions. Among them, the comparatively intense connecting transition, 945 keV has been found to decay from the 1768 keV level. A coincidence gate on 945 keV transition has been shown in Fig. 5.5(a). The presence of 291 keV, 714 keV and 961 keV transitions in coincide with 945 keV confirms the placement of it in the level scheme, decaying from the ($19/2^{+}$ spin) 1768 keV level. Another new 792 keV transition of E1 nature has also been observed in the coincidence spectrum of 945 keV and placed in the top of band B2 indicating different intrinsic configuration than B2 beyond 3443 keV level.

The presence of 792 keV in 1002 keV coincidence gate (Fig. 5.4(b)), confirms the presence of another 334 keV connecting transition from the 3443 keV level of band B2 to the 3108 keV level of band B1.

The spin and parity of the levels of band B2 is dependent on the nature of the connecting transitions from band B2 to band B1. Since the spin-parity assignment of the 1768 keV level is (so as the band B2) dependent on the nature of 945 keV transition, the determination of the multipolarity and type (E or M) of 945 keV transition, is very important. To find out the nature of the 945 keV transition and the delta mixing (δ) of the higher multipole order, the DCO ratio value as well as experimental Δ_{IPDCO} value have been compared with theoretical calculated values for different spin sequences. The DCO ratio value of the 945 keV transition is found to be 0.21(1) in the quadrupole gate of 291 keV transition (see Table 5.1), whereas the Δ_{IPDCO} value is coming out to be 0.015(5).

Different polarization values for 945 keV can be obtained for different possible $J^{\pi}{}_{i}$ to $J^{\pi}{}_{f}$ cases: $21/2^{+/-}$ to $17/2^{+}$, $19^{+/-}$ to $17/2^{+}$ and $17/2^{+/-}$ to $17/2^{+}$, considering different mixing ratio delta (δ) of the 945 keV transition with higher multipole order, following the prescription of Ref. [28]. A χ^2 (δ) analysis [27] from the present experimental data considering polarization measurements of 945 keV transition for different spin sequences was then carried out and is shown in Fig. 5.6. It can be seen from the figure that the χ^2 (δ) is minimum for the case $19/2^{+}$ to $17/2^{+}$. The possible delta (δ) mixing corresponding to this case is -1.5 or -2.2 (corresponding to $\tan^{-1}(\delta)$= -56° and -63°) and also mentioned in the plot. For further verification, different DCO ratio values of 945 keV for this possible spin sequence of $19/2^{+}$ to $17/2^{+}$ have been calculated using the code ANGCOR [26] considering different delta mixing in the 291 keV gate. A plot with calculated DCO ratio value in X axis and calculated polarization value in Y axis for $19/2^{+/-}$ to $17/2^{+}$ spin sequences has been done for comparing the experimental results and shown in Fig. 5.7. It is clear from the Fig. 5.7 that the experimental value matches well with the $19/2^{+}$ to $17/2^{+}$ case and the mixing ratio (δ) value is -1.9 which is also in good agreement with the Fig. 5.6 for $19/2^{+}$ to $17/2^{+}$ case.

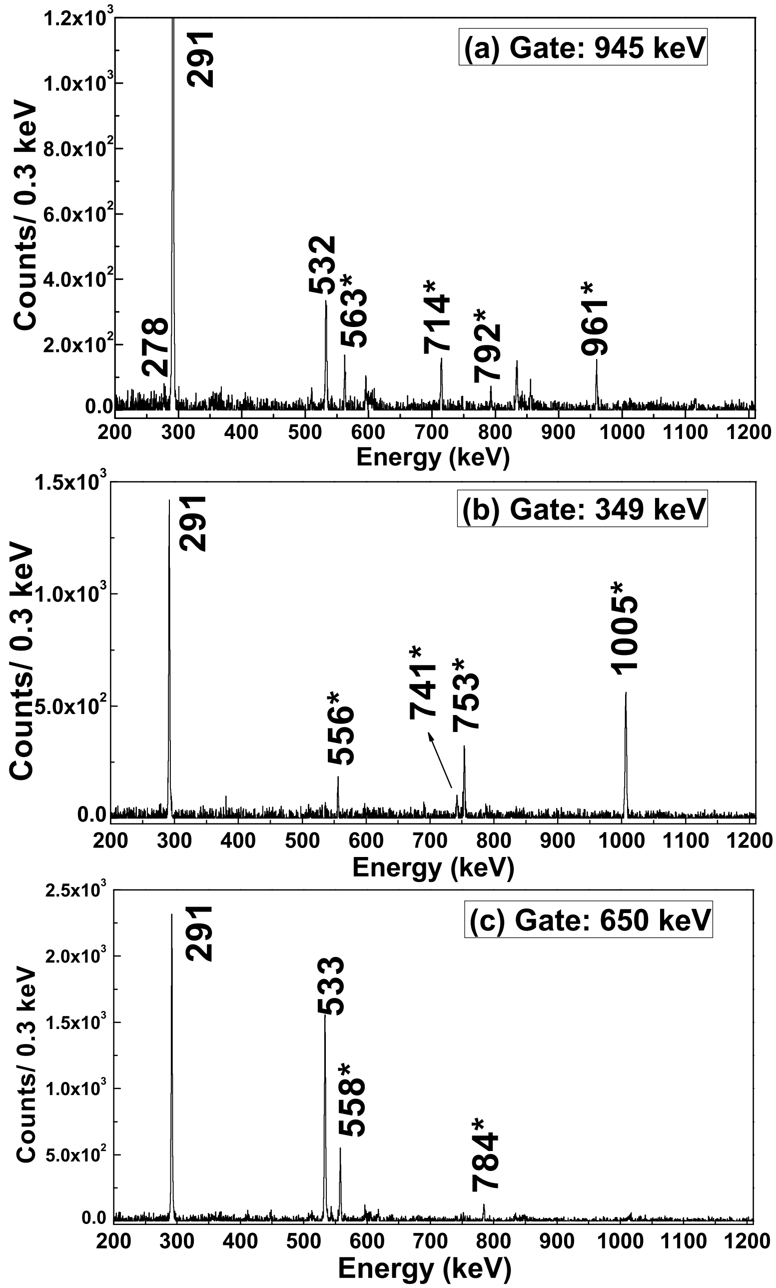

Figure 5.5: Coincidence spectra gated by (a) 945 keV and (b) 349 keV (c) 650 keV transitions corresponding to the band B2, B3 and B4 respectively in ^{199}Hg. '*'marked transitions are newly placed in the level scheme.

Comparing the experimental values of DCO ratio and polarization with theoretically determined values for different spin sequences, 945 keV transition has been found to be of M1+E2 nature

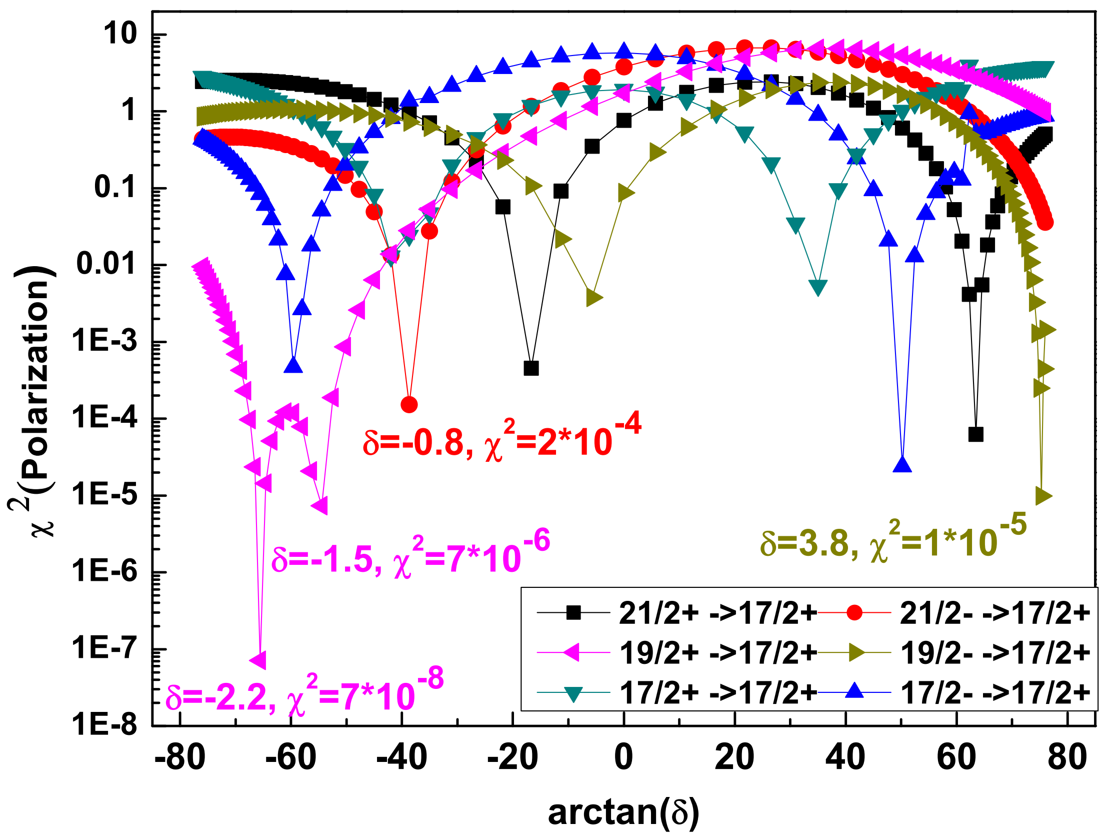

Figure 5.6: $\chi^2(\delta)$ analysis of Polarization of 945 keV transition as a function of arctan(δ).

with mixing $\delta = -1.9$. This mixing value of 945 keV indicates almost 78% of E2 admixture with M1 component and thus the spin and parity of 1768 keV level is fixed at $19/2^+$. Depending on that spin of 1768 keV level and the DCO ratio and Δ_{IPDCO} ratio values of 495, 714 and 961 keV transitions, all the spin-parities of the levels corresponding to band B2 have been confirmed.

Table 5.1: The energies of the γ ray transitions (E_γ), the energies of the initial levels (E_i), the spins and parities of the initial (J_i^π) and final (J_f^π) levels along with the relative intensities (I_γ) , DCO ratios (R_{DCO}) and IPDCO values (Δ_{IPDCO}) for all the transitions in ^{199}Tl from the present work are shown. The proposed multipolarities of the γ rays are also mentioned.

E_γ (in keV)	E_i (in keV)	$J_i^\pi \rightarrow J_f^\pi$	I_γ(Err) [1]	R_{DCO}(Err)	Δ_{IPDCO}(Err)	Deduced Multipol.
63.0(10) [2]	2486	$25/2^- \rightarrow 23/2^-$	-	-	-	(M1+E2)
136.2(3)	2764	$29/2^- \rightarrow 27/2^-$	0.755(10)	0.61(8) [3]	-	(M1+E2)
142.1(3)	2628	$27/2^- \rightarrow 25/2^-$	0.795(10)	0.56(18) [4]	-	(M1+E2)
155.5(4)	2486	$25/2^- \rightarrow 21/2^-$	1.99(5)	1.15(6) [3]	-	(E2)
158.5(1)	158	$5/2^- \rightarrow 1/2^-$	4.64(5)	-	-	E2 [5]
191.2(2)	4081	$33/2^- \rightarrow 31/2^{(-)}$	0.450(5)	0.33(5) [3]	-	(M1+E2)
203.9(2)	2628	$27/2^- \rightarrow 23/2^-$	0.900(10)	1.07(6) [3]	-	(E2)
255.6(3)	2884	$29/2^{(+)} \rightarrow 27/2^-$	0.0500(5)	0.54(3) [3]	-	(E1)
277.9(2)	2764	$29/2^- \rightarrow 25/2^-$	5.600(20)	1.03(1) [3]	0.15(3)	E2
291.2(1)	823	$17/2^+ \rightarrow 13/2^+$	100.00(11)	1.004(3) [4]	0.14(3)	E2
302.4(2)	3067	$31/2^- \rightarrow 29/2^-$	0.210(5)	0.60(7) [3]	-0.13(9)	M1+E2
334.1(10)	3443	$27/2^+ \rightarrow 29/2^+$	0.0600(10)	-	-	M1
349.3(2)	2178	$23/2^+ \rightarrow 19/2^+$	1.305(10)	0.95(8) [9]	0.11(2)	E2
360.4(2)	2846	$29/2^- \rightarrow 25/2^-$	0.920(15)	0.99(6) [3]	0.04(2)	E2
373.7(2)	532	$13/2^+ \rightarrow 5/2^-$	10.0(5)	-	-	M4 [5]
380.2(1)	2486	$25/2^- \rightarrow 25/2^+$	13.75(4)	1.11(1) [3]	-0.18(4)	E1
402.2(2)	4483	$37/2^{(-)} \rightarrow 33/2^{(-)}$	0.400(5)	0.74(11) [6]	0.20(17)	E2
412.0(10)	1768	$19/2^+ \rightarrow 21/2^+$	0.600(10)	0.83(3) [3]	-0.014(5)	M1+E2
438.2(3)	3067	$31/2^- \rightarrow 27/2^-$	3.180(20)	1.01(3) [4]	0.12(3)	E2

Table 5.1: Continued...

E_γ (in keV)	E_i (in keV)	$J_i^\pi \rightarrow J_f^\pi$	I_γ(Err) [1]	R_{DCO} (Err)	Δ_{IPDCO} (Err)	Deduced Multipol.
449.7(3)	1273	$15/2^+ \rightarrow 17/2^+$	0.795(10)	0.34(6) [9]	0.06(2)	M1+E2
454.0(10)	3219	$29/2^- \rightarrow 29/2^-$	0.395(5)	-	0.35(26)	(M1)
457.9(3)	2564	$27/2^+ \rightarrow 25/2^+$	0.590(5)	0.43(6) [3]	-0.18(8)	M1+E2
495.0(10)	1768	$19/2^+ \rightarrow 15/2^+$	0.650(15)	1.02(27) [7]	0.07(4)	E2
522.0(10)	2628	$27/2^- \rightarrow 25/2^+$	5.82(3)	0.456(6) [3]	0.09(2)	E1
532.0(10)	3296	$33/2^- \rightarrow 29/2^-$	1.70(4)	0.99(2) [4]	0.11(3)	E2
533.0(10)	1357	$21/2^+ \rightarrow 17/2^+$	69.20(13)	1.17(4) [8]	0.038(9)	E2
556.1(2)	1829	$19/2^+ \rightarrow 15/2^+$	1.00(5)	-	0.25(14)	(E2)
556.7(3)	2564	$27/2^+ \rightarrow 23/2^+$	0.965(10)	1.02(14) [4]	0.7(3)	E2
562.6(3)	2331	$21/2^- \rightarrow 19/2^+$	0.565(10)	0.35(6) [9]	0.16(5)	E1
635.3(2)	3702	$35/2^- \rightarrow 31/2^-$	0.32(8)	0.95(4) [9]	0.29(11)	E2
650.2(1)	2007	$23/2^+ \rightarrow 21/2^+$	2.945(20)	0.55(2) [9]	-0.005(1)	M1
708.0(1)	3132	$25/2^+ \rightarrow 23/2^-$	0.500(11)	0.39(10) [9]	0.08(4)	E1
714.0(10)	2483	$23/2^+ \rightarrow 19/2^+$	0.465(10)	1.02(25) [9]	0.010(4)	E2
732.9(2)	3219	$29/2^- \rightarrow 25/2^-$	0.755(15)	1.16(6) [3]	0.17(10)	E2
740.8(2)	1273	$15/2^+ \rightarrow 13/2^+$	2.170(10)	0.58(22) [7]	0.014(12)	M1+E2
749.5(2)	2106	$25/2^+ \rightarrow 21/2^+$	29.30(8)	0.92(1) [9]	0.12(2)	E2
752.6(2)	2931	$27/2^+ \rightarrow 23/2^+$	2.05(4)	1.08(7) [9]	0.012(3)	E2
779.7(3)	4076	$37/2^- \rightarrow 33/2^-$	0.355(7)	0.86(11) [6]	0.25(11)	E2
783.9(2)	3348	$31/2^+ \rightarrow 27/2^+$	0.810(5)	0.91(12) [3]	0.26(11)	E2
792.2(3)	4235	$29/2^- \rightarrow 27/2^+$	0.170(5)	0.36(14) [3]	0.17(20)	E1
821.5(3)	2178	$23/2^+ \rightarrow 21/2^+$	1.660(15)	1.13(6) [3]	0.12(4)	M1+E2
863.0(10)	2136	$(19/2)^+ \rightarrow 15/2^+$	0.93(2)	-	0.12(3)	(E2)
907.9(10)	3672	$31/2^- \rightarrow 29/2^-$	0.170(10)	0.25(5) [3]	-0.16(8)	M1+E2
939.6(2)	4641	$(39/2)^- \rightarrow 35/2^-$	0.145(10)	-	0.22(7)	(E2)
944.9(1)	1768	$19/2^+ \rightarrow 17/2^+$	3.60(3)	0.21(1) [9]	0.015(5) [10]	M1+E2

Table 5.1: Continued...

E_γ (in keV)	E_i (in keV)	$J_i^\pi \rightarrow J_f^\pi$	I_γ(Err) [1]	R_{DCO} (Err)	Δ_{IPDCO} (Err)	Deduced Multipol.
960.6(10)	3443	$27/2^+ \rightarrow 23/2^+$	0.38(4)	0.86(15) [3]	0.17(7)	E2
974.2(2)	2331	$21/2^- \rightarrow 21/2^+$	5.80(4)	1.01(2) [3]	-0.08(2)	E1 [5]
1001.7(2)	3108	$29/2^+ \rightarrow 25/2^+$	3.51(4)	0.99(5) [3]	0.14(4)	E2
1004.9(2)	1829	$19/2^+ \rightarrow 17/2^+$	3.55(4)	0.85(3) [9]	0.17(4)	M1+E2
1067.7(1)	2424	$23/2^- \rightarrow 21/2^+$	6.85(4)	0.49(1) [3]	0.05(1)	E1
1125.6(10)	3890	$31/2^{(-)} \rightarrow 29/2^-$	0.540(10)	0.55(5) [6]	-	(M1)
1126.7(10)	2483	$23/2^+ \rightarrow 21/2^+$	0.700(5)	0.34(6) [7]	-	(M1+E2)
1127.6(10)	4235	$29/2^- \rightarrow 29/2^+$	0.270(5)	-	-	(E1)
1160.7(4)	4268	$33/2^+ \rightarrow 29/2^+$	0.420(10)	1.2(4) [9]	0.09(5)	E2
1164.2(3)	3650	$29/2^- \rightarrow 25/2^-$	0.865(15)	0.61(2) [9]	0.18(7)	E2
1174.0(10)	3660	$27/2^+ \rightarrow 25/2^-$	0.455(15)	0.55(8) [3]	0.11(6)	E1
1336.6(10)	3443	$27/2^+ \rightarrow 25/2^+$	0.500(5)	-	-	(M1+E2)

The 1126 keV transition, connecting the sequence B8 with band B5, has already been reported in the earlier work [29]. Along with that, two more transitions of similar energy: 1127 keV and 1128 keV have also been observed in the present work. The presence of the 1127 keV interconnecting transition between band B2 and band B1 from 2483 keV level has been shown

[1] Relative γ ray intensities are estimated from prompt spectra and normalized to 100 for the total intensity of 291.0-keV γ ray.

[2] Unobserved transition, placed depending on coincidence relationship.

[3] From 291.0+533.0+750.0 keV combined (E2) DCO gate;

[4] From 533.0 keV (E2) DCO gate;

[5] The Multipolarity and the spins are adopted from Ref [28]

[6] From 278.0 keV (E2) DCO gate;

[7] From 961.0 keV (E2) DCO gate from INGA-VECC data;

[8] From 1002.0 keV (E2) DCO gate;

[9] From 291.0 keV (E2) DCO gate;

[10] From the VENUS data;

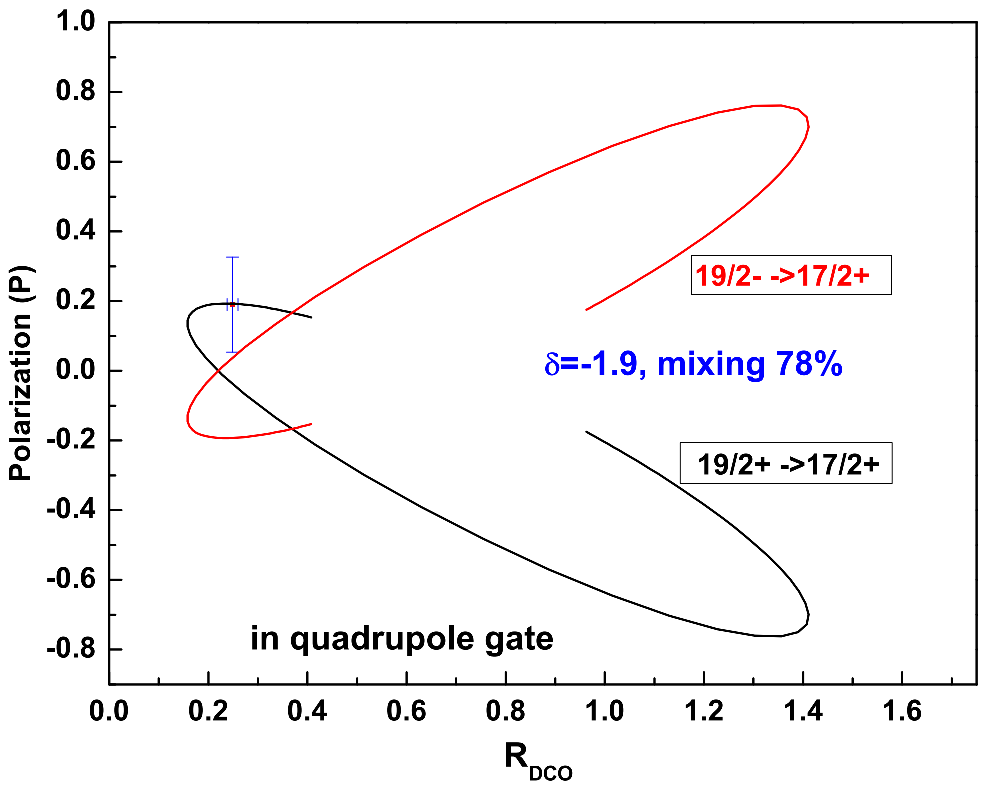

Figure 5.7: The calculated value of R_{DCO} and polarization for two possible spin sequences for the 945 keV considering different mixing ratio δ. The experimental value of the same has also been plotted for comparison.

in the gate of 533 keV in Fig. 5.4(a) which is placed just above 1357 keV level. The DCO ratio values of this 1127 keV transition has comes out to be 0.34(6) in the quadrupole gate of 961 keV (E2). The spin of the 2483 keV level is fixed as $23/2^{+}$ from the E2 nature of 714 keV transition. Therefore 1127 keV transition is happened to decay from $23/2^{+}$ spin to $21/2^{+}$ spin, which, in turn, make 1127 keV to be of highly mixed M1+E2 nature. From the R_{DCO} values listed in Table 5.1 and from the level spins of band B1 and B2, the other connecting transitions decaying from the band B2 to band B1 *e.g.* 450 keV, 412 keV *etc.* are also found to be of M1 nature with high E2 admixture.

Another band structure has been observed in parallel with the band B1 except band B2 from 1829 keV level and named as band B3 in Fig. 5.3. The band has been extended up to $27/2^{+}$

spin with two E2 transitions, 349 keV and 753 keV. The band B3 is connected with band B1 as well as to band B2 with 1005 keV, 822 keV and 556 keV transitions, respectively. The DCO and Δ_{IPDCO} ratio values of 1005 keV are found to be 0.85(3) (in quadrupole gate) and 0.17(4), respectively and the multipolarity is assigned as M1+E2 with a large E2 mixing. Thus the spin of the 1829 keV level has been fixed at $19/2^+$ from the nature of 1005 keV transition. The DCO ratio value of 556 keV transition could not be found from the present data but the IPDCO ratio value indicates it as electric transition. However, the spins of 1829 keV and 1273 keV levels have fixed it as E2 transition. If the multipolarity of 1005 keV was assigned as two (E2) then the spin of the 1829 keV would be $21/2^+$ and therefore the 556 keV γ ray would be of M3 nature, which is quite rare as well as unlikely. This is another reason to assign the multipolarity of 1005 keV as M1+E2. All the transitions belong to the band B3 as well as connecting transitions to band B1 (except 822 keV) and B2 has been shown in the coincidence spectrum of 349 keV in Fig 5.5(b).

The coincidence gate of a newly observed transition 650 keV has been shown in Fig 5.5(c). This transition is found in coincidence with 533 keV as can be observed from gated spectrum of 533 keV in Fig. 5.4(a). But the 750 keV transition is not in the coincidence with 650 keV transition (Fig 5.5(c)), which place the 650 keV transition on the top of 1357 keV level. The gate of 650 keV shows coincidence with newly observed 557 keV and 784 keV transition with it. The DCO and IPDCO ratio values of 557 and 784 keV transitions, listed in Table 5.1, indicate them as E2 transitions. The DCO ratio value of the connecting 650 keV transition is found to be 0.55(2) and the IPDCO ratio value comes out to be negative. Thus the 650 keV transition is turns out to be of M1 character. Therefore the spin of the band head of the band B4 (marked in the level scheme) is fixed at $23/2^+$ and the band has been extended upto $31/2^+$ spin. Another 458 keV transition has been observed to decay from 1564 keV $27/2^+$ level to the main band B1 at 2106 keV level and found to be of M1 character like the 650 keV transition. This band (B4) does not found to have any connections with the other two (band B2 and B3) band in the level scheme.

A single γ ray 863 keV has been found in coincidence with 741 keV transition only and also can be seen in the total projection in Fig. 5.2. It does not appear in any other coincidence gate as can also be seen from the coincidence spectra of 533 keV, 1002 keV or 945 keV *etc.* in Fig 5.4 and Fig. 5.5. So the 863 keV γ ray has been placed to decay from a discrete level at 2136 keV level to 1273 keV level.

Therefore a extended and improved level scheme of ^{199}Hg with respect to the last work is established in the present thesis. The interpretations of the structures of these newly found bands as well as the single particle levels are discussed in the following section.

5.4 Discussion

The level scheme from the present work represents a decoupled positive parity band structure above the $13/2^+$ isomer with a semi-decoupled negative parity band structure built on 2331 keV level in ^{199}Hg. Band structures parallel to the main yrast band have also been established for the first time from the present work, which are marked in the level scheme as B2, B3 and B4. Along with these band structures, a few discrete single particle levels also have been observed (marked as B7) to decay to the semi-decoupled negative parity band. The structure of the bands as well as the discrete levels have been discussed below.

5.4.1 Band B1

The analog of band B1 in ^{199}Hg, based on the high-j $\nu i_{13/2}$ configuration on top of the $13/2^+$ isomer, has been reported in all the odd-A Hg isotopes. For all the lower odd mass Hg isotopes including ^{197}Hg, this band has been observed beyond the band crossing. The band crossing for the $\nu i_{13/2}$ band in all odd mass Hg nuclei, as well as for the ground state band in all even Hg nuclei, are observed after $25/2^+$ and 6^+ spin, respectively. Prior to the present work, the $\nu i_{13/2}$ band in ^{199}Hg was known only up to $25/2^+$ spin. In the present work, this band B1 has been extended up to $31/2^+$ spin with observation of two new E2 transitions. The E (level energy) vs. I (level spin) of band B1 of ^{199}Hg along with the same band in lower odd mass Hg nuclei are plotted in Fig.5.8 and are fitted using the rotor equation

$$E(I) = E0 + m * I * (I + 1),\ where\ m = (\hbar^2/2\mathcal{J})$$

where $\mathcal{J}$ is the moment of inertia and $E0$ is a parameter corresponding to the initial energy of the band. One of the simplistic ways of determining whether a band corresponds to a deformed rotational character, is from the E vs. I plot, which can be fitted with a parabola in the case of a rotational band. The different slopes of the parabola indicate different moments of inertia and hence to the different origins of the band structures. It can be seen from figure 5.8 that the slope of all the fitted curves corresponding to band B1 ($\nu i_{13/2}$ band) in ^{199}Hg and the lower part of other odd Hg nuclei are very much similar. Hence the moment of inertia for the initial part of the bands are same for all the bands. It can be concluded that the band B1 is rotational in nature and originated from the same intrinsic structure, i.e $\nu i_{13/2}$ orbital as the other neighbouring odd mass Hg isotopes. Other than ^{199}Hg all the lower mass Hg isotopes show a different slope in the E vs I plot (as can be seen in 5.8) after $29/2^+$ spin and clearly that corresponds to a different moment of inertia. It is understood from the above observation that all the other isotopes exhibit a different structure after $29/2^+$ spin and in ^{199}Hg nucleus the same $\nu i_{13/2}$ configuration continue up to $33/2^+$ spin.

The aligned angular momentum (i_x) for the $\nu \mathrm{i}_{13/2}$ bands of different odd-A Hg nuclei is shown in Fig.5.9 as a function of rotational frequency ($\hbar\omega$). The $\nu \mathrm{i}_{13/2}$ bands for all the neighbouring odd mass Hg nuclei are showing a band crossing at almost same frequency($\hbar\omega$)$\sim$0.32 MeV except in ^{199}Hg. The i_x plot for this band shows a gain in alignment of more than 9 $\hbar$ for the neighbouring odd-Hg nuclei which can be achieved by breaking a nucleon pair in high-j orbital. Thus the band crossing in all the lower mass odd Hg isotopes is explained as the alignment of a pair of neutrons in the $\nu i_{13/2}$ orbital. Hence, the upper part of this band after band crossing corresponds to a 3-qp $(\nu i_{13/2})^3$ configuration. Unlike other odd mass Hg isotopes, only for ^{199}Hg nucleus, the band crossing has not been seen, which lead the same band continued up to $\hbar\omega \sim 0.55$ MeV (see Fig. 5.9). The band B1 is observed to see a gradual lowering in alignment (i_x) after $25/2^+$ spin which is also the case for the ground state band of ^{200}Hg. The alignment plot for all the neighbouring even mass Hg isotopes are plotted in Fig. 5.9 (lower panel). Starting from ^{190}Hg all the even mass Hg nuclei are experiencing a back-bending after

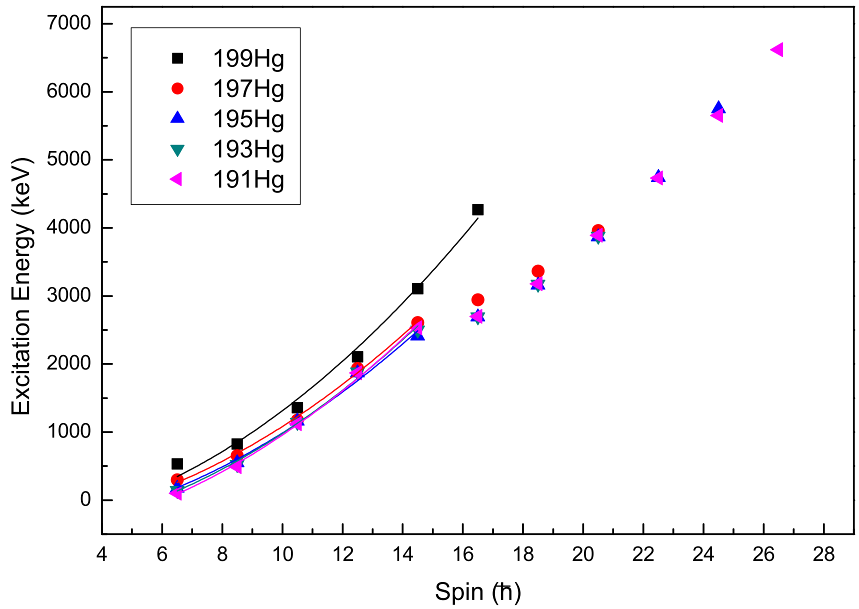

Figure 5.8: Energy vs Spin plot for $\nu i_{13/2}$ configuration B1 band for ^{199}Hg as well as for the analogous band in lower odd mass Hg isotopes. The level energies of the same bands of $^{191-197}$Hg are taken from ref. [42, 18, 15, 22, 28, 17] The solid lines are the fits using the rotational model formula (see text for details).

$\hbar\omega \sim 0.55$ MeV except ^{200}Hg which is interpreted as the same $\nu i_{13/2}$ pair break. One of the possible explanations for the non observation of the neutron pair alignment in $i_{13/2}$ orbital in ^{199}Hg could be Pauli blocking effect. As the $i_{13/2}$ orbital is occupied more and more with the increase of neutron number and approaching $N = 119$ in ^{199}Hg, the last valance neutron is in the Ω=1/2 projection of $i_{13/2}$ orbital in the oblate side (as can be verified from the Nilsson diagram) and the orbital is almost full. So a pair breaking in the last available $\Omega = 1/2$ projection of $\nu i_{13/2}$ orbital is blocked by the last odd neutron in $i_{13/2}$ orbital. The pair breaking in $\nu i_{13/2}$ for the ^{200}Hg is also not possible as the neutron number approaches $N = 120$ for this nucleus and the $i_{13/2}$ orbital is full. The pair breaking in other available orbitals ($\nu f_{5/2}$, $\nu p_{3/2}$ etc.) is probably energetically unfavourable and thus may be expected in higher frequency. The non observance of the transitions beyond $25/2^+$ for ^{199}Hg in previous studies is due to the non-yrastness of the $\nu i_{13/2}$ band beyond this spin. This explanation is supported by the sudden

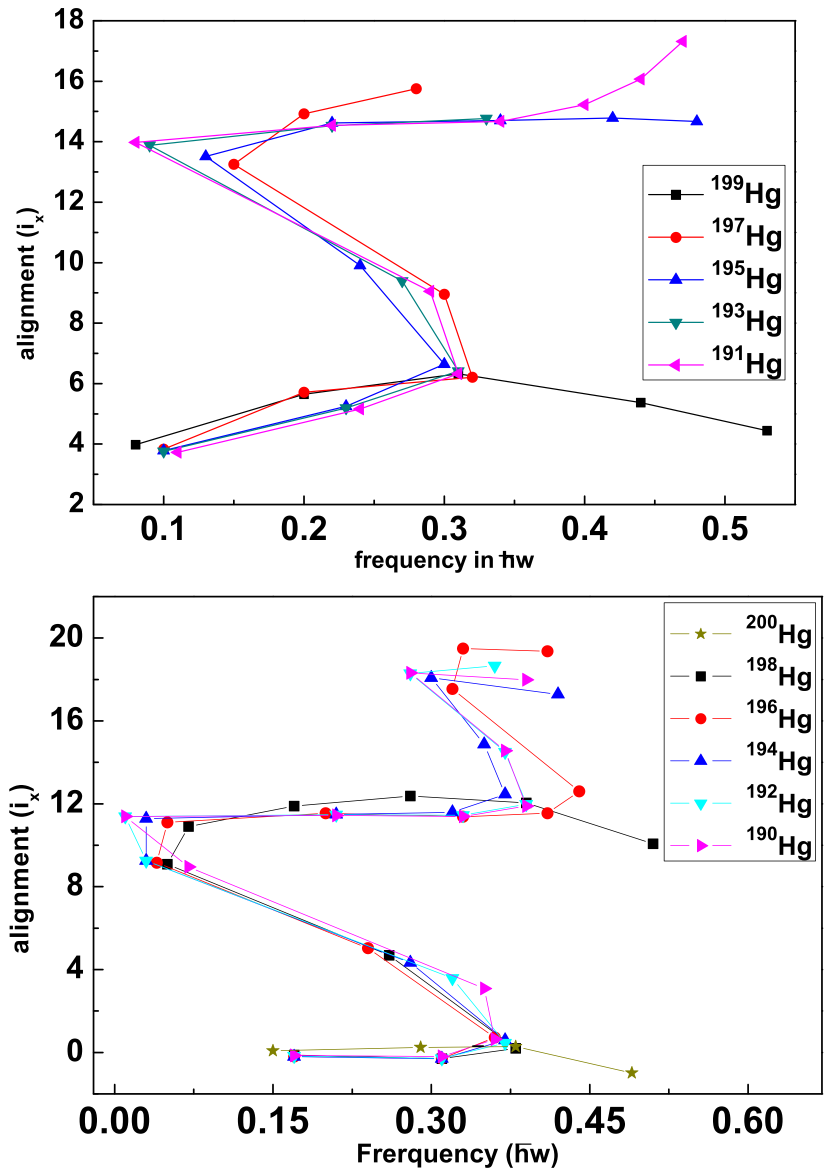

Figure 5.9: upper panel: Alignment plot for the $\nu i_{13/2}$ bands in odd-mass Hg isotopes. lower panel: Alignment plot for the ground bands in even-mass Hg isotopes. The level energies of the same bands of $^{191-197}$Hg are taken from ref. [42, 18, 15, 22, 28, 17]. The level energies of the same bands of $^{190-200}$Hg are taken from ref. [18, 19, 35, 43]. The Harris reference parameters are taken as $J_0 = 8\hbar^2 MeV^{-1} and\ J_1 = 40\hbar^4 MeV^{-3}$.

intensity drop of the transitions (1002 and 1161 keV) decaying from the non-yrast $29/2^+$ and $33/2^+$ levels as found in the present work. The non-yrast states are possible to observe for the first time due to the population of the excited states by light ion induced fusion evaporation process, as employed in the present work.

5.4.2 Band B2

In the present work, the band B2 is newly found as a rotational band with a sequence of E2 transitions 495, 714 and 961 keV as can be seen in Fig.5.3. No states corresponding to this band were observed in the previous studies by Mertin *et. al.* [28] and Negi *et. al.* [29]. Only the 1768 keV level and the transition 945 keV, decaying from that level to band B1 was reported long back in an (α, xn) reaction by Proetel *et. al.* [15]. But no states corresponding to the same band has been observed to decay from or feed to the 1768 keV level in that study.

To find out the structure (or configuration) of the band B2, the excitation energy vs spin plot as well as the aligned angular momentum (i_x), Moment of Inertia (MoI) as a function of rotational frequency ($\hbar\omega$) plot have been shown in Fig.5.10. All of these quantities have been compared with the yrast $\nu \mathrm{i}_{13/2}$ band (band B1). The E (level energy) vs. I (level spin) of the band B1 and band B2 of ^{199}Hg are fitted (see Fig.5.10(a)) using the rotor equation as discussed above. It has been observed that both the bands are nicely fitted with the equation and corresponds to almost same slope and therefore expected to have similar MoI. To verify it, the Kinematic Moment of Inertia (KMI) as well as Dynamic Moment of Inertia (DMI) corresponds to band B1 and B2, have been determined and shown in Fig.5.10(c) and Fig.5.10(d) respectively. Both the plots clearly show that band B1 and band B2 have same Moment of Inertia which quite obviously indicate that both of the bands are of same intrinsic configuration. With the establishment of the band B2 as a rotational band the aligned angular momentum (i_x) of band B2 has also been compared with that of B1, showing similar initial alignment of$\sim$5$\hbar$ which indeed the case for $\nu \mathrm{i}_{13/2}$ band for all other odd Hg isotopes.

To understand further about the partner band B2 with similar characteristics as of the yrast band a literature survey has been done and it has been found that the similar $15/2^+$ state (the band head of band B2) has also been observed in the lower mass odd Hg isotopes $^{191-193}$Hg [18]

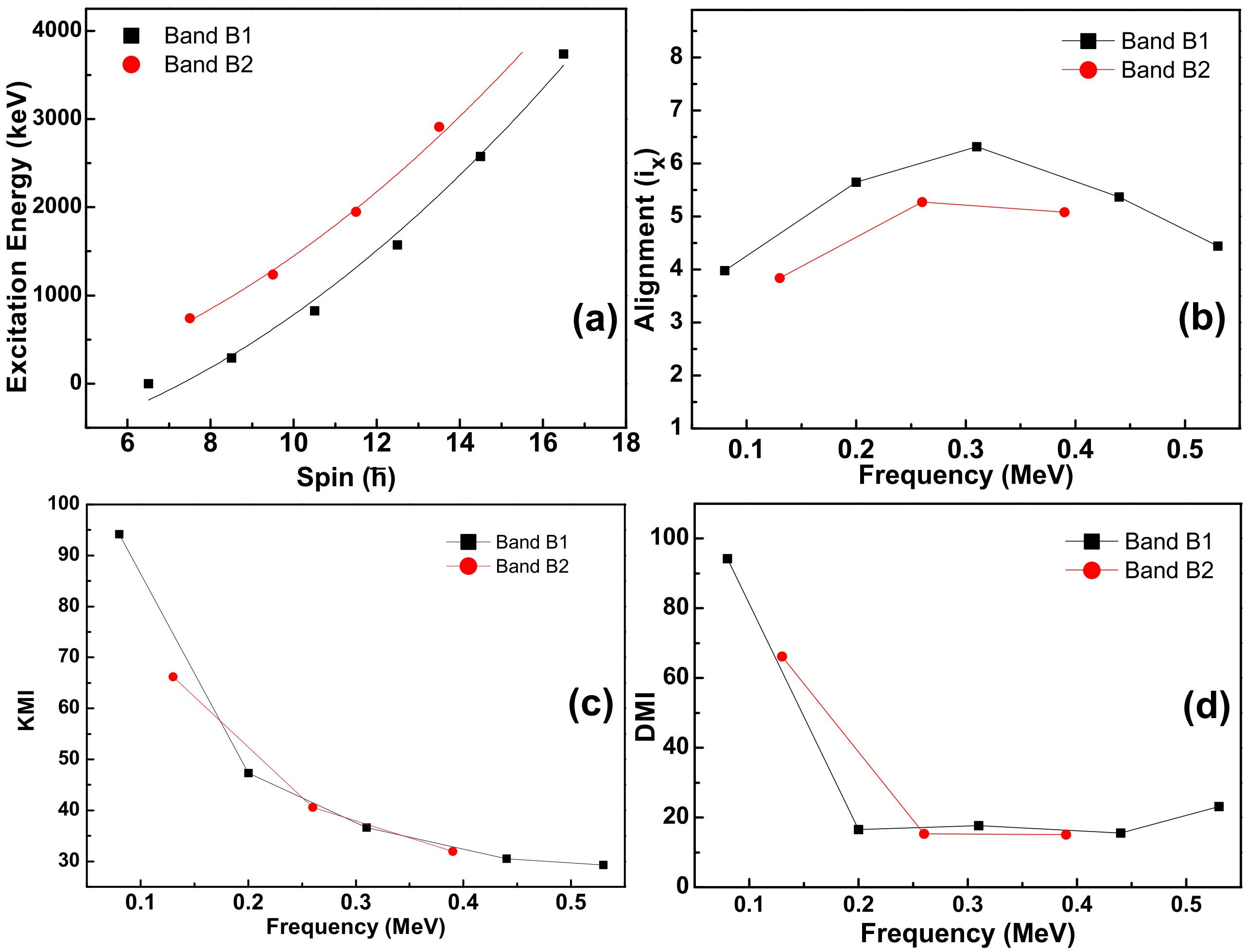

Figure 5.10: Comparison between the Band B1 and B2 of ^{199}Hg nucleus with $\nu i_{13/2}$ configuration. The figure represents the (a) Energy vs Spin plot (b) Alignment plot as a function of rotational frequency (c) Kinematic Moment of Inertia (KMI) as a function of rotational frequency and (d) Dynamic Moment of Inertia (DMI) as a function of rotational frequency. The Harris reference parameters are taken as $J_0 = 8\hbar^2 MeV^{-1} and\ J_1 = 40\hbar^4 MeV^{-3}$.

but nothing was inferred about the characteristics of the states but mentioned as the level of the partner band of the $\nu \mathrm{i}_{13/2}$ band.

Similar partner band has been also observed in odd-A Pt [44, 6] isotopes along with the same $\nu i_{13/2}$ yrast band as in the odd-A Hg isotopes. It may be noted that the odd-mass Pt ($Z = 78$) isotopes just have two proton less than the Hg ($Z = 80$) isotopes and the neutron Fermi level is exactly in the same region as the corresponding odd mass Hg nuclei. So the Hg isotopes are expected to exhibit similar structure as the odd mass Pt isotopes (e.g. the structure of ^{195}Hg is similar to that of ^{193}Pt). The level schemes of ^{191,193}Pt [6] show three levels with J^{π}= $11/2^{+}$, $15/2^{+}$ and $19/2^{+}$ which form a sequence of E2 transitions as inter band transitions and these levels were connected with the main yrast band (the $\nu i_{13/2}$ band) with M1+E2 transitions. A recent study on the Pt isotopes also reports similar kind of structure in ^{195}Pt [44]) but they could only identify J^{π}= $15/2^{+}$ and $19/2^{+}$ levels. These levels are also connected with the yrast band by M1+E2 transitions. Data for ^{197}Pt [44] are too less to confirm any of these side levels. The energy levels of the ^{191,193}Pt were theoretically reproduced by Saha *et. al.* [6] considering Triaxial Rotor Model calculations. The low-lying level structure of $\nu i_{13/2}$ as well as the partner band are remarkably well matched with the experimental results both for ^{191}Pt and ^{193}Pt considering the triaxial parameter γ=30° and quadrupole deformation parameter β_2=0.18. Therefore Khoo *et. al.* and Saha *et. al.* [5, 6]) both suggest that these two nuclei (^{191,193}Pt) have triaxial deformation associated with the $\nu i_{13/2}$ configuration. No such calculations considering triaxial core has been done for ^{195}Pt in Ref. [44] but they have done the Total Routhian Surface(TRS) calculations which suggest energy minimization at γ=-50° at 17/2 $\hbar$ spin associated with the $i_{13/2}$ band. This calculation suggests that the nucleus is not exactly oblate but has a tendency towards triaxiality at higher spin with calculated triaxial parameter γ=-75°. From the above experimental findings, it is therefore very much clear that this mass region, with the involvement of high-j $\nu i_{13/2}$ orbital is very much probable to have the triaxial shapes. The triaxial shape in a nucleus with unpaired proton and/or neutron can be manifested in its level scheme in the form of the appearance of band structures due to chiral symmetry breaking and wobbling motion. In support of that, the recent works on the ^{194,195,198}Tl (Z = 81) nuclei [13, 14, 15] also reported chirality as an experimental signature of triaxiality with the involvement of $\nu i_{13/2}$ orbital. Apart from chirality, another evidence of triaxial shape in nucleus is the wobbling motion and the observation of the corresponding wobbling partner bands. But no evidence of wobbling has been established in mass 190-200 region till date. As discussed above, with the availability of one odd neutron in the high-j $i_{13/2}$

orbital and the possible presence of the triaxially deformed shape, the odd mass Hg nuclei in 190-200 mass region are expected to exhibit wobbling motion.

Wobbling

A triaxial nucleus can have collective angular momentum components along all three principal axes, but generally it rotates around the axis with the largest MoI. Wobbling modes are created when this rotational motion is disturbed by the rotation about the other two principal axes and hence it precesses and wobbles around the axis with the largest MoI. The energy spectra related to the wobbling motion consists of the sequences of two $\Delta I = 2$ identical rotational bands built on different wobbling phonon excitation. These bands are called ($n_\omega = 0$) zero phonon (yrast) band, ($n_\omega = 1$) one phonon (wobbling) band and ($n_\omega = 2$) two phonon band etc. These bands have connections within themselves with $\Delta I = 1$, E2 transitions. Basically, the connecting transitions between the yrast and the wobbling bands should have large mixing of E2 component. The appearance of wobbling motion in even even nuclei are explained by Bohr and Mottelson in Ref. [45]. The wobbling motion has been reported in different mass region (around A$\sim$110, A$\sim$130, A$\sim$160) across the nuclear chart [46, 47, 48, 49, 50, 51, 52, 53, 54]. Among them the ^{135}Pr shows wobbling at low spin [49] and low deformation(ϵ_2=0.16). In almost all of these nuclei, the presence of an odd quasi-particle in high-j orbital modifies the wobbling motion significantly, which provides additional evidence for the triaxial shape. Very recently Frauendorf and Dönau [55] have analyzed the modification of the wobbling behavior semi-classically. According to them, the wobbling mode in an odd-mass nucleus can be characterized in two types, based on the coupling of the angular momentum of the odd particle with triaxial core, called as "transverse mode" and "longitudinal mode". In transverse mode, which is the case for most of the nuclei for which wobbling motion is reported, the angular momentum of the odd particle is perpendicular to the axis with the largest MoI, whereas for "longitudinal wobbling" the odd particle aligns along the medium axis i.e. the axis with the largest MoI. These two different modes of wobbling, transverse and longitudinal can be identified by the decrease or increase of the wobbling energy ($E_{wobb}(I) = \hbar\omega_{wobb}$), as a function of spin(I), respectively. E_{wobb} is defined as

$$E_{wobb}(I) = E(I, n_\omega = 1) - \left(\frac{E(I-1, n_\omega = 0) + E(I+1, n_\omega = 0)}{2}\right) \tag{5.1}$$

In the present work, the band B2 is observed to decay to the band B1 with the 741, 945, 1127 and 1337 keV transitions. The strongest connecting transition, i.e 945 keV, is found to be of highly mixed M1+E2 nature with 78% mixing ($\Delta = -1.9$) as discussed in Results section (see Fig. 5.7). The main experimental signature of wobbling motion, as a $\Delta I = 1$, predominantly E2 connecting transitions between the two wobbling partner bands, has been satisfied as the strongest connecting transitions from band B1 to band B2 are determined to be of highly mixed predominantly E2 nature. From the above analysis, in the present case, the yrast band B1 can be attributed as the ($n_\omega = 0$) zero phonon band whereas the band B2 is assumed to be generated from the $n_\omega = 1$ phonon oscillation. To explore the nature of wobbling motion in ^{199}Hg further, the wobbling energy E_{wobb} (or wobbling frequency $\hbar\omega_{wobb}$) has been plotted as a function of spin (I) for the yrast band (B1) and the partner band (B2) as per the Eq. 5.1 and shown in Fig. 5.11.

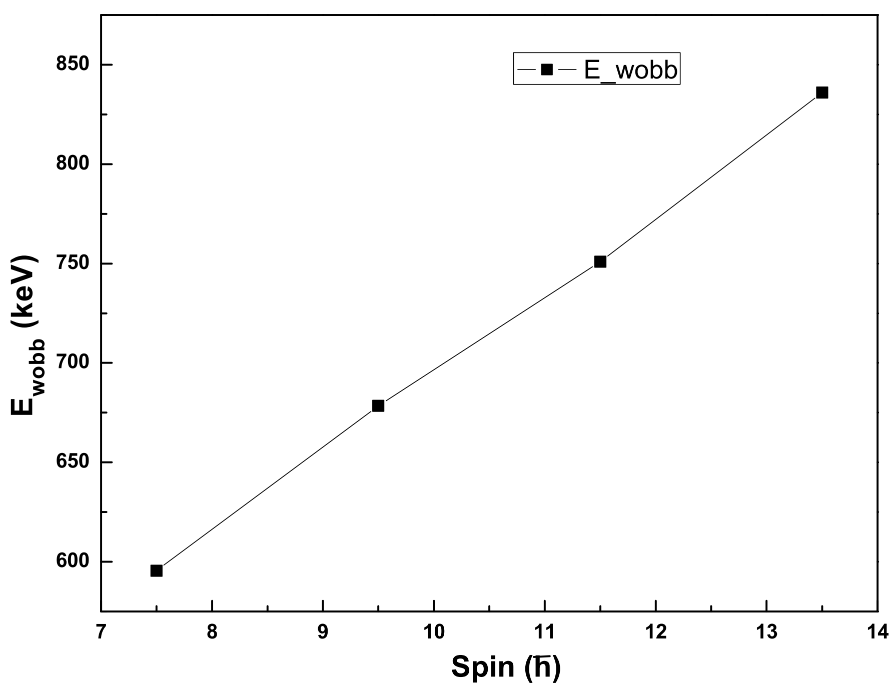

Figure 5.11: The wobbling energy E_{wobb} plot for the $\nu i_{13/2}$ bands in ^{199}Hg.

The increase of the E_{wobb} with increasing spin (I) further indicates the wobbling motion as the longitudinal wobbling. Therefore the band B2 in ^{199}Hg may be a possible wobbling partner of the yrast $\nu i_{13/2}$ band. Other than the strongest 945 keV connecting transition (from band B1 and B2), 741 keV is decaying to the isomeric 532.2 keV level, which barred the determination of it's DCO ratio value in a gate of intense known E2 transition. The DCO ratio value of the 741 keV in a weak 961 keV E2 gate (see Table 5.1) has indicate a mixed M1+E2 nature with a large error included. Two more connecting transitions, 450 keV and 412 keV from the band B2 to band B1 (see Fig. 5.3), have also been observed in the present work, but in this case they are decaying to the higher spin. Similar kind of connecting transitions from the lower spin states of wobbling partner band to the higher spin states of the main band were also seen and reported in the study on ^{105}Pd and ^{135}Pr [46, 49] nuclei earlier. This justify the presence of 450 keV and 412 keV connecting the newly observed possible wobbling partner band B2 to yrast band B1. The determination of mixing ratio of all the other connecting M1+E2 transitions (741, 1127, 1337 keV) would establish the band B2 as the wobbling partner band experimentally, which could not be possible due to limitation of statistics in the current data. If established, then this would be the first observation of wobbling motion in low spin, involving a odd neutron in high-j $i_{13/2}$ orbital in this mass region. The recent work on ^{199}Hg by Negi *et. al.* have not observed the band B2 but they have done a TRS calculation with $\nu i_{13/2}$ configuration. The TRS calculation shows a energy minimization at $21/2\hbar$ spin with the triaxial parameter $\gamma = -69°$ and deformation parameter ϵ_2=0.14 with a indication of increasing triaxiality at higher spin. It will be really interesting to calculate the triaxiality parameter at spin $15/2\hbar$ or less with same configuration to really understand the possibility of having triaxiality in this nucleus at low spin. Further, the theoretical Triaxial Rotor Model calculations is warrented to firmly establish the wobbling motion, leading to the triaxial shape of the ^{199}Hg nucleus.

5.4.3 Bands B3 and B4

The band B4 has been found to be connected with the band B1 by a 1005 keV transition at 823 keV level. This band also has been newly found in the present work as a sequence of E2 transitions, 349 keV and 753 keV with a band head spin-parity of $19/2^+$. The DCO ratio value of 1005 keV in the quadrupole gate of 291 keV has been determined as 0.85(3) and therefore, the transition is found to be as M1 transitions with large δ mixing of higher multipole E2. The band (B3) also have connections to both bands B1 (via highly mixed 1005 and 822 keV transition) and the band B2 (via 556 keV transition) which are identified as the $n_\omega = 0$ phonon and $n_\omega = 1$ phonon bands, respectively, in the previous subsection. In a wobbling motion (as already discussed in the previous subsection) the presence of several rotational bands are expected to exist which corresponds to different phonon vibration state. In the present work the band B3 in ^{199}Hg may correspond to the third wobbling band with $n_\omega = 2$ phonon state but we do not have enough information to confirm this conjecture. The extension of the band B3 up to higher spins would be interesting to infer about the origin of the rotational band.

The band B4 has a band head at $23/2^+$ and the band has been observed to have two E2 transitions (557 keV and 784 keV) which extends the band up to $31/2^+$ spin. This band interacts with the yrast band by M1 transitions. This connecting transitions have lesser E2 mixing as can be seen from the DCO ratio values of them (see Table 5.1). With the above observation, band B4 can be identified as the signature partner band of the yrast $\nu i_{13/2}$ band, but it has not been extended much.

More experimental data is therefore needed to firmly conclude about the nature of these two bands, B3 and B4.

5.4.4 Bands B5 and B6

The occurrence of negative parity band is a common feature of the odd-A as well as even-A Hg isotopes in this mass region with a band head of $21/2^-$ and 5^-, respectively. The negative parity 5^-, 7^- etc. states are generated with an intrinsic structure of two neutrons, one in high-j orbital ($i_{13/2}$) completely decoupled from the core and another one in the opposite parity low-j orbital. The band B5 and the band B6 are the two sequences of negative parity levels with E2 transitions and connected by M1+E2 transitions. These bands are connected with the yrast band (B1) by four intense transitions. Basically, the negative parity bands become yrast after 25/2 spin and the change in parity of these two bands are suggesting a change in configuration. The level structure of these bands is remarkably similar to the structure of the negative-parity bands in the adjacent even Hg isotopes. These bands in the odd-A Hg isotopes are described as semi decoupled bands. The states in this band are generated from the coupling of $i_{13/2}$ neutron with the negative parity states of the neighbouring even Hg isotopes. The 5^- state in even Hg isotopes has the 2-qp configuration of $(\nu i_{13/2}) \otimes \nu(j_-)^1$ where the other neutron is in the available low-j (j_-) $3p_{3/2}$,$3p_{1/2}$ or $2f_{5/2}$ orbital [14]. Hence the configuration of the band B5 and B6 is $(\nu i_{13/2})^2 \otimes \nu(j_-)^1$ where $j_- = f_{5/2}, p_{3/2}, p_{1/2}$.

5.4.5 Bands B7 and B8

Few discrete levels with one or two connecting transitions from each level to the B5 and B6 bands have been established for the first time in the present work. These levels are not forming any regular pattern, considering the spins and parities of the states. Thus the levels are identified as generated from pure single particle structure. Considering the energy of the levels as well as the connections with the negative parity bands, the intrinsic configuration of the levels can be attributed to generate from a 3-qp structure, as in the bands B5 and B6. The different parities and spins of the levels are expected due to the the possibility of different coupling combinations of the $\nu i_{13/2}$, $\nu f_{5/2}$, $\nu p_{3/2}$, $\nu p_{1/2}$ orbitals.

The band B8 was extended extensively in the latest work by Negi *et. al.* and assigned as a tentative positive parity band. In the present work few of the levels of the said band has also been identified but Δ_{IPDCO} value of the connecting transition 1126 keV (DCO ratio indicate the multipolarity as one)could not be determined due to limited statistics. But the spin and parity of the 3650 keV level of band the B8 is assigned as $29/2^-$ from the DCO and Δ_{IPDCO} ratio value of the connecting 1164 keV transition. Thus as apart of the band B8, the spin and parity of the 3890 keV level was tentatively assigned as $31/2^-$ in the present work. These states of the band B8 were assigned +ve parity in Ref [29] and was described as the 3-qp part of band

B1. However, if these states are of -ve parity, as tentatively assigned in this work, then these configuration would not hold.

5.5 Summary

The yrast and near yrast structure in ^{199}Hg have been explored by using the fusion evaporation reaction ^{198}Pt(α,3n) at K-130 Cyclotron, Kolkata with 36 MeV α beam and studied by γ ray spectroscopic techniques. The properties of the excited states of the ^{199}Hg have been studied using two different set ups, VENUS which consists of 6 Compton-suppressed Clover HPGe detectors and INGA with a larger number of Clover detectors in 90° angle for Polarization measurements. The significant extension of level scheme of ^{199}Hg have been done through the observation of new band structure as well as single particle levels via placement of 31 new transitions up to the excitation energy of $\sim$ 4.6 MeV and spin of 19.5$\hbar$. The yrast $\nu i_{13/2}$ band has been extended up to $31/2^+$ spin states for the first time, with no band crossing observed but it has been found that remarkable similarity of the low-lying states in the $\nu i_{13/2}$ band in odd-A Hg nuclei continues to persist in the $N = 119$ isotope. The non-observance of the pair breaking in the $\nu i_{13/2}$ unlike the neighbouring odd mass Hg isotopes is inferred as the Pauli blocking effect of the odd neutron in the last available space in $i_{13/2}$ orbital as the neutron number reach $N = 119$ in case of ^{199}Hg. The similar alignment pattern (like the $\nu i_{13/2}$ band in ^{199}Hg) of the ground state band for the next even-even ^{200}Hg nucleus ($N = 120$) is also supports the fact that non-availability of the $i_{13/2}$ orbital cause the continuation the same band. A non-yrast $\Delta I = 2$, E2 band is observed to appear as a partner of yrast $\nu i_{13/2}$ band and it has been found to decay to the yrast band with a set of $\Delta I = 1$, predominantly E2 transitions. The experimental facts about the multipolarity of the strongest connecting transition are verified with the calculated value and a high δ mixing is determined for the it. The experimental findings therefore, may lead the inference towards the first observation of wobbling bands in this mass region, if established by the theoretical calculations. Since in the neighbouring region is established as a rich ground to find triaxial shapes from the earlier studies, the possibility of the appearance of this kind of exotic structure is expected. The increasing value of E_{wobb} as a function of spin suggests ^{199}Hg nucleus as a possible longitudinal wobbler which involves an odd neutron in high-j $i_{13/2}$ orbital. Along with the observation of $n_\omega = 0$ and $n_\omega = 1$ band, another rotational band has been also identified, but the nature of the band could not be confirmed as $n_\omega = 2$ band or as any other different configuration due to the non observation of that band up to higher spins. Another new partner band with $23/2^+$ band head has been established for the first time and interpreted as the signature partner band of the yrast 1-qp $i_{13/2}$ band.

The negative parity semi-decoupled band has also been observed in the present work and the spins and parities of the states are determined which was tentatively assigned previously. It was confirmed from the spin and parity of the states belong to this band that the same structure $(\nu i_{13/2})^2 \otimes \nu(j_-)^1$ where $j_- = f_{5/2}, p_{3/2}, p_{3/2}$ is continued up to $39/2^-$ spin. The tentatively assigned negative positive parity band B8 is not well developed in the present study to infer the nature of this band. But the non observation of any direct connecting transition from band B8 to the $\nu i_{13/2}$, 1-qp band raise a concern about the assignment of 3-qp $(\nu i_{13/2})^3$ structure to this high spin band by the previous work [29].

More theoretical and experimental work are needed to establish the band B1, B2 and B3 as wobbling bands in this nucleus. If confirmed, this will be the first case in which $n_\omega = 0$, 1 and 2 wobbling phonon excitation would be observed. Also it will be the first of wobbling bands in a nucleus which lies so close to both the proton and the neutron shell closure.

Bibliography

[1] H. Pai *et al.*, Phys. Rev C **85**, 064313 (2012).

[2] P.L. Masiteng *et al.*, Phys. Lett. B **719**, 83 (1988).

[3] T. Roy *et al.*, Phys. Let. B **782**, 768 (2018).

[4] E.A. Lawrie *et al.*, Phys. Rev. C **78**, 021305(R) (2008).

[5] T. L. Khoo, F. M. Bernthal, C. L. Dors, M. Piiparinen, S. Saha, P. J. Daly, and J. Meyer-Ter-Vehn, Phys. Let. **60**, 341 (1976).

[6] S. K. Saha, M. Piiparinen, J. C. Cunnane, and P. J. Daly, Phys. Rev. C **15**, 94 (1977).

[7] A. Covello and G. Sartoris, Nucl. Phys. A **93**, 481 (1967).

[8] I. Hamamoto, Phys. Rep. **10**, No.2, 63 (1974).

[9] K. Heyde *et al.*, Phys. Rep. **102**, No. 5&6, 291 (1983).

[10] S. Nandi *et al.*, Phys. Rev C **99**, 054312 (2019).

[11] Soumik Bhattacharya *et al.*, Phys. Rev. C **98**, 044311 (2018).

[12] Soumik Bhattacharya *et al.*, Phys. Rev. C **95**, 014301 (2017).

[13] S. Das Gupta *et al.*, Phys. Rev C **88**, 044328(2013).

[14] H. Beuscher, W. F. Davidson, R. M. Lieder, A. Neskakis and C. Mayer-Boricke. Phys. Rev. Lett. **32** (1974) 843

[15] D. Proetel, D. Benson, Jr., A. Gizon, J. Gizon, M. R. Maier, R. M. Diamond and F. S. Stephens, Nucl. Phys. A **226** 237 (1974).

[16] D. Proetel, R. M. Diamond and F. S. Stephens, Nucl. Phys. A**231** 301 (1974).

[17] R. M. Lieder *et al.*, Nucl. Phys. A **248**, 317 (1975).

[18] H. Hübel, A. P. Byrne, S. Ogaza, A. E. Stuchbery, and G. D. Dracoulis, Nucl. Phys. A **453**, 316 (1986).

[19] H. Helppi, S. K. Saha, P. J. Daly, S. R. Faber, and T. L. Khoo, Phys. Rev. C **28**, 1382 (1983).

[20] C. Gunther *et. al.* Phys. Rev. C **15**, 1298, (1977).

[21] H. Helppi, S. K. Saha, M. Piiparinen, C. L. Dors and P. J. Daly. Phys. Rev. C **23**, 5, (1981).

[22] N. Nenoff *et al.*, Nucl. Phys. A **629**, 621 (1975).

[23] K. Neergard, P. Vogel, and M. Radomski, Nucl. Phys. A **238**, 199 (1975).

[24] S. W. Yates, J. C. Cunnane, R. Hochel and P. J. Daly, Nucl. Phys. A**222**, 301 (1974).

[25] M. J. Joyce *et al.*, Phys. Let. B **340**, 150 (1994).

[26] C. Ellegaard, J. D. Garrett, O. Denmark and J. R. Lien Nucl. Phys. A **307**, 125 (1978).

[27] G. J. Mathews *et al.*, Phys. Rev C **11**, 2 (1975).

[28] D. Mertin, R. Tischler, A. Kleinrahm, R. Kroth, H. Hübel, and C. Günther, Nucl. Phys. A **301**, 365 (1978).

[29] D. Negi *et al.*, Phys. Rev. C **100**, 014329 (2019).

[30] Soumik Bhattacharya *et al.* DAE Symp. of Nucl. Phys. **61**, 98,(2016).

[31] http://www.tifr.res.in/ pell/lamps.html

[32] Soumik Bhattacharya *et al.* DAE Symp. of Nucl. Phys. **63**, 1156,(2018).

[33] S. Das *et. al.*, Nucl. Instrum. Methods Phys. Res. A **893**, 138 (1995).

[34] D. C. Radford, Nucl. Instrum. Methods Phys. Res. A **361**, 297 (1995).

[35] A. Kramer-Flecken *et al.*, Nucl. Instrum. Methods Phys. Res. A **275**, 333 (1989).

[36] K. Starosta *et al.*, Nucl. Instrum. Methods Phys. Res. A **423**, 16 (1999).

[37] Ch. Droste *et al.*, Nucl. Instrum. Methods Phys. Res. A **378**, 518 (1996).

[38] J.K. Deng *et al.*, Nucl. Instrum. Methods Phys. Res. A **317**, 242 (1992).

[39] L. Peter Ekström and Anders Nordlund, Nucl. Instrum. Methods Phys. Res. A **313**, 421 (1992).

[40] E. S. Macias *et al.*, Comput. Phys. Commun. **11**, 75 (1976).

[41] F. Dönau, Nucl. Phys. A **471**, 469 (1987).

[42] D. Ye *et. al.*, Nucl. Phys. A **537**, 207 (1992).

[43] A. Görgen, *et al.* Eur. Phys. J. A **6**, 141 (1999).

[44] S. G. Wahid *et al.*, Phys. Rev. C **100**, 014328 (2019).

[45] A. Bohr, B. Mottelson, Nuclear Structure, vol. II, Benjamin, Inc., New York, (1975).

[46] J. Timar, *et al.* Phys. Rev. Lett. **122**, 062501 (2019).

[47] S. J. Zhu, *et al.* Int. J. Mod. Phys. E **18**, 1717 (2009).

[48] Y. X. Luo, *et al.* Nucl. Phys. A **919**, 67 (2013).

[49] J. T. Matta, *et al.* Phys. Rev. Lett. **114**, 082501 (2015).

[50] P. Bringel, *et al.* Eur. Phys. J. A **24**, 167 (2005).

[51] S. W. Ødeġard, *et al.* Phys. Rev. Lett. **86**, 5866 (2001).

[52] G. Schönwaβer, *et al.* Phys. Lett. B **552**, 9 (2003).

[53] H. Amro, *et al. Phys.* Lett. B **553**, 197 (2003).

[54] D.J. Hartley, *et al.* Phys. Rev. C. **80**, 041304(R) (2009).

[55] S. Frauendorf and F. Dönau, Phys. Rev. C **89**, 014322 (2014).

Chapter 6

Deformed band structures at high spin in ^{200}Tl

6.1 Introduction

Nuclei with either odd proton or odd neutron near a doubly magic shell closure have proved to be wealthy in understanding the evolution of available orbitals, responsible for the nuclear shapes and structure of excited states in nearby nuclei. The odd-odd nuclei are known to provide access to valuable information for the proton-neutron residual interaction. Near the shell closure the nuclei are expected to execute single particle excitation, whereas the nuclei, in mid shell region rather exhibits collective motions. The nuclei in between, i.e. which are few nucleon away from the doubly magic ^{208}Pb ($Z = 82$ and $N = 126$) are of special interest in this regard to understand the various types of particle-core coupling and collective excitation [1, 2].The interplay of single-particle and collective excitation near a shell closure can be probed by investigation of high spin states of nuclei with few valence nucleons outside the even-even core. In this region the available high-j orbital comes down in energy as a function of deformation and drives the nuclei towards deformation to posses minimum potential energy. In particular, intrinsic states based on intruder orbitals play an important role to study the deformation-driving effects near a shell closure [3]. Odd mass Thallium isotope reflects the effect of single proton on the shape and structure of the core and studied in chapter 4. The evolution of the shapes and structures as a function of angular momentum and excitation energy in Thallium (Tl) isotopes, with only one proton hole and odd number of neutron holes with respect to the ^{208}Pb core, can provide valuable information about the interaction of valence particles with the underlying core, around $Z = 82$.

Spectroscopy of odd-odd Tl isotopes is the subject of many recent experimental investigations. The chain of odd-odd Tl isotopes exhibits a variety of shapes and structures, ranging from simple low-spin single-particle excitations in ^{202,206}Tl [4, 5], to complex configurations involving core excitations in neutron rich ^{204}Tl [6] near ^{208}Pb core. Whereas with a few neutrons away from magic shell closure, oblate deformed band structures based on intruder configuration in $^{190-200}$Tl isotopes [7, 8, 9, 10, 11, 12] have been reported. Observation of some exotic collective structures in Thallium isotopes, like a magnetic rotational band in ^{194}Tl [9], as well as chiral band structures associated with the triaxial deformation in ^{194,195,198}Tl [13, 14, 15] reported from the studies in the recent years, also boosted up the interest of exploration for such kind of a exotic structure in these region. For odd-odd Tl isotopes the ground state spin is 2^- corresponding to the occupation of the $\pi s_{1/2}$ orbital below the $Z = 82$ spherical core and the $\nu p_{3/2}$ orbital below $N = 126$. The $\Omega = 9/2$ projection of intruder $\pi h_{9/2}$ orbital above the $Z = 82$ shell closure is accessible by the odd proton with a small oblate deformation. A remarkable systematics of collective oblate yrast structures based on high-j proton intruder orbital $\pi h_{9/2}$ and neutron orbital $\nu i_{13/2}$ have been observed over a large isotopic chain of Tl nuclei, ranging from neutron deficient ^{190}Tl (N=109) [7] near the mid-shell to ^{200}Tl ($N = 119$) [12] near the shell closure. The configuration of these deformed band structures can be understood from the observation of the presence of collective bands based on high-j orbitals $\pi h_{9/2}$ and $\nu i_{13/2}$ in neighboring odd-A Tl (have only one valance proton) and Hg nuclei (have only one valance neutron) respectively. But in most of those cases, high spin states beyond the first band crossing are not investigated in detail, except in few cases, such as, in ^{194}Tl [9, 13], ^{198}Tl [15]. In ^{200}Tl only a few members of the $\pi h_{9/2} \otimes \nu i_{13/2}$ oblate band structure are known [12] and also in heavier Tl isotopes beyond ^{200}Tl, $\pi h_{9/2} \otimes \nu i_{13/2}$ oblate band could not be observed. As one moves towards $N = 126$ shell closure, the heavier Tl isotopes are expected to have spherical structure and coupled states of ^{208}Pb core with the valence particles are observed. In this regards respect to that, ^{200}Tl is the last nucleus in the odd-odd Thallium chain, after which the single particle excitations take over the collective structures with increasing neutron number. With $N = 119$ i.e. 7 neutrons less than the magic shell closure, thus ^{200}Tl is thus situated on the boundary of collective oblate deformation resulting from deformed Hg core and spherical shape dominated by single particle excitations with respect to the ^{208}Pb core. In addition, the recent observations of chiral partner bands in ^{194}Tl [13] and ^{198}Tl [15] have generated further interest in high spin structure of next odd-odd isotope ^{200}Tl.

Information on the low-spin states in ^{200}Tl come from the study of Electron-capture-decay (EC-decay) of ^{200}Pb [16]. Prior to the present work, the only high spin γ ray spectroscopic information on ^{200}Tl was known from ^{6}Li induced fusion evaporation reaction [12], measured using two Ge(Li) detectors. With the availability of new generation of high resolution, high efficiency detector arrays, more complete information about the detail band structure of ^{200}Tl has become possible to obtain. The present thesis reports the high spin structure of ^{200}Tl beyond band crossing of yrast oblate structure and observation of other near-yrast band structures [17].

6.2 Experiment

The high spin states in ^{200}Tl have been populated by the fusion-evaporation reaction ^{198}Pt(^{7}Li,5n) at the beam energy of 45 MeV, obtained from the BARC-TIFR Pelletron LINAC facility at Mumbai, India. The target used was a 1.3 mg/cm^2 thick ^{198}Pt self-supporting foil with 95.7% enrichment. Other than the dominant fusion evaporation channels resulting to ^{200,201}Tl, significant contributions of ^{198,199}Au and ^{199,200}Hg residues resulting from α and t capture of ^{7}Li beam, having (α+t) cluster structure, were observed in the present experiment. The measurements were carried out with the Indian National Gamma Array (INGA), configured with 15 Compton suppressed Clover HPGe detectors for the present experiment, to detect the γ rays in coincidence as well as in singles mode. The time stamped data were acquired using a

Digital data acquisition system developed by XIA LLC with a sampling rate of 100MHz. Further details of this data acquisition system can be found in Ref [18]. The energy and efficiency calibration of each detector were carried with ^{133}Ba and ^{152}Eu standard sources, placed at the target position. The details of the experimental set up is described in the Chapter 3.

6.3 Data Analysis

The time stamped data obtained with the digital DAQ were sorted using the Multi pARameter time-stamped based COincidence Search (MARCOS) [18] sorting program, developed at TIFR, Mumbai as also mentioned in chapter 3. The symmetric E_γ-E_γ matrix and E_γ-E_γ-E_γ cube were formed using a coincidence window of 400 ns and with the gain of 0.5 keV/channel and 2keV/channel respectively. The analysis of E_γ-E_γ matrices and γ-γ-γ cube were carried out using Radware [19] and INGASORT [20] analysis packages to obtain the coincidence relationships among various transitions. The intensities and different coincidence relationships were utilised further to construct the level scheme.

A representative coincidence spectrum corresponding to the (sum gate of) 119, 217, 230 or 348 keV gamma transitions of the yrast band in ^{200}Tl, obtained from the E_γ-E_γ matrix, is shown in Fig. 6.1. Most of the new transitions placed in the level scheme of ^{200}Tl can be identified from this coincidence spectrum. A total of 60 new transitions in ^{200}Tl have been assigned from the present work. As the gamma ray energies are very similar of those in the residues arising from different incomplete fusion channels, the coincidence relationships were mainly obtained from the double gated spectra generated from the E_γ-E_γ-E_γ cube. In this analysis procedure, the information on yields of complete and incomplete fusion, the capture of various cluster fragments and the particle gated gamma spectra obtained from the same reaction previously [21], have also been utilized for the assignment of γ rays in ^{200}Tl.

The transitions from the nuclei which were produced in the same reaction can be seen from the Fig 6.2. The First panel is showing the total projection from the data taken with "singles" trigger condition. Different dominated channels,like ^{201}Tl and ^{200}Hg which were also produced

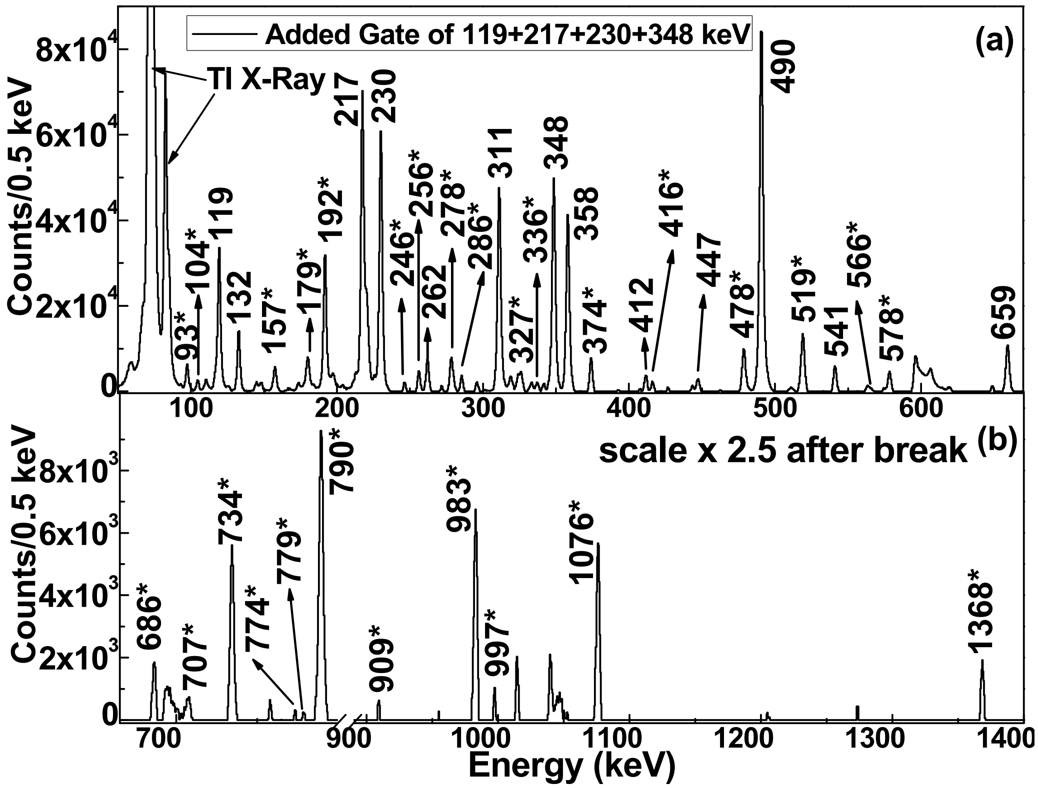

Figure 6.1: Spectrum of γ rays detected in coincidence with the 119, 217, 230 or 348 keV γ transitions. (a) The lower energy part and (b) the higher energy part of the spectrum. The new peaks observed in the present work are marked as '*'.

from the Lithium induced fusion reaction along with the ^{200}Tl nuclei, are shown in different colours. The double gates are showing the transitions corresponding to ^{200}Tl and ^{200}Hg respectively. ^{200}Hg mainly produced by the fusion of break up channel from the ^{7}Li beam and almost all the gamma transitions from the yrast band of ^{200}Hg can be seen from Fig 6.2(c).

The information on the multipolarities of the γ rays were primarily obtained from the analysis of the ratio of Directional Correlation from Oriented states (DCO) [22], for which an asymmetric γ-γ matrix, with 157° (θ_1) and 90° (θ_2) detectors. The definition of R_{DCO} value has been obtained from the assymetric matrix as the definition given in Chapter 3.

The R_{DCO} values are determined for the known E1, E2 and M1 transitions of neighboring Tl, Hg and Au nuclei, populated in the same reaction. For example, in case of ^{201}Tl, populated in

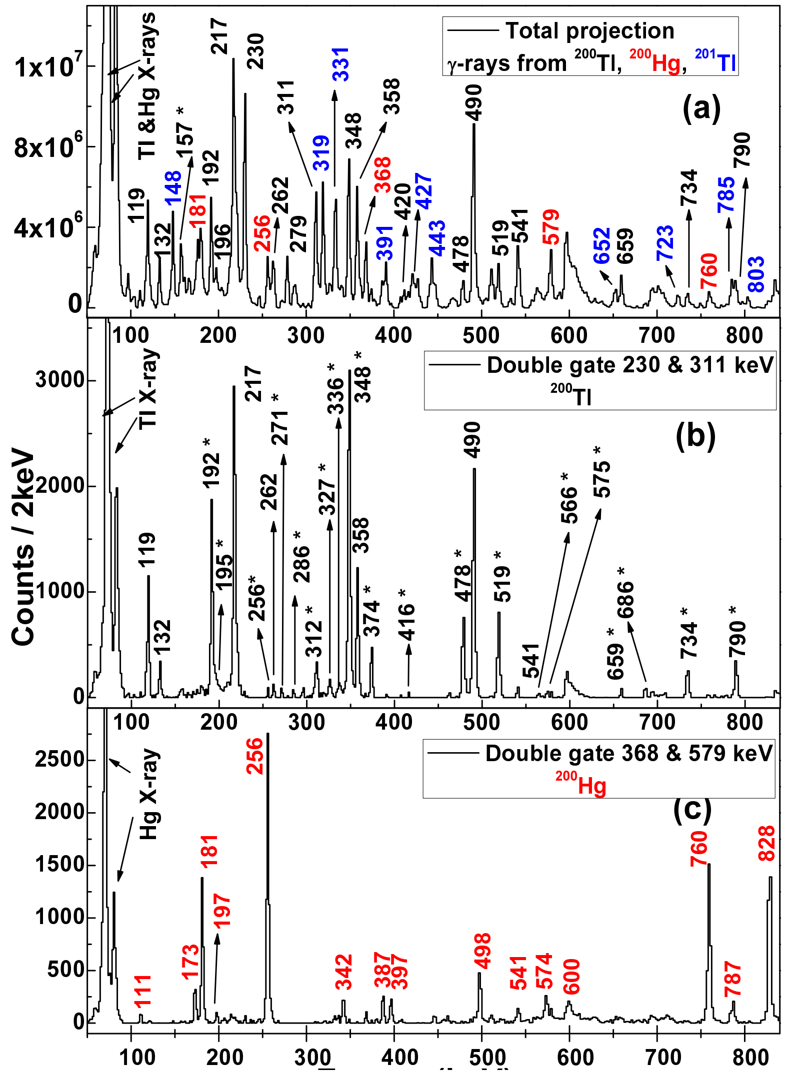

Figure 6.2: (a) Total projection from the experimental data showing the transitons corresponding to ^{200}Tl, ^{200}Hg,^{201}Tl nuclei. Coincidence spectra corresponding to double gates of (b) 230 & 311 keV, (c) 368 & 579 keV transitions from E_γ-E_γ-E_γ cube pertaining to the yrast band of ^{200}Tl and ^{200}Hg respectively. '*' marked transitions are newly placed in level scheme.

the same experiment, the DCO ratio values of the 423 keV (E2) and 120 keV (M1) transitions come out as 1.92(4) and 1.04(14), respectively when gated by the known dipole(E1) transition of 785 keV. From the 652 keV quadrupole (E2) gate, DCO ratio of the 1142 keV (E1) γ-transition comes out as 0.46(4), whereas for 443 keV (E2) transition, the value of R$_{DCO}$ is 0.99(4). Details can be found in the Ref. [17]. So, in the present experimental condition, the values of R$_{DCO}$

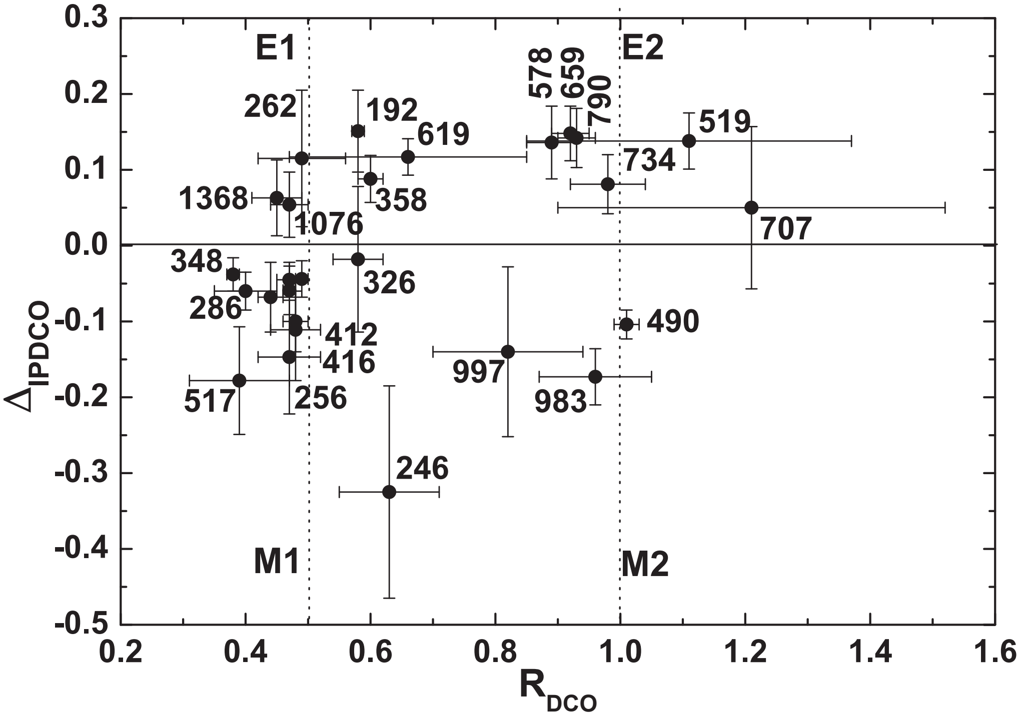

Figure 6.3: DCO ratio vs polarization asymmetry (IPDCO) of various transitions corresponding to ^{200}Tl obtained with different quadrupole gates as indicated. The dotted lines at X-axis correspond to the values for a dipole and quadrupole transitions in a pure quadrupole gate, respectively and are shown to guide the eye. The dotted line at Y-axis is to guide the eye for $+ve$ and $-ve$ values of IPDCO for electric and magnetic transitions, respectively.

come out to be ~ 0.5 (1.0) for pure stretched dipole (quadrupole) transitions when gated with a stretched pure quadrupole transition. On the other hand for a stretched pure dipole gate, in the above set up the values are found to be ~ 1.0 (2.0) for pure stretched dipole (quadrupole) transitions. The multipolarity of various transitions in ^{200}Tl are obtained from the deduced DCO ratios, either from the known quadrupole gate of 659 keV (E2) and dipole gate of 358 keV (E1) or gate of the other deduced dipole or quadrupole transitions, as shown in Table 6.1. As a gating transition, E2 or E1 transitions have been chosen mostly (wherever possible) due to their less mixing probabilities with higher order multipolarity.

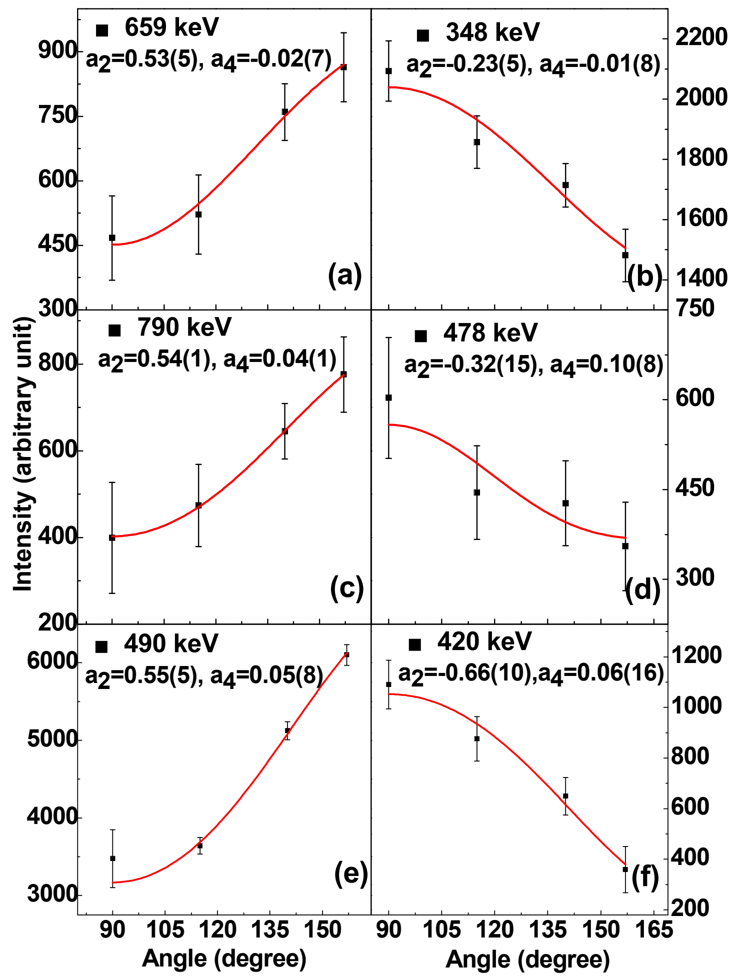

Figure 6.4: Angular distribution of various transitions in ^{200}Tl obtained in the present work. (a),(c),(e) Quadrupole transitions. (b),(d),(f) Dipole transitions.

The polarization information regarding the type (electric or magnetic) of the transitions are determined from the Integrated Polarization Directional Correlation (IPDCO) asymmetry parameter following the prescription of Ref. [23, 24]. The definition of IPDCO asymmetry parameter(Δ_{IPDCO}) is elaborately described in chapter 3 and has been followed to obtain the nature of transitions in the present work. The asymmetry factor $a(E_\gamma)$ as defined in Chapter 3 is the correction factor due to geometrical asymmetry of the INGA detector array w.r.t. the target position. The $a(E_\gamma)$=N$_\parallel$/N$_\perp$ factor has been found out at different γ ray energy from isotropic ^{133}Ba and ^{152}Eu radioactive sources placed at target position. For the present setup,

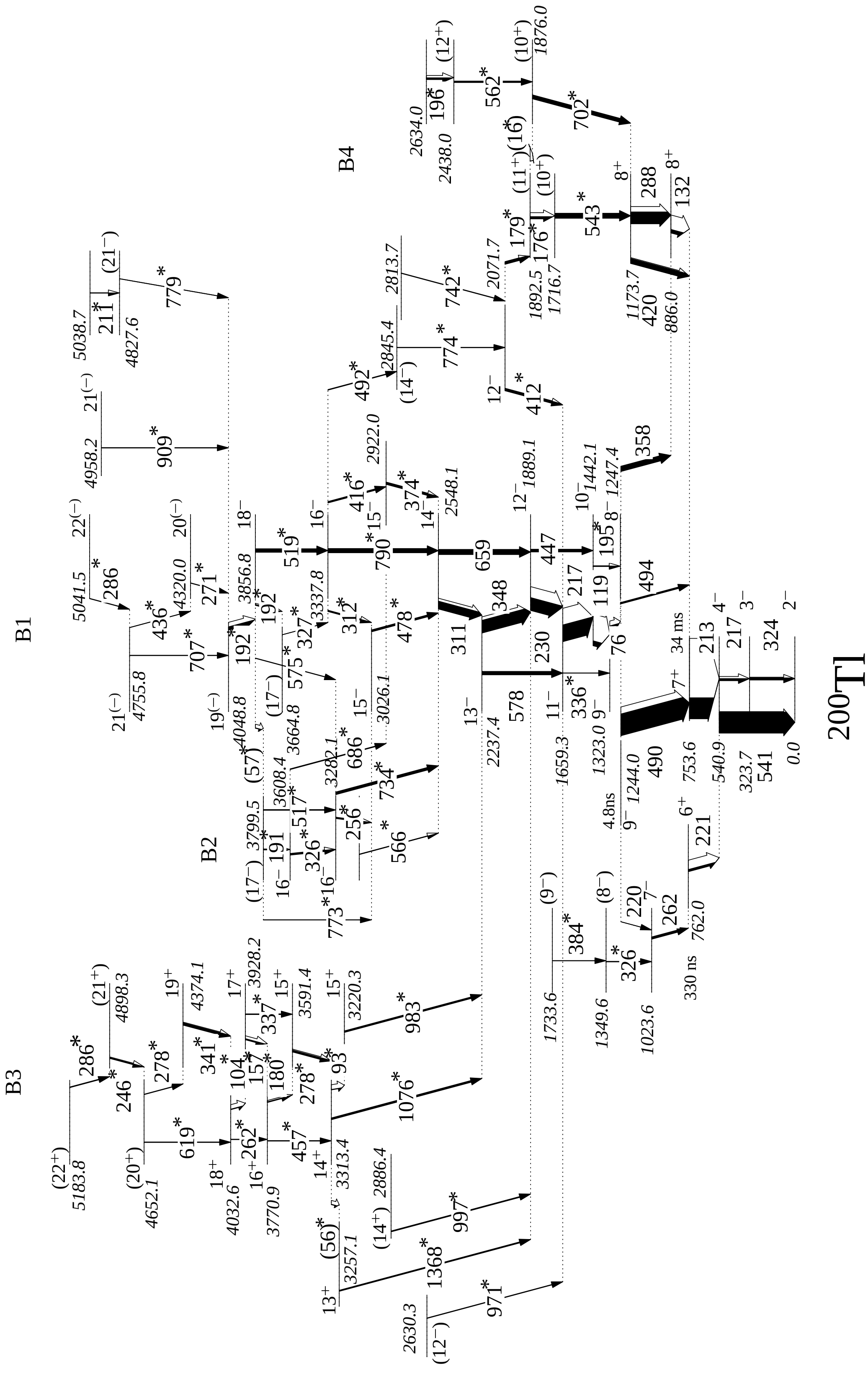

Figure 6.5: Level scheme of ^{200}Tl, as obtained from the present work. New transitions are marked as '*'.

this correction factor was obtained as 1.037(37) from the fitting of its variation as a function of γ ray energy [25]. In order to find the Δ_{IPDCO} ratio, two asymmetric E_γ-E_γ matrices corresponding to parallel and perpendicular scattered events of the 90° Clover detectors were constructed as described in Chapter 3. The positive and negative values of the Δ_{IPDCO}, calculated from the parallel and perpendicular scattering components, correspond to the electric and magnetic transitions respectively. To verify the consistency of the polarization analysis in the present work, the electromagnetic nature of the known transitions in ^{201}Tl,^{199,200}Hg, ^{198,199}Au nuclei, produced in the same reaction, were reproduced from the polarization measurements and the results were found to be in well agreement with the previous results. The deduced Δ_{IPDCO} values for the transitions in ^{200}Tl from the present analysis are given in Table 6.1. The DCO ratio and Δ_{IPDCO} of various known and new transitions are also shown in a separate plot in Fig. 6.3.

For a stretched (I= J_i - J_f, J_i and J_f being the spin of initial and final states and I is the multipolarity of the emitted transition) pure transition, a unique multipolarity and parity of the corresponding state can be assigned from the measurement of R$_{DCO}$ and Δ_{IPDCO}. But, in case of non-stretched ($I < J_i$ - J_f) or mixed transitions, the angular distribution of individual transition along with the polarization measurement is advantageous. The calculated angular distribution coefficients and polarization for different mixing ratio (δ) for various possible spin sequences also need to be compared with the experimental values in order to assign the spin-parity of the corresponding state. For this purpose, the data set taken in singles mode in different angles were fitted with the Legendre polynomial(as described in Chapter 3. Eq. 1.12) to obtain angular distribution of the γ rays, corrected by the detector efficiency for corresponding angle. Angular distribution of some of the known as well as new transitions in ^{200}Tl are shown in Fig. 6.4. Multipolarities of various transitions have been deduced on the basis of both R$_{DCO}$ values and angular distribution, wherever possible.

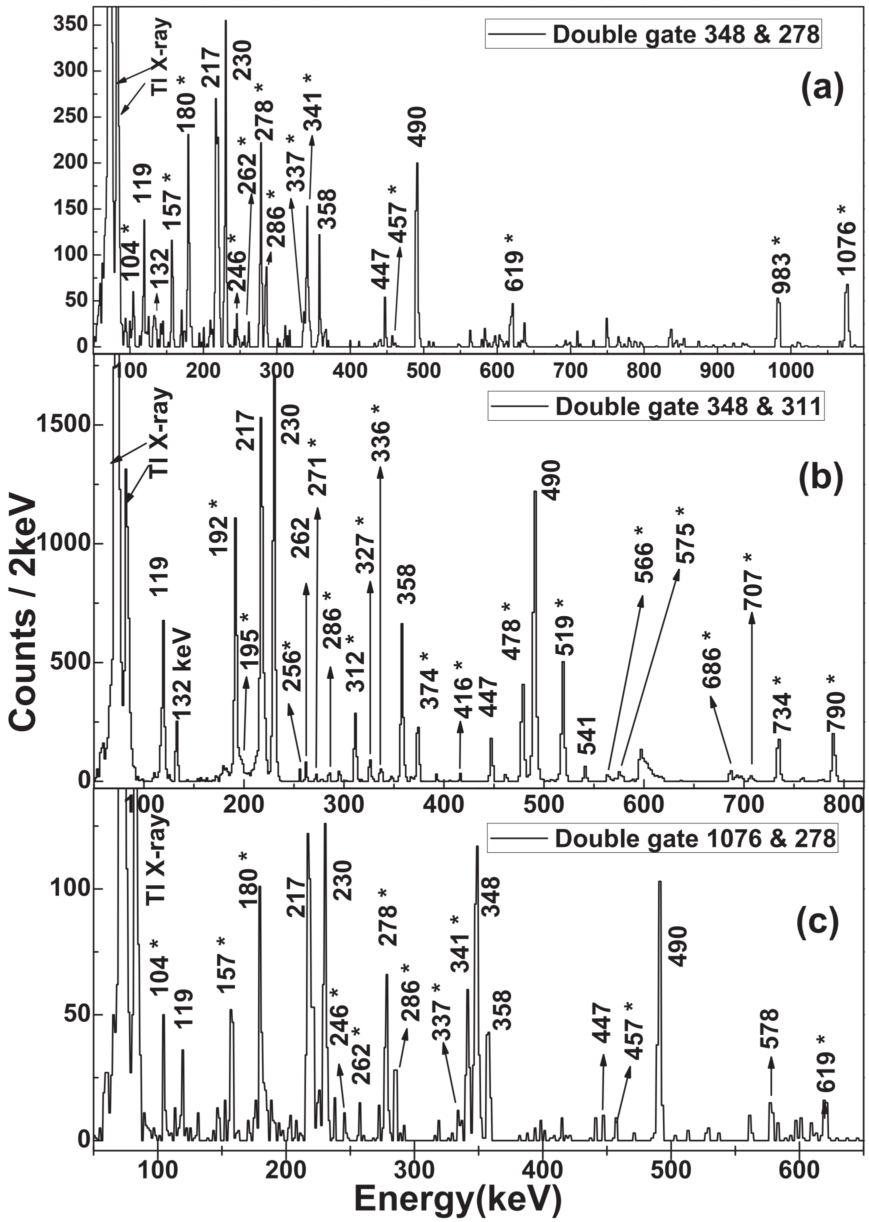

Figure 6.6: Coincidence spectra corresponding to double gates of (a) 348 & 278 keV, (b) 348 & 311 keV, (c) 1076 & 278 keV transitions from E_γ-E_γ-E_γ cube pertaining to the band B1 and B3 in ^{200}Tl. '*' marked transitions are newly placed in level scheme.

6.4 Results

Fig. 6.5 represents the level scheme of ^{200}Tl, obtained from the present work. The construction of the level scheme of ^{200}Tl is based on coincidence relations of the transitions, intensity balance

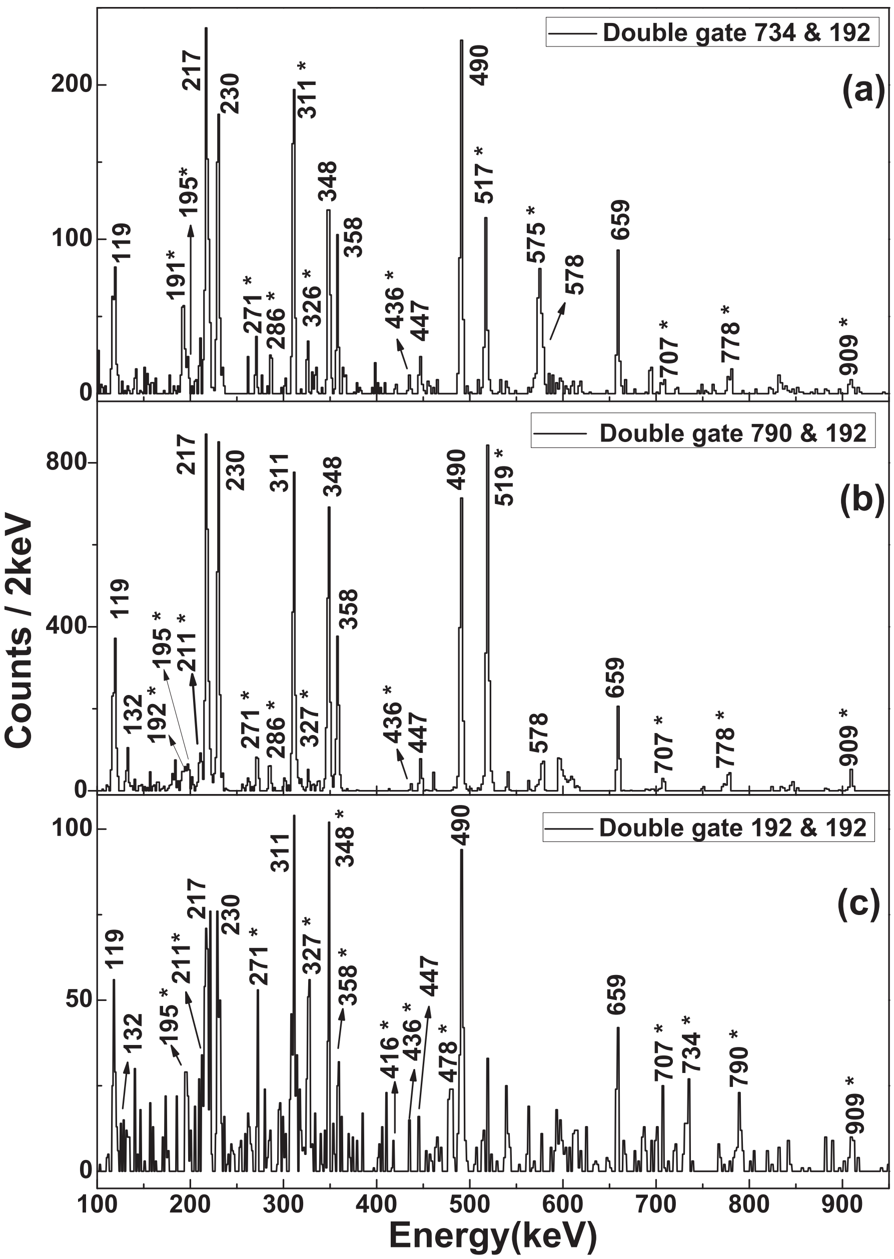

Figure 6.7: Coincidence spectra corresponding to double gates of (a) 734 & 192 keV, (b) 790 & 192 keV, (c) 192 & 192 keV corresponding to the transitions from E_γ-E_γ-E_γ cube of band B1 and B2 in ^{200}Tl. '*'marked transitions are newly placed in level scheme.

of each levels, R_{DCO}, Δ_{IPDCO} values and angular distribution measurements. The transitions up to 2548.1 keV (14^-) level, except a few crossover $E2$ transitions, in the yrast band B1 and transitions up to 1173.7 keV level in band B4 were only known from the previous work by Kreiner *et. al.* [12]. The present level scheme significantly extends the yrast band (B1) compared to earlier work [12] as well as several new band structures (B2, B3 and B4) has been observed. Few new discrete excitate levels have also been observed. A total of 60 new transitions in ^{200}Tl have been identified and placed in the level scheme, which are marked with asterisks in Fig. 6.5. The energies, relative intensities of the γ rays and assigned spin-parity of various levels placed in the level scheme of ^{200}Tl from the present work are tabulated in Table 6.1, along with other relevant quantities. The band sequences B2, B3 are completely new and reported for the first time in the present work. The existence of band B3 and the various connecting transitions between band B1 and B3 can be seen from Fig. 6.6(a-c). The Fig. 6.7(a-c) represents the cascade and parallel sequences pertaining to the new transitions of band B1 reported in the present work. Various new transitions in band B4 and the coincidence relationships among them are represented in Fig. 6.10(a-c).

The band B1 has been extended with the observation of a sequence of new M1+E2 transitions of 478, 312, 327, 192 (doublet), 271 and 286 keV and some of the crossover E2 transitions up to spin (22^-) as shown in Figs. 6.1 and 6.6(b). Placement of a doublet 311-312 keV transitions in the level scheme (Fig. 6.5) could be verified from the existance of another 311(or 312) keV transition in the double gate of 348 & 311 keV and 230 & 311 keV, as shown in Fig. 6.6(b) and Fig. 6.2(b) respectively. Individual intensities of the doublet(311 and 312) have been obtained from their intensities in 490 and 659 keV gates respectively, after proper normalization. Beyond 2548.1 keV (14^-) state few parallel branches have been observed . The 734 keV and 790 keV transitions are parallel to each other as they are not in coincidence. The placement of 478-312 keV and 416-374 keV cascades in parallel to 790 keV transition were established from the coincidence spectrum of 790 keV and 192 keV in fig. 6.7(b). 192 keV transition is present in coincidence with 517, 519, 734 and 790 keV as well as in self coincidence. The presence of cascades 734-192-191 keV and 790-192-192 keV are evident from the double gates shown in Fig. 6.7(a-c). The above observations point towards the multiple placements of 192 keV transition and they are place adjacently from different facts. From Fig. 6.7(a) and (b) it is clear that 790 and 734 keV select parallel cascades with two different transitions of nearby energies of 519 and 517 keV respectively. The separate sets of levels, connected by 734 keV to the band B1 is identified as a separate band structure B2. Fig. 6.7(c) shows that 192-192 keV cascade is in coincidence with both 734 and 790 keV transitions but not with either of 517 or 519 keV transitions. Thus the only possibility to place the second (and third) 191(192) keV transition is in parallel to 517(519) keV. The presence of 327 and 326 keV transitions in coincidence with 790 and 734 keV in fig. 6.7(b and a) respectively confirm the placement of 327-192 keV and 326-191 keV cascades in parallel to 519 (band B1) and 517 keV (band B2) respectively, as shown in Fig. 6.5. The 734 and 790 keV transitions are found to be of pure E2 nature from their R_{DCO} and Δ_{IPDCO} measurements, as clearly seen from Fig. 6.3 and Table 6.1. Thus, the R_{DCO} and Δ_{IPDCO} of 517 and 519 keV transitions were found to be M1 and E2 character from respective coincidence spectra of 734 and 790 keV (E2)transitions. The presence of 191 keV γ ray in the double gate of 734 & 192 keV supports the placement of an unobserved (due to high threshold of 50 keV) 57 keV low energy transition between 3856.8 and 3799.5 keV levels. The band B1 and band B2 are connected to each other via various transitions like 575 keV and 686 keV transition which can be verified from the coincidence double gate of 734 & 192 keV in fig. 6.7(a) and 348 & 311 keV in fig. 6.6(b) respectively. The R_{DCO} and Δ_{IPDCO} of 192 keV, placed between 4048.8 and 3856.8 keV levels could be found from 519 keV (E2) gate, as only this particular 192 keV uniquely is in coincidence with 519 keV transition. The 192-327 keV cascade was found to be very weak and assumed to be of (M1+E2) character as their multipolarities could not be deduced directly from R_{DCO} measurements. The intensities of γ rays placed in the level scheme above 4048.8 keV state of band B1 were relatively weak. All newly placed 271, 436, 707 keV transitions above 4048.8 keV level Other than 286 keV transition (which can be confirmed from added double gate of various transitions) can be seen in the coincidence double gate 192 & 192 keV in fig. 6.7(c). The placement of few discrete levels have been established from the coincidence relations in the present work, decaying through 971, 997 and 1368 keV γ rays, parallel to each other, connecting to the 1659.3 and 1889.1 keV levels respectively of the band B1. Details of the analysis can be found in Ref. [17]

Table 6.1: The energies (E_γ) and relative intensities (I_γ) of the γ rays placed in ^{200}Tl along with the spin and parity of the initial (J_i^π) and the final (J_f^π) states and the energy of the initial state (E_i). The measured values of R_{DCO} and Δ_{IPDCO} are also shown along with the proposed multipolarities of the γ rays.

E_γ (in keV)	E_i (in keV)	$J_i^\pi \rightarrow J_f^\pi$	I_γ(Err) [1]	R_{DCO} (Err)	Δ_{IPDCO} (Err)	Deduced Multipole.
(3.4) [2]	1247.4	$(8^-) \rightarrow (9^-)$	-	-	-	(M1+E2)
(16.5) [2]	1892.5	$(11^+) \rightarrow (10^+)$	-	-	-	(M1+E2)
(56.7) [2]	3856.8	$18^- \rightarrow (17^-)$	-	-	-	(M1+E2)
(56.3) [2]	3313.4	$14^+ \rightarrow 13^+$	-	-	-	(M1)
76.1(1)	1323.0	$9^- \rightarrow 8^-$	-	-	-	(M1+E2)
93.1(3)	3313.4	$14^+ \rightarrow 15^+$	2.04(51)	-	-	(M1)
104.4(2)	4032.6	$18^+ \rightarrow 17^+$	2.19(9)	0.99(18) [3]	-	M1+E2
119.2(1)	1442.1	$10^- \rightarrow 9^-$	19.36(96)	1.11(3) [3]	-	M1
132.4(1)	886.0	$8^+ \rightarrow 7^+$	10.79(54)	1.30(3) [3]	-	M1+E2
157.3(1)	3928.2	$17^+ \rightarrow 16^+$	4.53(17)	0.91(14) [3]	-	M1
175.7(1)	1892.5	$(11^+) \rightarrow (10^+)$	10.56(45)	0.75(12) [4]	-	(M1+E2)
179.2(1)	2071.7	$12^- \rightarrow (11^+)$	11.92(48)	0.82(8) [4]	-	(E1)
179.8(1)	3770.9	$16^+ \rightarrow 15^+$	2.88(14)	1.08(7) [3]	-	M1+E2
191.0(1)	3799.5	$(17^-) \rightarrow 16^-$	-	0.55(4) [5]	-	(M1)
192.0(2)	3856.8	$18^- \rightarrow 17^-$	3.40(19)	-	-	(M1+E2)
192.0(1)	4048.8	$19^{(-)} \rightarrow 18^-$	12.62(66)	0.58(1) [6]	-	(M1+E2)
194.7(1)	1442.1	$10^- \rightarrow 8^-$	2.06(33)	-	-	(E2)
196.0(1)	2634.0	$(-) \rightarrow (12^+)$	1.58(22)	-	-	(-)
211.0(2)	5038.7	$(-) \rightarrow (21^-)$	0.70(15)	-	-	(M1+E2)
213.0(2)	754.0	$7^+ \rightarrow 4^-$	-	-	-	E3 [9]

Table 6.1: Continued...

E_γ (in keV)	E_i (in keV)	$J_i^\pi \rightarrow J_f^\pi$	I_γ(Err) [1]	R_{DCO} (Err)	Δ_{IPDCO} (Err)	Deduced Multipole
217.0(2)	541.0	$4^- \rightarrow 3^-$	-	-	-	M1[9]
217.2(1)	1659.3	$11^- \rightarrow 10^-$	66(3)	0.42(3)[7]	-0.06(3)	M1+E2
220.4(1)	1244.0	$9^- \rightarrow 7^-$	-	0.84(17)[7]	0.35(2)	E2
221.0(1)	762.0	$6^+ \rightarrow 4^-$	-	-	-	(M2)
229.8(1)	1889.1	$12^- \rightarrow 11^-$	51(2)	0.46(1)[7]	-0.04(2)	M1+E2
246.2(1)	4898.3	$(21^+) \rightarrow (20^+)$	3.57(12)	1.08(22)[3]	-0.32(14)	(M1+E2)
256.0(1)	3282.1	$16^- \rightarrow 15^-$	3.34(25)	0.47(7)[7]	-0.15(8)	M1
261.7(1)	4032.6	$18^+ \rightarrow 16^+$	1.53(13)	-	0.06(9)	(E2)
261.6(1)	1023.6	$7^- \rightarrow 6^+$	-	0.49(7)[7]	0.12(9)	E1
271.2(3)	4320.0	$20^{(-)} \rightarrow 19^{(-)}$	0.93(3)	0.33(4)[6]	-	(M1+E2)
278.0(1)	3591.4	$15^+ \rightarrow 14^+$	7.48(25)	0.76(5)[3]	-0.07(5)	M1+E2
278.0(1)	4652.1	$(20^+) \rightarrow 19^+$	1.12(17)	-	-	(M1+E2)
285.5(1)	5183.3	$(22^+) \rightarrow (21^+)$	1.80(11)	-	-0.08(15)	(M1+E2)
285.7(1)	5041.5	$22^{(-)} \rightarrow 21^{(-)}$	0.99(19)	0.40(5)[6]	-0.06(2)	M1+E2
287.7(1)	1173.7	$8^+ \rightarrow 8^+$	56(1)	1.33(5)[4]	0.13(7)	M1 + E2
310.7(1)	2548.1	$14^- \rightarrow 13^-$	31(2)	0.47(2)[5]	-0.05(2)	M1
311.7(1)	3337.8	$16^- \rightarrow 15^-$	3.78(32)	0.39(4)[7]	-	(M1+E2)
324.0(3)	324.0	$3^- \rightarrow 2^-$	-	-	-	M1[9]
326.0(2)	1349.6	$(8^-) \rightarrow 7^-$	-	-	-	(M1+E2)
326.4(1)	3608.4	$16^- \rightarrow 16^-$	1.61(16)	0.58(4)[5]	-0.02(9)	M1+E2
327.0(2)	3664.8	$(17^-) \rightarrow 16^-$	0.34(7)	-	-	(M1+E2)
336.3(3)	1659.3	$11^- \rightarrow 9^-$	2.51(33)	0.89(13)[7]	-	E2
337.0(4)	3928.2	$17^+ \rightarrow 15^+$	-	-	-	(E2)
341.5(1)	4374.1	$19^+ \rightarrow 18^+$	9.40(14)	0.77(13)[3]	-0.15(17)	M1
348.3(1)	2237.4	$13^- \rightarrow 12^-$	50(1)	0.72(1)[3]	-0.04(2)	M1+E2
358.1(1)	1244.0	$9^- \rightarrow 8^+$	36.83(67)	0.60(2)[7]	0.09(3)	E1

Table 6.1: Continued...

E_γ (in keV)	E_i (in keV)	$J_i^\pi \rightarrow J_f^\pi$	I_γ(Err) [1]	R_{DCO} (Err)	Δ_{IPDCO} (Err)	Deduced Multipole
373.9(1)	2922.0	$15^- \rightarrow 14^-$	7.48(38)	0.44(4)[7]	-0.04(4)	M1+E2
384.0(1)	1733.6	$(9^-) \rightarrow (8^-)$	-	-	-	(M1+E2)
412.4(1)	2071.7	$12^- \rightarrow 11^-$	10.12(53)	0.84(20)[3]	-0.10(4)	M1
415.8(1)	3337.8	$16^- \rightarrow 15^-$	4.93(35)	0.48(4)[6]	-0.11(7)	M1
420.0(1)	1173.7	$8^+ \rightarrow 7^+$	23.21(61)	-	0.02(3)	M1+E2
435.8(1)	4755.8	$21^{(-)} \rightarrow 20^{(-)}$	-	-	-	(M1)
447.0(2)	1889.1	$12^- \rightarrow 10^-$	10.49(51)	1.07(8)[7]	0.05(4)	E2
457.3(8)	3770.9	$16^+ \rightarrow 14^+$	1.95(9)	-	-	(E2)
478.0(1)	3026.1	$15^- \rightarrow 14^-$	6.74(49)	0.30(2)[7]	-0.03(3)	M1+E2
490.4(1)	1244.0	$9^- \rightarrow 7^+$	100(4)	1.01(2)[7]	-0.10(2)	M2
492.4(1)	3337.8	$16^- \rightarrow (14^-)$	2.34(18)	0.86(14)[6]	-	(E2)
493.8(7)	1247.4	$8^- \rightarrow 7^+$	5.89(69)	-	-	(E1)
517.4(1)	3799.5	$17^- \rightarrow 16^-$	2.64(14)	0.39(8)[5]	-0.18(7)	M1+E2
519.1(1)	3856.8	$18^- \rightarrow 16^-$	13.86(58)	0.82(4)[8]	0.14(4)	E2
541.0(4)	541.0	$4^- \rightarrow 2^-$	-	-	-	E2[9]
543.1(1)	1716.7	$(10^+) \rightarrow 8^+$	19.77(45)	1.29(19)[4]	0.06(4)	(E2)
562.0(3)	2438.0	$(12^+) \rightarrow (10^+)$	5.73(17)	1.20(17)[4]	-	(E2)
565.9(3)	3114.0	$(-) \rightarrow 14^-$	3.59(43)	-	-	-
574.7(2)	3856.8	$18^- \rightarrow 16^-$	1.36(38)	0.70(11)[5]	-	(E2)
578.3(2)	2237.4	$13^- \rightarrow 11^-$	13.43(63)	1.87(15)[3]	0.14(5)	E2
619.5(3)	4652.1	$(20^-) \rightarrow 18^-$	1.98(9)	-	0.12(2)	(E2)
659.0(1)	2548.1	$14^- \rightarrow 12^-$	20.42(78)	1.02(9)[8]	0.14(4)	E2
686.4(1)	3608.4	$16^- \rightarrow 15^-$	2.93(30)	0.73(11)[7]	-0.10(5)	M1+E2
702.2(2)	1876.0	$(10^+) \rightarrow 8^+$	15.24(78)	0.92(11)[4]	0.11(5)	(E2)
707.2(3)	4755.8	$21^{(-)} \rightarrow 19^{(-)}$	1.57(51)	1.44(25)[6]	0.05(11)	E2
734.4(2)	3282.1	$16^- \rightarrow 14^-$	10.18(53)	0.85(5)[7]	0.08(4)	E2

Table 6.1: Continued...

E_γ (in keV)	E_i (in keV)	$J_i^\pi \rightarrow J_f^\pi$	I_γ(Err) [1]	R_{DCO} (Err)	Δ_{IPDCO} (Err)	Deduced Multipole
742.0(2)	2813.7	$(-) \rightarrow 12^-$	2.80(89)	-	-	(E2)
773.4(2)	3799.5	$(17^-) \rightarrow 15^-$	1.13(17)	-	0.07(3)	(E2)
773.8(2)	2845.4	$(14^-) \rightarrow 12^-$	1.07(9)	1.60(55) [6]	-	(E2)
778.8(2)	4827.6	$21^{(-)} \rightarrow 19^{(-)}$	2.19(22)	1.35(28) [6]	-	(E2)
789.7(1)	3337.8	$16^- \rightarrow 14^-$	16.88(72)	0.85(6) [7]	0.15(4)	E2
909.4(2)	4958.2	$21^{(-)} \rightarrow 19^{(-)}$	1.85(20)	0.85(7) [6]	-	(E2)
971.0(2)	2630.3	$(12^-) \rightarrow 11^-$	1.85(17)	-	-0.21(10)	(M1)
982.9(2)	3220.3	$15^+ \rightarrow 13^-$	5.82(36)	1.82(19) [3]	-0.17(4)	M2
997.3(2)	2886.4	$(14^+) \rightarrow 12^-$	2.42(20)	1.78(59) [3]	-0.14(11)	(M2)
1076.2(2)	3313.4	$14^+ \rightarrow 13^-$	6.97(40)	0.95(10) [3]	0.05(4)	E1
1368.1(2)	3257.1	$13^+ \rightarrow 12^-$	4.23(28)	1.03(13) [3]	0.06(5)	E1

The coincidence of all transitions of band B1 with 490 keV transition (decaying from 1244.0 keV level) confirms the connection of the 1244.0 keV level with band B1. This is evident from the coincidence spectrum of Fig. 6.1, obtained from γ-γ matrix and the double gates shown in Fig. 6.6 and Fig. 6.7. However, the absence of 494 keV from the coincidence gate of 490 keV

[1] Relative γ ray intensities are estimated from prompt spectra and normalized to 100 for the total intensity of 490.4-keV γ ray.

[2] Unobserved transitions

[3] From 358.1 keV (E1) DCO gate;

[4] From 132.4 keV (M1+E2) DCO gate;

[5] From 734.4 keV (E2) DCO gate;

[6] From 519.1 keV (E2) DCO gate;

[7] From 659.0 keV (E2) DCO gate;

[8] From 789.7.0 keV (E2) DCO gate;

[9] Adopted from Ref. [12]

it was also confirmed that 1244.0 and 1247.4 keV levels must be connected by an unobserved 3 keV transition, as also reported in Ref. [12]. In the present work, the spin-parity of 1244.0 keV level with a half life of 4.8 ns has been determined as 9^-, in contrast to the assignment of 7^- by Kreiner et al. [12].

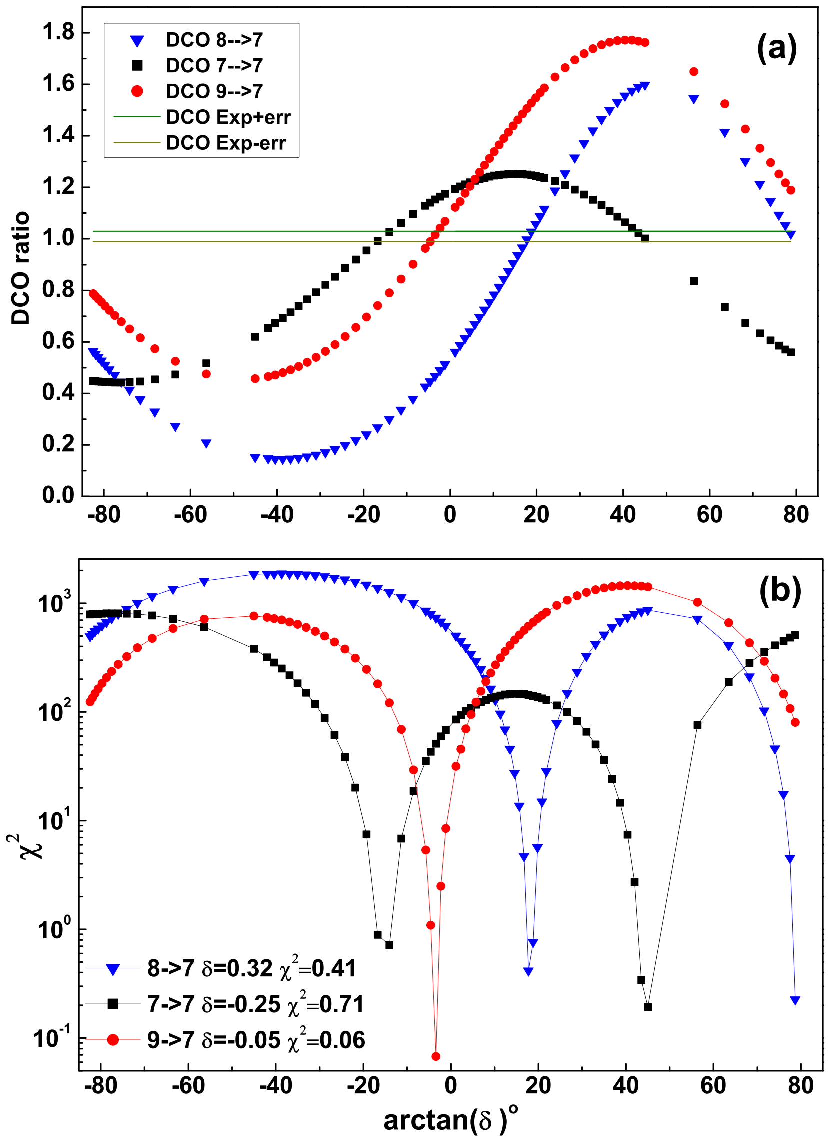

Figure 6.8: a) Different values for DCO ratio for possible spin sequences of 490 keV transition as a function of mixing ratio delta(δ) in a quadrupole 659 keV(E2) transition. b) $\chi^2(\delta)$ analysis of DCO ratio of 490 keV transition as a function of arctan(δ).

The assignment of spin-parity as 9^- to the 1244.0 keV level was based on the DCO ratio and polarization measurements of the decaying 490 keV transition along with the detail analysis of angular distribution data. The DCO ratio of 490 keV transition was obtained from the 659 keV pure E2 gate, as the other dipole transitions below 659 keV in band B1 have mixing of higher multipolarities. The DCO ratio value 1.01(2) of 490 keV transition from 659 keV gate results into a quadrupole character of 490 keV transition. The 230 keV transition in the same cascade of band B1 was found to be of predominantly M1 character from its DCO ratio in 659 keV gate. So the DCO ratio of 490 keV transition was also cross checked from the gate of 230 keV and a value of 2.00(2) was obtained, which also indicate the quadrupole character of 490 keV transition. The measurement of Δ_{IPDCO} of 490 keV transition clearly indicates the 490 keV to be of magnetic character. The values of DCO ratio and Δ_{IPDCO} of 490 keV fall in the $M2$ region in Fig. 6.3. The quadrupole nature of 490 keV is also evident from the independent measurement of its angular distribution data, obtained in singles mode, as shown in Fig. 6.4(e). 490 keV transition decays to the isomeric level 753.6 keV with fixed 7^+ spin and parity.

Since the spin-parity assignment of the 1244.0 keV level is very much dependent on the nature of 490 keV transition, the conclusion about the multipolarity and type (E or M) of 490 keV transition, was obtained by comparing the above experimental data related to 490 keV with various calculations. Depending on the initial state (1244.0 keV) spin and parity different DCO ratio values can be obtained for different possible multipolarity considering mixing delta δ of the 490 keV transition with higher multipolarity. The Different DCO ration value for 490 keV for three possible spin sequences of 7 to 7, 8 to 7 and 9 to 7 have been calculated using the code ANGCOR [26] and considering the multipolarity and spin sequence of all the intermediate transitions between 490 keV and the gateing transition 659 keV and shown in fig. 6.8(a). The DCO ratio with different mixing δ indicate the experimental value to match with 9 to 7 spin sequence for lower delta mixing. For a conclusive result, the chi square minimization calculation [27] has been done and showed in the fig. 6.8(b). It has been established that (9 to 7 transition) quadrupole corresponds to minimum chi-square value of 0.06 with a lesser mixing ratio than the other possible multipolarity.

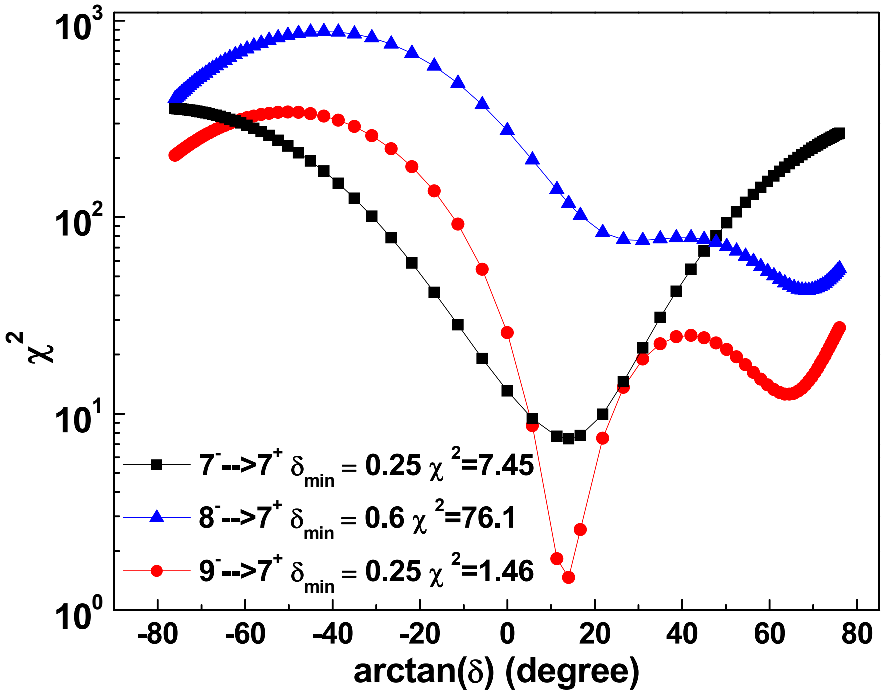

Figure 6.9: $\chi^2(\delta)$ analysis of angular distribution and polarization of 490 keV transition.

To verify further, and have a conclusive assignment of the spin parity of 1244.0 keV level the polarization (P) and angular distribution coefficients (a_2, a_4) were calculated [28] for $J^{\pi}{}_i$ to $J^{\pi}{}_f$ cases of 7^- to 7^+, 8^- to 7^+ and 9^- to 7^+ for various mixing ratios δ. A similar χ^2 (δ) analysis [27] of the present data considering both angular distribution and polarization measurements of 490 keV transition was then carried out and is shown in Fig. 6.9. It can be seen that the χ^2 values of 7.45, 76.12 and 1.46 are obtained for 7^- to 7^+, 8^- to 7^+ and 9^- to 7^+ respectively, resulting into a minimum χ^2 for the case of 9^- to 7^+ with lowest mixing ratio (δ). With the above analysis, it was concluded that the 9^- to 7^+ assignment to 490 keV transition is the most probable one and therefore a spin-parity of 9^- was assigned to 1244.0 keV level. The 9^- assignment to 1244.0 keV level is also consistent with the Weisskopf estimate of half-life of 32 ns for this level in comparison with the reported measured half-life of 4.8 ns. The 220 keV transition, decaying out from this 1244.0 keV level and 262 keV transition, following the 220 keV transition were found to be of E2 and E1 character, respectively, from the present measured values of R_{DCO} and Δ_{IPDCO}. Thus, the spin-parity assignment of 762.0 and 1023.6 keV levels were also modified as 6^+ and 7^- respectively, compared to previous work [12]. The multipolarity of 221 keV transition between 762.0 and 540.9 keV levels could not be determined in this work because of the 330 ns lifetime of the 762.0 keV level. However, the assignment of spin-parity of 6^+ to 762.0 keV level fixes the nature of 221 keV transition as M2 type. The Weisskopf estimate of a half-life of 1.77 μsec for this transition also corroborates well with the measured half-life of 0.33 μsec of this 762.0 keV level. This fact is further consistent with the assignment of spin-parity of 9^- to the 1244.0 keV level. The halflife of the level 1244.0 keV is 4.8ns which is now well reproduce from the Weisskopf estimation for the transition 9^- to 7^+ as 32 ns. All the weisskopf estimated half-lives for the previously assigned and presently assigned spin-parity of the level have been tabulated in Table 6.2. All the calculated half-lives considering the new level scheme is matching with the experimental results.

Table 6.2: The comparison of the experimental half lives ($T_{1/2}$) of different levels of ^{200}Tl with Weisskopf estimation from single particle structure according to the previously assigned and newly proposed spin-parity of the levels.

$Transitions$ (keV)	$Previous$ $(J_i \rightarrow J_f)$	$Weisskopf$ $T_{1/2}\ prev.$	$Proposed$ $(J_i \rightarrow J_f)$	$Weisskopf$ $T_{1/2}\ present$	$Expt.$[1] $T_{1/2}$
213	$7^+ \rightarrow 4^-$(E3)	25 ms	$7^+ \rightarrow 4^-$(E3)	25 ms	25 ms
490	$7^- \rightarrow 7^+$(E1)	1.7 fs	$9^- \rightarrow 7^+$(M2)	32 ns	4.8 ns
220	$7^- \rightarrow 6^+$(E1)	18.5 fs	$9^- \rightarrow 7^-$(E2)	15 ns	4.8 ns
221	$5^+ \rightarrow 4^-$(E1)	18.5 fs	$6^+ \rightarrow 4^-$(M2)	1.77μs	0.33 μs

[1]Experimental half lives are taken from the Ref. [12].

The double gates shown in Fig. 6.6 establish the presence of a band B3, connected to the main yrast band B1 at 2237.4 keV (13^-) level, by 983 and 1076 keV transitions. From fig. 6.6(a) and (b) it can be clearly seen that all the transitions of band B3 are in coincidence with 348 keV transition of band B1, but not with the other higher spin members of the band B1 beyond 2237.4 keV level. The connections of band B3 and band B1, i.e., 983 and 1076 keV transitions can be seen from Fig. 6.6(a) and all other coincident transitions of band B3 are evident from the double gate of 1076 & 278 keV, shown in Fig. 6.6(c). The double placement of 278 keV γ ray is also clear from this spectrum as another 278 keV transition is seen in coincidence. The intensities of 278 keV doublet were estimated by subtracting the intensity of 278 keV transition in the gate of 619 keV from the total intensity with proper normalization. The relative placements and coincidence relationships of the observed transitions of band B3 are checked from gated spectra corresponding to various γ rays. The top most transitions in both band B1 and band B2 is of same energy, 286 keV. The presence of both the transitions in different branch (B1 and B2) can be seen, comparing the double gate of 790 & 192 keV and 1076 & 278 keV in fig. 6.6(c) and in fig. 6.7(b) respectively. These two double gates are selecting two different path but both have 286 keV in coincidence. The 1076 keV transition is found to be of E1 type from R_{DCO} and Δ_{IPDCO} measurements, as shown in Table 6.1, which fixes the parity of the new band B3 as positive. The 983 keV transition is found to be of quadrupole character from the R_{DCO} measurements as well as from angular distribution. The quadrupole nature of 983 keV along with its measured Δ_{IPDCO} make it a M2 type transition. R_{DCO} and Δ_{IPDCO} ratio for the low energy 93 keV transition cannot be found but its assignment is fixed by determining the spin-parity of 3313.4 and 3220.3 keV levels.

The band (B4) is also extended up to an excitation energy of 2634.0 keV. The 132 and 288 keV transitions of this band and the 420 keV crossover transition, were known from previous work [12]. In Ref. [12], a 176 keV γ ray was also placed above 1173.7 keV level, but in the present work two γ rays with close-by energies of 176 and 179 keV have been observed and placed in the level scheme from the intensity balance and coincidence relationships of the transitions in band B4. From Fig. 6.10(a) and (b), it is also evident that two parallel branches starting with 543 keV and 702 keV transitions are present above 1173.7 keV level as none of them were seen in coincidence to each other. The 702 keV transition is in coincidence with only 179 keV, but the 543 keV transition is in coincidence with both 176 and 179 keV. The observation of 179 keV in the double gate of 420 & 702 keV (Fig. 6.10(a)), establishes the presence of a 16 keV unobserved transition from 1892.5 keV to 1876.0 keV level. The spin-parity of 886.0 keV level of band B4 was fixed as 8^+ from the fact that 358 keV E1 transition decays to this level from 1244.0 keV (9^-) level of the band B1. The 132 keV transition between 886.0 (8^+) and 753.6 (7+) keV states was found to be a (M1+E2) transition from the DCO ratio analysis, though the Δ_{IPDCO} could not be determined for this low energy transition, as it did not have significant scattering to the neighboring crystal of the Clover detectors. The angular correlation was also calculated using the code ANGCOR [26] to compare with the experimental DCO ratio value which suggests 132 keV transition to be of mixed multipolarity. For 420 keV transition, as it is not in coincidence with any of the known pure transitions, its DCO ratio could not be determined. But the angular distribution of 420 keV transition suggests it to be of dipole nature and the Δ_{IPDCO} value indicates a mixed nature of this transition. Thus the spin-parity of the 1173.7 keV has been assigned as 8^+ and 420 keV are determined to have a mixed M1+E2 nature. Angular distribution of 288 keV transition suggests it to be of quadrupole nature, but the spin of 1173.7 keV transition makes it to be a non-stretched M1+E2 (8^+ to 8^+) transition.

The tentative spin-parity of the other levels in band B4 have been determined from the R_{DCO} values of the 702, 562, 543 and 176 keV transitions from 132 keV gate. Though 132 keV transition is found to be of mixed (M1+E2)type, but the R_{DCO} values of the 702, 562, 543 and 176 keV transitions in 132 keV gate was compared with the theoretical angular correlation calculation taking into account the mixing of the gating transition 132 keV. The estimation of the mixing of the transition 132 keV has been done comparing the DCO ratio value of 132 keV in the gate of 659 keV using the ANGCOR code. The Δ_{IPDCO} for none of the above transitions could be obtained due to their weak intensities. Thus the spin-parity of band B4 above 1173.7 keV was assigned tentatively. The coincidence relationships among various transitions of band B4 and band B1 establish 179 keV as the connecting transition between 1892.5 keV (11^+) level of band B4 to the 2071.7 keV (12^-) level, which is in turn connected to the main band B1 by a 412 keV (M1+E2) transition. This leads 179 keV as of E1 character.

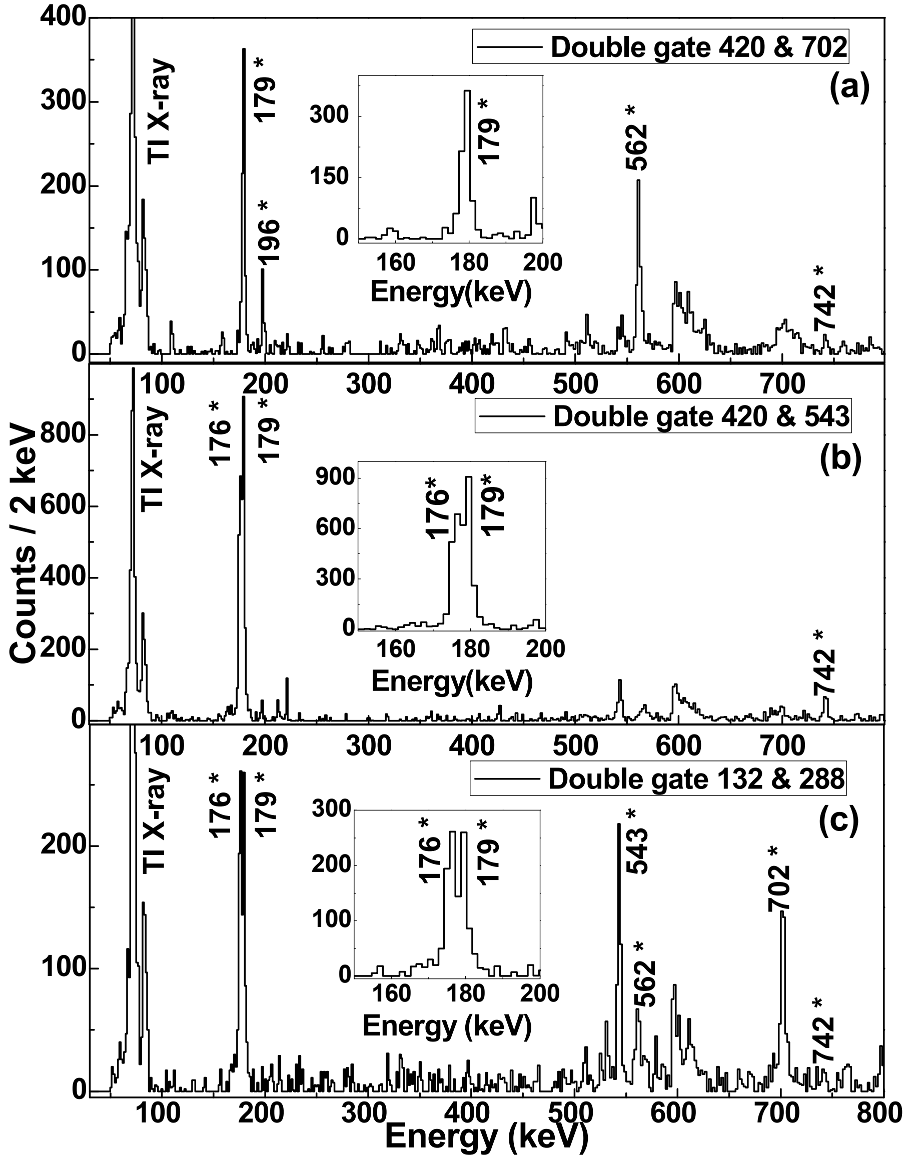

Figure 6.10: Coincidence spectra corresponding to double gates of (a) 420 & 702 keV, (b) 420 & 543 keV, (c) 132 & 288 keV transitions corresponding to the band B4 in ^{200}Tl.

The band B4 is also connected to the band B1 at 3337.8 keV level by 774 keV and 492 keV transitions in cascade. The presence of 492 keV transition could be established from the double gate of 519 keV (of band B1) & 288 keV (of band B4)(not shown). As the spin-parities of 3337.8 keV and 2071.7 keV levels are fixed as 16^- and 12^- respectively, thus the 492 and 774 keV transitions between these two levels are assigned as E2. This is also corroborated by the DCO ratio of these two transitions, as shown in Table 6.1, though the Δ_{IPDCO} of 492 keV and 774 keV transition could not be measured because of their weak intensities.

6.5 Discussion

The proton and the neutron Fermi levels in ^{200}Tl lie just below the $Z = 82$ and $N = 126$ spherical shell closure, with one proton and seven neutrons removed from the closed shell. For the odd proton, the shell model positive parity $s_{1/2}$, $d_{3/2}$ and negative parity $h_{9/2}$ orbitals are available and indeed the configuration of the ground and the first excited states in the neighboring odd-A Tl isotopes are known to be as $1/2^+$ and $3/2^+$ respectively. For the odd neutron hole, the negative parity orbitals $p_{1/2}$, $p_{3/2}$ and $f_{5/2}$ are available to generate the low spins, whereas, the unique positive parity high-j $i_{13/2}$ orbital comes into play at higher spins. Thus for the odd-odd ^{200}Tl, the low spin states will have negative parity with configuration resulting from the above orbitals for odd proton and odd neutron holes [16]. The 2^- ground state and low-lying 3^- and 4^- states in ^{200}Tl are obtained from the $\pi s_{1/2} \otimes \nu f_{5/2}$ and $\pi d_{3/2} \otimes \nu f_{5/2}$ configurations. The 7^+ isomeric state observed in the odd-odd Tl isotopes, has the dominant configuration of $\pi s_{1/2} \otimes \nu i_{13/2}$ coupled to a weakly deformed oblate core of ^{198}Hg. This isomer is a spin gap isomer with involvement of high-j $\nu i_{13/2}$ orbital, whereas the below states are generated from orbitals with small j value ($\nu f_{5/2}$). The low-lying 6^+ state at 762.0 keV is also likely to have the same configuration. In ^{198}Tl, this 6^+ state is known at similar excitation energy of 674 keV [11].

6.5.1 Band B1

With the available orbitals below $Z = 82$ shell closure, the deformation driving intruder $h_{9/2}$ orbital also becomes available for the odd proton in Tl isotopes for oblate deformation. Band structure with collective features having intrinsic configuration of $\pi \mathrm{h}_{9/2} \otimes \nu \mathrm{i}_{13/2}$ have been observed in all odd-odd Tl isotopes in $A = 190 - 200$ mass region. Isomeric states based on $\pi h_{9/2}$ configuration in ^{199}Tl and on $\nu i_{13/2}$ configuration in ^{199}Hg are known at the excitation energies of 748.9 keV and 532.5 keV, respectively [30, 31] and for both the cases oblate band structures have been identified based on those configurations. In the case of ^{200}Tl, the odd proton and odd neutron are coupled with ^{198}Hg core and the excited state corresponding to $0^{+}(^{198}\mathrm{Hg})\otimes\pi h_{9/2}\otimes\nu i_{13/2}$ configuration is, therefore, expected at an excitation energy of $(748.9+532.5=)1281.4$ keV. The excitation energy of the 8^{-} band head of the observed band structure (B1) has been found to be at 1247.4 keV, which is in very good agreement with the expected energy of the above configuration. Therefore, the band B1 is identified to have the intrinsic configuration $\pi \mathrm{h}_{9/2}\otimes\nu \mathrm{i}_{13/2}$.

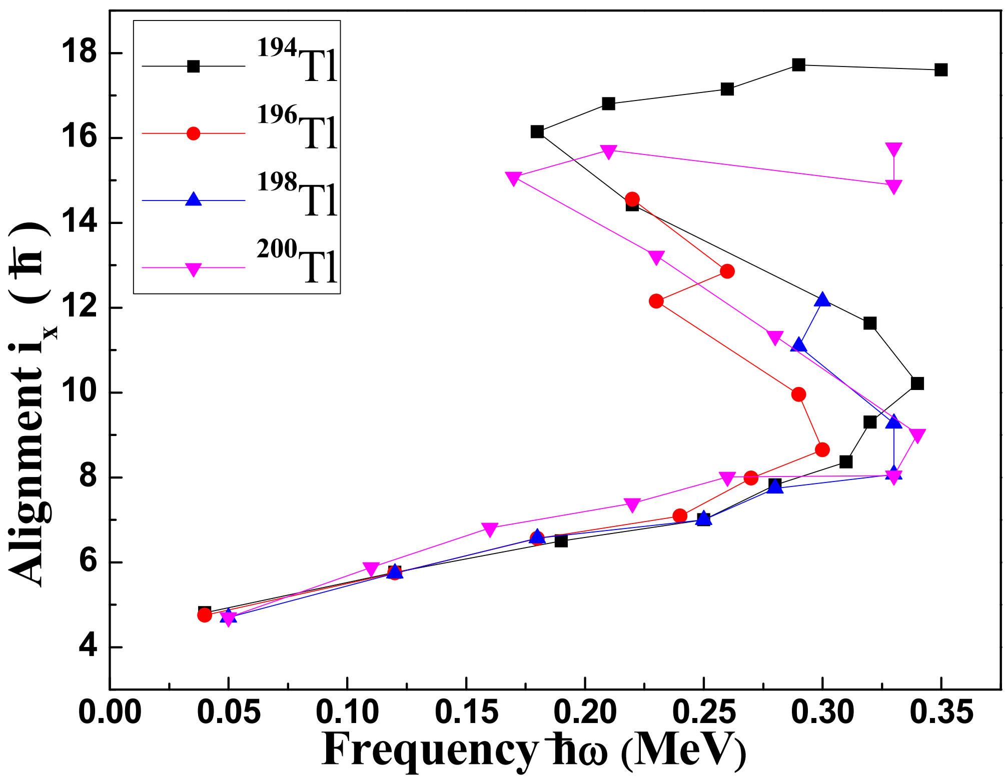

Figure 6.11: Alignment plot for the $\pi h_{9/2}\otimes\nu i_{13/2}$ bands in odd-odd Tl isotopes. The level energies of same bands of $^{194-198}$Tl are taken from Ref [9, 10, 15] respectively. The Harris reference parameters are taken as $J_0 = 8\hbar^2 MeV^{-1} and\ J_1 = 40\hbar^4 MeV^{-3}$.

The aligned angular momentum, i_x as described in chapter 2. is a quantity that extends the understanding of the collectivity of a nucleus. To understand the collective features and band crossing in ^{200}Tl i_x has been plotted as a function of rotational frequency in Fig. 6.11 for the yrast $\pi h_{9/2} \otimes \nu i_{13/2}$ bands in ^{200}Tl along with the neighbouring odd-odd Thallium isotopes from ^{194}Tl to ^{198}Tl. This figure shows that the first band crossing for the $\pi h_{9/2} \otimes \nu i_{13/2}$ band (band B1) in ^{200}Tl takes place at a rotational frequency of $\hbar\omega = 0.34$ MeV. The gain in alignment for ^{200}Tl after the first crossing is about $7\hbar$. The crossing frequency and the gain in alignment in ^{200}Tl are very much similar to those in the lighter odd-odd isotopes of Thallium as shown in Fig. 6.11. The high alignment gain indicates the involvement of a high-j orbital, in which a pair of nucleon breaks the pairing and their angular momenta contribute in the total angular momentum. The band crossing in the lighter Thallium isotopes are attributed to the alignment of a pair of neutrons in the $i_{13/2}$ orbital, which seems to be the case for ^{200}Tl as well. The similarities in the alignment gain and frequencies show that the collective rotational nature of the $\pi h_{9/2} \otimes \nu i_{13/2}$ band for the lower mass Tl isotopes still persists for ^{200}Tl, having similar deformation.

The alignment gain due to proton and neutron in an odd-odd nucleus can be interpreted from the systematics of the neighboring odd-proton and odd-neutron nuclei. The alignment for ^{199}Tl which has only one odd proton hole (no odd neutron) along with those for different bands in ^{200}Tl(one extra odd neutron with respect to ^{199}Tl) are shown in the Fig.6.12 to understand the alignment in ^{200}Tl. It can be seen from the figure that the initial alignment of band B1 in ^{200}Tl is about $5.5\hbar$ higher than the initial alignment in ^{199}Tl. The extra alignment in ^{200}Tl is due to the odd-neutron in the $i_{13/2}$ orbital. The large difference in the alignment (i_x) indicates that the odd-neutron must lie in the low-Ω orbital of $i_{13/2}$. From the Nilsson diagram one can see that it is true for oblate deformation as $\nu 1/2^+[660]$ and $\nu 3/2^+[651]$ Nilsson orbitals are situated near the neutron Fermi level of ^{200}Tl at an oblate deformation of $\epsilon \sim 0.1$. In the present work, the band B1 has been extended to higher spins beyond the first band crossing, similar to recently observed high spin structure in ^{194}Tl [13].

The Kinematic Moment of Inertia(KMI) for the yrast $\pi h_{9/2} \otimes \nu i_{13/2}$ band (band B1) has been plotted in Fig. 6.13as a function of rotational frequency ($\hbar\ \omega$). The KMI of ^{200}Tl along with the other odd-odd Thallium nuclei show similarity like the alignment plot, which represents that the Moment of Inertia(MoI) for all of the nearby even mass Thallium nuclei are almost similar. The KMI first decrease rapidly with frequency and then become almost constant. As

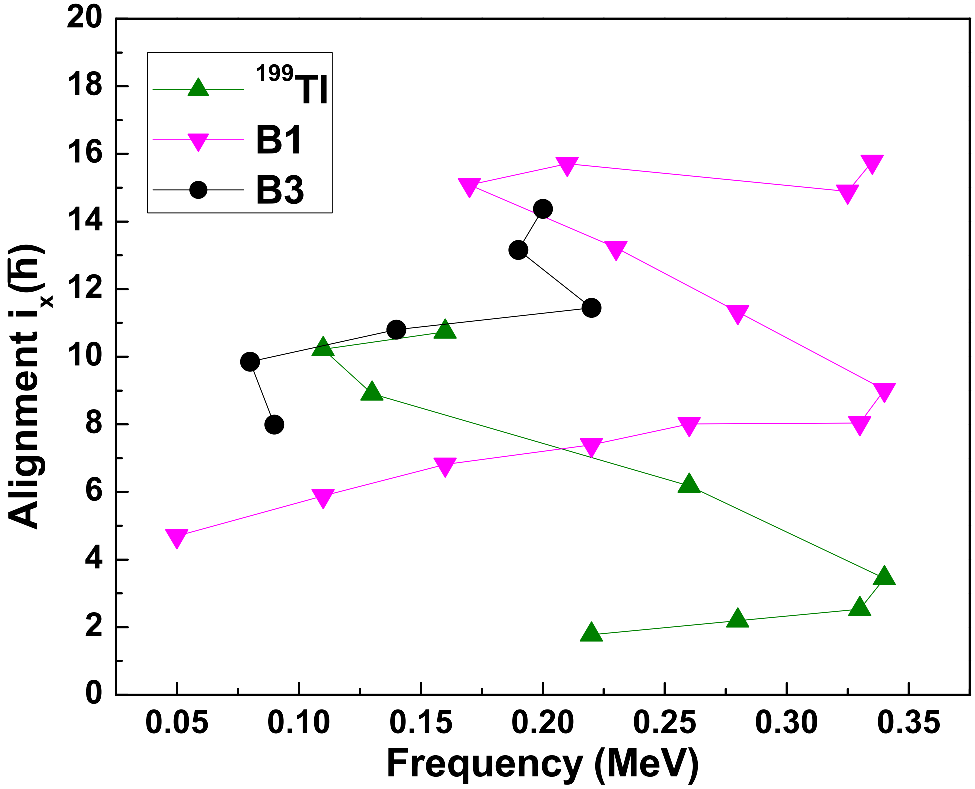

Figure 6.12: Alignment (i_x) as a function of rotational frequency ($\hbar\omega$) for the bands in ^{200}Tl. The same for the $9/2^-$ band in the odd-proton nucleus ^{199}Tl is also shown. The Harris reference parameters are taken as $J_0 = 8\hbar^2 MeV^{-1} and\ J_1 = 40\hbar^4 MeV^{-3}$.

already observed from Fig. 6.11 the band crossing appears for all Thallium isotope at frequency around 0.34 $\hbar$ also reproduce in the Fig. 6.13 at same frequency. A sudden rise in KMI after 0.34 $\hbar$ represent a increase in the MoI in the system due to the pair breaking and contribution of extra two nucleon in the total angular momentum. The total energy of the system remains same but due to the increase in the MoI the rotational frequency has a decreasing value.

The energy staggering, defined by, $S(I) = [E(I) - E(I-1)]/2I$, where, $E(I)$ is the energy of the state with spin I, is plotted as a function of spin (I) for the band B1 in Fig. 6.14, along with the same bands in neighbouring odd-odd $^{194-198}$Tl nuclei. It can be seen from this figure that the $S(I)$ of all odd-odd Tl isotopes show remarkable similarity including the low spin signature inversion at 11$\hbar$. This signature inversion was interpreted [7] as due to the J-dependence of

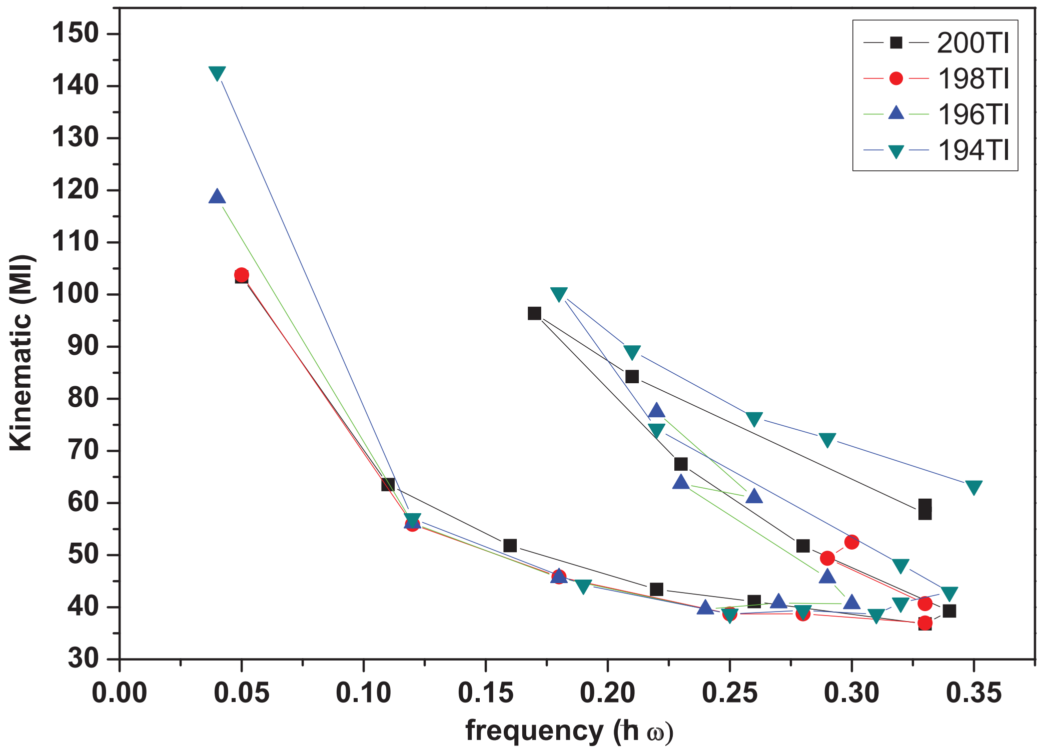

Figure 6.13: Kinematic Moment of Inertia (KMI) plot for the $\pi h_{9/2} \otimes \nu i_{13/2}$ bands as a function of frequency in odd-odd Tl isotopes. The level energies of same bands of $^{194-198}$Tl are taken from Ref [9, 10, 15] respectively. The Harris reference parameters are taken as $J_0 = 8\hbar^2 MeV^{-1} and\ J_1 = 40\hbar^4 MeV^{-3}$.

the residual p-n interaction. The similarities in the staggering plot indicates no appreciable change in the residual p-n interaction in the Tl isotopes even for neutron number as large as $N = 119$. It can be seen that they start to behave differently after the neutron pair alignment. However, all of them, except ^{194}Tl, show a second inversion at the similar spin of about $19\hbar$. As the level scheme of ^{200}Tl has been extended further in this work, it can observed that this second inversion is recovered quickly and follows the trend as in lighter isotope ^{194}Tl.

In support of the assignment of two quasi-particle (qp) configuration $\pi h_{9/2} \otimes \nu i_{13/2}$ to band B1 before band crossing and the four quasi-particle configuration $\pi h_{9/2} \otimes \nu i_{13/2}^{-3}$ due to the alignment of pair of neutron in $i_{13/2}$ orbital after the band crossing, comparison of experimental $B(M1)/B(E2)$ values (i.e. the ratio of the transition probability of the decaying M1 and E2

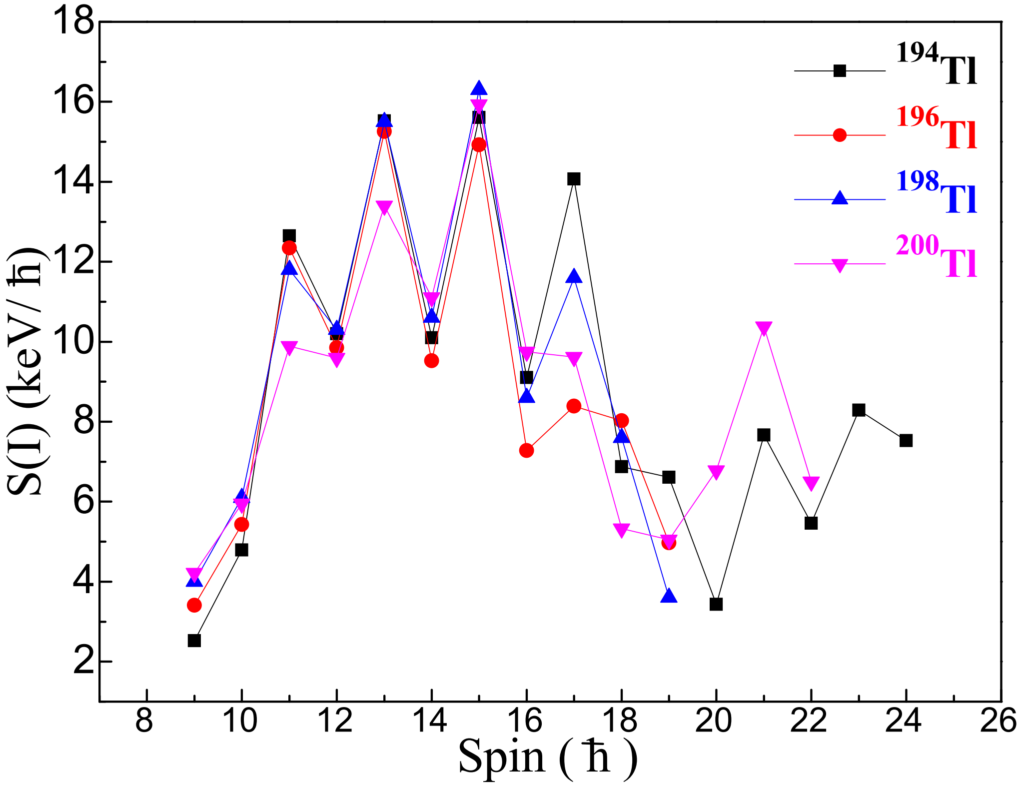

Figure 6.14: Staggering ($S(I) = [E(I) - E(I-1)]/2I$) plot for the $\pi h_{9/2} \otimes \nu i_{13/2}$ bands in odd-odd Tl isotopes. Data for $^{194-198}$Tl are taken from Ref [9, 10, 15] respectively.

transition from same level) of the levels belong to band B1 with the theoretical ones has been done. These calculation satisfactorily reproduce the experimental result with the above assignments. The theoretical $B(M1)$ and $B(E2)$ values were calculated using the geometrical model following the prescription of Ref. [29]:

$$B(M1; I \rightarrow I-1) = \frac{3}{8\pi}[(g_p - g_R)A + (g_n + g_R)B]^2(\mu_N^2), \tag{6.1}$$

$$A = (1 - \frac{K^2}{I^2})^{1/2}\Omega_p - i_p\frac{K}{I} \tag{6.2}$$

$$B = (1 - \frac{K^2}{I^2})^{1/2}\Omega_n - i_n\frac{K}{I} \tag{6.3}$$

$$B(E2; I \rightarrow I-2) = \frac{5}{32\pi}{Q_0}^2 cos^2(\gamma + 30^o) \times (1 - \frac{K}{I-1})^2(e^2b^2) \tag{6.4}$$

The $g_{p(n)}$, $i_{p(n)}$ and $\Omega_{p(n)}$ in Eq. 6.1- 6.3 represent the g-factor, alignment and angular momentum component on the symmetry axis for proton(neutron) respectively. For the calculated $B(M1)/B(E2)$ in Fig. 6.15, the values for K=6, i_p=1.5 and i_n=6.5 were taken from the band properties of neighboring odd-A nuclei. The values for g_p, g_n and rotational g-factor were taken as 0.86, -0.16 and 0.3, respectively from Ref. [7] and assumed to be same for the case of ^{200}Tl. An oblate shape with deformation $\beta_2 \sim 0.12$ has been assumed to calculate Q_0. The value of Ω_p and Ω_n were taken as 4.5 and 1.5 respectively, corresponding to the occupation of $\Omega = 9/2$ orbital for proton and $\Omega = 3/2$ orbital for neutron. The calculated and measured B(M1)/B(E2) values are shown in Fig. 6.15. Good match of the experimental and calculated values before and after band crossing supports the assigned $\pi h_{9/2} \otimes \nu i_{13/2}$ configurations of band B1. The experimental B(M1)/B(E2) values are calculated by the formula :

$$\frac{B(M1; I \rightarrow I-1; \gamma_1)}{B(E2; I \rightarrow I-2; \gamma_2)} = \frac{0.6968 E_{\gamma 2}^5}{\lambda E_{\gamma 1}^3 (1+\delta^2)} (\frac{\mu_N}{eb})^2, \lambda = \frac{I_{\gamma 2}}{I_{\gamma 1}} \tag{6.5}$$

Where $I_{\gamma 1(\gamma 2)}$ is the intensity of the transition $\gamma_1(\gamma_2)$ and δ is the mixing ratio of M1 with E2.

6.5.2 Band B2

The band B2 consists of a set of levels which lie very close in energy to the levels in band B1 around the band-crossing region of band B1. The Excitation energy(E) vs spin(I) is shown in Fig.6.16 for different bands in ^{200}Tl. It is evident from this plot that the excitation energy of the levels belongs to band B2 lies very close to the main sequence of band B1. In fact some of the levels in band B2 lie below those in band B1 for the same value of spin. Moreover, several interconnecting transitions have been observed between these bands. This indicates that the configurations of these two bands are similar, if not same.

Doubly degenerate bands for the $\pi h_{9/2} \otimes \nu i_{13/2}$ band have been reported in the neighboring odd-odd isotopes of ^{198}Tl and ^{194}Tl[13, 15]. The side bands in those cases were observed in the lower energy region before the band crossing. In ^{200}Tl, we have not observed any indication of such bands in the lower energy region, but it is interesting to note the similarities in bands B1

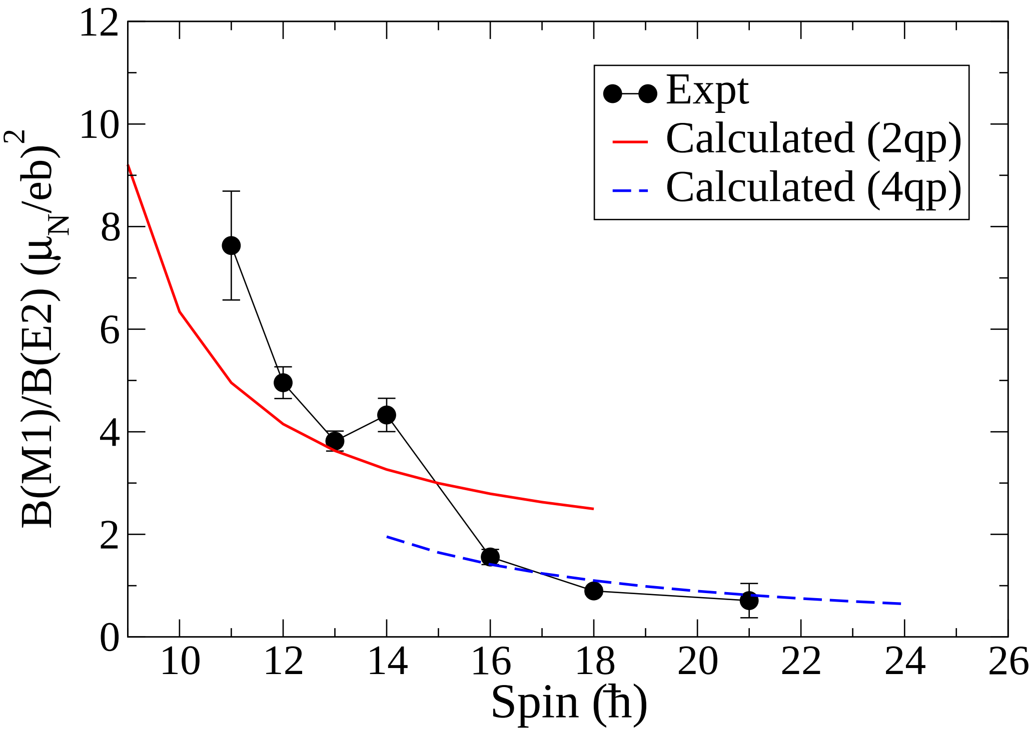

Figure 6.15: Experimental B(M1)/B(E2) of band B1 before and after band crossing is compared with that of calculation for two and four quasi-particle (qp) configurations (see text).

and B2 around the band crossing region. However, whether these bands can be considered as doubly degenerate bands are yet to be confirmed as the side bands are not well developed.

Another possible interpretation for the band B2 can also be given as alignment of a pair of protons in terms of the alignment of. The $\pi h_{11/2}$ alignment has been observed in the odd-A Hg isotopes ^{193,195}Hg [32, 33] after the neutron pair alignment. However, as the neutron number increases, the neutron alignment frequency also increases. For ^{200}Tl it may so happen that the proton and neutron alignment frequency becomes similar as the neutron number approaches to $N = 119$. The cranked shell model calculations (discussed in the next section) shows that the proton pair breaking is expected at a slightly higher rotational frequency of $\hbar\omega \sim 0.4$ MeV. The $\pi h_{11/2}$ orbital is also a high-j orbital like $\nu i_{13/2}$ and similar to the neutrons, the proton alignments will also take place in the upper half of the $\pi h_{11/2}$ orbital for oblate deformation. Therefore, the alignment gain for the protons would be similar to those of neutrons as observed.

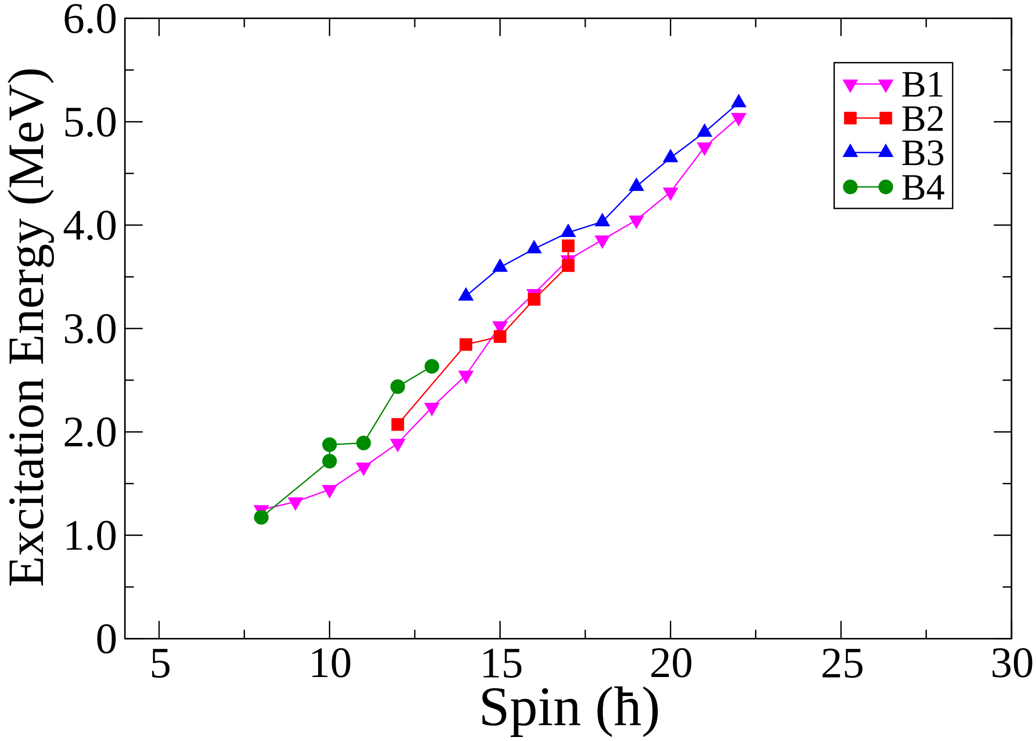

Figure 6.16: Spin vs. excitation energy plots of different bands in ^{200}Tl.

6.5.3 Band B3

The band B3 has been assigned as a positive parity band based on 14^+ state at 3.3 MeV of excitation energy. The similarities in excitation energy of this band with band B1, as can be seen in Fig.6.16, indicates that it should be a four quasi-particle (qp) in nature. This band has strong decay paths to the band B1. Therefore, the configuration of this band is expected to have similarities with the band B1. The band head of band B3 suggests involvement of another negative parity orbital as well as after pair breaking the two nucleon may stay in different orbitals. In comparison with the similar band observed in ^{198}Tl [34] and the available single particle levels near the Fermi surface, the configuration of the band B3 is assigned as $\pi h_{9/2} \otimes \nu i^{-2}_{13/2} \nu(f_{5/2}p_{3/2})$. It may be noted here that the spin and the excitation energy of the band head of this band in ^{198}Tl was observed at lower values. In the present work, we have not observed the lower spin members of this band. The alignment plot in Fig.6.12 shows that this band has about $4\hbar$ of additional alignment than the 2-qp band B1 but the alignment gain is little bit less compared to the 4-qp part of band B1 which is interpreted as the alignment of a pair of neutrons in the $i_{13/2}$ orbital in band B1. It, therefore, suggests that the out of the two additional neutrons in this 4-qp band, one of them should be in a low-j orbital and hence supporting the assigned configuration.

6.5.4 Band B4

The sequence B4 does not represent a well-formed rotational band. It can be seen from Fig.6.16 that this band remains within the 2-qp part of the main band. The 8^+ state in ^{200}Tl can be obtained from the coupling of $\pi d_{3/2}$ and $\nu i_{13/2}$ with the ground state in ^{198}Hg. The $\pi d_{3/2}$ state in ^{199}Tl is situated at 367 keV excitation energy and the $\nu i_{13/2}$ state in ^{199}Hg at 532 keV. The 886.0 keV excitation energy of the 8^+ state in ^{200}Tl is in excellent agreement with the sum of these two excitation energies ($367 + 532 = 899\ keV$). Moreover, the $5/2^+$ state corresponding to the $\pi d_{5/2}$ orbital in ^{199}Tl is situated about 350 keV above its $\pi d_{3/2}$ state. The excitation energy of the second 8^+ state in ^{200}Tl is close to this. Therefore, the possible configuration of the two 8^+ states in ^{200}Tl is $\pi(d_{3/2}, d_{5/2}) \otimes \nu i_{13/2}$.

6.5.5 Other states and structures

A sequence of levels starting with the 7^- state at 1023.6 keV has been observed up to 9^- state. Assuming a rotational structure, an aligned angular momentum of about $3\hbar$ has been obtained for this structure. The most probable configuration for this structure would be $\pi h_{9/2} \otimes \nu i_{13/2}$ but involving the $\Omega = 9/2$ and 5/2 orbitals in proton and neutrons, respectively. The configuration of the 12^- state at about 2071.7 keV in ^{200}Tl can be assigned from the coupling of the low-lying states in ^{200}Tl with the two neutron state in ^{198}Hg [35]. The first observed negative parity band head in ^{198}Hg is a 5^- state at 1.6 MeV of excitation energy with a configuration of $\nu i_{13/2} \nu p_{3/2}$. The configuration of the 12^- state at 2071.7 keV in ^{200}Tl can be assigned as the coupling of its 7^+ state (configuration $\pi s_{1/2} \otimes \nu i_{13/2}$) with the 5^- state in ^{198}Hg. This state can also be formed from the two maximally aligned quasi-particles in $\pi h_{11/2}$ and $\nu i_{13/2}$ orbitals. It was predicted to be at about 1.7 MeV in the neighboring isotope ^{198}Tl [10] for a deformation of $\beta_2 \sim 0.15$. A tentatively 12^- state observed in the same nucleus ^{198}Tl at an excitation energy of 1736.0 keV might corresponds to this state [34]. However, no well developed rotational band structure observed on top of this band in either of the nuclei, although the similar configuration yielded very well developed band structures in $^{190-194}$Au nuclei [36].

6.6 TRS calculations

In order to have information on the different deformations of the band structures in ^{200}Tl, the Total Routhian Surface (TRS) calculations were carried out by the Strutinsky shell correction method using deformed Woods-Saxon potential. In the TRS method, the calculation of the single particle shell energies are performed considering Lipkin-Nogami pairing [37, 38, 39, 40]. For all of these calculations, the universal parameter set was used [41]. The Routhian energies (E_{TRS}) were calculated in $(\beta_2, \gamma, \beta_4)$ deformation mesh points with minimization on β_4. The detailed outline of the calculation procedure is described in the Ref. [43]. The Routhian (potential) surfaces are plotted in the conventional $\beta_2 - \gamma$ plane.

The TRS plot for the $\pi h_{9/2} \otimes \nu i_{13/2}$ band with band head of 8^- in ^{200}Tl is shown in Fig. 6.17(left panel) for the rotational frequency of $\hbar\omega = 0.0$ MeV i.e. in lower spin. It can be seen from the figure, that a minimum occurs at an oblate deformation ($\gamma = -60°$), similar to those calculated for the neighboring isotopes ^{194,198}Tl for the same configuration [9]. However, the value of deformation parameter $\beta_2 = 0.13$ obtained for the yrast band in ^{200}Tl is slightly less compared to the lighter Thallium isotopes for which $\beta_2 \sim 0.15$ was obtained. The similarities in the calculated deformations for the odd-odd Tl isotopes corroborate well with their alignment and staggering patterns. The nice minimum observed in the TRS calculations at oblate deformation continues to stay upto the rotational frequency of $\hbar\omega = 0.30$ MeV. At higher frequencies, the intense minima at oblate shape, disappears and the surfaces become $\gamma-$soft with larger (β_2 value) deformation. For this configuration, this $\gamma-$softness continues even at higher rotational frequencies of $\hbar\omega = 0.50$ MeV beyond the experimental band crossing (observed at a rotational

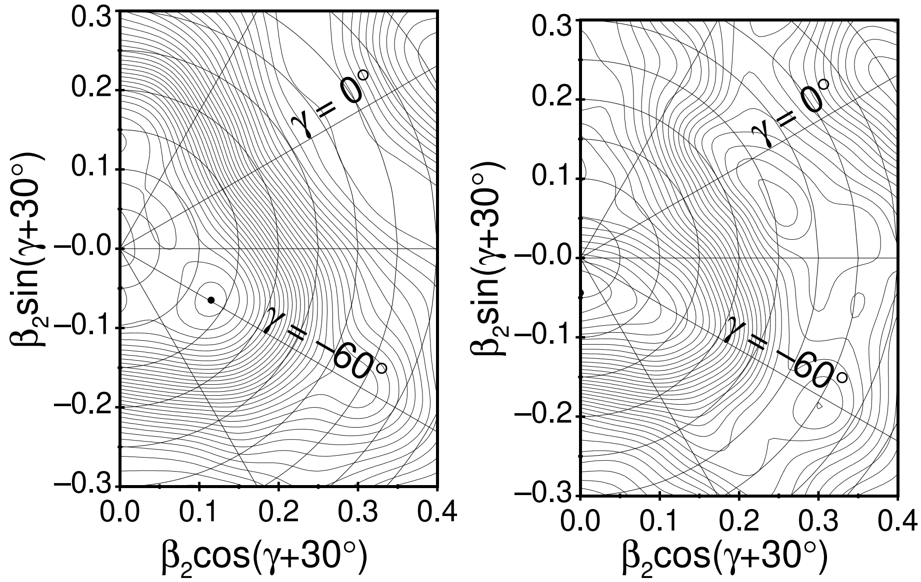

Figure 6.17: Total Routhian Surface (TRS) calculations for the band B1 with configuration of $\pi h_{9/2} \otimes \nu i_{13/2}$ in ^{200}Tl for (a) rotational frequency $\hbar\omega$ = 0.0 MeV (left panel) and for (b) rotational frequency $\hbar\omega$ = 0.0 MeV.(right panel) $\gamma = 0°$ and $\gamma = -60°$ lines correspond to prolate and oblate deformations, respectively. The contours are in 400 keV apart from each other.

frequency of $\hbar\omega = 0.34$ MeV) in this band. A typical TRS plot at higher rotational frequency of $\hbar\omega = 0.45$ MeV for this configuration is shown in Fig. 6.17(right panel). It indicates that the nucleus ^{200}Tl becomes $\gamma-$soft after the band crossing.

For the 7^- ($\pi 9/2^-[505] \otimes \nu 5/2^+[642]$) state at 1023.6 keV excitation energy we have performed configuration-constrained potential energy surface calculations which is shown in Fig. 6.18(a). In the calculations the given orbits are tracked and blocked using the average Nilsson number technique [42]. The minimum, in this case occurs almost at the same deformation as in band B1 at $\beta_2 = 0.12$ and $\gamma = -60°$. However, the energy at the minimum is somewhat higher than the minimum obtained for band B1 at low rotational frequency. With increasing rotational frequency the energy difference increases and the higher spin states in the 7^- band quickly become non-yrast. This is the possible reason for the non-observation of the higher spin states of this 7^- band.

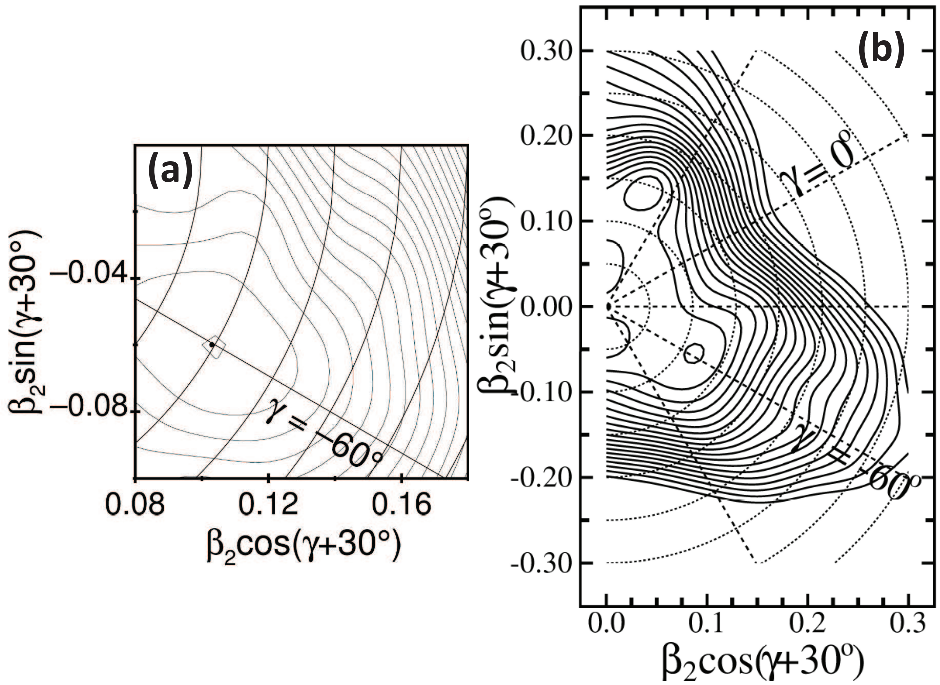

Figure 6.18: (a)Calculated configuration-constrained potential energy surface for the 7^- state with the configuration of $\pi 9/2^-[505] \otimes \nu 5/2^+[642]$ in ^{200}Tl. (b) Total Routhian Surface (TRS) calculations for the $\pi h_{9/2} \otimes \nu i_{13/2}^{-2}$ $(f_{5/2}p_{3/2})$ 4-qp configuration corresponding to the band B3 in ^{200}Tl at the rotational frequency $\hbar\omega = 0.11$ MeV. The contours are in 400 keV interval.

The TRS plot for band B3 with the 4-qp configuration of $\pi h_{9/2} \otimes \nu i_{13/2}^{-2}\nu$ $(f_{5/2}p_{3/2})$ is shown in Fig. 6.18(b). This plot shows that a minimum occurs at a triaxial deformation with the triaxiality parameter $\gamma \sim 40°$ and with $\beta_2 \sim 0.14$. A second minimum, is also appears in the TRS plot, within an energy gap of about 500 keV along the oblate ($\gamma \sim -60°$) axis with a slightly less deformation of $\beta_2 \sim 0.12$.

The single particle Routhians are calculated for proton and neutrons in ^{200}Tl and also plotted for two deformation parameters corresponding to bands B1 and B3 in Fig. 6.19 and Fig. 6.20, respectively as a function of rotational frequency $\hbar\omega$. It can be seen from Fig. 6.19 that the second crossing of neutron positive parity orbital (originated from $\nu i_{13/2}$ orbital) takes place at a rotational frequency of about $\hbar\omega = 0.35$ MeV. This crossing is responsible for the observed band crossing in band B1 at 16^- spin. The crossing frequency found from the TRS calculation is in very good agreement with the experimentally observed band crossing frequency of band B1 (see Fig. 6.12). The slope of a Routhian in Fig 6.19 and 6.20 provides the aligned angular

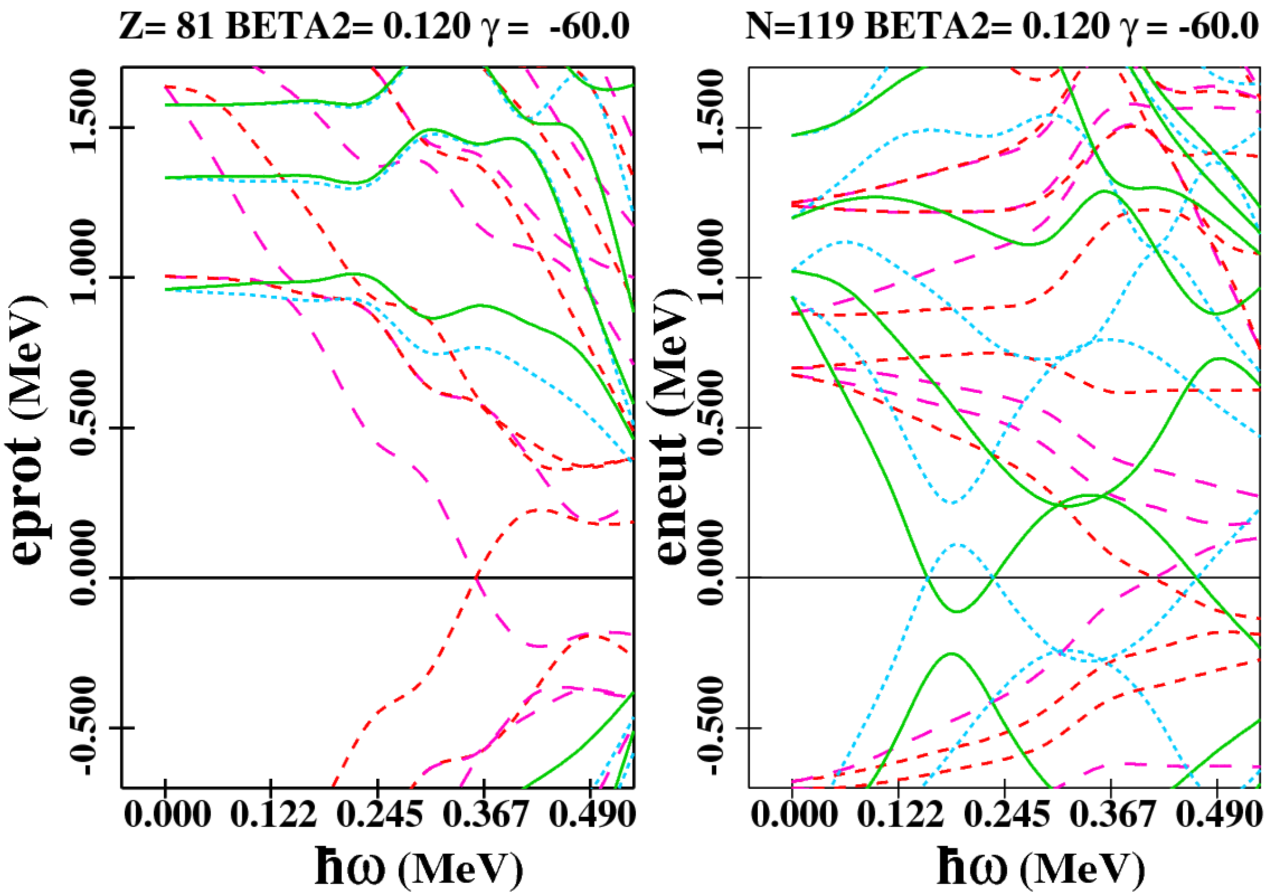

Figure 6.19: Plots of single proton (left) and single neutron (right) Routhians of ^{200}Tl as a function of rotational frequency $\hbar\omega$ for deformation parameter $\beta_2 = 0.12$ and $\gamma = -60°$ (corresponding to the calculated deformation of band B1). Solid (green) and dotted (cyan) lines correspond $\alpha = +1/2$ and $\alpha = -1/2$ signature partners, respectively, for the positive parity orbitals while large-dashed (pink) and dashed (red) lines correspond to the same signature partners for the negative parity orbitals.

momentum corresponding to that orbital and subsequently, gives the gain in alignment if the observed band crossing corresponds to the particle alignment in that orbital. The slope of the neutron Routhians in Fig. 6.19, corresponding to the alignment of band B1, gives the alignment gain of $6.6\hbar$ which is in excellent agreement with the experimentally observed gain in alignment of band B1.

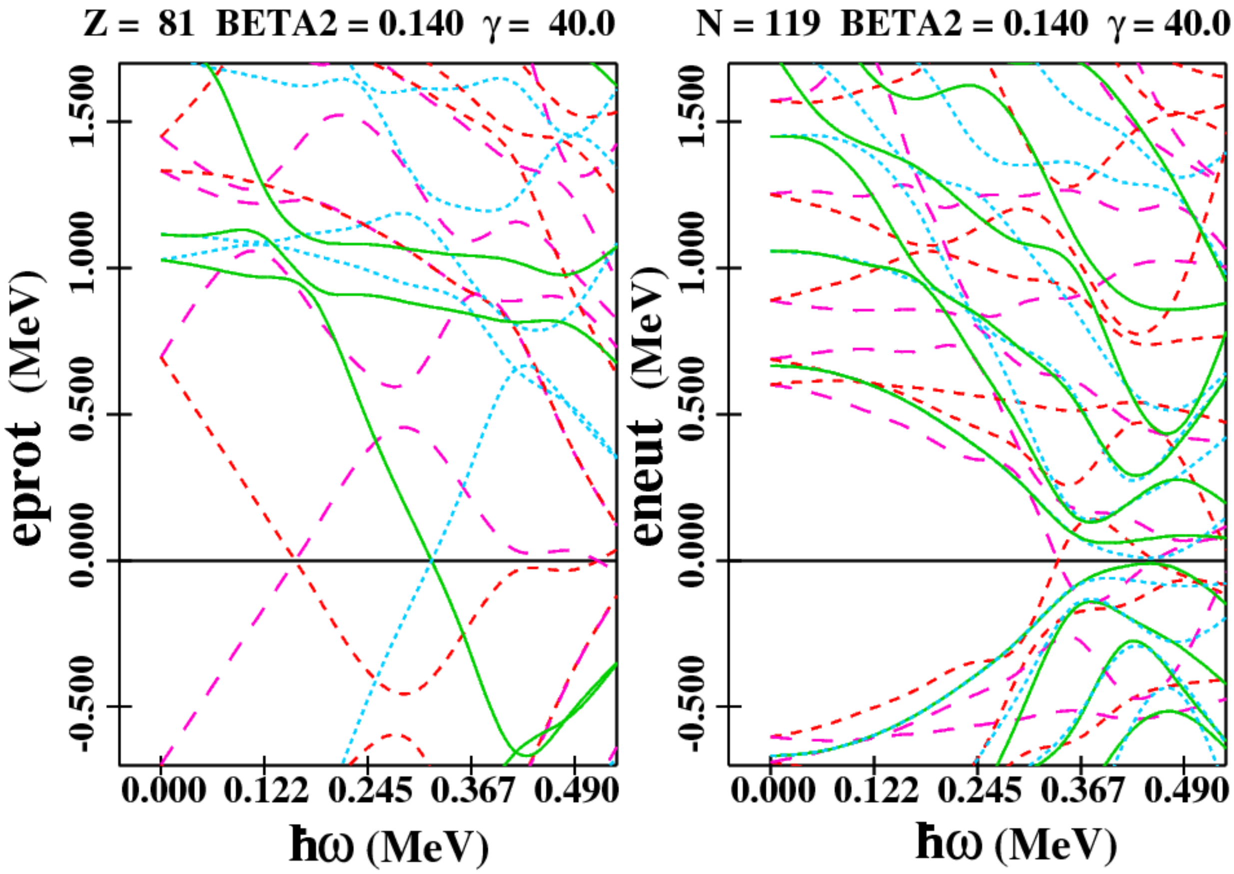

Figure 6.20: Same as Fig.6.19 but for deformation parameter $\beta_2 = 0.14$ and $\gamma = 40°$ corresponding to the calculated deformation of band B3. Left panel is for single proton Routhians and the right panel is corresponding to neutrons.

The single proton Routhians, shown in Fig. 6.19(left panel) indicates that the proton crossing takes place at a rotational frequency of about $\hbar\omega \sim 0.4$ MeV, which is slightly higher compared to the neutron crossing frequency ($\hbar\omega \sim 0.35$)showed in the Fig. 6.19 (right panel) and also compared to the experimentally observed crossing frequency. However, it should be noted that the slope of the Routhians for the protons and the neutrons are very similar as has been observed for bands B1 and B2. Therefore, the band B2 might be inferred as the proton pair alignment.

The calculated single particle Routhians for protons and neutrons corresponding to the deformation of band B3 in ^{200}Tl are shown in Fig. 6.20 as a function of rotational frequency. The proton crossing takes place at rotational frequency of $\hbar\omega \sim 0.26$ MeV, for the deformation corresponding to the band B3, where as the neutron crossing takes place at much higher frequency as shown in Fig. 6.20 right panel. The proton crossing frequency is in good agreement with the observed crossing frequency of band B3 at $\hbar\omega \sim 0.22$ MeV. Therefore, the band crossing in this band is originated due to the alignment of a pair of protons in negative parity orbital. The slope of this Routhian plots indicates an alignment gain of about $4\hbar$ and the observed alignment gain for band B3 seems to approach this value as shown in Fig. 6.12.

6.7 Summary

High spin states in ^{200}Tl have been populated by using the fusion evaporation reaction ^{198}Pt(^{7}Li,5n) at the beam energy of 45 MeV at BARC-TIFR Pelletron facility and studied by γ ray coincidence spectroscopic techniques using the INGA setup of 15 clover HPGe detectors. The level scheme of ^{200}Tl has been extended significantly, up to the excitation energy of $\sim$ 5.2 MeV and spin of $22\hbar$, through the observation and placement of 60 new transitions in the level scheme. To assign the spin and parity of the state, DCO, IPDCO and Angular Distribution measurements have been carried out. A few band structures involving the intruder $\pi h_{9/2}$ and high-j neutron orbitals have been observed in this odd-odd nucleus. The systematics of the ^{200}Tl are compared with the band structures in the other odd-odd Tl isotopes. It has been observed that upto $N = 119$, remarkable similarity in the $\pi h_{9/2} \otimes \nu i_{13/2}$ band in odd-odd Tl nuclei continues to persists. The shape and band crossing phenomena are discussed in the light of the cranking model calculations with Woods-Saxon potential. Oblate deformation is obtained for the 2-qp bands in ^{200}Tl while interestingly, the 4-qp band seems to have a triaxial deformation from the TRS calculations. The band crossing frequencies and the alignment gains in these bands are well reproduced by the cranking calculations. The calculations also predict that the $\pi h_{9/2} \otimes \nu i_{13/2}$ band becomes γ-soft after the band crossing due to the alignment of a pair of neutrons in $\nu i_{13/2}$ orbital. It would be interesting to extend the 4-qp bands to higher rotational frequencies to compare their shape and alignment gains.

Bibliography

[1] I. Hamamoto, Phys. Rep. **10**, No.2, 63 (1974).

[2] K. Heyde *et al.*, Phys. Rep. **102**, No. 5&6, 291 (1983).

[3] M. Huyse *et al.*, Phys. Lett. B **201**, 293 (1988).

[4] N. Fotiades *et al.*, Phys. Rev C **76**, 014302 (2007)

[5] O. Hausser *et al.*, Phys. Lett. B **64**, 273 (1976).

[6] R. Broda *et al.*, Phys. Rev. C **84**, 014330 (2011).

[7] C. Y. Xie *et al.*, Phy. Rev. C **72**, 044302 (2005).

[8] A. J. Kreiner *et al.*, Phy. Rev. C **21**, 933 (1980).

[9] H. Pai *et al.*, Phys. Rev C **85**, 064313 (2012).

[10] A. J. Kreiner, M. Fenzl and W. Kutschera, Nucl. Phys. A **308**, 147 (1978).

[11] A. J. Kreiner, M. Fenzl, S. Lunardi and M.A.J. Mariscotti, Nucl. Phys. A **282** 243 (1977).

[12] A. J. Kreiner *et al.*, Phys. Rev C **23**, 748 (1981).

[13] P. L. Masiteng *et al.*, Phys. Lett. B **719**, 83 (2013).

[14] T. Roy *et al.*, Phys. Lett. B **782**, 768 (2018).

[15] E. A. Lawrie *et al.*, Phys. Rev. C **78**, 021305(R) (2008).

[16] R. E. Doebler, Wm. C. McHarris, Phys. Rev C **2**, 2422 (1970).

[17] Soumik Bhattacharya *et al.*, Phys. Rev. C **95**, 014301(2017).

[18] R. Palit *et al.*, Nucl. Instrum. Methods Phys. Res. A **680**, 90 (2012).

[19] D. C. Radford, Nucl. Instrum. Methods Phys. Res. A **361**, 297 (1995).

[20] R. K. Bhowmik, S. Muralithar, R.P. Singh, Proc. DAE Symp. on Nucl. Phys., **44B**, 422 (2001).

[21] A. Srivastava *et al.*, Phys. Lett. B **718**, 931 (2013).

[22] A. Kramer-Flecken *et al.*, Nucl. Instrum. Methods Phys. Res. A **275**, 333 (1989).

[23] K. Starosta *et al.*, Nucl. Instrum. Methods Phys. Res. A **423**, 16 (1999).

[24] Ch. Droste *et al.*, Nucl. Instrum. Methods Phys. Res. A **378**, 518 (1996).

[25] S. Das Gupta *et al.*, Phys. Rev C **88**, 044328(2013).

[26] E. S. Macias *et al.*, Comput. Phys. Commun. 11, 75 (1976).

[27] L. Peter Ekström and Anders Nordlund, Nucl. Instrum. Methods Phys. Res. A **313**, 421 (1992).

[28] J. K. Deng *et al.*, Nucl. Instrum. Methods Phys. Res. A **317**, 242 (1992).

[29] F. Dönau, Nucl. Phys. A **471**, 469 (1987).

[30] Soumik Bhattacharya *et al.*, Phys. Rev. C **98**, 044311(2018).

[31] D. Mertin *et al.*, Nucl. Phys. A **301**, 365(1978).

[32] H. Hubel *et al.*, Nucl. Phys. A **453**, 316 (1986).

[33] N. Nenoff *et al.*, Nucl. Phys. A **629**, 621 (1998).

[34] E. A. Lawrie *et al.*, Eur. Phys. Jour. A **45**, 39 (2010).

[35] C. Günther *et al.*, Phys. Rev. C **15**, 1298 (1977).

[36] A. Neskakis *et al.*, Nucl. Phys. A **390**, 53 (1982).

[37] W. Nazarewicz *et al.*, Nucl. Phys. A **435**, 397 (1985).

[38] W. Nazarewicz *et al.*, Nucl. Phys. A **512**, 61 (1990).

[39] W. Satula, R. Wyss, and P. Magierski, Nucl. Phys. A **578**, 45 (1994).

[40] F. R. Xu, W. Satula, and R. Wyss, Nucl. Phys. A **669**, 119 (2000).

[41] J. Dudek, Z. Szymanski, and T. Werner, Phys. Rev. C **23**, 920 (1981)

[42] F. R. Xu, P.M Walker, J.A. Sheikh, and R. Wyss, Phys. Lett. B **435**, 257 (1998)

[43] G. Mukherjee *et al.*, Nucl. Phys. A **829**, 137 (2009).

STATEMENT BY AUTHOR

This dissertation has been submitted in partial fulfillment of requirements for an advanced degree at Homi Bhabha National Institute (HBNI) and is deposited in the Library to be made available to borrowers under rules of the HBNI.

Brief quotation from this dissertation are allowable without special permission, provided that accurate acknowledgement of source is made. Requests for permission for extended quotation from or reproduction of this manuscript in whole or in part may be granted by the Competent Authority of HBNI when in his or her judgement the proposed use of the material is in the interests of scholarship. In all other instances, however, permission must be obtained from the author.

Soumik Bhattacharya

DECLARATION

I, hereby declare that the investigation presented in the thesis has been carried out by me. The work is original and has not been submitted earlier as a whole or in part for a degree/diploma at this or any other Institution/University.

Soumik Bhattacharya

List of Publication arising from the thesis

In Journal

1. **Yrast and non yrast spectroscopy of ^{199}Tl using α-induced reaction .**
   Soumik Bhattacharya, S. Bhattacharyya, R. Banik, S. Das Gupta, G. Mukherjee, A. Dhal, S. S. Alam, Md. A. Asgar, T. Roy, A. Saha, S. Nandi, T. Bhattacharjee, A. Choudhury, Debasish Mondal, S. Mukhopadhyay, P. Mukhopadhyay, S. Pal, Deepak Pandit, I. Shaik, and S. R. Banerjee.
   Phys. Rev. C Vol. **98**, 044311 (2018).

2. **Deformed band structures at high spin in ^{200}Tl.**
   Soumik Bhattacharya, S. Bhattacharyya, S. Das Gupta, H. Pai, G. Mukherjee, R. Palit, F.R. Xu, Q. Wu, A. Shrivastava, Md.A. Asgar, R. Banik, T. Bhattacharjee, S. Chanda, A. Chatterjee, A. Goswami, V. Nanal, S.K. Pandit, S. Saha, J. Sethi, T. Roy and S. Thakur.
   Phys. Rev. C Vol. **95**, 014301 (2017).

In Conferences/Symposia :

1. **High spin band structure in ^{200}Tl.**
   Soumik Bhattacharya, S. Bhattacharyya,S. Dasgupta,H. Pai,G. Mukherjee,R. Palit,A. Shrivastava,T. Bhattacharjee,S. Chanda,A. Chatterjee,V. Nanal,S.K. Pandit,S. Saha,S. Thakur.
   Proceedings of International Symposium on Nuclear Physics, DAE, Vol **58**, 200 (2013).

2. **Clover detector setup at VECC**

   Soumik Bhattacharya, B. Dey,A. Saha,A. Choudhury,S. Bhattacharyya,T. Bhattacharjee,S.R. Banerjee,S. Das Gupta,Debasish Mondal,G. Mukherjee,S. Mukhopadhyay,P. Mukhopadhyay,D. Pandit,S. Pal,T. Roy,I. Seikh.

   Proceedings of International Symposium on Nuclear Physics, DAE, Vol. **58**, 904 (2013).

3. **Angular distribution and polarization for transitions in ^{200}Tl.**

   Soumik Bhattacharaya, S. Bhattacharyya, S. Dasgupta, H. Pai, G. Mukherjee, R. Palit, A. Shrivastava, T. Bhattacharjee, S. Chanda, A. Chatterjee, V. Nanal, S.K. Pandit, S. Saha, and S. Thakur

   Proceedings of the DAE Symp. on Nucl. Phys. Vol. **59**, 120 (2014).

4. **VECC array for NUclear Spectroscopy (VENUS)**

   Soumik Bhattacharya, R. Banik, S. S. Alam, A. Saha1, Md. A. Asgar, T. Roy, A. Chowdhury, I. Seikh, P. Mukhopadhyay, A. Dhal, T. Bhattacharjee, S. Bhattacharyya*, G. Mukherjee, S. Mukhopadhyay, D. Mondal, D. Pandit, S. Pal and S. R. Banerjee.

   Proceedings of the DAE Symposium on nuclear physics, Vol. **61**, 98 (2016).

5. **Oblate band structure based on $\pi h_{9/2}$ orbital in ^{199}Tl.**

   Soumik Bhattacharya, S. Bhattacharyya, R. Banik, G. Mukherjee, S. Das Gupta, S.S. Alam, A. Dhal, Md. A. Asgar, T. Roy, A. Saha, T. Bhattacharjee, S. Mukhopadhyay, D. Pandit, D. Mondal, S. Pal and S. R. Banerjee.

   Proceedings of the DAE Symposium on nuclear physics Vol **61** 188 (2016).

6. **Deformed structure based on $\nu i_{13/2}$ orbital in ^{199}Hg.**

   Soumik Bhattacharya, S. Bhattacharyya, R. Banik, S. Das Gupta, S. S. Alam, A. Dhal, Md. A. Asgar, T. Roy, A. Saha, T. Bhattacharjee, S. Mukhopadhyay, D. Pandit, D. Mondal, S. Pal, S. R. Banerjee.

   Proceedings of the DAE Symposium on nuclear physics Vol. **62**, 118 (2017).

7. **VECC-INGA: An exploration of nuclear structure with light ions.**

   Soumik Bhattacharya, R. Banik, S. Nandi, Sajad Ali,S. Chattterjee, S. Das, S.

Samanta,K. Basu, A. Choudhury, A. Adhikari, S. S. Alam, Shabir Dar, B. Das, Sangeeta Das, A.Dhal, A. Mondal, K. Mondal, P. Mukhopadhyay, H.Pai,P. Ray, A. Saha, I. Shaik, C. Bhattacharya,G. Mukherjee, R. Raut, S. S. Ghugre, A. Goswami, S. Bhattacharyya. Proceedings of the International Symposium on nuclear physics, DAE Vol. **63**, 1156 (2018).

8. **Near-yrast exotic structure in ^{199}Hg.**

   Soumik Bhattacharya, S. Bhattacharyya, S. Das Gupta, R. Banik, G. Mukherjee, A. Dhal, S. Nandi, Md. A. Asgar, T. Roy, R. Raut, S. S. Ghugre, S. K. Das, S. Chatterjee, S. Samanta, Shabir Dar, A. Goswami, Sajad Ali, S. Mukhopadhyay, Debasish Mondal, S. S. Alam, T. Bhattacharjee, A. Saha, Deepak Pandit, Surajit Pal, S. R. Banerjee and S. Rajbanshi.

   Proceedings of the DAE Symposium on nuclear physics Vol. **64**, 276 (2019).

(B) Other publications (in refereed journals)

1. **High spin spectroscopy of ^{201}Tl.**

   S. Das Gupta, S. Bhattacharyya, H. Pai, G. Mukherjee, **Soumik Bhattacharya**, R. Palit, A. Shrivastava, A. Chatterjee, S. Chanda, V. Nanal, S. K. Pandit, S. Saha, J. Sethi, and S. Thakur.

   Phys. Rev. C Vol. **88**, 044328 (2013).

2. **Lifetime measurement and decay spectroscopy of ^{132}I.**

   S. Bhattacharyya, D. Banerjee, S. K. Das, **Soumik Bhattacharya**, S. Dasgupta, T. Bhattacharjee, P. Das, R. Guin, G. Mukherjee, H. Pai.

   EPJ Web of Conferences Vol. **66**, 02009 (2014).

3. **Role of p-induced population of medium-mass (A 150) neutron-rich nuclei.**

   D. Banerjee, A. Saha, T. Bhattacharjee, R. Guin, S. K. Das, P. Das, Deepak Pandit, A.

Mukherjee, A. Chowdhury, **Soumik Bhattacharya**, S. Das Gupta, S. Bhattacharyya, P. Mukhopadhyay and S. R. Banerjee.
Phys. Rev. C Vol. **91**, 024617 (2015).

4. **A new high-spin isomer in ^{195}Bi.**
T. Roy, G. Mukherjee, N. Madhavan, T.K. Rana, **Soumik Bhattacharya**, Md.A. Asgar, I. Bala, K. Basu, S.S. Bhattacharjee, C. Bhattacharya, S. Bhattacharya, S. Bhattacharyya, J. Gehlot, S.S. Ghugre, R.K. Gurjar, A. Jhingan, R. Kumar, S. Muralithar, S. Nath, H. Pai,c, R. Palit, R. Raut, R.P. Singh, A.K. Sinha, and T. Varughese.
Eur. Phys. J. A Vol. **51**, 153 (2015).

5. **Exclusive measurement of isospin mixing at high temperature in ^{32}S.**
Debasish Mondal, Deepak Pandit, S. Mukhopadhyay, Surajit Pal, Srijit Bhattacharya, A. De, **Soumik Bhattacharya**,S. Bhattacharyya, Balaram Dey, Pratap Roy, K. Banerjee.
Phys. Let. B. Vol. **763**, 422 (2016).

6. **Return of backbending in ^{169}Tm and the effect of the N=98 deformed shell gap.**
Md. A. Asgar, T. Roy, G. Mukherjee, A. Dhal, **Soumik Bhattacharya**, S. Bhattacharyya, C. Bhattacharya, S. Bhattacharya, A. Chaudhuri, K. Banerjee, S. Kundu, S. Manna, R. Pandey, J. K. Meena, R. Palit, S. Biswas, S. Saha, J. Sethi, P. Singh, and D. Choudhury.
Phys. Rev. C Vol. **95**, 031304(R) (2017).

7. **Evolution of triaxial shapes at large isospin: Rh isotopes.**
A. Navin, M. Rejmund, S. Bhattacharyya, R. Palit, G.H. Bhat, J.A. Sheikh, A. Lemasson, **S. Bhattacharya**, M. Caamaño, E. Clément, O. Delaune, F. Farget, G. de France, B. Jacquot.
Phys. Let. B. Vol. **767**, 480 (2017).

8. **Experimental Determination of η/s for Finite Nuclear Matter.**
Debasish Mondal, Deepak Pandit, S. Mukhopadhyay, Surajit Pal, Balaram Dey, Srijit Bhattacharya, A. De, **Soumik Bhattaacharya**, S. Bhattacharyya, Pratap Roy, K

Banerjee and S. R. Banerjee.
Phys. Rev. Let. Vol. **118**, 192501 (2017).

9. **Prompt-delayed γ-ray spectroscopy with AGATA, EXOGAM and VAMOS++.**
   Y. H. Kim, A. Lemasson, M. Rejmund, A. Navin, S. Biswas, C. Michelagnoli, I. Stefan, R. Banik, P. Bednarczyk, **S. Bhattacharya**, S. Bhattacharyya, E. Clément, H. L. Crawford, G. De France, P. Fallon, J. Goupil, B. Jacquot, H. J. Li, J. Ljungvall, A. O. Macchiavelli, A. Maj, L. Ménager, V. Morel, R. Palit, R. M. Pérez-Vidal, J. Ropert and C. Schmitt.
   Eur. Phys. J. A Vol. **53**, 162 (2017).

10. **Excited negative parity bands in ^{160}Yb.**
    A. Saha, T. Bhattacharjee, D. Curien, I. Dedes, K. Mazurek, S. R. Banerjee, S. Rajbanshi, A. Bisoi, G. de Angelis, **S. Bhattacharya**, S. Bhattacharyya, S. Biswas, A. Chakraborty, S. Das Gupta, B. Dey, A. Goswami, D. Mondal, D. Pandit, R. Palit, T. Roy, R. P. Singh, M. S. Sarkar, S. Saha, J. Sethi.
    Phys. Scr. Vol. **93**, (2018) 034001.

11. **Spectroscopy of low lying states in ^{150}Sm.**
    A. Saha, T. Bhattacharjee, S. S. Alam, D.Banerjee, M. S. Sarkar, S. Sarkar, J. B. Gupta, P. Das, **S.Bhattacharya**, D. Pandit, R. Guin, S. K. Das, S. R. Banerjee.
    Nucl. Phys. A Vol. **976**, 1 (2018).

12. **Observation of multiple doubly degenerate bands in ^{195}Tl.**
    T.Roy, G. Mukherjee, Md. A. Asgar, S. Bhattacharyya, **Soumik Bhattacharya**, C. Bhattacharya, S. Bhattacharya, T. K. Ghosh, K. Banerjee, Samir Kundu, T. K. Rana, P. Roy, R. Pandey, J. Meena, A. Dhal, R. Palit, S. Saha, J. Sethi, Shital Thakur, B. S. Naidu, S. V. Jadav, R. Dhonti, H. Pai, A. Goswami.
    Phys. Let. B. Vol. **782**, 768 (2018).

13. **Slow fission of highly excited plutonium nuclei.**
    A. K. Sikdar, A. Ray, Deepak Pandit, B. Dey, Sarmishtha Bhattacharyya, **Soumik Bhat-**

tacharya, A. Bisoi, A. De, S. Paul, Srijit Bhattacharya, and A. Chatterjee.
Phys. Rev. C Vol. **98**, 024615 (2018).

14. **Deformed band structures in neutron-rich $^{152-158}Pm$ isotopes.**
S. Bhattacharyya, E. H. Wang, A. Navin, M. Rejmund, J. H. Hamilton, A. V. Ramayya, J. K. Hwang, A. Lemasson, A. V. Afanasjev, **Soumik Bhattacharya**, J. Ranger, M. Caamaño, E. Clément, O. Delaune, F. Farget, G. de France, B. Jacquot, Y. X. Luo, Yu. Ts. Oganessian, J. O. Rasmussen, G. M. Ter-Akopian, and S. J. Zhu.
Phys. Rev. C Vol. **98**, 044316 (2018).

15. **A Compton suppressed detector multiplicity trigger based digital DAQ for gamma-ray Spectroscopy.**
S. Das, S. Samanta, R. Banik, R. Bhattacharjee, K. Basu, R. Raut, S.S. Ghugre, A.K. Sinha, **Soumik Bhattacharya**, S. Imran , G. Mukherjee, S. Bhattacharyya, A. Goswami, R. Palit and H. Tan.
Nucl. Inst. and Meth. Phys. Res. A Vol. **893**, 138 (2018).

16. **Spectroscopy of a tetrahedral doubly magic candidate nucleus $^{160}_{70}Yb_{90}$.**
A. Saha, T. Bhattacharjee, D. Curien, J. Dudek, I. Dedes, K. Mazurek, A. Góźdź, S. Tagami, Y. R. Shimizu, S. R. Banerjee, S. Rajbanshi, A. Bisoi, G. De Angelis, **Soumik Bhattacharya**, S. Bhattacharyya, S. Biswas, A. Chakraborty, S. Das Gupta, B. Dey, A. Goswami, D. Mondal, D. Pandit, R. Palit, T. Roy, R. P. Singh, M. Saha Sarkar, S. Saha and J. Sethi.
J. Phys. G Vol. **46**, (2019) 055102.

17. **Effect of neutron alignments on the structure of ^{197}Tl.**
S. Nandi, G. Mukherjee, T. Roy, R. Banik, A. Dhal, **Soumik Bhattacharya**, S. Bhattacharyya, C. Bhattacharya, Md. A. Asgar, H. Pai, S. Rajbanshi, Pratap Roy, T. K. Ghosh, K. Banerjee, T. K. Rana, Samir Kundu, S. Manna, R. Pandey, A. Sen, S. Pal, S. Mukhopadhyay, D. Pandit, D. Mandal, and S. R. Banerjee.
Phys. Rev. C Vol. **99**, 054312 (2019).

18. **Effects of one valence proton on seniority and angular momentum of neutrons in neutron-rich $^{122-131}_{51}Sb$ isotopes.**

    S. Biswas, A. Lemasson, M. Rejmund, A. Navin, Y. H. Kim, C. Michelagnoli, I. Stefan, R. Banik, P. Bednarczyk, **S. Bhattacharya**, S. Bhattacharyya, E. Clément, H. L. Crawford, G. de France, P. Fallon, G. Frémont, J. Goupil, B. Jacquot, H. J. Li, J. Ljungvall, A. Maj, L. Ménager, V. Morel, R. Palit, R. M. Pérez-Vidal, J. Ropert, D. Barrientos, G. Benzoni, B. Birkenbach, A. J. Boston, H. C. Boston, B. Cederwall, J. Collado, D. M. Cullen, P. Désesquelles, C. Domingo-Pardo, J. Dudouet, J. Eberth, V. González, L. J. Harkness-Brennan, H. Hess, A. Jungclaus, W. Korten, M. Labiche, A. Lefevre, R. Menegazzo, D. Mengoni, B. Million, D. R. Napoli, A. Pullia, B. Quintana, D. Ralet, F. Recchia, P. Reiter, F. Saillant, M. D. Salsac, E. Sanchis, O. Stezowski, Ch. Theisen, J. J. Valiente-Dobón, and M. Zieliska.

    Phys. Rev. C Vol. **99**, 064302 (2019).

Other results reported in Conferences/Symposia :

1. **Investigation of isomers around mass 200 region.**

   S. Das Gupta, S. Bhattacharyya, H. Pai, G. Mukherjee, **Soumik Bhattacharya**, R. Palit, A. Shrivastava, A. Chatterjee, S. Chanda, V. Nanal, S.K. Pandit, S. Saha, J. Sethi, S. Thakur.

   Proceedings of the International Symposium on nuclear physics, DAE, Vol **58**, 212 (2013).

2. **Digital Pulse Processing and DAQ System for INGA at VECC.**

   S. Chatterjee, S. Das, S. Samanta, K. Basu, R. Raut, S. S. Ghugre, A. K. Sinha, R. Banik, S. Bhattacharya, S. Nandi, A. Dhal, A. Choudhury, P. Mukhopadhyay, S. Imran, S. Bhattacharyya, G. Mukherjee, C. Bhattacharya, S. Ali, P. Ray, S. Rajbanshi, H.Pai, A. Goswami and H. Tan.

   Proceedings of the International Symposium on nuclear physics, DAE, Vol **63**, 1100 (2018).

Dedicated to my 'Parents',

Shri Saibal Kanti Bhattacharya and Smt. Banani Bhattacharya,

who supported me all the way

ACKNOWLEDGMENTS

I gratefully acknowledge the constant and invaluable academic and personal support received from my supervisors Dr. Sarmishtha Bhattacharyya throughout my thesis work. I am really thankful and indebted to her for having been the adviser everyone would like to have, for helping me to find my firm grounding in the research problem and without her dedicated supervision it would have been never possible to complete this thesis.

I am extremely grateful to Dr. Gopal Mukherjee for always extending his support in every field towards me. He has literally guided me through the rough paths of research. I was extremely fortunate to have him by my side to ease the problems I faced during my research work. I am really thankful to him for his clear and enthusiastic discussion and doubt clearing sessions. Thank you Sir.

I am very much indebted to Prof. Dinesh Kumar Srivastava, former Director, Variable Energy Cyclotron Centre (VECC), Prof. Sailajananda Bhattacharya, Former Head, Physics Group, VECC, Prof. Sudhee Ranjan Banerjee, Former Head, experimental nuclear physics division, VECC, for giving me the encouragement and kind support. I express my sincere gratitude to our Division Head, Dr. Chandana Bhattacharya, for being extremely caring and for her guidance during the course of the work. I am grateful to our Director, Dr. Sumit Som as well to our Group Head and Former dean, HBNI Prof. Jane Alam for providing a vibrant working atmosphere and full fledged facility which helped me immensely to complete my thesis work.

The excellent support and encouragement received from Mrs. Anindita Chowdhury, Mr. Pulak Mukhopadhyay and Imran Seikh of 'Physics Lab', VECC, is very much appreciated. Without your support it would be 10 times more difficult. I am very much indebted to Tanmoy Da, Asgar, Soumen, Arunabha, Safikul and all the other members of Experimental Nuclear Physics Division, VECC for their suggestions and help through out my Ph. D. work.

I would like to express my special thanks to my junior Ranabir for helping me out throughout my research work. I very much appreciate his help in almost every area and also the mental support provided by him. Thank you brother for being there.

I am extremely grateful to Dr. Supriya Mukhopadhyay, Dr. T. K. Ghosh, Dr. Deepak Pandit, Dr. Pratap Roy, Dr. Tumpa Bhattacharjee, VECC, Dr. Rudrajyoti Palit from TIFR, Mumbai, Prof. Amit Roy, Prof. Partha Chowdhury, Lowell University, Dr. Rajarshi Raut and Dr. S. S. Ghugre from UGC, DAE CSR, Kolkata center for their encouragement and kind support. I have really enjoyed the discussion with them on various physics issues.

I would like to give my sincere thanks to Late Professor Asimananda Goswami from Saha Institute of Nuclear Physics for his helps and suggestions at various stages of my work. I miss you very much sir. Your useful suggestions and experience in Physics as well as in experimental aspects will be missed.

It is my great pleasure to thank Hari Da and Shinjinee Di for their constant enthusiasm and kind support throughout my thesis work. Your early stage guidance is very much appreciated to understand the field of research. I am really thankful to God having such seniors like you two. Thank you.

I am really grateful to Debasish, Arindam Da, Santu, Chandrasekhar, Chiranjib, Pratanu, Arup for their encouragement and inspiration.

I would like to mention a special thanks to all of my friends as well as physics teachers (Late Prof. Swapan Kumar Dutta, Prof. A. Chakraborty and others) throughout different part of my life, without whom it would never been possible to start the journey of physics for me. Thank you Abhishek, Aritra Saha(late), Sayak, Shantanob(Bhola), Asim, Avijit, Sanjoy, Arif, Avik (kaka), Ayan. I would never understand the complex problems of physics without your sensible teaching throughout the journey.

The help of all the collaborators in the present work, from different institutions (VECC, TIFR, IUAC, UGC-DAE-CSR, SINP), in India are gratefully acknowledged. The effort of the operators of the accelerators at VECC, TIFR and all the participating group in the CLOVER Array Collaboration are acknowledged.

I am deeply indebted and grateful to my Maa-Baba, Didibhai and my wife Dipanwita and rest of my family members. I do appreciate the unlimited support, love and encouragement that you have given to me during my study. Without them I would be nothing. Thank you very much. At this moment, I very much remember with gratitude that my mother, father and elder sister who always encouraged my likings and gave confidence to produce my best.

Last but the most importantly I would like to extend my heartiest congratulations to my wife to make my journey smooth, to understand my passion and accepting my escape of household duty. This is your degree too. Thank you for your unending support and love.

I sincerely apologize inadvertent omission of any name from the above list of acknowledgment.

Soumik Bhattacharya